CONTROLLING MIXING AND SEGREGATION IN TIME PERIODIC GRANULAR FLOWS

by

Tathagata Bhattacharya

Master of Technology, Indian Institute of Technology (IIT),

Kanpur, India, 2002

Bachelor of Engineering, The University of North Bengal,

Darjeeling, India, 2000

Submitted to the Graduate Faculty of

the Swanson School of Engineering in partial fulfillment

of the requirements for the degree of

Doctor of Philosophy

University of Pittsburgh

2011

UNIVERSITY OF PITTSBURGH

SWANSON SCHOOL OF ENGINEERING

This dissertation was presented

by

Tathagata Bhattacharya

It was defended on

September 22, 2011

and approved by

Joseph J. McCarthy, Ph.D., Professor, Department of Chemical and Petroleum Engineering

Robert S. Parker, Ph.D., Associate Professor, Department of Chemical and Petroleum

Engineering

Sachin S. Velankar, Ph.D., Associate Professor, Department of Chemical and Petroleum

Engineering

Albert C. To, Ph.D., Assistant Professor, Department of Mechanical Engineering and

Materials Science

Dissertation Director: Joseph J. McCarthy, Ph.D., Professor, Department of Chemical and

Petroleum Engineering

ABSTRACT

CONTROLLING MIXING AND SEGREGATION IN TIME PERIODIC
GRANULAR FLOWS

Tathagata Bhattacharya, PhD

University of Pittsburgh, 2011

Segregation is a major problem for many solids processing industries. Differences in particle size or density can lead to flow-induced segregation. In the present work, we employ the discrete element method (DEM) – one type of particle dynamics (PD) technique – to investigate the mixing and segregation of granular material in some prototypical solid handling devices, such as a rotating drum and chute. In DEM, one calculates the trajectories of individual particles based on Newton's laws of motion by employing suitable contact force models and a collision detection algorithm. Recently, it has been suggested that segregation in particle mixers can be thwarted if the particle flow is inverted at a rate above a critical forcing frequency. Further, it has been hypothesized that, for a rotating drum, the effectiveness of this technique can be linked to the probability distribution of the number of times a particle passes through the flowing layer per rotation of the drum. In the first portion of this work, various configurations of solid mixers are numerically and experimentally studied to investigate the conditions for improved mixing in light of these hypotheses.

Besides rotating drums, many studies of granular flow have focused on gravity driven chute flows owing to its practical importance in granular transportation and to the fact that the relative simplicity of this type of flow allows for development and testing of new theories. In this part of the work, we observe the deposition behavior of both mono-sized and polydisperse dry granular materials in an inclined chute flow. The effects of different parameters such as chute angle, particle size, falling height and charge amount on the mass

fraction distribution of granular materials after deposition are investigated. The simulation results obtained using DEM are compared with the experimental findings and a high degree of agreement is observed. Tuning of the underlying contact force parameters allows the achievement of realistic results and is used as a means of validating the model against available experimental data. The tuned model is then used to find the critical chute length for segregation based on the hypothesis that segregation can be thwarted if the particle flow is inverted at a rate above a critical forcing frequency. The critical frequency, f_{crit}, is inversely proportional to the characteristic time of segregation, t_s. Mixing is observed instead of segregation when the chute length $L < U_{avg}t_s$, where U_{avg} denotes the average stream-wise flow velocity of the particles.

While segregation is often an undesired effect, sometimes separating the components of a particle mixture is the ultimate goal. Rate-based separation processes hold promise as both more environmentally benign as well as less energy intensive when compared to conventional particle separations technologies such as vibrating screens or flotation methods. This approach is based on differences in the kinetic properties of the components of a mixture, such as the velocity of migration or diffusivity. In this portion of the work, two examples of novel rate-based separation devices are demonstrated. The first example involves the study of the dynamics of gravity-driven particles through an array of obstacles. Both discrete element (DEM) simulations and experiments are used to augment the understanding of this device. Dissipative collisions (both between the particles themselves and with the obstacles) give rise to a diffusive motion of particles perpendicular to the flow direction and the differences in diffusion lengths are exploited to separate the particles. The second example employs DEM to analyze a ratchet mechanism where a current of particles can be produced in a direction perpendicular to the energy input. In this setup, a vibrating saw-toothed base is employed to induce different mobility for different types of particles. The effect of operating conditions and design parameters on the separation efficiency are discussed.

Keywords: granular flow, particle, mixing, segregation, discrete element method, particle
    dynamics, tumbler, chute, periodic flow inversion, collisional flow, rate-based separation,
    ratchet, static separator, dissipative particle dynamics, non-spherical droplet.

TABLE OF CONTENTS

LIST OF TABLES

LIST OF FIGURES

PREFACE

I am extremely grateful to my advisor, Prof. J. J. McCarthy, for his untiring guidance, support, and encouragement throughout the journey of my PhD work. Though his spirited thinking has definitely helped me in fulfilling my intellectual curiosities, the wisdom I gained while working with him would stay with me for a life-time.

I am also indebted to all the members of my PhD committee for their insightful comments and suggestions, which added immensely to the quality of this work.

I would like to thank my friends and colleagues who accompanied me through all the life's ups and downs during my stay at Pittsburgh, particularly, Adel Alenzi and Ashish Yeri. I am also grateful to my past lab-mates: Deliang Shi, Isabel Figueroa, Suman Hajra and Watson Vargas, for their timely help. I also enjoyed working with the REU students, especially, Samantha Schmidt and Sheryl Chocron.

I would also like to thank the management and my past colleagues at Tata Steel, where I worked for five years prior to the beginning of my PhD work. It was during my research at R&D, Tata Steel, that I found granular flows to be fascinating, and thus, the first seeds of curiosity about particle flows were sown.

Finally, I would like to dedicate this work to my late grandfather, Shri Bijoy Krishna Bhattacharya, for showing us the value of education. It would be squarely unfair if I fail to acknowledge the support and sacrifice of my wife, Aditi Datta, who being an active researcher herself, was always there with a smiling face in times of troubles. My daughter, Adrita, who was born in the first year of my graduate studies, made my journey much more bearable with her million-dollar smiles. I also acknowledge my parents and parents-in-law for extending invaluable assistance in many ways from day-one of my graduate studies.

1.0   INTRODUCTION

Granular materials are ubiquitous. It is hard to find a process industry that does not handle granular materials in any form. These materials are widely used in chemical, pharmaceutical, cement, agricultural, food, construction, minerals and metallurgical industries, to name a few. Although very common, granular materials pose unique challenges and display counter-intuitive behavior that makes research in this field exciting and stimulating. Understanding the fundamental behavior of these materials can determine the success or failure of a vast number of man-made and natural processes. In fact, this class of materials ranks second, behind water, on the scale of priorities of human activities and endeavors [5]. Hence, even a fractional advance in our understanding of the behavior of granular materials can have a profound impact on our economic and general well-being [5]. Granular processing accounts for as much as $61 billion in the USA, 40% of the value added by the chemical industry [6]. Approximately one-half of the products, and more than three-quarters of the raw materials used in chemical industries, are in granular form [7]. Mixing of powders is critical in industries such as pharmaceutical [8] and food [9]. There are other operations that require the transfer of heat or mass within the granular materials, like the calcination of minerals in rotary kilns [10], or the drying of fruits and grains [11] or producing carbon nano-tubes in a rotary reactor [12]. Transporting, mixing, blending, pressing, heating, coating, granulation and drying of granular materials are a few of the many examples where the understanding of the flow of granular materials is critical for success of the operation.

An important phenomenon concerning the flow of granular materials is segregation or de-mixing. Particle segregation has been a topic of intense research and industrial frustration for many decades [13–16]. Small differences in any mechanical property of the particles (size, density, shape, etc.) lead to flow induced segregation where one type of particle tends

1

to segregate or leave the main stream of particles due to the differences. Processing of these materials typically leads to pattern formation [17, 18], layering [19, 20] or complete separation of the materials [21–23]. Segregation is unique to granular materials and has no parallels in fluids. Also, contrary to fluid mixing, where more agitation implies better mixing [24], a granular system might segregate into different regions in a container when agitated strongly. Segregation is undesirable in most of the particle processing industries as it creates non-uniform product quality, which may result in dramatic revenue losses. In order to emphasize the importance of the understanding of granular flow, consider the example of manufacturing of tablets in a pharmaceutical industry: reliable and uninterrupted flow of well-blended powders is key to the success of a tableting process. Unavoidable segregation occurs during transfer of materials from the blender to the tableting press as this process requires the blended material to flow through many solids handling devices such as chutes or hoppers. A batch of powder, potentially worth millions of dollars, would have to be discarded if only five tablets do not conform to the final product quality due to the strict quality control standards enforced in these industries [25].

A common feature of these materials is structural evolution on a number of different length and time scales. Furthermore, they are not easily characterized as a solid or a liquid or a gas [26], often possessing very complex rheological properties governed by intermediate scale structure. This intermediate scale structure is between macro or continuum scale and the atomic scale, and corresponds to microscale or mesoscale. Granular materials share much of the complex behavior common to soft matter or complex fluids [27]: segregation and pattern formation, flow by rearrangement of grains, and solid and liquid-like behavior. The physics of two interacting particles in a granular assembly is well understood, however, the complexity arising from the interactions of an assembly of particles is not well understood. Hence, a common goal of those studying granular material is to relate macrostructural (bulk) behavior to the underlying microstructural (discrete) dynamics and kinematics.

Mixing of granular materials is, without exception, accompanied by segregation, avalanching, stratification etc., however, the fundamentals of the processes still defy understanding. While a qualitative understanding of the mechanisms of segregation has existed for some time now [14, 28, 29], there are remarkably few models that give quantitative predictions of

the extent of segregation [30]. Such information is particularly important in the analysis and design of industrial mixing operations. Modeling of mixing and segregation requires the confluence of several tools, including the three primary approaches, namely continuum based approach, discrete approach and kinetic theory based approach. None of these approaches, however, is wholly satisfactory by itself. Most of the current practices are heuristic with limited possibilities of generalization. The absence of general constitutive equations to predict the extent of segregation is clearly an impediment to systematic approaches to the problem. Moreover, the approaches are regime dependent, which may require adopting different sub-viewpoints.

The broad objective of the present work is to examine the segregation phenomena (with the central theme on size driven segregation as density segregation is somewhat understood [30]), what causes it, and investigate ways to control it. We investigate the segregation phenomenon in two industrially relevant granular systems: The effect of different operating parameters on mixing/segregation in a prototypical solids mixer (a rotating drum , chapter 3) and also in a simple flow device (a chute, chapter 4). Recently [31], it has been suggested that segregation in particle mixers can be thwarted if the particle flow is inverted at a rate above a critical forcing frequency. Therefore, in the present work, we also attempt to test this hypothesis on mitigating segregation based on fundamental physics of granular flow in those prototypical solids flow devices.

While segregation is often an undesired effect, sometimes separating the components of a particle mixture is the ultimate goal in many industrial processes. As part of the present work, we investigate two novel rate-based separation devices, which require no or small energy input and are environmentally benign (green). This constitutes the subject matter of chapter 5. There, we examine how a drift-diffusive motion can be generated in a collisional granular flow, which in turn, could be used to separate a granular mixture. Possibilities of another method of separation using a ratchet mechanism are also demonstrated.

The great majority of existing models of granular flow were developed using classical continuum theory. Although the continuum models are readily accessible and in extensive use, they possess no length scale, and hence, cannot accommodate microstructure (or, the information about individual particles). There is now experimental evidence [5] which suggests

that microstructural mechanisms control the bulk behavior of granular media. A second approach, called the discrete element method (DEM), is an alternative choice that deals explicitly with the microstructure. DEM uses the techniques of molecular dynamics simulation to capture the motion of every particle in a large assembly. In this approach, properties of particles such as size, shape, and density can be directly specified, thus DEM is a suitable tool for analyzing segregation. Details such as velocity and concentration profiles for every component in a mixture can be obtained. However, the number of particles and their shapes that can be simulated in DEM is limited by computer power, such that many industrial scale processes are beyond the reach of DEM. Moreover, DEM might not be able to predict the results well when the system is scaled-up (unless the actual system is simulated). In contrast, continuum theories do not have the limitations of scale-up to larger system sizes as these models are based on constitutive relations (sometimes obtained by fitting phenomenological equations to various data, such as output from DEM). The continuum theories are broadly based on the transport equations obtained using kinetic theories, in some cases including empirical corrections for inter-particle friction. The continuum model has been successful in predicting experimentally measured stresses and flow profiles for particles in shear flows and chute flows.

The lack of a comprehensive theory has promoted the advance of numerical simulations in the field of granular materials. Therefore, a large part of the work presented in the following chapters is carried out using DEM (also known as particle dynamics (PD)). First developed by Cundall and Strack [2] in 1979, DEM has emerged as a successful simulation technique to study granular flows, giving insight into phenomena ranging from force transmission, agglomerate formation, flow of cohesionless materials, pneumatic conveying, fast fluidization, etc. This simulation technique is based on Newton's laws of motion – also known as the Lagrangian approach – according to which individual particles are treated as contacting bodies. The trajectories of each particle (i.e., position, velocity, orientation, etc.) give insight into the macroscopic flow of the granular assembly. At the heart of this methodology lies an efficient contact detection algorithm and a model to calculate the contact properties between particles. DEM is used not only to model the flow of the granular material but also

to simulate processes that involve the transfer of heat [32–34] and mass [31,35]. For the sake of completeness, Chapter 2 will discuss the necessary background of the particle dynamics technique.

The remainder of this dissertation is organized as follows: Chapter 2 covers the relevant background about the mechanisms of mixing and segregation including a literature review of the body of knowledge on free surface segregation. Understanding of the free surface segregation phenomenon is very important as this type of segregation is prevalent in the systems studied in the current work. This chapter also describes the simulation methodology, namely the particle dynamics (PD) technique, covering different force models and contact detection algorithm. Also included is a description of various mixing indices used to quantify mixing and segregation in a particulate system. Chapter 3 presents the experimental and simulation results regarding the control of segregation in a tumbler mixer. The hypothesis regarding a critical forcing frequency is tested in a baffled tumbler, which is also utilized as a feed-back tool to select the most successful baffle configuration from a host of promising designs of tumbler mixers. Chapter 4 deals with another granular system of industrial importance – a chute flow. A chute flow segregation tester is described where DEM results are validated with experimental data. The validated DEM model is then used to corroborate the continuum-derived hypothesis of critical forcing frequency in a chute flow. Results demonstrating the development of a characteristic segregation time along with a critical chute length (beyond which segregation will prevail) are presented. The following chapter (Chapter 5) proposes two novel rate-based separation devices, which require little or no energy input to separate particles in a granular mixture. The first rate-based separation study involves probing the dynamics of gravity-driven particle flow through an array of obstacles, and in the second example, DEM is employed to analyze a ratchet mechanism where a directed current of particles can be produced perpendicular to the direction of energy input. Methods to characterize the systems with respect to their separation capability are elaborated, which include simulation, theory and experiments. Finally, Chapter 6 closes with a brief summary along with an outlook on future extensions. Also covered is a short discussion on the remaining challenges to link the fundamental physics of particle flow and the industrial needs.

2.0   BACKGROUND

In this chapter, we provide the background information relevant to understanding the problems that we mentioned in the Introduction chapter. Especially, the past work by other researchers in the area of segregation is briefly reviewed and possible shortcomings or gaps in their work are highlighted.

2.1   THE BASICS OF SEGREGATION

We first present a general discussion of free surface segregation as this is very relevant to what follows in the next chapters. As we continue to review, we also present a historical perspective of the study of segregation.

One of the earliest studies on segregation dates back to 1939. In 1939, a Japanese researcher, Yositisi Oyama, reported a work that dealt with mixing of two granular materials in a rotating cylinder (see reference in Otino, 2010 [36]). It is worth mentioning here that in the same year, Brown [13] reported the fundamental principles of segregation and pointed out that segregation is often a surface phenomena. Though Oyama was investigating mixing of two solids, he found out the occurrence of what is now known as "axial segregation". The knowledge of segregation and its effects were long known to the engineers as they had to deal with poor product quality due to segregation. In fact, there was a patent in 1904 which sought to prevent the occurrence of clinker rings in rotary kilns due to axial segregation [36]. The focus was on how to mitigate segregation by solving the problem on a case-by-case basis rather than the fundamental understanding of it. Therefore, we observe that the early studies on segregation were carried out in pockets, mainly by industrial researchers, even

long before the scientific community took a serious look at it. During the late 80's, this field became a hotbed for research as physicists acknowledged that the physics of granular materials are largely unexplored [37] and engineers stressed that a better understanding of granular materials would have a tremendous benefit to industry [6]. Also, the attention of some of the influential physicists (like Nobel Laureate de Gennes [38]) in granular research caused a strong growth in research and publication in this field.

In many industrial processes (such as in pharmaceuticals or food), the goal is to blend two or more particulate materials uniformly, where size segregation is undesired. However, in some cases (such as in mining and agricultural engineering [39]), size segregation or separation is intended. Standish [40] outlined several mechanisms for segregation which are of particular relevance to shearing flow. The actual segregation patterns are numerous and depend on the prevailing segregation mechanism – the most prevalent being the percolation mechanism, i.e., sifting of fines through the voids of larger particles, either spontaneous [41] or shear-induced (mainly in size segregation). Spontaneous percolation takes place when the ratio of the percolating particle diameter to the bed particle diameter is less than a threshold (0.1547 [41]). The following summarizes different mechanisms as described by Standish:

- Percolation or consolidation trickling mechanism
- Angle of repose mechanism
- Inertia mechanism
- Trajectory mechanism (fluid resistance mechanism)

The angle of repose mechanism leads to separation of the material having the steepest angle of repose. The inertia mechanism generally refers to the segregation of coarse particles to the base of a heap, for example, because larger particles would roll down a larger distance. Segregation may occur due to fluid resistance or drag on a particle which is of interest in a fluidized system (such as in a blast furnace where the particles land on the stock-line from a chute against hot ascending gas). Particles would segregate due to fluid resistance and this force resisting the motion of particles is a strong function of the particle shape. Apart from the above classifications, some researchers also suggested a similar classification for segregation mechanism (although many more have been identified in the literature [42]):

percolation/sieving, fluidization, convection, and trajectory segregation. These four mechanisms are nearly similar to the ones proposed by Standish [40] and share many common features. They have been pictorially described in Figure 1.

Amongst the early literature [13, 14, 28, 43–48], Drahun et al. [49] seem to be the first workers who have done extensive experimentation on this particular topic by analyzing the effects of various variables on segregation. They have reported comprehensive findings on the mechanism of free surface segregation along a slope, which can be helpful in understanding exactly the same phenomena occurring in a tumbler or in a chute flow. Their report also contained an assessment of previous work (15 references therein) performed on the mechanism of segregation. They observed that although the existence of free surface segregation had long been recognized, there had been few attempts to produce theories that would predict quantitatively the amount of segregation. Most investigators were primarily interested in the prevention of segregation rather than the factors that caused it. Therefore, attempts were made to solve a particular problem on an ad-hoc basis without fundamental understanding of its occurrence. Moreover, the results of some of the studies are not generic and are not applicable universally. Drahun et al. noted that, in general, analytical models do not capture the key features of free surface segregation satisfactorily (e.g., the predictive models by Matthee [45] and Tanaka [46]). Drahun et al.'s study was conducted with binary systems where one component was present in small quantities. The experimental setup permitted the slope length, solids flow rate and solids fall height to be varied independently in order to assess the effects of independent variables (e.g., size, density, shape, free fall height, etc.) on the rate and extent of segregation. Results were presented in dimensionless form and the major findings from their work are summarized below:

- Free surface segregation occurs by avalanching, inter-particle percolation and particle migration.
- Both diameter and density have a significant effect on segregation. Smaller particles sink by percolation and are found closer to the pouring point, whereas large particles rise to the surface by particle migration and are found at the extreme end of the surface. On the other hand, the denser particles are found near the pouring point and less dense particles at the far end. This gives rise to stratification.
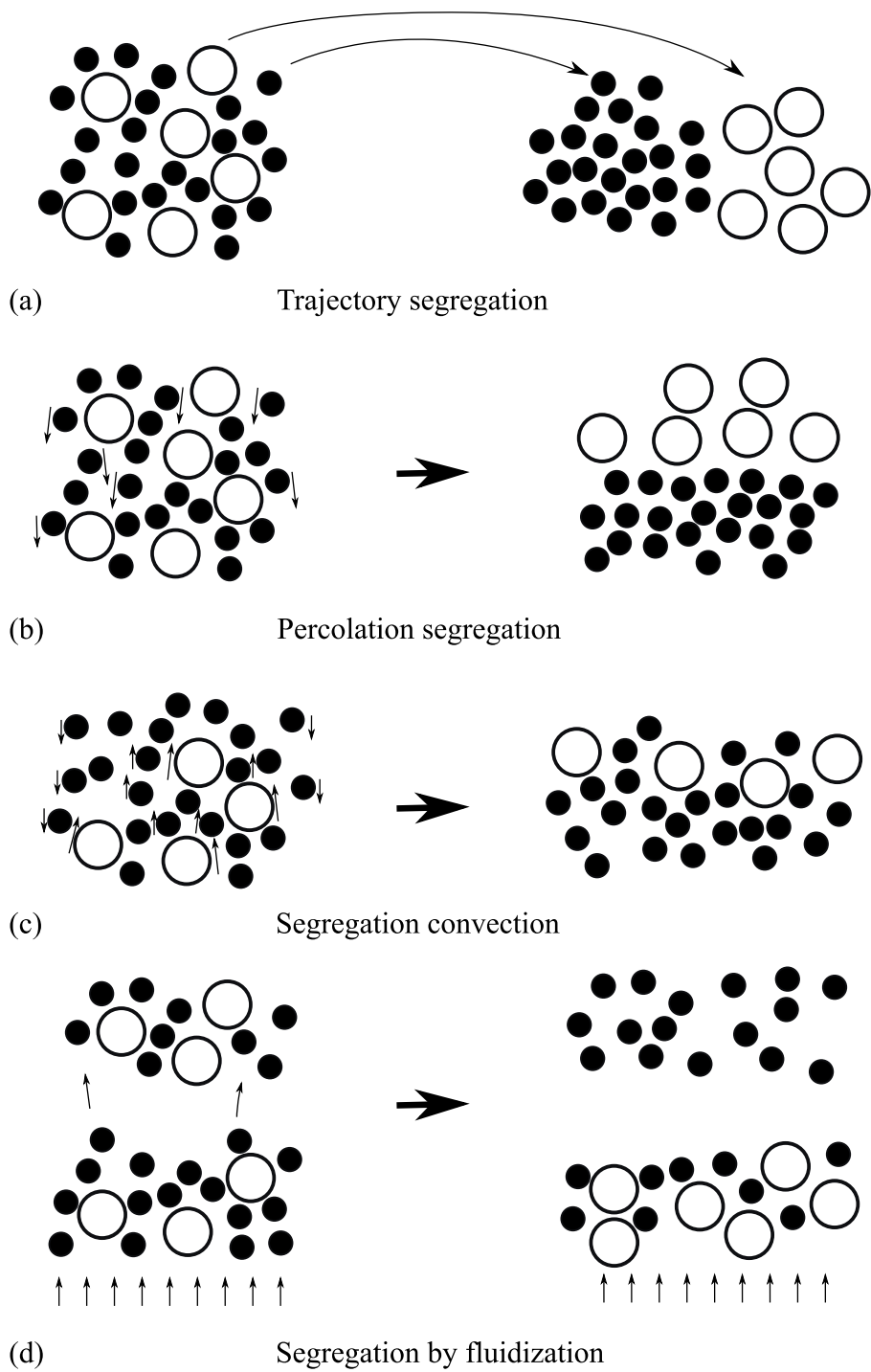
Figure 1: Various segregation mechanisms (illustration obtained from Figueroa [1] with permission).

- An increase in particle velocity onto the inclined surface influences the material distribution controlled by diameter but not that controlled by density. In particular, if the free fall height is increased, the smaller particles bounce down the free surface to the far end.
- A slight segregation in a feeding device like conveyor or hopper can markedly influence the free surface segregation.
- Free surface segregation can be minimized by appropriate balance of size ratio and density ratio.
- Particle shape, unless extreme such as needles or platelets, does not have much effect on segregation.
- Surface roughness or the surface friction arising out of the shape has no effect on segregation. Rolling and sliding do not contribute greatly to segregation.

Recently, Makse et al. [50] has provided some explanations to the above mentioned phenomena, especially, stratification or layering. When poured between two vertical plates, a granular mixture spontaneously stratifies into alternating layers of small and large particles whenever the large particles have larger angle of repose than the small ones. Makse et al. also found spontaneous segregation, without stratification, when the large particles have smaller angle of repose than the small ones.

Tanaka et al. [46] developed a first principle 2D mathematical model, which is capable of describing the movement of only two particles relative to one another using a critical friction coefficient as the determining factor for one of the two particles' movement. It was originally used to quantify the segregation phenomena in flows from hoppers. This model was later modified by Kajiwara et al. [51] and Tanaka et al. [52] to analyze the segregation phenomena in an industrial process: Distribution of coke and iron ore at the top of a blast furnace. The mathematical model used a discrete approach to analyze the granular flow problem. In their work, the distinct (or discrete) element method (DEM) technique was employed. The constitutive equation for interaction between two particles was described by a Voigt-Kelvin rheological model with a slider and dashpot. Previously, Cundall and Strack (1979) [2] described a similar discrete model to capture the behavior of an assembly of particles, but they did not employ a viscous effect when approximating the sliding condition. Later, Kajiwara et al. [51] used a slider and dashpot, which represented

the kinetic energy dissipation of particles, and the accuracy of the model was enhanced. In their study, the dashpot factor was experimentally determined. In their report, the authors cited a few references where different techniques were reviewed and their drawbacks in effectively modeling the flow dynamics of granular material were mentioned. They found that there is extensive literature on the flow of granular materials under the assumption of continuum, but those studies lack generality and cannot capture the segregation phenomena with higher analytical accuracy. Kajiwara et al. also claimed that their work has led to a better understanding of the solids flow in the process and can remove the inherent difficulties in a continuum approach. Their model was used to examine segregation during discharge from a hopper. Specifically, they analyzed the particle size distribution when a stone box (one type of insert) was used in the hopper: the stone box suppressed the variation of particle size distribution during discharge in the radial direction. Kajiwara et al.'s model also precisely described the frictional wall effect in solids flow and bridge formation. In a nutshell, this work was one of the first computational efforts to apply DEM to understand the segregation phenomena in an industrial process.

Since DEM is computationally demanding, Kajiwara and Tanaka's group developed another model [53] based on percolation theory to examine the sieving behavior of smaller particles on a slope and to study segregation. The percolation frequency of the small particle is determined by particle size ratio and the velocity gradient. Earlier, Bridgwater et al. [48] had shown the functional behavior of this percolation frequency using experiments.

There have been many efforts to model the free surface segregation in simple shear flows (such as in pile/heap formation) based on continuum principles. Some of the first studies were done by Bouchaud et al. (BCRE model, after Bouchaud, Cates, Ravi and Edwards) [54] and Mehta et al. [55]. In the BCRE model, they considered single-species sandpile (no segregation) and used two coupled variables to describe the evolution of sand piles. The two variables were the height of the sand pile $h(x,t)$ (which corresponds to static bed), and the local thickness of the rolling layer, $R(x,t)$. BCRE also proposed a set of convective-diffusion equations for the rolling grains, which was later simplified by de Gennes [56]. Recently, Boutreux and de Gennes (BdG model) [57] extended the BCRE model for the case of two species (the so-called "minimal" model). In this model, grains with different surface

11

properties but of equal size were considered. Since the minimal model does not take into account the size difference between the grains, Boutreux had treated the important case (the so-called "canonical" model) where the grains differed only in size (surface properties being the same), in a second article [58,59] of the series started by BdG [57]. Boutreux [59] argued that unlike Makse et al. [60] (whose modification of first BdG model [57] applies only to a case with large difference of size), their generalization is applicable for situations where the species have a small difference of sizes. In the last and third paper of the BdG series [61], Boutreux et al. presented the generalization of the minimal model for surface flows of granular mixtures (referred to as the general case of the canonical model). The final model [61] takes into account both the differences in surface properties and the size of the grains.

More recently, Jop, Forterre and Pouliquen [62] proposed a constitutive law for dense granular flows based on continuum method using a simple visco-plastic approach. They observed that a continuum description of free surface flows is at present debatable because of the fact that granular materials can behave [26] like a solid (in a sand pile), a liquid (when poured from a silo) or a gas (when strongly agitated). For the two limiting cases, solids and gases, constitutive equations have been proposed based on kinetic theory for collisional rapid flows, and soil mechanics for slow plastic flows. The intermediate dense regime, where the granular material flows like a liquid, still lacks a unified view and has motivated many studies over the past decade. Though Jop et al.'s work [62] does not consider any difference in particle sizes (no segregation), it is a step forward in developing continuum based segregation models. Additional work along this line can be found in a recent review by Campbell [63].

The above paragraphs provide a general background of the free surface segregation. Review of the segregation phenomena pertaining to a specific system such as in a rotating tumbler and in a chute is presented in the corresponding chapters. In the next section, for completeness, we briefly review the numerical techniques used in the direct simulations of granular flow systems in this dissertation.

2.2   MODELING: PARTICLE DYNAMICS

Particle dynamics (PD), which is also known as the discrete element method (DEM), has been quite successful in simulating granular materials [64–76], yielding insight into such diverse microscopic phenomena as force transmission [77], packing [78], wave propagation [70], agglomeration formation and breakage [79], cohesive mixing [80], bubble formation in fluidized beds [72], and segregation of free-flowing materials [21]. This method, originally developed by Cundall and Strack in 1979 [2], is based on the methodology of molecular dynamics (MD) for the study of liquids and gases (Allen and Tildesley, 1987 [81]). A recent review (up to the year 2006) on particle dynamics theory and its applications can be found in Zhu et al. [82] and in Zhu et al. [64], respectively. The basic advantage of particle dynamics over continuum techniques is that it simulates effects at the particle level owing to its first-principle nature ("exact numerical experiment" [16]). No global assumption is needed as is customary in a continuum description. Individual particle properties can be specified directly, and the assembly performance, like segregation, is simply an output from the simulation. Also, the growth of this technique can be attributed, in part, to the ever increasing speed of modern computers.

Currently, a million particles can be easily simulated using high performance computing (HPC) which involves the application of highly scalable parallel processing and tremendous acceleration from general purpose GPUs (graphics processing units) [83] to push the computation power to petascale levels. Roth et al., 2000 [84] and Kadau et al., 2006 [85] have already demonstrated this with billions of particles in a molecular dynamics run. Though particle dynamics (PD) algorithms are similar in structure with molecular dynamics (MD), PD simulations are computationally more expensive due to the peculiar interaction of granular particles: Particles exert forces on each other only when they are in mechanical contact. In MD, particles can interact even when they are not in mechanical contact (influence zone of particles is defined by a "cut-off" distance). This "cut-off" distance in MD is usually more than PD (in PD, it is summation of the contacting particles radii). The computational intensity is also aggravated by the fact that the granular particles are rather rigid and their repulsive force grows steeply with the compression once the particles are in contact. This

condition dictates a very small integration time step for the computation of the trajectories in order to obtain reliable results.

This section is organized as follows: First we discuss a general DEM algorithm, then two important parts of a DEM algorithm are elicited – contact force modeling and the contact detection algorithm.

2.2.1 General DEM Algorithm

2.2.1.1 Hard-sphere vs. Soft-sphere Depending on the bulk density and characteristics of the flow to be modeled, two different methods of calculating the trajectories are used: Hard-sphere model and soft-sphere model.

The *hard-sphere* model works in rapid, not-so-dense flows (like "granular gases" [86]) where the collisions are instantaneous (i.e., duration of a collision, $t_c = 0$) and the typical duration of a collision is much shorter than the mean time between successive collisions. While in a true "dilute flow", particles only rarely experience multi-body interactions, in this technique they cannot be in contact with more than one other particle. As the name suggests, the particles do not suffer any deformation to generate the contact forces. The central idea of hard-sphere modeling is to track the next collisions and the particle trajectories are obtained from a set of collision rules (no integration is performed) which relate the post-collision velocities as a function of pre-collision velocities (using coefficient of restitution, both for normal and tangential directions). Hence, during the time intervals between collisions, the particles move along known ballistic trajectories. In this regime, one applies the conservation of linear and angular momentum for each collision sequentially – one collision at a time [87]. This method is also known as an "event-driven" algorithm. At low particle concentration, this algorithm is much more efficient than force-based soft-sphere method since the numerical integration of the equations of motion is avoided. Instead, the dynamics of the system is determined by a sequence of discrete events. The enormous gain in the simulation speed is the main motivation for using this approach.

However, in this dissertation, we employ a *soft-sphere* approach owing to the fact that our systems can be characterized by slow, dense granular flows where particles have enduring

contacts and multi-particle collisions are highly likely. As the name suggests, the particles can deform and forces arise because of this deformation. As will be discussed in the next sub-section, particle trajectories are obtained via integration of forces at discrete time intervals as the simulation marches forward in time. That is why this method is also known as "time-step-driven" simulation.

2.2.1.2 Equations of Motion In the soft-sphere PD or DEM model (we use PD or DEM interchangeably or synonymously throughout this document), bulk flow of the granular materials is captured via simultaneous integration of the interaction forces between individual pairs of particles in contact, and the trajectories are obtained by explicit solution of Newton's equations of motion for every particle [2, 81].

The equations (Newton's laws of motion) that describe the particle motion are:

Linear Motion:

$$m_p \frac{d\vec{v}_p}{dt} = -m_p \vec{g} + \vec{F}_n + \vec{F}_t \tag{2.1}$$

Angular Motion:

$$I_p \frac{d\vec{\omega}_p}{dt} = \vec{F}_t \times \vec{R} \tag{2.2}$$

where m_p, $\vec{v}_p$, I_p, $\vec{\omega}_p$, $\vec{R}$, $\vec{F}_n$ and $\vec{F}_t$ are the particle mass, particle velocity, particle mass moment of inertia, particle angular velocity, particle radius, normal force and tangential force acting on a particle, respectively. The simplest model for a granular particle is a sphere as particle collisions can be identified in a very simple way (it is complicated for any other shape, see Section 2.2.3). For spherically-symmetrical particles, the normal force $\vec{F}_n$ causes changes of the translational motion of the particles; the tangential force $\vec{F}_t$ causes changes in both the rotational and translational motion of the particles. Both components of the force are functions of the relative positions of the particles $(\vec{r}_i - \vec{r}_j)$ and of the relative velocity $(\vec{v}_i - \vec{v}_j)$. The models used to calculate the contact forces between particles are indeed the essence of this simulation technique and are based on contact mechanics considerations [88]. A separate section (see Section 2.2.2) has been devoted for this purpose. The above two differential equations form a system of coupled nonlinear differential equations and cannot

be solved analytically (cannot be directly integrated). The approximate numerical solutions of these equations, i.e., the computation of the trajectories of all particles of the system by numerical integration is the ultimate objective of DEM. We elaborate on the integration scheme and general flow of our DEM algorithm in the next sections.

2.2.1.3 Boundary Conditions Just as a problem in continuum mechanics needs initial and boundary conditions (the similarity between continuum mechanics and discrete system is that we start with a system of differential equations, and hence initial and boundary conditions are needed for both to solve), the description of a particle system is complete only when the behavior of the particles at the boundary is properly described and if the initial conditions, both particle coordinates and velocities, are supplied.

For our boundary conditions, we use both periodic and wall boundaries. The wall boundary is obtained by building up the walls from particles which obey the same rules of interaction as the particles of the granular materials themselves. By choosing appropriate sizes and positions of the wall particles, boundaries (like container walls, inclined surfaces, etc.) with adjustable roughness can be obtained. This kind of boundary can be easily incorporated in the DEM algorithm without needing any extra interaction rules – the particle-particle force laws can still be applied to the walls too. The wall or boundary particles do not interact with each other and they can have a prescribed motion (like rotation). An alternative to the use of boundary/wall particles is the use of mathematical smooth walls (flat surfaces); however, the use of these types of walls necessitates special treatment, such as rolling friction, which we will discuss briefly later. Our simulations are periodic in the z direction so that any particle which leaves the system at one side is re-inserted at the opposite side. Such boundary conditions are used to mimic infinitely extended systems (i.e., a cylinder with a periodic z direction is equivalent to a cylinder with infinite length). Algorithmic implementation of periodic boundary conditions is rather simple in granular systems (PD) as the particle interactions (forces) are short-ranged (as opposed to MD).

2.2.1.4 Initial Conditions Coming back to the initial conditions for DEM, the values of the coordinates $\vec{r}_p(t=0)$, the velocities $\vec{v}_p(t=0)$ and angular velocities $\vec{\omega}_p(t=0)$ should

be specified for $p = 1, ..., N$, where N is the total number of particles in the system. A typical initial condition for our simulations is obtained by allowing a bed of particles arranged in a randomly perturbed lattice to settle under the action of gravity so that a relaxed state is obtained. Initial positioning of the particles in the lattice sites should avoid large overlaps as this would generate very large spurious forces, which are unrealistic, and the simulation would not proceed further.

2.2.1.5 Integration Scheme and Time-Step Now we turn our attention to the integration scheme and time-step used in our algorithm. From the position of particles, all forces acting on each particle are determined and the net acceleration of the particle is obtained, both linear and angular. The position and orientation at the end of next time-step is then evaluated explicitly using the method of integration (one type of "finite-difference" method) initially adopted by Verlet and attributed to Störmer [81] :

$$\dot{x}_{t+\frac{1}{2}\Delta t} = \dot{x}_t + \frac{1}{2}\ddot{x}_t \Delta t \tag{2.3}$$

$$x_{t+\Delta t} = x_t + \frac{1}{2}(\dot{x}_t + \dot{x}_{t+\Delta t})\Delta t \tag{2.4}$$

The time-step Δt should be chosen to be sufficiently small such that any disturbance (in this case a displacement-induced stress on a particle) does not propagate further than that particle's immediate neighbors within one time-step. Generally, this criterion is met by choosing a time-step which is smaller than r/λ, where r is the particle radius and λ ($\lambda \propto \sqrt{E/\rho}$) represents the relevant disturbance wave speed (for example, dilatational, distortional or Rayleigh waves [68]). Under these conditions, the method becomes explicit, and therefore at any time increment the resultant forces on any particle are determined exclusively by its interaction with the closest neighbors in contact. Thornton and Randall [68] suggest the time-step be chosen to correspond with Rayleigh wave speed ($\propto \sqrt{\frac{G}{\rho}}$) so that

$$\Delta t = \frac{\pi R}{\alpha_o}\sqrt{\frac{\rho}{G}} \tag{2.5}$$

17

where R is the particle radius, α_o is a constant (taken to be $0.1631\nu + 0.8766$ in our case), ρ is the density of the particle and G is the shear modulus, and ν is the Poisson ratio of the particle. To be on the safe side, we have used one quarter of the time-step value given by the above Equation 2.5, which yielded a time-step $\Delta t \approx 10^{-6}$ s.

A flow chart of the DEM algorithm is given in Figure 2.

2.2.2 Force Models

The force models are integral to soft-sphere simulation. The forces on the particles include external forces (e.g., gravity) and contact forces – normal repulsion and tangential friction.

The force between contacting particles is described by

$$
\vec{F}_{ij} = \begin{cases} \vec{F}_{ij}^n + \vec{F}_{ij}^t & if \ \alpha > 0 \\ 0 & otherwise \end{cases}
\tag{2.6}
$$

where α is a computational "overlap" to mimic the deformation of particles and is given by $\alpha = (R_i + R_j) - S_{ij}$. R_i and R_j are the particle radii and S_{ij} is the distance (separation) between the centers of particles i and j. For two-dimensional systems, the normal and the tangential components can be written in the form $\vec{F}_{ij}^n = F_{ij}^n \, \hat{\mathbf{e}}_{ij}^n$, $\vec{F}_{ij}^t = F_{ij}^t \, \hat{\mathbf{e}}_{ij}^t$, with the unit vectors $\hat{\mathbf{e}}_{ij}^n = \frac{\vec{r}_i - \vec{r}_j}{|\vec{r}_i - \vec{r}_j|}$, $\hat{\mathbf{e}}_{ij}^t = \begin{pmatrix} 0 & -1 \\ 1 & 0 \end{pmatrix} \cdot \hat{\mathbf{e}}_{ij}^n$.

Now, we briefly review the historical background of the approaches for modeling normal and tangential forces. After that, we focus mainly on what our approach is. The accuracy of DEM primarily depends on the ability to describe the mechanics of the contacts between particles. The first attempt to study the mechanics of elastic contacts between particles was done by Hertz in 1882 [89]. Hertz predicted static normal compression between the two bodies as a function of the mechanical properties of the materials and assumed that there is no energy loss due to elastic wave propagation. Therefore, the coefficient of restitution was equal to 1.0. Several models have been proposed to overcome this shortcoming [2, 72, 73, 90–92]. Cundall and Strack [2] first proposed a force model accounting for the contact mechanics through the use of a spring, a dashpot and a slider configuration, as shown in Figure 3.
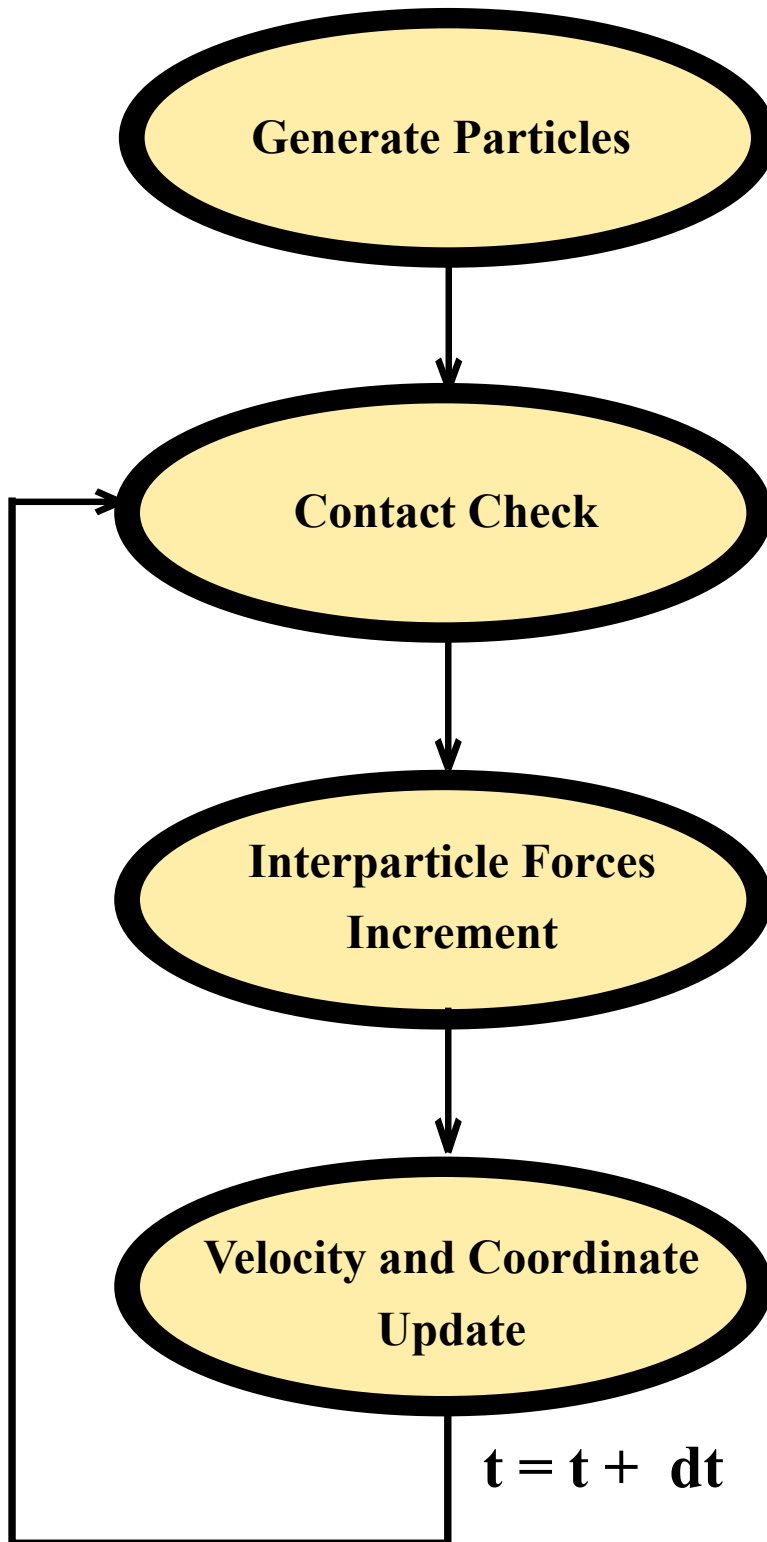
Figure 2: Flow chart of a typical DEM algorithm.
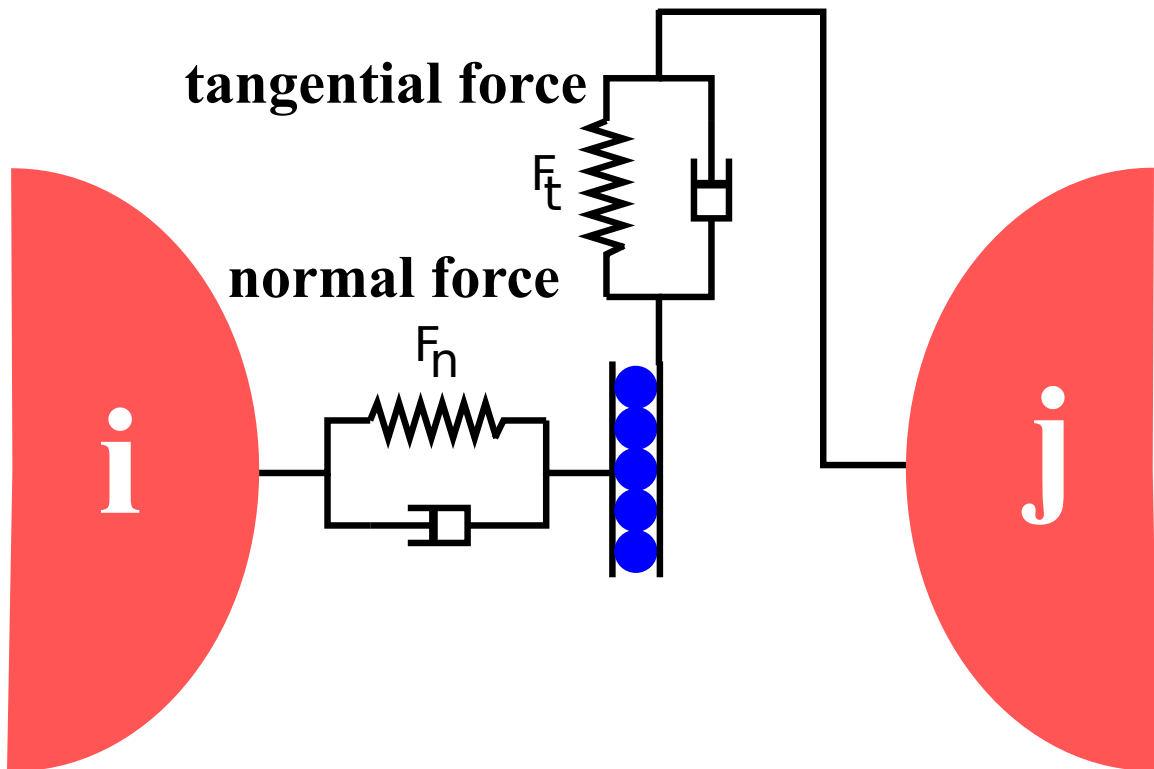
Figure 3: Schematic of a simple DEM force model (spring-dashpot) as was used by Cundall and Strack [2]. The spring is used for the elastic deformation while the dashpot accounts for the viscous dissipation.

Walton and Braun proposed a normal contact model which was able to mimic elasto-plastic and plastic collisions giving restitution coefficients in good agreement with experimental results [73]. With respect to tangential loads between particles, Mindlin and Deresiewicz [93] described the microslip and sliding processes as a result of variable normal and tangential forces. The deformation is contact history dependent and contact mechanics models with different approaches have been proposed [2, 68, 72, 79].

A thorough description of the interaction laws from contact mechanics and their merits can be found in references [82, 94–97]; therefore, they are not reviewed here. We only discuss the models employed in the present work.

2.2.2.1 Normal Forces Two approaches are used to model normal forces in this work: a Hertzian spring-dashpot model and an elasto-plastic material model [98, 99]. In both cases, the deformation of the particles is mimicked via a computational "overlap" α, as discussed before. Again, in both cases, during the initial stages of loading, the normal force, F_n, is purely elastic and is given by

$$F_n = k_n \alpha^{3/2} \tag{2.7}$$

where k_n is the normal force constant from the Hertz theory [88]. This constant is a function of the particle radii, R_i, and elastic properties (Young's modulus, E_i, and Poisson ratio, ν_i):

$$k_n = \frac{4}{3} E^* \sqrt{R^*} \tag{2.8}$$

where R^* and E^* are given by

$$\frac{1}{E^*} = \frac{1 - \nu_1^2}{E_1} + \frac{1 - \nu_2^2}{E_2} \tag{2.9}$$

$$\frac{1}{R^*} = \frac{1}{R_1} + \frac{1}{R_2} \tag{2.10}$$

respectively. At this point the two models differ in their mode of energy dissipation. In the case of the spring-dashpot model, a damping term that is proportional to the relative normal velocity between particles is linearly added to the repulsive force from Equation 2.7. While the expression of the damping term can take several forms, we choose the one suggested by

Oden and Martins [91] due to the fact that it qualitatively reproduces the experimentally observed dependence of the coefficient of restitution on impact velocity for many engineering materials (i.e., a power law decrease). Combining the repulsive force and this dissipation term yields what we refer to as our *elastic* model henceforth, given as

$$F_n = k_n \alpha^{3/2} - \gamma_n \alpha \dot{\alpha} \tag{2.11}$$

where $\dot{\alpha}$ is the relative normal velocity (v_n) of the particles, and γ_n is a damping parameter that is assumed to be adjustable and is simply supplied as a constant in the model (we used $\gamma_n = \frac{0.0015E}{1-\nu^2}$).

In contrast, in our elasto-plastic model (referred to as *plastic* model henceforth), dissipation is assumed to arise from the plastic deformation of the center of the contact spot. In this model, once the normal force exceeds a yield force, F_y, further loading is given by the linear expression

$$F_n = F_y + k_y(\alpha - \alpha_y) \tag{2.12}$$

In this expression, k_y is the plastic stiffness which is related to the yield force by $k_y = (3/2)(F_y/\alpha_y)$, and α_y is the deformation at the point of yield (i.e., where both Equation 2.7 and 2.12 give $F_n = F_y$). Unloading (see Figure 4) prior to exceeding the yield limit is purely elastic, while unloading after the yield limit is given by

$$F_n = F_{max} - k_n \sqrt{\bar{R}}(\alpha_{max} - \alpha)^{3/2} \tag{2.13}$$

where F_{max} and α_{max} are the maximum force attained during loading and deformation, respectively, and $\bar{R}$ is dimensionless and given by the ratio of the new contact curvature due to plastic deformation, R_p, to R^*,

$$\bar{R} = \frac{R_p}{R^*} = \frac{F_y}{F_{max}} \left(\frac{2F_{max} + F_y}{3F_y} \right)^{3/2} \tag{2.14}$$

Reloading after initial yield follows the same path as Equation 2.13 up to the maximum prior force, at which point the contact continues to deform plastically (Equation 2.12).
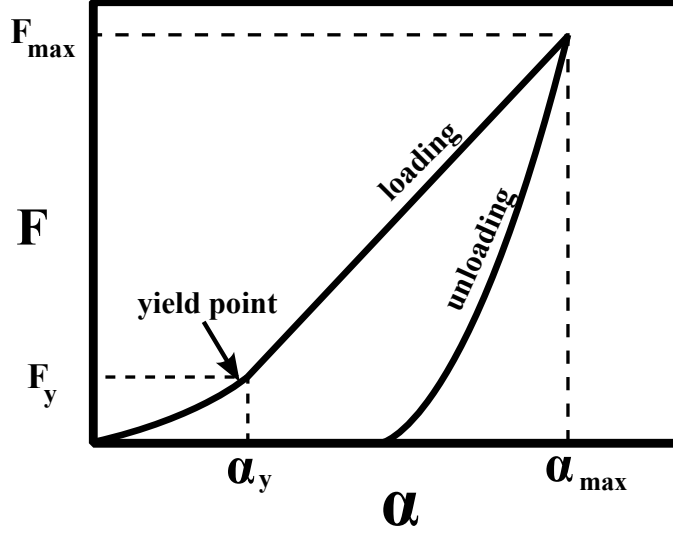
Figure 4: Schematic showing force-displacement curve of elasto-plastic deformation for dry particles.

While the yield force, F_y, can be loosely related to the yield stress (σ_y) of the bulk material, in this work, we treat it in the same manner as γ_n from the spring-dashpot model.

2.2.2.2 Tangential Forces   In our case, we used a simple "history dependent" tangential force model which is very close to the model developed by Walton and Braun [73]. For each time-step, the new tangential force acting at a particle-particle contact, F_t, is given as:

$$F_t = F_{t_o} - k_t \Delta s \tag{2.15}$$

where F_{t_o} is the old tangential force and $k_t \Delta s$ is the incremental change in the tangential force during the present time-step due to relative particle motion; i.e., Δs is the tangential displacement during the present time-step. This displacement is calculated from the component of velocity tangent to the contact surface, v_t (i.e., $\Delta s = v_t dt$ where dt is the time-step). The tangential stiffness, k_t, is not a constant and depends upon the overlap α :

$$k_t(\alpha) = 8G^* a = 8G^* \sqrt{R^* \alpha} \tag{2.16}$$

23

where a is the radius of the contact spot $(= \sqrt{R^* \alpha})$ and G^* is given by

$$\frac{1}{G^*} = \frac{2 - \nu_1}{G_1} + \frac{2 - \nu_2}{G_2} \tag{2.17}$$

where G_i is the shear modulus of the particle i. In this model, we must impose a discontinuity in order to limit the tangential force to the Amonton's law limit ($F_t \leq \mu_f F_n$, where μ_f is the coefficient of sliding friction).

Note that, there is no source of energy dissipation (prior to macroscopic sliding) in our tangential force model, though it can be incorporated using a more involved model where k_t will assume different values depending upon loading, unloading and reloading [68, 100].

2.2.2.3   Comments on Rolling Friction   As mentioned earlier in Section 2.2.1.3, we do not consider any rolling friction. However, a small discussion on this contentious issue is presented here for completeness. Rolling friction is a rarely employed force in mainstream DEM simulations [101]. Nevertheless, there are two potential reasons for inclusion of such a force when modeling real particles: to dissipate energy when particles roll on a smooth surface, and to approximate the behavior of slightly aspherical particles. If rolling friction is not considered, a spherical particle will continue to roll on a flat surface without stopping. (As we have seen earlier, inter-particle forces act at the contact point between particles and not at the mass center of a particle. This generates a torque and causes the particle to rotate. The torque has contributions from two components of the tangential and asymmetrical normal traction distributions (on the contact spot). In comparison with the contribution of the tangential component, the determination of the contribution of the asymmetric normal component, usually known as rolling friction torque, is very difficult and is still an active area of research [88, 102–104]. The rolling friction torque is considered to be negligible in many DEM models [82]. However, it has been shown that the torque plays a significant role in some cases involving the transition between static and dynamic states, such as the formation of shear band and heaping, and movement of a single particle on a plane [82].

2.2.3 Contact Detection Algorithm

Clearly, the necessity of a large number of particles coupled with small time-steps, makes DEM a very computationally intensive technique. This situation can be exacerbated in applications where multiple particle sizes or complex particle shapes are required. This problem, however, can be partially overcome by the use of more effective contact detection algorithms. However, contact detection itself can take up to 60% of the total CPU time in some problems. Therefore, a current direction of research is to develop efficient algorithms to minimize CPU time. There has been a considerable amount of research performed [3, 81, 105–124] on the topic of finding nearest neighbors and detection of contacts between many bodies, both on spherical shapes and irregular shapes. Most of these algorithms can be classified as body-based search or space-based search (alternatively, tree based search or cell/bin based search). It is worth mentioning here that most of these search algorithms were originated from general computing algorithms of computer science which were normally used for traditional computing, computer graphics (CAD), animation, computational geometry, collision detection and motion planning in robotics [125–129]. Now, we briefly review the algorithm that we adopted for the present work along with its merits and demerits. We also shed some light onto how the shortcomings of the algorithm employed here can be addressed.

Algorithms employing binary search (i.e., tree-based [129]) has a total contact detection time which scales as $T \propto N \, ln(N)$, where N is the total number of particles. Another body-based search scheme which employs Delaunay triangulation [112] also has complexity varying between $O(N^2)$ and $O(N \, ln(N))$. Some of these algorithms perform better for either loose or dense packing. Table 1 shows different algorithms and their complexity. In this work, we use the so-called No Binary Search (NBS) algorithm of Munjiza et al. [3], which is a cell based algorithm. This algorithm is suitable for assembly of particles whose sizes are close to each other and the total contact detection time scales as $T \propto N$, which is a performance superior to binary search algorithms. The NBS algorithm works well both for loose and dense packing as it is independent of packing density. This is because the outer loop is always over the total number of particles and not on the number of cells. If there is a particle size distribution, the size of the cell is taken as the maximum diameter of the particle, and the algorithm becomes

somewhat less efficient owing to the fact that more contact checking within a cell is needed as there can be many more particles in a cell (more than the optimum number of particles in a cell). Therefore, NBS works well if d_{large}/d_{small} is small (close to 1.0) and if the mean number of particles in a cell is $1.0 - 5.0$ [121]. To overcome this difficulty for different sized particles (polydispersity), very recently, some cell-based hierarchical search algorithms or multi-grid search algorithms have been proposed [115, 120–122]. In this approach, depending upon its size, a particle belongs to a layer of grids (or cells/bins) suitable for that size range. Therefore, different layers of grids are possible and contact detection is performed in and between different layers hierarchically.

In the present work, we also modify the NBS algorithm, specifically via examination of the looping behavior of the algorithm. In NBS, the outer loop is always over the total number of objects (and not over the number of bins or cells). We find that the use of efficient data structures and abstractions of C++, which is an object-oriented (OOP) language, enables us to have an outer loop, which will go over the total number of non-empty bins. Preliminary investigation [130] shows that the resulting code is more than three times faster than our implementation of the original NBS algorithm in C. Figure 5 shows the effectiveness of this modified NBS algorithm.

Table 1: Different contact detection algorithms and their scaling

Algorithm	Scaling
List algorithm (e.g., [81, 105])	$T \propto N^2$
Binary search (tree-based, e.g., [108])	$T \propto N\,ln(N)$
No binary search (NBS, cell-based, e.g., [3])	$T \propto N$
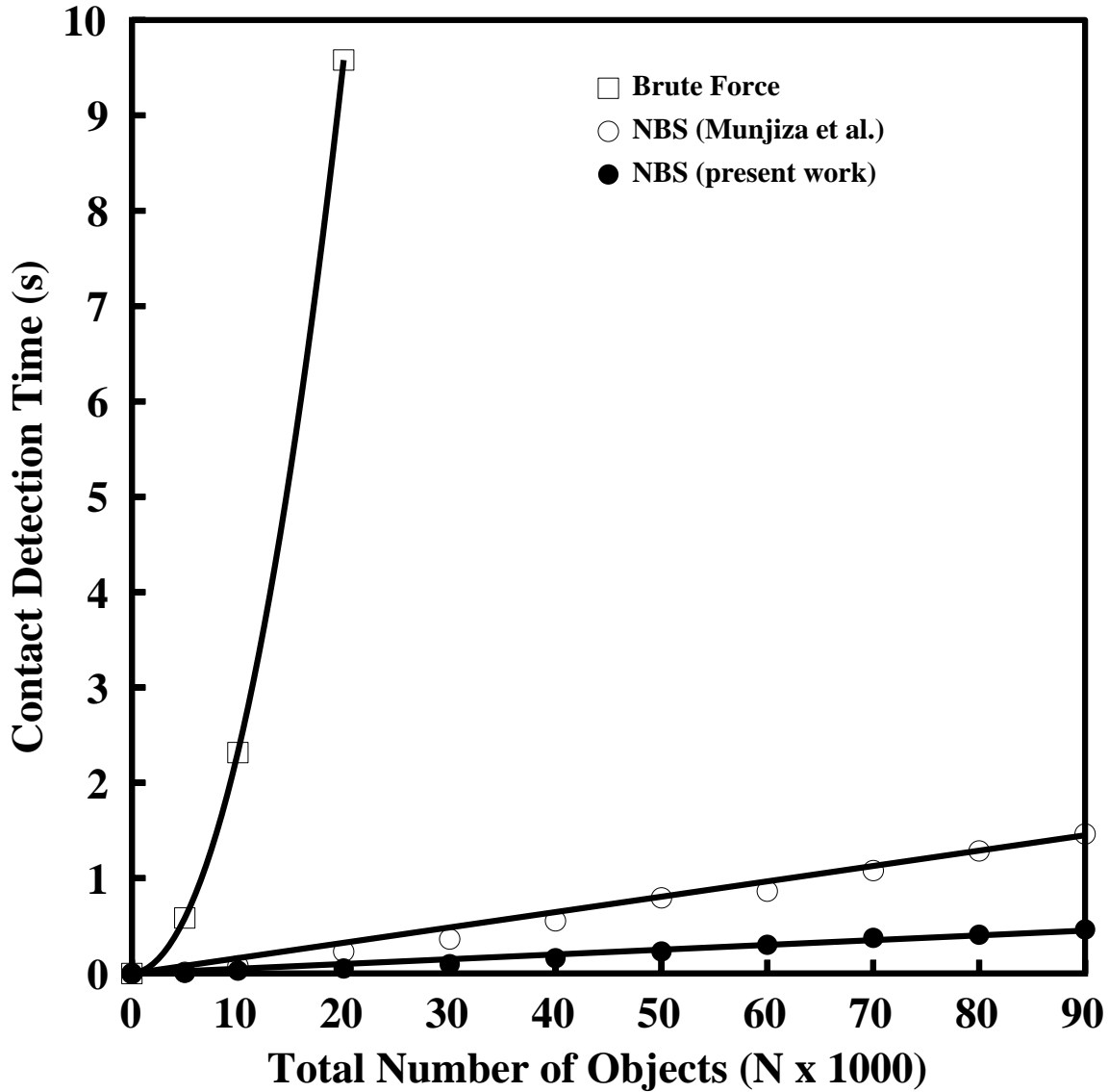
Figure 5: Total contact detection time as a function of total number of particles. [∘] corresponds to our implementation of the original NBS algorithm of Munjiza et al. [3] in C and [•] corresponds to the modification of the outer loop of the NBS algorithm using an efficient data structure in C++. A naive brute force method where all particles are searched against all other particles has also been included. Total contact detection time has been obtained by running the outer loop 10 times in a 3.2 GHz, Intel Xeon processor.

2.3 MIXING & SEGREGATION MEASURES

In this section, information about how to quantify mixing and segregation is presented. Fan et al. [131] have described a number of mixing indices for various types of mixing situations (such as in tumbler mixer, fluidized bed, etc.). A number of indices are used to quantify the efficiency of mixing and this background information would be used to characterize the systems described in the succeeding chapters. Merits and demerits of various mixing indices have been examined by Rollins et al. [132]. Although (as noted by Fan et al. [131]) the representation of the complex characteristics of a solids mixture via any available mixing index appears to be far from satisfactory, in this work, we have employed multiple indices to probe and ascertain the performance of a system.

Danckwerts [133] used the term "scale of scrutiny" as the maximum size of the segregating regions that can cause the mixture to be considered acceptable for its intended use. For a given powder, its quality of mixing decreases as the scale of scrutiny, with the extreme case where each sample contains only one particle. In this section, some measures that attempt to quantify the degree of mixing are described, among them Intensity of Segregation (IS), which is the mixing measure frequently used in this work.

2.3.1 Intensity of Segregation

The Intensity of Segregation (IS) is essentially the standard deviation of the concentration calculated at multiple locations in the granular bed, and is calculated using the following expression:

$$IS = \sigma = \sqrt{\frac{\sum_{i=1}^{N_c}(C - \langle C \rangle)^2}{N_c - 1}} \tag{2.18}$$

where N_c is the number of concentration measurements, C is the concentration of the tracer particles in the designated measurement location, and $\langle C \rangle$ is the average concentration of that type of particle in the entire bed. It should be noted that large values (approaching 0.5 for a equi-volume mixture) of IS correspond to a segregated state while smaller values denote more mixing. This particular index will be revisited in Section 3.3 when the experimental procedure in a tumbler mixer will be discussed.

2.3.2 Lacey Mixing Index

The Lacey mixing index [134] is defined as a function of the variance (σ^2) of the composition of the actual mixture, the variance σ^2 of the composition of the corresponding completely segregated mixture (σ^2_{SEG}, that is, its upper limit), and the variance of the perfectly mixed granular material (σ^2_{MIX}, lower limit):

$$\text{Lacey mixing index, } M_L = \frac{\sigma^2_{SEG} - \sigma^2}{\sigma^2_{SEG} - \sigma^2_{MIX}} \tag{2.19}$$

In other words, this index represents the ratio of the degree of mixing achieved to the maximum mixing possible. A Lacey mixing index equal to 1 corresponds to a perfectly mixed state, and value of 0 corresponds to complete segregation. It is to be noted here that, by switching σ_{MIX} with σ_{SEG} in the above equation for M_L, a derived index [$(1\text{-}M_L)$] can be used to follow the evolution of a system from a complete mixed state to a segregated state. In Section 4.4.2.4, we have used this derived index to examine the onset of segregation in a periodic chute flow when the system started from a mixed state.

2.3.3 Poole Mixing Index

The mixing index as described by Poole [135] is defined as:

$$\text{Poole mixing index, } M_P = \frac{\sigma^2}{\sigma^2_{MIX}} \tag{2.20}$$

A value of 1 for the Poole mixing index represents a perfect mixture, and this index increases as the mixing quality decreases.

2.3.4 Relative Standard Deviation (RSD)

The RSD is defined as below:

$$\text{RSD} = \frac{\sigma}{\langle C \rangle} \tag{2.21}$$

where σ, and $\langle C \rangle$ bear the same meanings as described in the sub-section on Intensity of Segregation (Section 2.3.1). The global state of mixing is better reflected by the RSD, which is also often the measure used in industrial settings. We have used this index in Section 4.4.2.4 to examine the onset of segregation in a periodic chute flow, in addition to IS and $(1\text{-}M_L)$.

3.0 CONTROLLING SEGREGATION IN TUMBLERS

Tumblers or rotating drums play an important role in many solids processing industries. In this Chapter, we examine how segregation can be controlled in this type of device. We begin with a brief review of the background on mixing and segregation in tumblers.

3.1 MIXING AND SEGREGATION IN ROTATING DRUMS

The flow behavior in a rotating cylinder is very complex. Henein et al. [136] and Mellmann [137] observed six regimes of flow with increasing cylinder speed of rotation: slipping, slumping, rolling, cascading, cataracting and centrifuging (see Figure 6). In industrial applications, rotating drums are operated at rolling or continuous flow regimes. In the continuous flow regime, a thin layer of particles moves at high velocity in the free surface (called the shear layer), whereas the rest of the bed rotates as a solid body (called the passive layer) [138]. Diffusive mixing and segregation of particles are due to the flow of particles in the shearing layer only, and therefore, it is the shearing layer which needs particular attention if something has to be done to thwart segregation. Therefore, the background on free surface flow from the previous Chapter is of particular help to devise theories that would help in describing the segregation phenomena in a tumbler.

There has been extensive research performed [10, 12, 21, 131, 136–220] addressing the mixing and segregation in rotating drums or tumblers. These studies can be broadly classified into the following three groups based on their focus [16]: (a) studies of the time evolution of the mixed state, (b) studies of axial dispersion, and (c) studies of radial (or transverse) mixing. A few important aspects will be reviewed here.
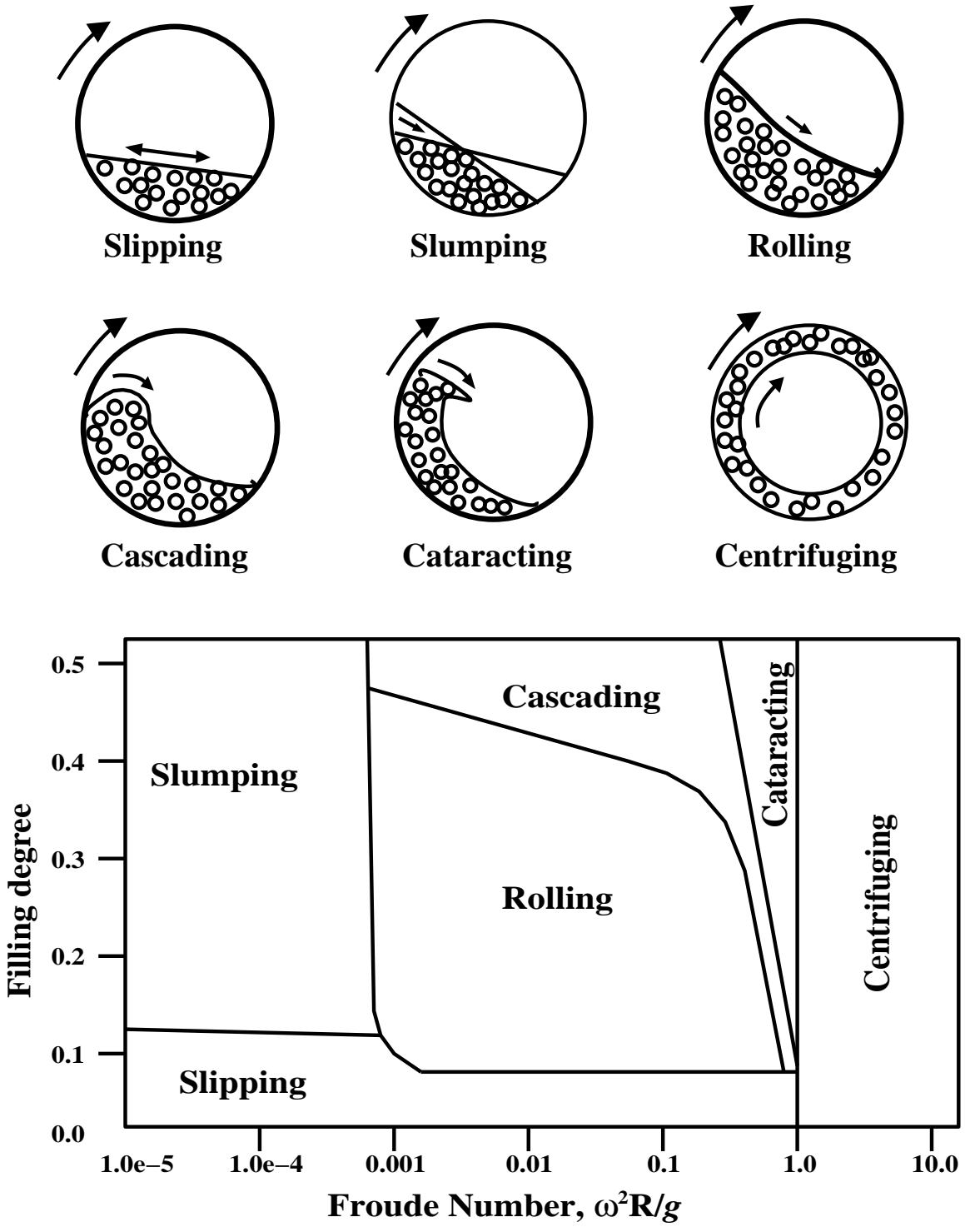
Figure 6: Different regimes of flow in a rotating drum (illustration obtained from Vargas [4] with permission).

The first category of studies focuses on characterizing the efficiency of mixers by determining the time evolution of a global mixing index. A mixing index is normally a statistical measure that reflects the extent of mixing. Several indices are available (refer to the discussion in Chapter 2, Section 2.3). These indices are typically determined by sampling the granular bed composition at different (usually random) positions within the mixer. A typical measure of the mixed state is the Intensity of Segregation (IS) (Danckwerts [133]), defined as the standard deviation of the number fraction of the tracer particles from the mean value. We will elaborate on experimental IS more later in Section 3.3. A key result common to many such studies is that, initially, the Intensity of Segregation decays exponentially with time. Although this approach has been useful for determining the effect of system parameters (e.g., baffles, Wes et al. [215]) on the rate of mixing in a particular mixer, it gives little insight into fundamental mechanisms of mixing.

Studies of axial dispersion [213, 217, 219, 220] investigate the axial mixing which is determined primarily by particle diffusion (effective diffusion coefficient in the axial direction) in the flowing layer and is typically slow. Investigations (Rao et al. [206]) show that the axial dispersion increases with rotational speed of the mixer and particle size.

The issue of transverse mixing in a rotating drum in the continuous-flow regime was first studied by Hogg and Fuerstenau [217] and Inoue et al. [218] using idealized flow models. Visualization studies of the evolution of mixing with colored tracer particles were carried out by Lehmberg et al. [214], and recently a continuum analysis and experiments for mixing in this regime were presented by Khakhar et al. [21]. Although most of the studies focused on the slow continuum regime, recently many studies have also been performed on the slumping or avalanching regime.

Mixing in the slumping (avalanching) regime has been studied by many workers [172, 183, 187, 191, 195, 200]. Geometrical aspects dominate in the slumping regime, whereas dynamic effects predominantly control mixing in the cascading or continuous-flow regime [16].

Turning our focus back to the relevance of free surface segregation in tumblers, one can note that a consequence of shear layer segregation in a rotating cylinder is radial segregation, in which denser particles or smaller particles migrate towards the core of the cylinders. The experimental work of Nityanand et al. [208] illustrates the typical behavior of systems with

size segregation. Percolation dominates at low rotation rate (RPM) of the cylinder and the smaller particles sink to lower levels in the flowing layer and thus form a core at the centre. However, at higher rotational speeds, the segregation pattern reverses, with the smaller particles at the periphery instead of the core. These results reflect the challenge of the segregation processes in the shearing layer.

Recent studies of radial segregation have focused primarily on the dynamics and extent of segregation in the low-rotational-speed regime [16]. 2D DEM simulations were used to study the density segregation [204] and size segregation [194] in the rolling regime. Size segregation in two dimensions has been reported by Clément et al. [199] in the avalanching regime and by Cantelaube and Bideau [198] in the rolling regime experimentally. Smaller particles formed the central core in both these experiments. Cantelaube and Bideau also reported the statistics of trapping of the small particles at different points in the layer. Baumann et al. [201] suggested a similar trapping mechanism for size segregation based on computations using a 2D heaping algorithm, and Prigozhin and Kalman [188] proposed a method for estimating radial segregation based on measurements taken in heap formation. Khakhar et al. [21] have reported experiments and theory of density segregation. They proposed a constitutive model for the segregation flux in cascading layers and validated the model by both particle dynamics and Monte Carlo simulations for steady flow down an inclined plane. Earlier, Alonzos et al. [205] showed how an optimum combination of size and density differences can be used to minimize segregation.

Very recently, Gui et al. [141] studied the microscopic and macroscopic characteristics of mixing based on fractal dimension analysis and Shannon entropy analysis, respectively. They found, by numerical analysis on the dimension of the fractal interface, that a slow rotational speed is favorable for particle mixing. Recent DEM studies on unbaffled tumblers by Arntz et al. [143] concentrated on the effect of drum rotational speed and fill level on mixing. They studied many regimes such as rolling, cascading, cataracting and centrifuging. Their studies indicate that good mixing is possible for Froude Numbers in the range $0.25 < Fr < 0.68$. Also, high fill fractions ($>65\%$) show the most intense segregation, which is at variance with the earlier prediction by Dury and Ristow [221]. It is well established that mixing and segregation

34

patterns are sensitive to the container geometry and fill level [152,185,197]. The dynamics of mixing and segregation are still not well understood, and therefore, all the designs of solids mixers currently are empirical. Several approaches have been proposed to control or eliminate segregation. McCarthy et al. [197] found that the mixing is enhanced in the avalanching regime for an odd number of baffles. Wightman and Muzzio [212] performed experiments for size segregation in a drum, both for pure rotation and rotation with vertical rocking. They found that rocking accelerates axial mixing. Samadani and Kudrolli [176] found that segregation could be reduced by adding a small volume fraction of fluid. Recently, Li and McCarthy [160] found that segregation could be turned on or off by adding small amounts of moisture in multi-sized mixture with particles having different surface characteristics. Hajra and Khakhar [161] found that segregation could be eliminated by using a small (in comparison to the diameter of the cylinder) rotating impeller placed at the axis of rotation, that is, in the flowing layer. Jain et al. [153], Thomas [177] and Hajra and Khakhar [222] performed experiments for binary mixtures composed of different size and different density particles and they found that mixing can occur instead of segregation if the denser beads are bigger, and also if the ratio of particle size is greater than the ratio of particle density.

Khakhar and Ottino [223] have summarized the findings of many studies of granular flow in tumblers so that they can be applied to the design and scale up for problems of industrial importance. For summaries of recent work on mixing and segregation in tumblers, one can refer to Duran [224] or Ristow [225].

One can observe that the solutions to combat segregation based on the past studies can be categorized into two groups: Change the particles or change the process [226]. Changing the particles may involve controlling inter-particle adhesion or balancing the differences in size and density. Changing the process may involve geometrical changes (such as manipulating baffles) or operational changes (such as varying the tumbler rotational speed). Looking back at the developments on the design of baffles for rotating cylinders, we find that very little is known from a theoretical point of view on the effect of baffles on solid mixing, even in simple cases limited to monodispersed systems. Industries use empirical designs based on

past experience, which often have no theoretical basis. Moreover, a literature search yields no previous studies dealing with issues involving novel baffle shapes and their placements in a solid mixer and how their designs will affect segregation.

Recently, Shi et al. [31], have shown that periodic flow inversions either manually – in a chute – or via selective baffle placement in a tumbler-type mixer – can serve as a generic method for eliminating segregation in free-surface flows, perhaps the most common and well-studied of granular flows [39, 75, 227].

In this work, for the first time, we use experiments and simulations to study the effects of various design and operating parameters, such as baffle shape and placement, on mixing of binary mixtures with different sizes or densities. We show that periodic flow inversion can be used to reduce segregation in a rotating cylinder, where different baffle shapes and placements were engineered based on the hypothesis of flow modulation, and some of these novel designs yielded excellent mixing results in actual experiments. Attempts are made to link this technique to the probability distribution of the number of times a particle passes through the flowing layer per rotation of the drum, and using this information, predictions are made as to which baffle configurations would produce better mixing. In order to achieve this objective, the numerical experimental tool DEM (Discrete Element Method) has been extensively used in the present study.

In the next section, we take a brief look at the hypothesis of flow modulation as mentioned above. Mathematical expressions describing the hypothesis in a tumbler are also presented. This is expected to aid in designing actual or numerical experiments to corroborate the hypothesis, either directly or indirectly.

3.2   HYPOTHESIS: TIME MODULATION IN A TUMBLER

Time-modulation in fluid mixing and other dynamical systems [24] is a fairly common practice, but has found only limited applications in granular processing [197, 228, 229]. As already mentioned in Section 3.1, Shi et al. [31] have shown that periodic flow inversions via selective baffle placement can serve as a generic method to thwart segregation. The key to adapting

this idea to free-surface segregation lies in recognizing two important facts: that it takes a finite time for material to segregate and that there is always a preferred direction that particles tend to segregate. For example, in a free-surface flow, small particles need time to percolate through the flowing layer (also, smaller particles travel faster than the larger particles [230]); thus, if the flow is interrupted before the small particles could reach the bottom of the flowing layer, segregation can be prevented. This relatively simple observation can be employed to engineer systems that counteract segregation.

In order to capitalize on the fact that this flow interruption can thwart segregation, one next needs to invert the flowing layer, prior to reinitiating the flow. One way to achieve this two-step process in a continuous flow is to invert the flowing layer at a sufficiently high frequency, f_{crit}, $f_{crit} > t_S^{-1}$, where t_S is the characteristic segregation time. A critical issue with this technique is that a full understanding of segregation kinetics – and therefore, the characteristic segregation time, t_S – is still lacking. However, this hypothesis can well be tested *indirectly* for many baffle configurations in a rotating tumbler or *directly* in a chute flow segregation tester (Chapter 4) using scaling arguments and utilizing existing theoretical tools [21, 30].

Now we attempt to derive an expression for critical forcing frequency in an unbaffled tumbler owing to its simplicity as a model system. As a closed-form expression of the critical forcing frequency for baffled tumbler is not available at present due to the inherent complexity of the flow, the hypothesis of time modulation can be translated into some other indirect measure (like the number of layer passes a particle makes) to implement it in a baffled tumbler and to apply this knowledge in understanding the behavior of baffled tumblers. In fact, one of the objectives of this present work is to take up this challenge and apply this hypothesis to explain the behavior of baffled tumblers.

For size segregation, the segregation velocity takes the form $v_S = K_T(1-\bar{d}) + fK_S(1-\bar{d})$ [21], where $(1-\bar{d})$ is the dimensionless particle size difference, f is the number fraction of the segregating species, K_S and K_T are segregation constants, which depend on the local number density ratio, local void fraction and granular temperature, respectively. For an unbaffled tumbler, the characteristic segregation time may then be written as $t_S = \delta_o/[K_T(1 - \bar{d}) + fK_S(1 - \bar{d})]$, where δ_o is the maximum shear layer thickness and also corresponds to the

characteristic length for segregation. The expression for t_S above can also be recast as $t_S = \delta_o/[\xi(1-\bar{d})]$, where $\xi = (K_T + fK_S)$. Again, due to current theoretical uncertainty and the time-varying nature of our flow (as well as our granular temperature, pressure, etc.), ξ is treated as a fitting parameter that is a function of the local number density, the granular temperature and the composition of the mixture [21]. Referring to the work by Khakhar et al. [223], the thickness of the shear layer at the midpoint is given by $\delta_o/R = (\omega/\dot{\gamma}_o)^{1/2}$, such that the time for size segregation can be written as

$$t_S = \left(\frac{\omega}{\dot{\gamma}_o}\right)^{1/2} \frac{R}{\xi(1-\bar{d})} \tag{3.1}$$

where, $\dot{\gamma}_o$ is the shear rate at midpoint of the layer and is given by

$$\dot{\gamma}_o = \left[\frac{g\sin(\beta_m - \beta_s)}{cd\cos(\beta_s)}\right]^{1/2} \tag{3.2}$$

The parameter c in Equation 3.2 is the dimensionless collisional viscosity and it is approximately constant with a value of ≈ 1.5 for all Froude numbers $Fr = \omega^2 R/g$ and size ratios $s = d/R$ [223]. β_s and β_m are the static and dynamic angles of repose, respectively. The critical perturbation frequency, f_{crit} is then given by

$$f_{crit} = \frac{1}{t_S} = \left(\frac{\dot{\gamma}_o}{\omega}\right)^{1/2} \frac{(1-\bar{d})\xi}{R} \tag{3.3}$$

In order to suppress segregation in an unbaffled tumbler, a forcing frequency should be chosen such that the mean residence time of the particles in the layer $\tau_{mean} = 2\pi/\sqrt{\omega\dot{\gamma}}$ [155] is less than the time of segregation t_S. The effective forcing frequency is then given by,

$$f_e = \frac{1}{\tau_{mean}} = \frac{\sqrt{\omega\dot{\gamma}_o}}{2\pi} \tag{3.4}$$

and the ratio of frequencies (using Equations 3.3 and 3.4) is given by

$$\frac{f_e}{f_{crit}} = \frac{\omega R}{2\pi(1-\bar{d})\xi} = \frac{\dot{\gamma}_o\delta_o^2}{2\pi R(1-\bar{d})\xi} \tag{3.5}$$

A similar procedure can be crafted for density segregation [144], resulting in an expression for the frequency ratio of the form

$$\frac{f_e}{f_{crit}} = \frac{\omega R}{2\pi(1-\bar{\rho})K_S} = \frac{\dot{\gamma}_o \delta_o^2}{2\pi R(1-\bar{\rho})K_S} \tag{3.6}$$

where $(1-\bar{\rho})$ is the dimensionless density difference and K_S is a segregation constant that depends on local void fraction and granular temperature.

The fact that all the relations used in developing the frequency ratios above are based on data for monodispersed system and for unbaffled tumblers, might render our analysis somewhat limited for application in the baffled cases. Nevertheless, as we mentioned earlier, we show that this general theory can still be applied *indirectly* to explain the behavior of baffled tumblers.

3.3 EXPERIMENTS

Experiments are carried out in a quasi-2D rotating cylinder (1.5 cm in length and 13.8 cm in diameter), which is mounted on a circular plate attached to a bigger rotating drum (see Figure 7 for the setup). The bigger drum is rotated using a computer controlled stepper motor at a fixed rate (6 RPM). The cylinder is made up of two sets of transparent glass discs, which is fitted face to face to close the cylinder. This arrangement also helps in dispensing particles when a particular experiment is completed. We used nearly spherical cellulose acetate beads as the model particles. We mainly focus on size segregation experiments and binary mixtures (equal volume, 50:50 v/v) composed of 2 mm and 3 mm acetate beads are used.

In a typical experimental run, particles are placed in the cylinder using a divider so that the initial particle bed remains completely segregated (see Figure 7 or Figure 8). All experiments are carried out using 50% cylinder fill fraction. A digital camera (Nikon D200) with a resolution of 6 Mega pixels is used to capture the photographs as the experiment progresses and the evolution of the system from a complete segregated state to a mixing state is observed. Digitized images are also taken at low shutter speeds in a separate experiment to calculate the shearing or flowing layer thickness (δ_0) at the layer mid point [231] when no baffle was used. Photographs are captured at every half cylinder rotation. An image analysis
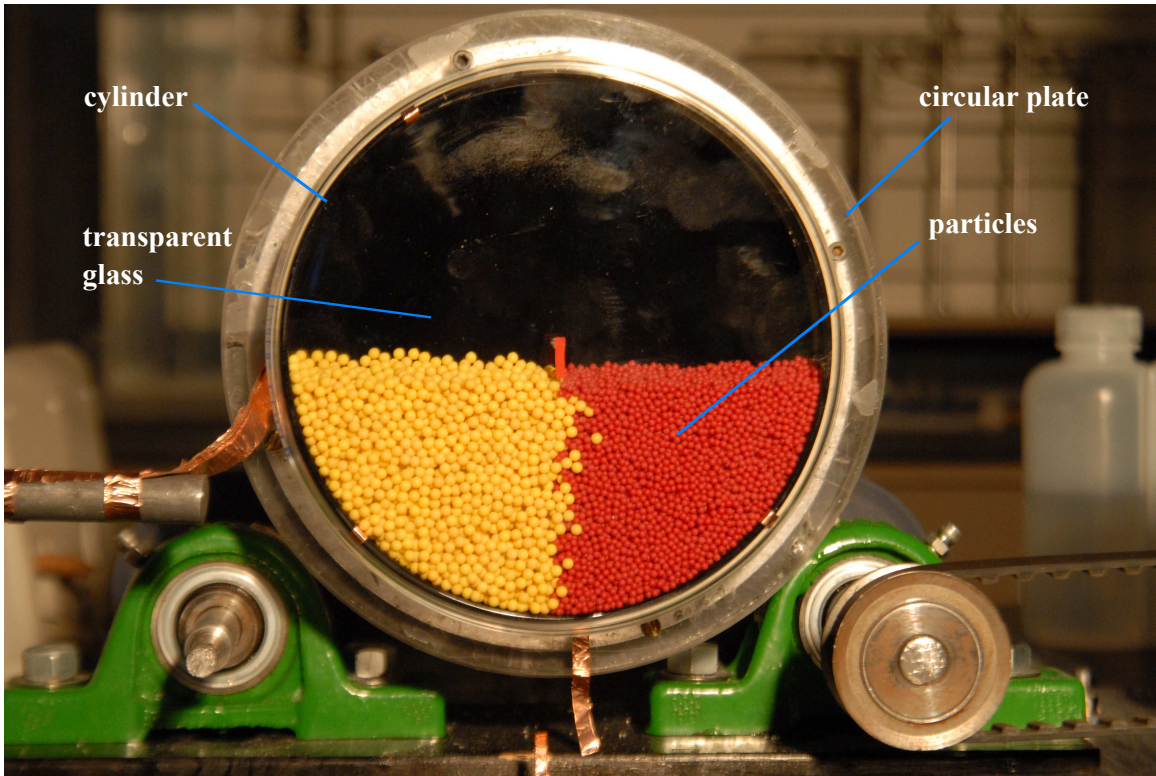
Figure 7: The experimental setup for rotating drum.

technique, which relies on the colors of the particles to identify different sized particles, is used to compute the distribution of particles as a function of time. This procedure yields the information required to calculate the Intensity of Segregation (IS) (refer to Section 2.3) using Equation 2.18 for each experimental run.

With regards to the quantification of mixing, it is important to measure the extent of mixing in order to investigate the performance of a mixer. As discussed in Section 2.3, several methods of mixing measures are available in the literature. Among them, mixing index [158] or Intensity of Segregation [133] are most commonly used. In this study, we have used the Intensity of Segregation (IS) as the method of measurement of mixedness. Low IS means good mixing. The captured images from experiments are divided into N_c number of uniformly distributed boxes or cells and the concentration C at the center of a cell is calculated from the fraction of particles with a specific color (denoting a specific-sized particle) [21] in that cell. The mean value of the concentration, $< C >$, of a particular species is the average concentration of all the cells. Also, as the IS is plotted over time as the mixing process evolves, the asymptotic state is defined as the number of revolutions after which the Intensity of Segregation becomes flat.

Both the DEM simulations and the experiments use cellulose acetate particles in thin ($\approx$ 6-7 particle deep) and $\approx$ 40-60 particle wide tumblers. The simulated particle sizes and densities (as well as vessel size) are matched to their corresponding experiments as closely as possible; however, the particle stiffness and other parameters used have been reduced in order to decrease necessary simulation time (a practice shown to have essentially no impact on flow kinematics [232]) in some simulations (using so-called "soft" particles). Table 2 lists the material properties used in the simulations. Note that an elasto-plastic model with actual material properties is used when the objective is to compare simulation results with the experimental data. On the other hand, fictitious "soft" material properties are used for performing other studies (e.g., effect of number of baffles, etc.) when comparison with experimental data is not the primary aim.

Table 2: Material properties used in the simulations

Parameter	Value
Young's Modulus (E, GPa)	1.5 (acetate), 0.03 (soft)
Density (ρ, kg/m^3)	1300 (acetate), 1000 (soft)
Coefficient of Friction (μ)	0.30
Poisson Ratio (ν)	0.43 (acetate), 0.33 (soft)
Yield Stress (σ_y, MPa)	30.0 (acetate), 0.3 (soft)

3.4   RESULTS

In this section, we present the results obtained for different configurations of baffles for mixing in a tumbler. Both simulation and experimental results are presented, and they are also analyzed in light of the hypothesis that periodic flow inversion can thwart segregation (as described in Section 3.2).

All modeling/experimental results are discussed by considering the optimum baffle size ($L/D = 0.5$), which was experimentally obtained by Hajra et al. [139]. The focus of discussion here is on size segregation, however in what follows, we will see that the type of segregation (density/size) has no impact in developing arguments about why a special case (baffle configuration) is better or in testing our hypothesis.

3.4.1   Effect of Baffle Shape

In this section, we examine how baffle shape affects mixing. We use four different shapes of baffles: flat, S-shaped, reverse S-shaped, and C-shaped (Figure 8). The effective length of the baffles remains constant. The effective length is defined as the length of the tightest bounding box enclosing the baffle in question. Figure 9 shows the experimental and corresponding

Figure 8: Different baffle shapes considered for this study: C-shaped, S-shaped, Reverse S-shaped and Flat baffle, respectively. Effective length of all types of baffles is constant (equal to the optimum baffle length). The cylinder is rotated at 6 RPM. Also, note that the initial bed is completely segregated with one quarter of the cylinder filled with one kind of particles and the other quarter with the second kind of particles.

simulation images, which depict the asymptotic results for different shapes of baffles. The experimentally calculated IS is plotted in Figure 10 (size segregation) and Figure 11 (density segregation) as a function of time. For size segregation, the asymptotic average IS values (and standard deviation in parentheses) for the flat, reverse S, S and C-shaped baffles are 0.21 (0.01), 0.21 (0.01), 0.18 (0.01) and 0.19 (0.02), respectively. The corresponding IS values (and standard deviation) for density segregation case are 0.20 (0.02), 0.23 (0.02), 0.21 (0.01) and 0.20 (0.01), respectively. One can observe that there is no dramatic difference in mixing for the types of baffles considered. Since the asymptotic IS values are all well below 0.25, which is a threshold to determine if a system is mixed or segregated, this suggests that a flat baffle may very well be used as compared to other sophisticated designs like a C-shaped or an S-shaped baffle.

3.4.2 Effect of Baffle Placement

In this section, we investigate how the placement of a baffle within the tumbler with respect to the axis of rotation can change the extent of mixing. We shift the baffle, both in the transverse and radial directions, and the baffle position becomes asymmetric with respect
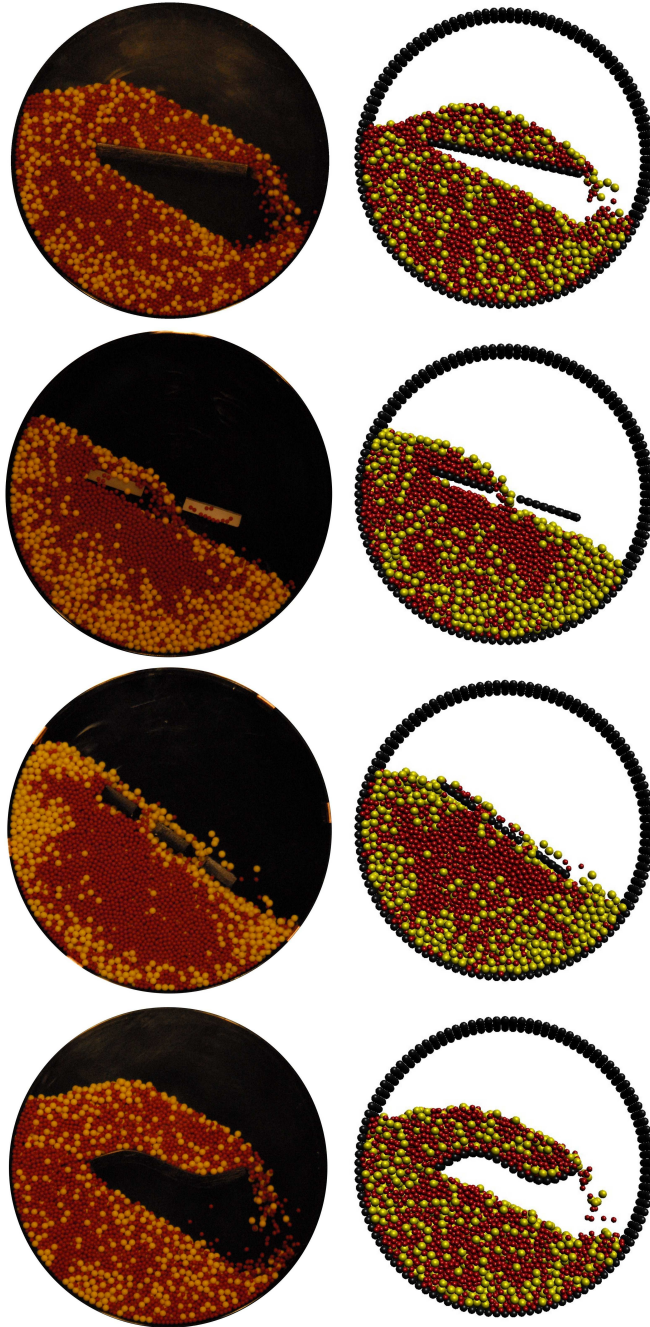
Figure 9: Comparison of experimental and DEM results for various baffle shapes. The images show asymptotic (steady-state) mixing state of the rotating drum containing 2 mm and 3 mm acetate beads. Left column shows experimental results and the right column shows results obtained from DEM. A good agreement is observed between these two.
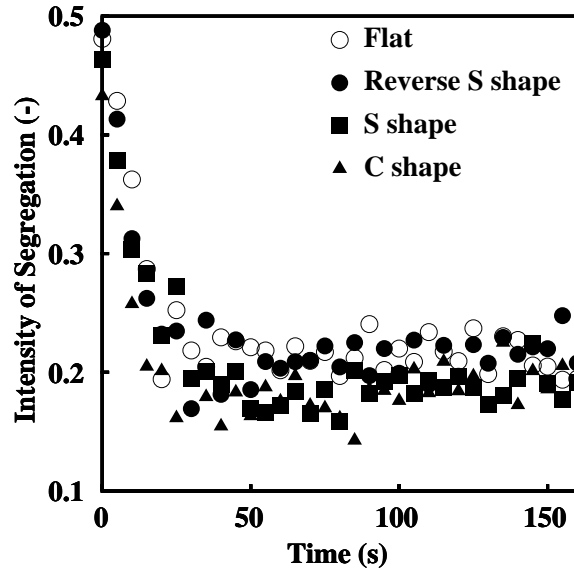
Figure 10: Quantitative results for size segregation in a rotating cylinder with different baffle shapes as indicated in the legend. The cylinder is rotated at 6 RPM.
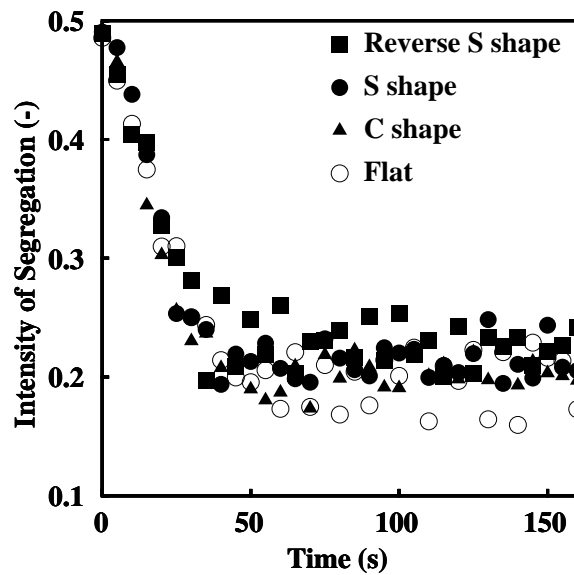
Figure 11: Quantitative results for density segregation in a rotating cylinder with different baffle shapes as indicated in the legend. The cylinder is rotated at 6 RPM.

to the axis of rotation. Again, the motivation for doing this emanated from our hypothesis that the more we invert the flowing layers, the better mixing we expect.

A few baffle positions are considered for this investigation on baffle placement: symmetric baffle placed at the free surface, symmetric baffle placed within the shear layer, baffle placed outside the flowing layer, completely asymmetric placement and baffles with segments (two/three segments). Figure 12 shows a schematic of the various baffle configurations studied in this work. The maximum shear layer thickness δ_0 is calculated using a technique described by Orpe et al. [231] so that we may properly place the baffles, as described. The shear layer thickness (δ_0) is found to be approximately 15 mm for size segregation experiments. Figure 13 shows a qualitative comparison between experiments and simulations for various baffle placements when the mixing process has reached an asymptotically unchanging state. We observe that DEM reproduces the asymptotic behavior quite well. Figure 14 shows the calculated experimental IS values over time for various baffle configurations for 2 mm and 3 mm acetate beads. The asymptotic average IS values for the different cases are 0.25 (baffle placed in passive layer or outside shear layer), 0.23 (baffle placed in shear layer) and 0.21 (baffle placed on free surface). The corresponding standard deviations are 0.02, 0.01 and 0.01, respectively. Therefore, one can observe that the case where the baffle was placed on the free surface or within the shear layer, produces a low IS (less than 0.25) and yields a good mixing.

3.4.3   Effect of Tumbler Filling Fraction

In this section, we discuss how the filling level of the tumbler affects the mixing behavior. We present only simulation results here. The filling level is varied between 20-70% and in all the cases, a flat baffle is axially placed on the free surface. Figure 15 shows the asymptotic average value of the Intensity of Segregation (IS) obtained from DEM simulations plotted against different filling fractions. It is to be noted here that all of the fill levels produce reasonably good mixing results as the Intensity of Segregation (IS) is below 0.25 in all cases. However, within themselves, the best possible mixing is obtained when the tumbler is half filled under the given conditions.
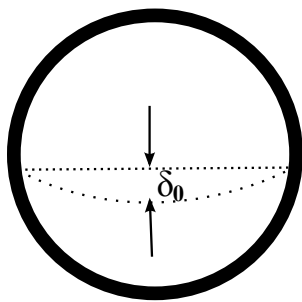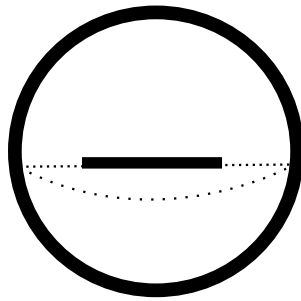
unbaffled **symmetric on free-surface** **within shear layer**
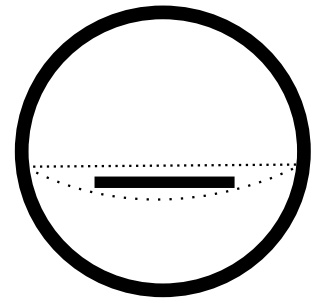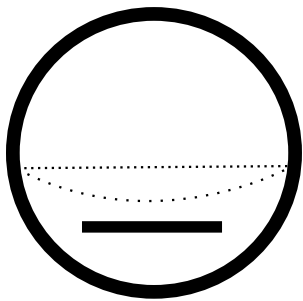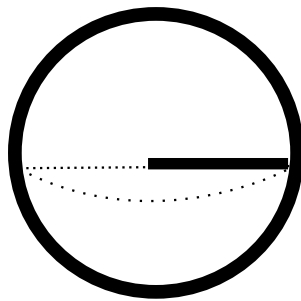
outside shear layer **asymmetric** **two-segmented**
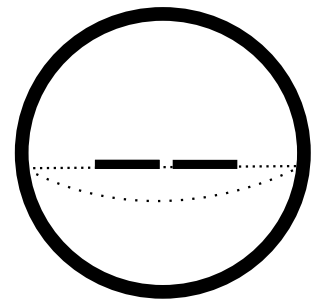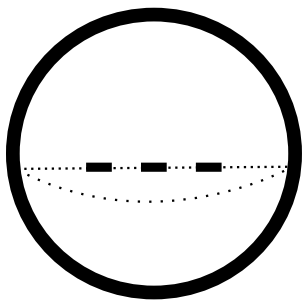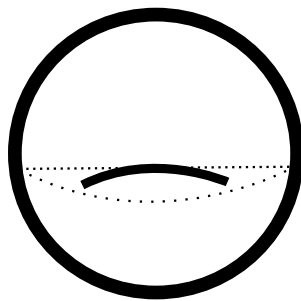
three-segmented **C-shaped** **S-shaped**
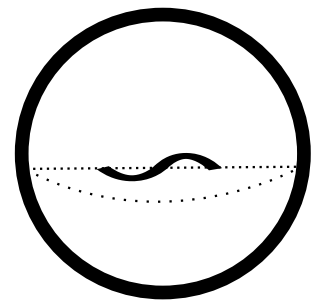
Figure 12: Schematic showing various baffle configurations and baffle placements. Note that δ_0 is the maximum depth of the shear layer.

47
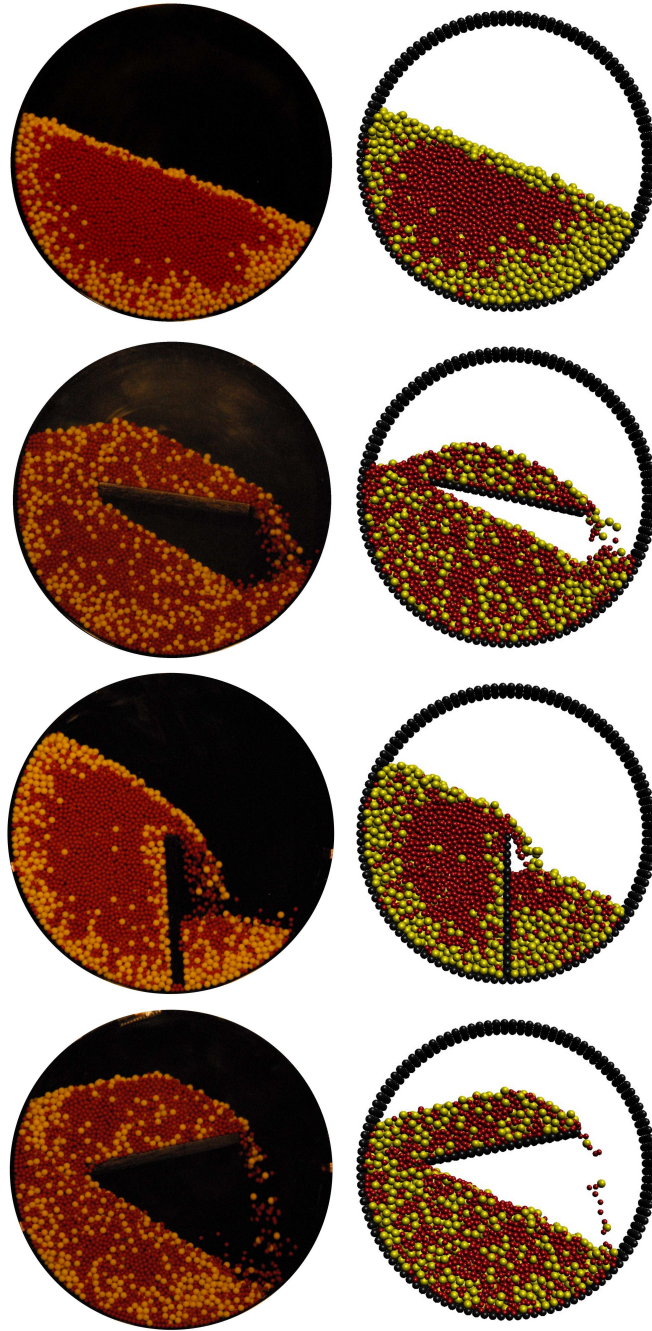
Figure 13: Images showing qualitative comparison between experiments and DEM simulations of the asymptotic state of mixing in rotating tumblers with various novel baffle configurations. An unbaffled case (top) has also been shown for comparison. The emphasis here is on different kinds of baffle placements within the tumbler. Two different sized particles are considered: 2 and 3 mm acetate beads. The effective length of the baffles is fixed and the cylinder is rotated at 6 RPM.
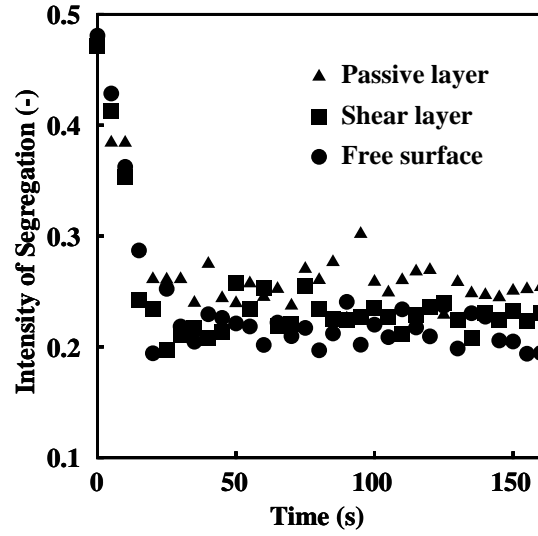
Figure 14: Quantitative results for size segregation for a rotating cylinder with a flat optimum sized baffle fixed at different locations as indicated in the legend. The cylinder is rotated at 6 RPM.
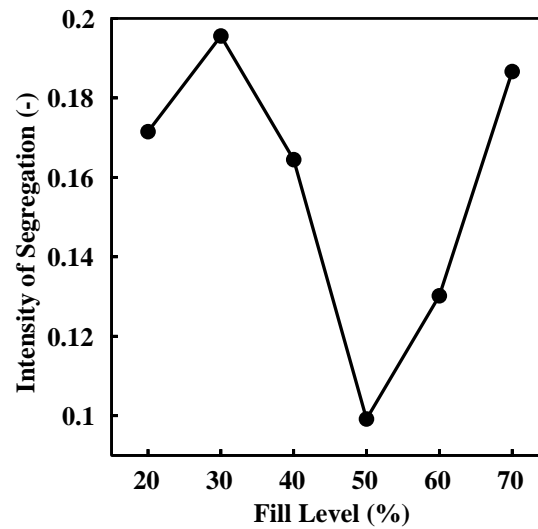
Figure 15: Asymptotic average Intensity of Segregation (IS) is plotted against different filling levels in a rotating tumbler. In all cases, a flat optimum baffle is placed on the free surface of particle bed.

3.4.4   Hypothesis Testing via Layer-Pass Simulations

In the previous section, we have shown both experimentally and by way of simulations that segregation can be reduced if we consider changing baffle shapes or their placement in the tumbler. We also recognize that this enhancement in mixing is due to the flow modulation introduced by the periodic alteration of the flowing layer and hence the effective direction of segregation as discussed in Section 3.2. In this section, we attempt to explain what causes a specific baffle configuration to yield better mixing. Numerical experimentations on the various baffle configurations are used to demonstrate that periodic flow inversion by way of layer passes is the key to better mixing. Out of many combinations of baffle configurations, we choose some of the candidates that show good mixing (results) from simulations and experiments (already discussed) to investigate why a particular configuration is better than others.

Going back to the flow modulations introduced by baffles, one observes that the static portion of the bed in a rotating drum simply "stores" the material and returns it, for its next pass through the surface layer (after it undergoes a full 180-degree change in orientation). Moreover, in an unbaffled tumbler, the flowing layer itself also induces a 180-degree orientation change, so that for a full rotation the bed and layer effects on orientation cancel each other. Now if we place baffle near the axis of rotation and near to the shearing layer, we periodically alter the flowing layer so that we achieve both (i) a smaller average uninterrupted flow length, L, and (ii) periodic variations in the effective direction of segregation with respect to the tumbler streamlines. The fact that the static bed and the flowing layer(s) no longer produce related orientations, is key to the results reported here.

To visualize what happens for different baffle configurations, we use non-segregating particles in a rotating drum for our simulations. In this way, by using identical (same size and density) particles we can focus our attention only on a single variable, i.e., the effect of baffles (not the effect of particle properties themselves) on the flowing layer and flow inversions. This allows us to single out the effect of baffles on the patterns of flowing layers. The results obtained through DEM are post-processed in the following way to obtain meaningful images and plots: Individual particles are tracked to determine whether it is in a

shearing (flowing) layer or not. To accomplish this goal, we first calculate the time averaged velocity field from identical configurations of the tumbler for a number of revolutions. Then, using the time averaged velocities, the vorticity (i.e., curl of velocity, $\nabla \times \tilde{\mathbf{V}}$) is calculated and stored as a lookup table. Since the particles within the static bed do not move relative to one another, obtaining a non-zero value for the vorticity implies that the particles are found within a shearing/flowing layer (note that the introduction of baffles will lead to potentially more than the one flowing layer that is obtained in a non-baffled tumbler).

The vorticity is obtained in the following way. Only the x and y components of the velocity field are considered as we are interested in the vorticity in the z direction. Using a suitable grid, the average velocities of each of the discrete particles can be mapped onto the grid and the curl can be calculated. By doing this, we obtain a reference lookup table of vorticity values on the grid points at different time instances for one complete revolution of the tumbler. In the next step, we consider a number of revolutions of the tumbler and in each instance of time, we re-map the reference curl values (from the grids) onto discrete particles using the lookup table corresponding to the same tumbler configuration. Re-mapping is done using a suitable interpolation scheme [233]. A cut-off curl value is used, above which, a particle would be thought to be in the shearing layer. In the present study, a cut-off curl of 0.3 is used, which gives accurate flowing layer boundaries as verified by the video obtained from temporal images. Finally, the number of times a particle passes through a shearing layer for certain revolutions of the tumbler is counted and a distribution is obtained. Eight revolutions (3rd to 10th, as the flow reaches a steady state from the 3rd revolution) of the tumbler are found to be suitable for obtaining the distribution and it is observed that the distribution does not change significantly if more revolutions (more averaging time) are considered. A single pass through the shearing layer would re-orient the particles by 180 degrees; therefore, the segregation direction (orientation) will change during the mixing process if the particles pass through the layer, on average, in fewer than half a rotation.

Figure 16 shows shearing layers for different baffle configurations. Two different colors are used to demarcate flowing and static layers. Figure 17 shows the probability distribution of the number of layer passes a particle takes per rotation of the drum for many different baffle configurations. On examining this plot, we observe that, as expected, the unbaffled

51
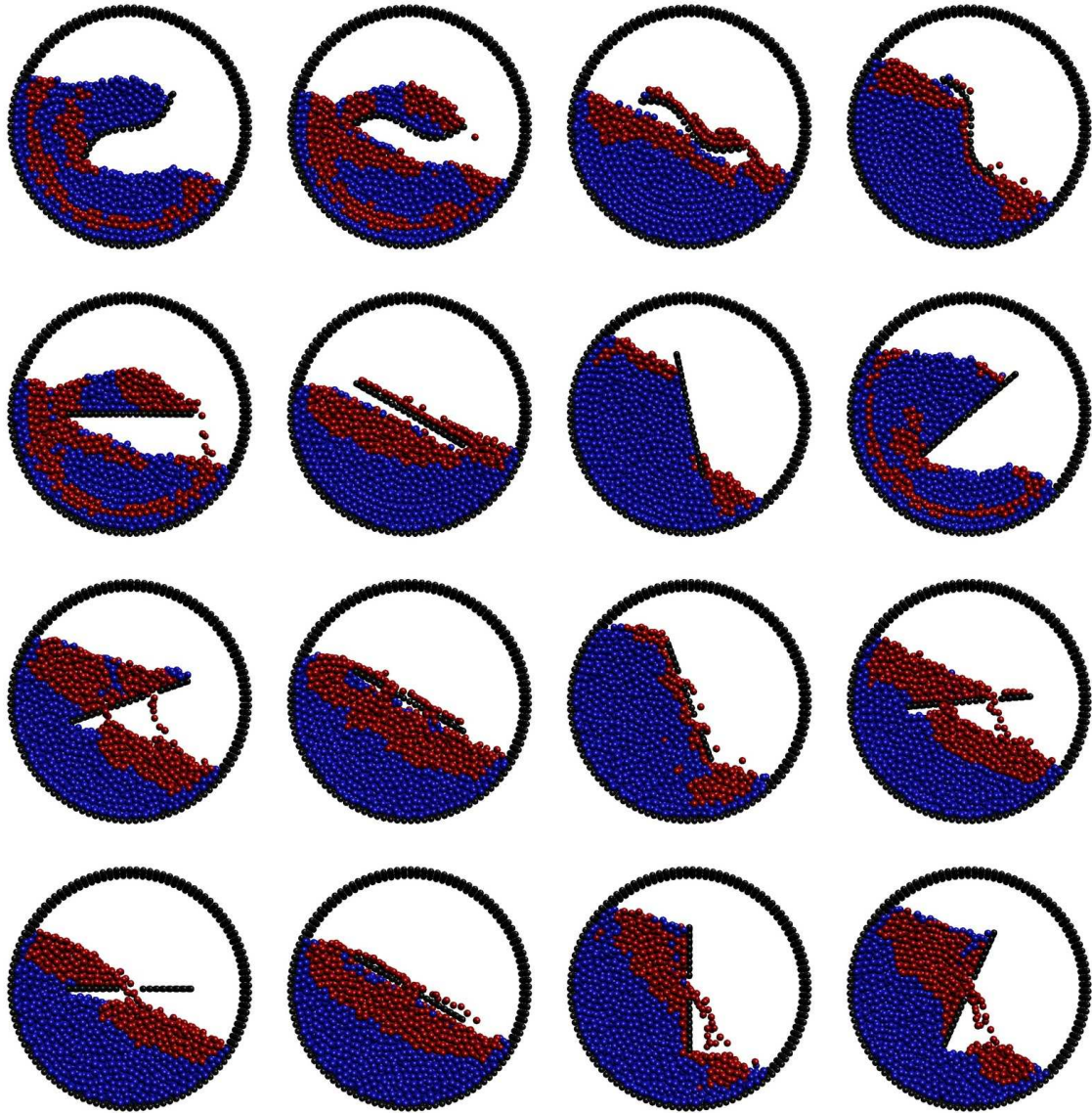
Figure 16: Snapshots showing the evolution of the shearing layer at different times (time increases from left to right) for a few baffle configurations obtained from DEM. The baffle configurations (top to bottom) are S-shaped, flat, three-segmented and two-segmented baffles. Dark (red) particles are in the shearing layer and the lighter (blue) particles constitute the static bed in these pictures.
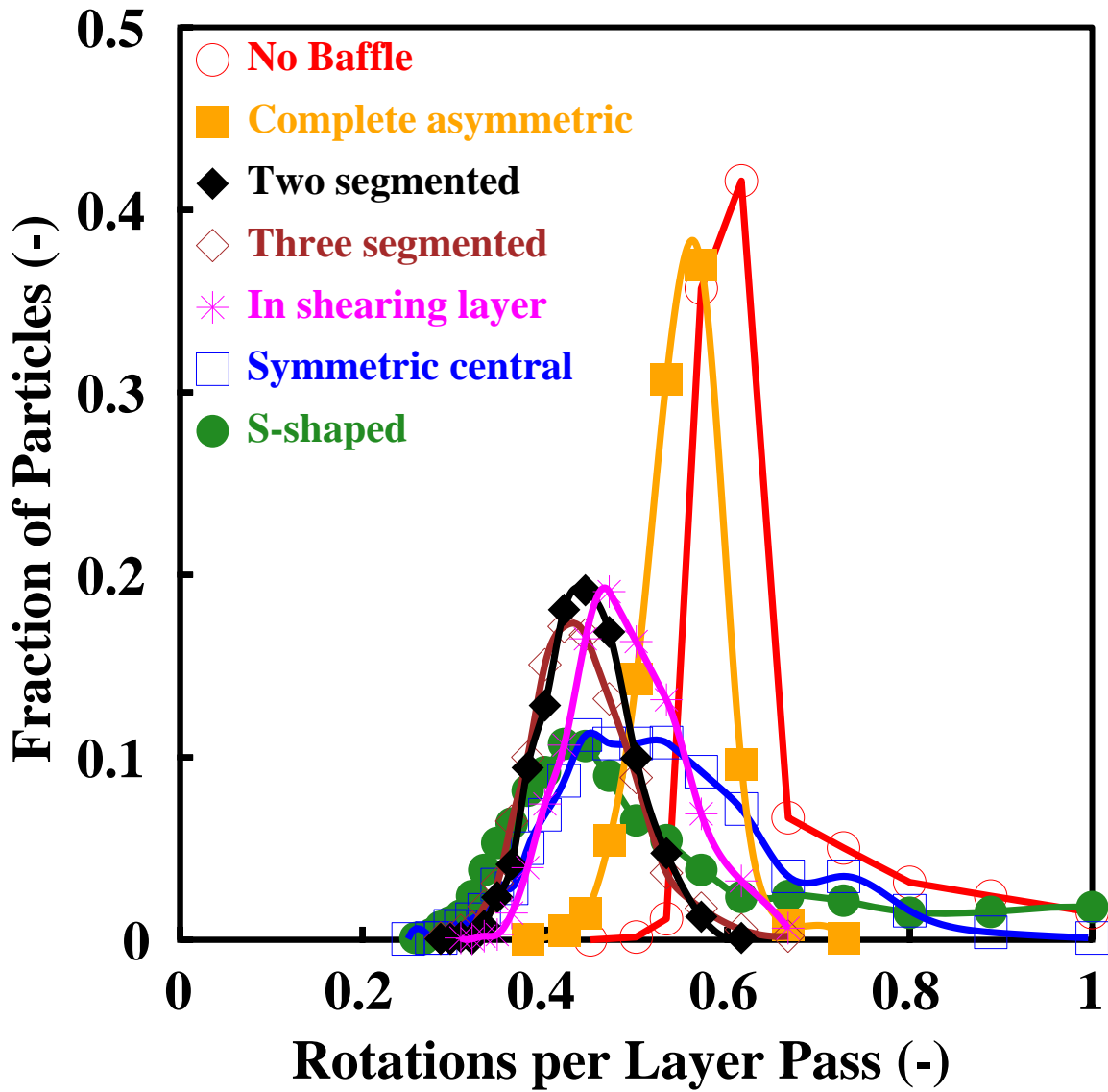
Figure 17: Probability distribution of the number of layer passes a particle takes per rotation of the drum for many different baffle configurations.

case exhibits a very narrow distribution centered on about 0.5 rotations. This result implies that, for an unbaffled tumbler, essentially all of the particles pass through the layer in half of a revolution (so that the solid body rotation and layer pass cancel each other and effectively yield a constant orientation). In contrast, the other promising baffles (such as segmented, symmetric, S-shaped, etc.) result in much broader distributions suggesting that the orientation of a particle will become essentially uncorrelated to its previous orientation as the layer passes and solid body rotation will not be commensurate. Therefore, these candidates are expected to produce better mixing results as per our hypothesis.

Now, we take a look at the real experimental data to see whether the above candidates are really good or not in terms of mixing performances. Figure 18 shows the comparison of experimental IS values for various promising baffle configurations. This plot shows that a flat baffle of optimum length or a S-shaped baffle of optimum length is expected to have better mixing as the asymptotic IS values are lower in comparison to other cases. Therefore, our expectation is that these candidates should also have broadened layer pass distributions. Now, we plot (in Figure 19) the layer pass peak heights (from Figure 17) – a measure of broadening, higher peak height means lower broadening – with the asymptotic IS values, obtained from both experiments (Figure 18) and simulations, for different baffle configurations (seven different promising configurations are tested) – and we get what we expected as per our hypothesis. As we go down in IS, the layer pass peak height also decreases, showing a better mixing. Therefore, a flat baffle of optimum length fitted at the center symmetrically or a novel S-shaped baffle produces a better mixing than other types of baffles.

We believe that this characterization tool built on the hypothesis mentioned earlier can be effectively used to test different baffle configurations and predict their performance, even for actual industrial solids mixers.

3.4.5 Application of Layer Pass to Other Cases

In this section, we attempt to apply the previously built concept of layer pass simulations to three other cases: Optimization of the shape of S-shaped baffles, performance of an X-shaped baffle, and lastly, to examine the effect of the number of baffles on mixing.
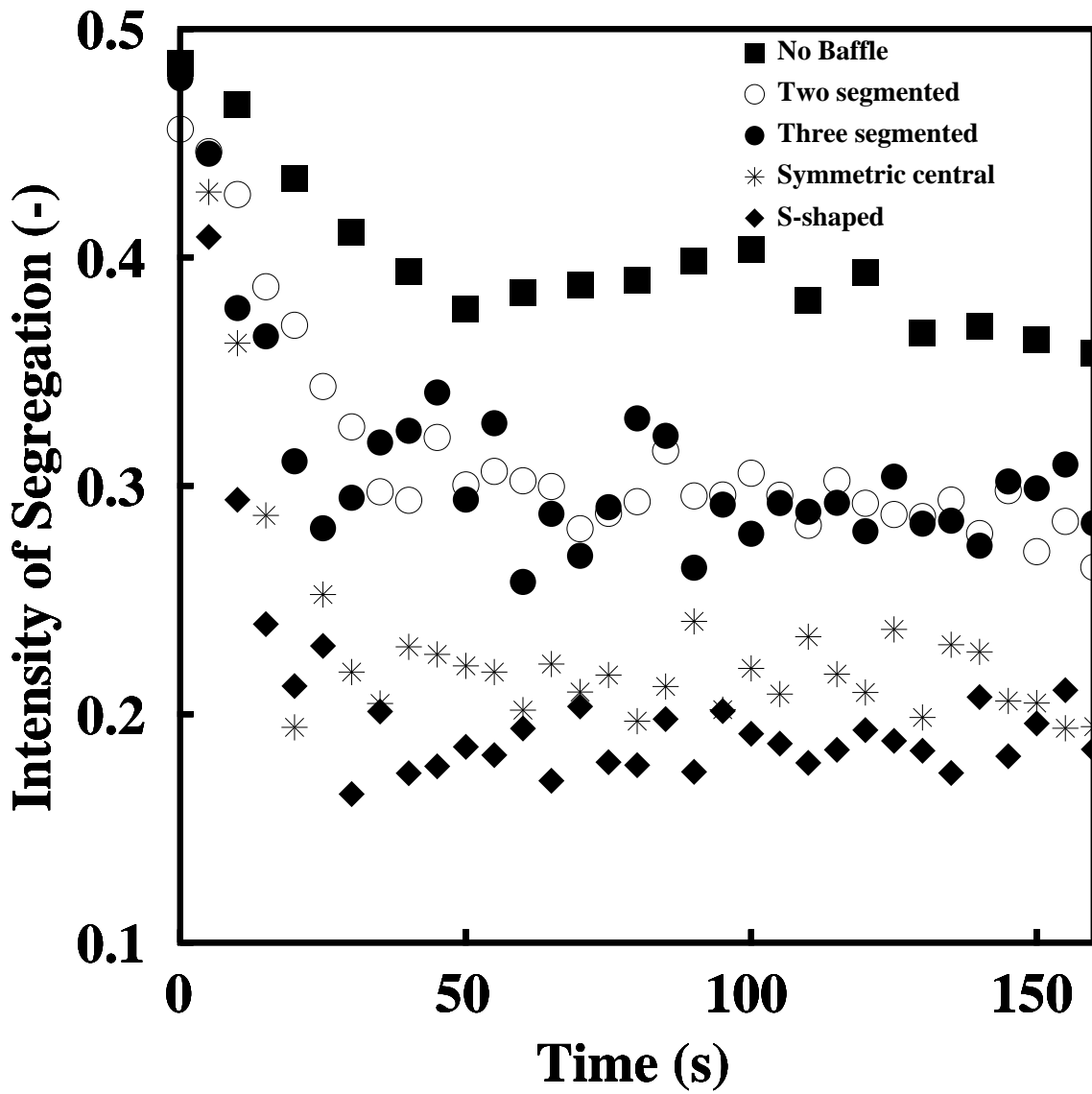
Figure 18: Quantitative results obtained from size segregation experiments for a rotating cylinder with various promising designs of baffles. The cylinder is rotated at 6 RPM.
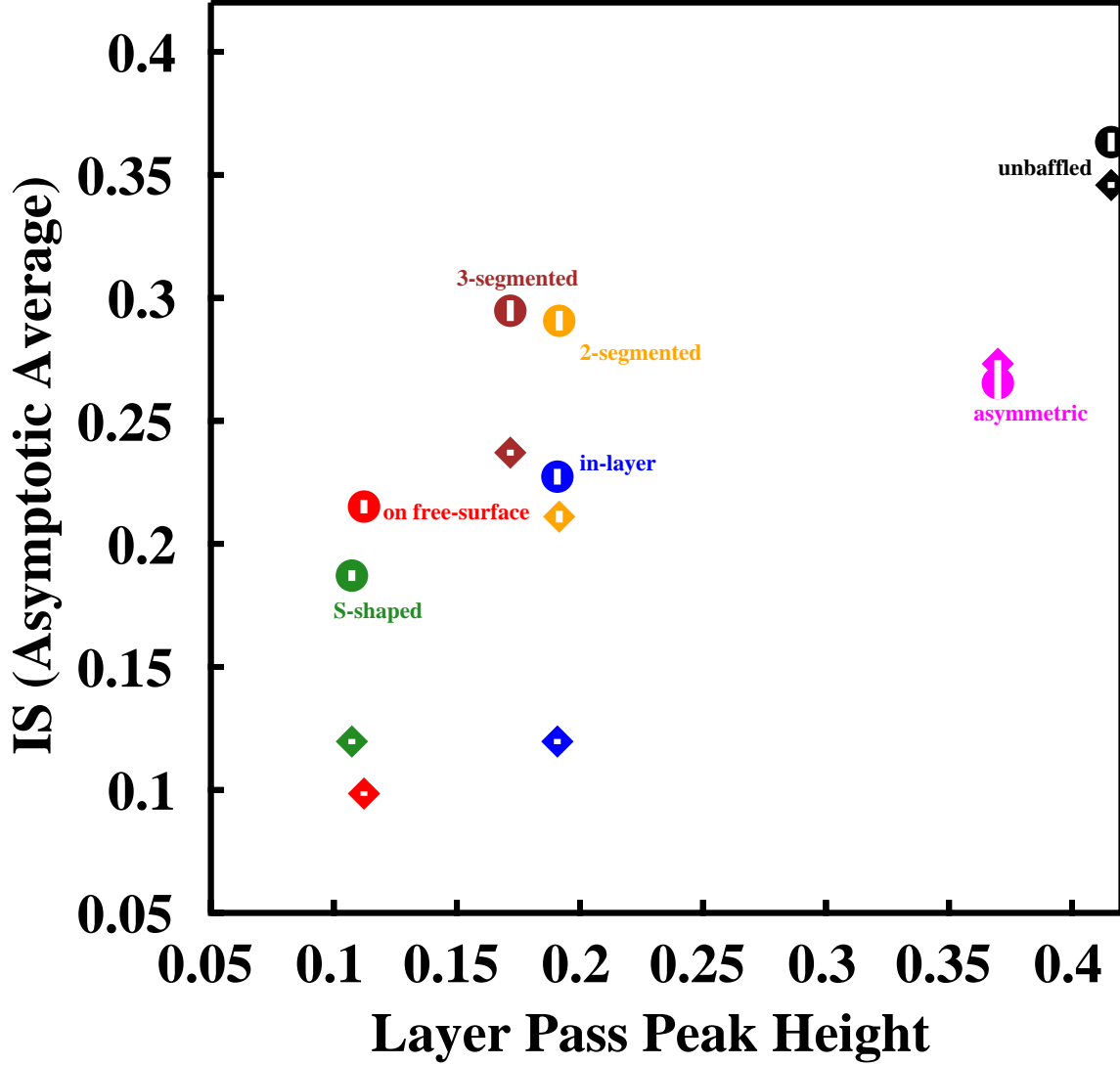
Figure 19: Correlation between layer pass peak height and the asymptotic IS obtained from experiments and DEM modeling. Each color-coded point corresponds to a particular baffle configuration as labeled, and for each configuration (color), symbols ● (filled circle) and ♦ (filled diamond) represent experiment and simulation, respectively. Note that the error bars are very small (short white lines inside symbols) as average IS values are calculated when the asymptotic state is reached.
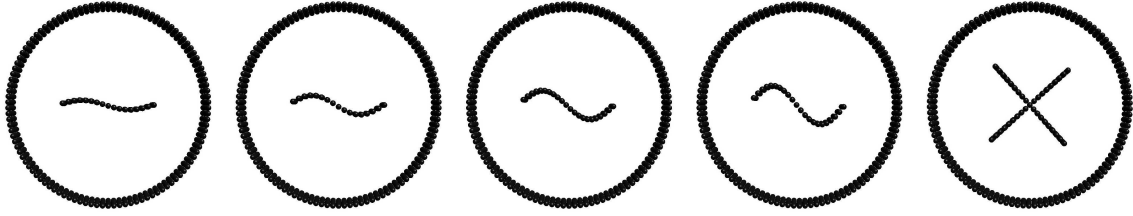
Figure 20: Various S-shaped baffles and a typical X-shaped baffle have been shown here. For the first four pictures, the amplitude of the S shape A is varied from 5% to 20% of L with an increment of 5%. L is the effective length of the baffle.

3.4.5.1 Optimizing S-shaped Baffles We have seen that the S-shaped baffle performs better in terms of mixing. Therefore, we take a closer look at the shape of the S-shaped baffle, and attempt to explore the parameters of the S shape in the hope of obtaining better mixing. Different S shapes are formed by varying the amplitude of a sinusoidal curve. The S shapes are generated from $y = A \sin(2\pi \frac{x}{L})$, and we vary the amplitude A at four different levels (refer to Figure 20). We perform similar layer pass simulations on these four S shapes, and it turns out that, the mixing performance does not change significantly if the shape is altered. This is evident from Figure 21: all the distributions overlap with each other.

3.4.5.2 S Shape vs. X Shape X-shaped baffles are widely used in many industrial solids mixers. We compare the layer pass results of an S-shaped baffle and an X-shaped baffle (refer to Figure 22). The effective lengths and other simulation parameters are kept fixed for both the cases. We can clearly see from Figure 22 that the distribution for X-shaped baffle is slightly shifted toward the left and the peak height is also little smaller. Therefore, we expect the X-shaped baffle to perform somewhat better in terms of mixing.

3.4.5.3 Effect of the Number of Baffles As we mentioned earlier, conventionally, baffles are placed at the periphery (wall) of tumblers in industrial applications. Little is known about the effect of the number of baffles on mixing in a solids mixer. Therefore,
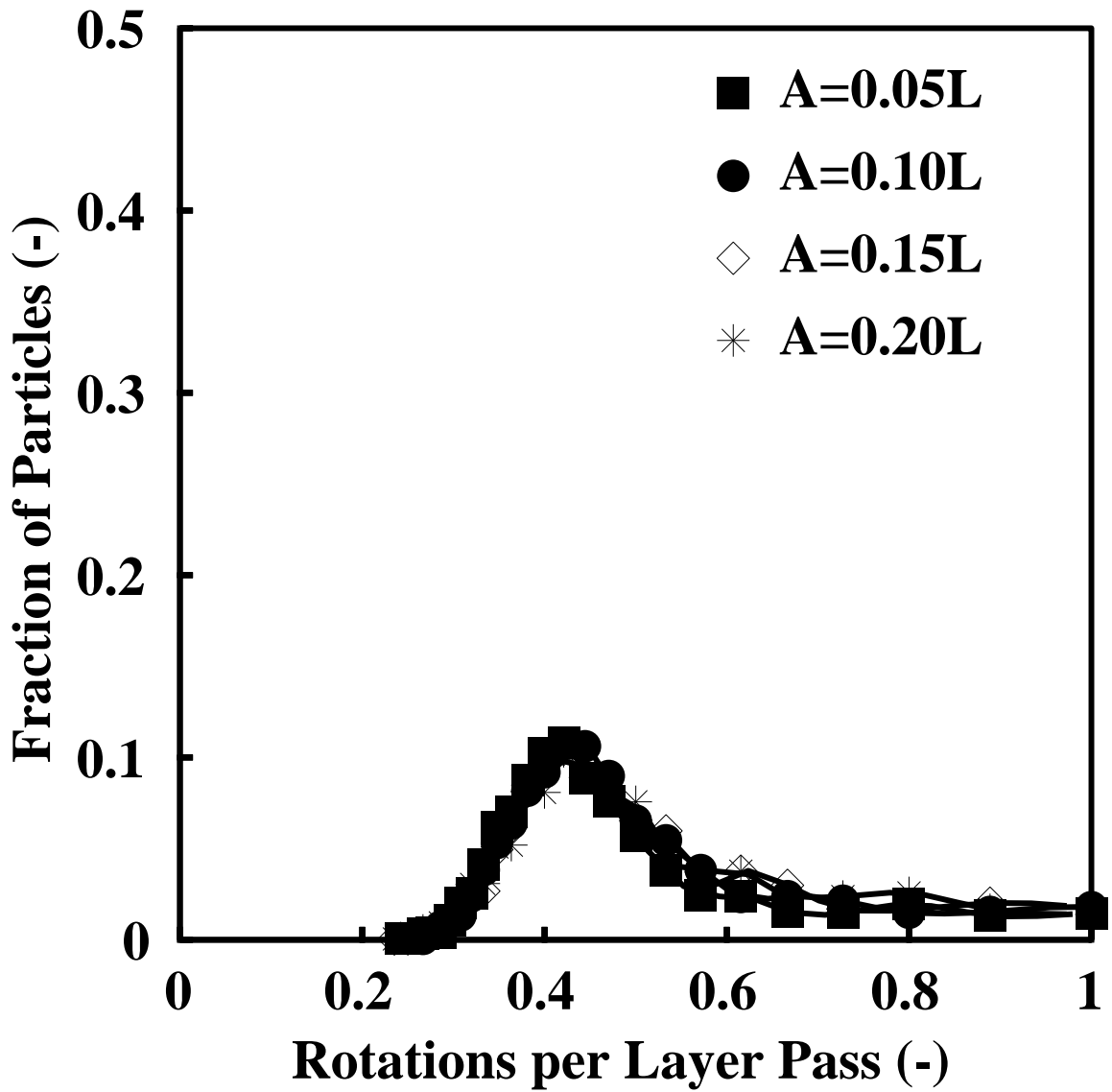
Figure 21: Probability distribution of the number of layer passes a particle takes per rotation of the drum for many different S-shaped baffles. A is varied from 5% to 20% of L with an increment of 5%. L is the effective length of the baffle.
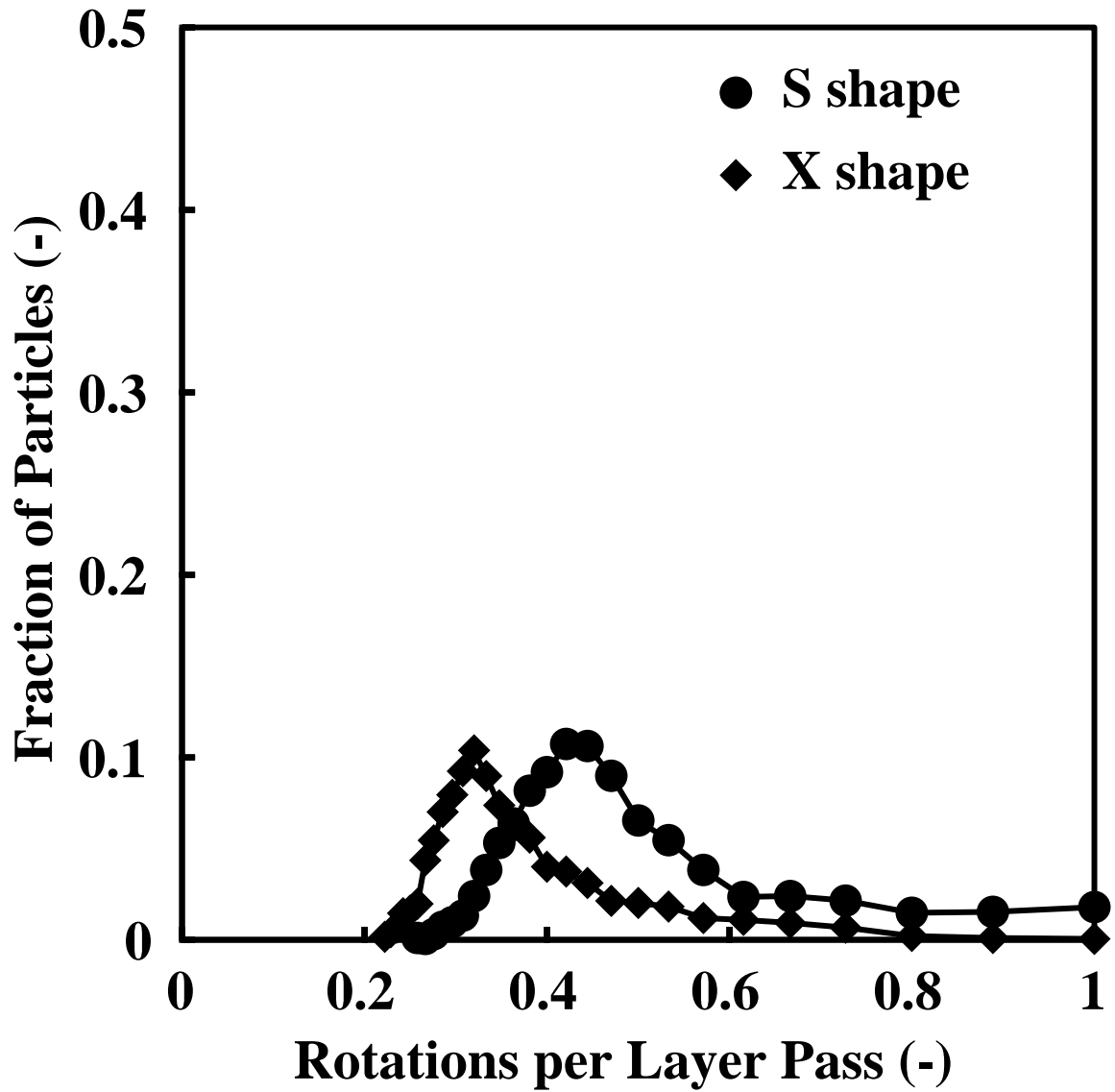
Figure 22: Probability distribution of the number of layer passes a particle takes per rotation of the drum for S and X-shaped baffles.

starting with a base case of no baffle attached to the wall, we systematically vary the number of baffles in a tumbler up to eight in number. These different cases are shown in Figure 23. These radial baffles are oriented in such a way that they have equal angular distance. For example, for a case with 6 baffles, the baffles make an angle of 60 degrees with each other if extended up to the centre. The baffle length is the same for all the cases ($L \approx D/4$). As usual, other parameters like number of particles, etc., remain unchanged for all the cases to single out the effect of only one parameter (i.e., the effect of number of baffles) on the mixing. We perform similar layer pass simulations as discussed in Section 3.4.4 and plot the results in Figure 24. We observe that, except in the cases with no baffle or one baffle, all other distributions are centered around 0.5 rotations per layer pass (the range of peak positions for all cases is 0.44 – 0.53). Surprisingly, a wider distribution is obtained when there is no baffle or just a single baffle fitted to the wall of the tumbler. As more baffles are added, the distributions become narrower, suggesting a poor mixing outcome. Figure 24 strongly suggests that even an unbaffled tumbler has a better mixing performance compared to a tumbler with a number of baffles fitted radially to the wall (as normally used in industrial practices). The mixing performance gets worse as more and more radial baffles are added to the tumbler. This observation again bolsters the fact that mixers with novel designs of baffles placed axially in or near the shearing layers are expected to outperform any conventional solids mixers where baffles are fitted radially to the wall of the device.
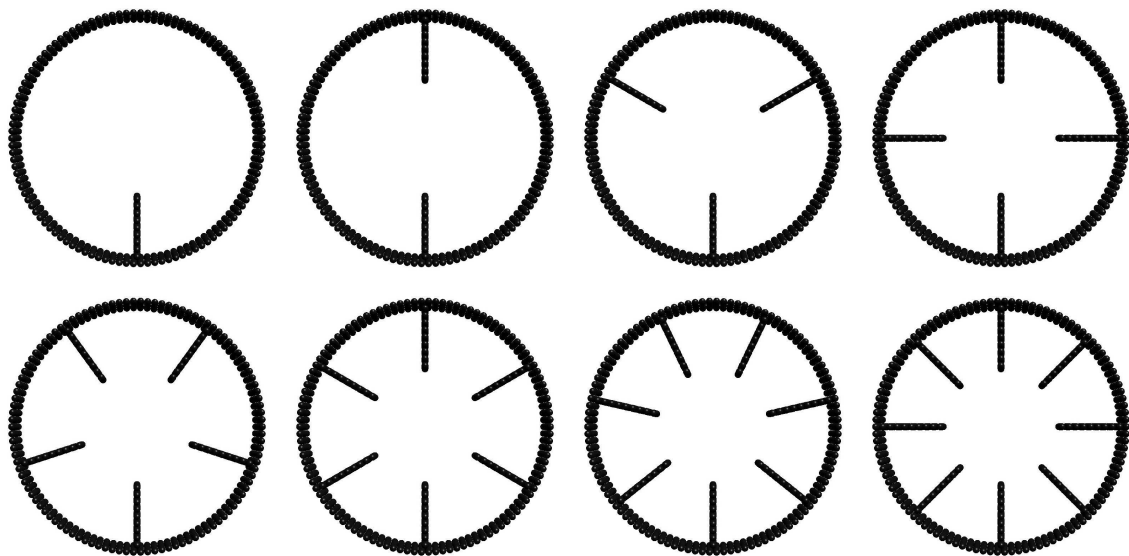
Figure 23: Tumblers fitted with various numbers of radial baffles at the wall. Up to eight baffles have been considered.
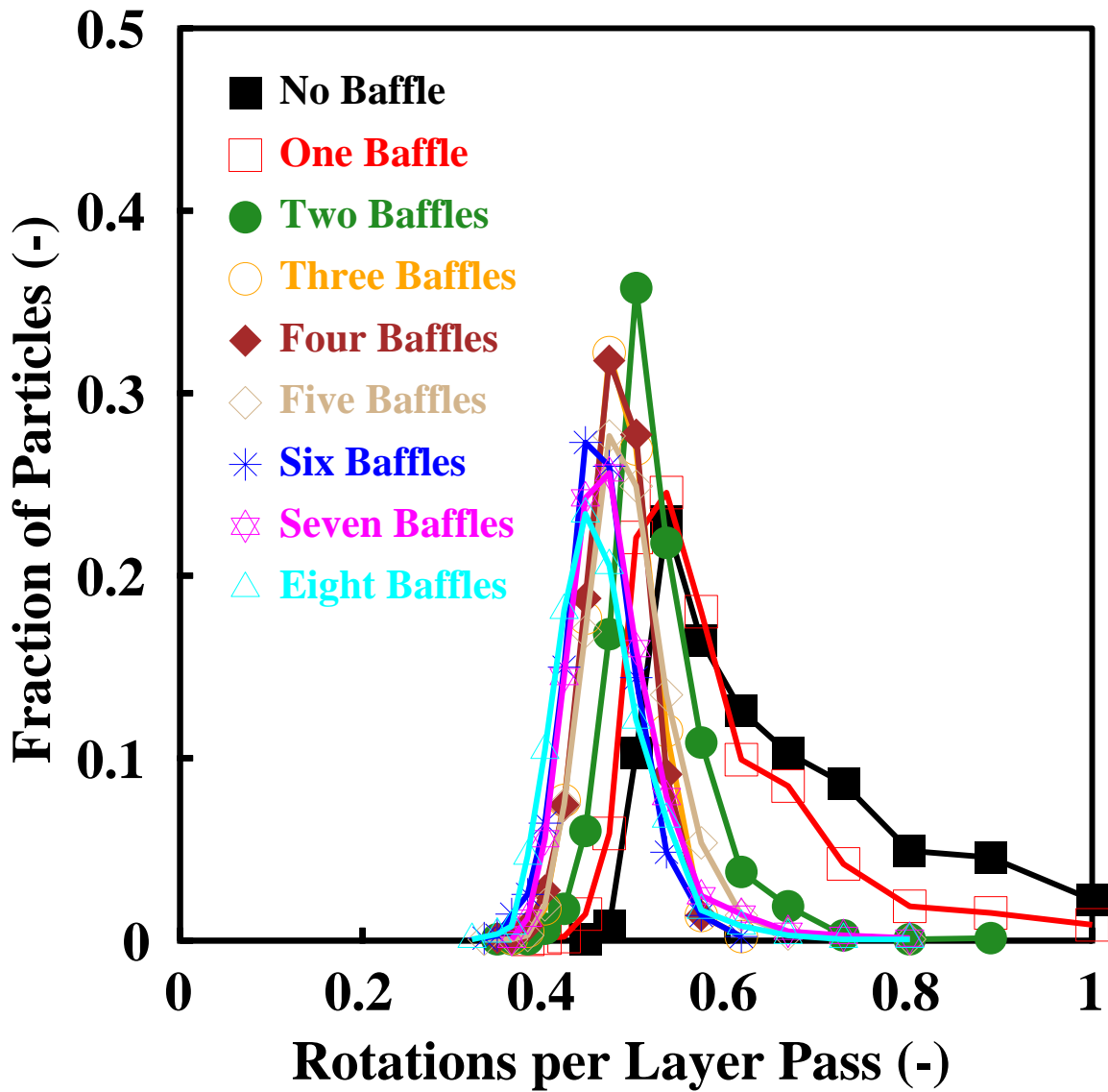
Figure 24: Probability distribution of the number of layer passes a particle takes per rotation of the drum for various number of radial baffles fitted to the wall of a tumbler.

4.0   SEGREGATION IN A CHUTE FLOW

4.1   MOTIVATION & BACKGROUND

At the very outset, let us take a brief look at why chutes are an important part of the solids processing industry. As an example, we briefly describe the importance of understanding segregation in chute flows in the steel industry, as we have noted that earlier work on segregation in industrial cases mostly pertained to metallurgical industry.

Traditionally, metallurgical industries have used chutes to transfer and distribute granular materials (such as coke, iron ore, etc.). The distribution of coke, ore, sinter and other raw materials at the stock level of a blast furnace is very crucial for its smooth operation. This is achieved with the use of a rotating chute (see Figure 25) whose rotation rate (RPM) and inclination angle can be adjusted as needed. The hopper situated above the chute contains the charge which consists of materials of various sizes with different physical properties and it is difficult to distribute uniformly, while still maintaining a minimum resistance to the ascending hot gas flow. This hot gas actually reduces the metallic charge (iron ore) and produces hotmetal or liquid iron (which is later converted to steel). "Burden distribution" is a generic term used to denote the radial ore/coke distribution as well as the particle size distribution in the top part of a blast furnace. Owing to the differences in particle size and density, the burden materials tend to separate from the main stream and get distributed radially at the top of the furnace as per the principles of segregation. Therefore, segregation plays a major role in determining the fate of any burden distribution scheme. Different burden distribution strategies (i.e., using different chute RPM and angle) may yield different segregation patterns, and in turn, will produce different voidage across the particle bed in the top of a furnace. Since voidage distribution has a close relationship with gas utilization in a
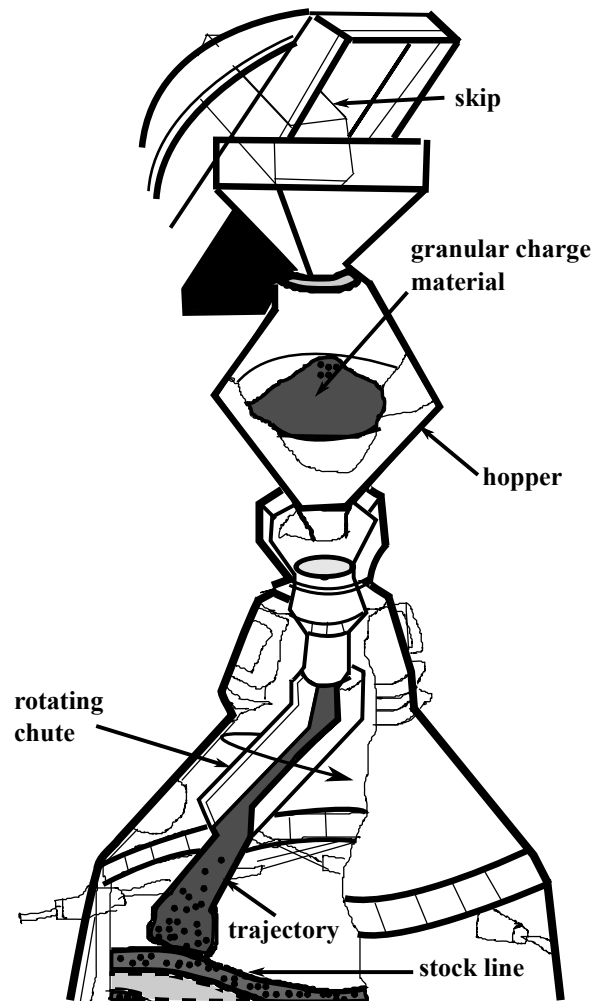
Figure 25: Example of chute flow in actual practice. An industrial chute is used for transfer and distribution of granular materials on top of a blast furnace for producing liquid iron in a steel plant. This illustration shows a bell-less top (BLT) charging device.

furnace, the fuel rate can be effectively reduced if the extent of gas utilization is improved. Non-uniform distribution of the charge materials results in a non-uniform radial distribution of particle size and voidage and hence permeability of the particle bed. The resulting non-uniform radial distribution of the gas flow affects the charge descent rate because the ascending gas finds the path of least resistance and the gas will flow through the areas of higher permeability. The resulting non-uniform flow of gas in the other localities leads to inadequate utilization of its thermal and chemical energies and hence leads to inferior fuel efficiency, uneven descent of burden, lower productivity and excessive wall build-up or higher thermal load on the walls of the blast furnace. This amounts to a recurring loss of revenue in ironmaking. This discussion only highlights the industrial impact of segregation during chute flow for one specific industry, as there are numerous applications of chute flow in many other industries. It is clear that it is important to understand and control the segregation in a chute flow.

A literature review reveals that there have been many studies [16, 30, 39, 87, 234–249] of granular flow, which focused on chute flows because of the practical importance of such flows in granular transportation and the relative simplicity of this type of flow (which allows for detailed development and testing of theory [30]).

Savage and Lun [39] observed that in a chute flow, for high solid volume fractions, large voids are less likely to be formed than small voids. As a result, smaller particles percolate through the voids created by larger particles and descend to layers below. This results in a net segregation flux of the smaller particles in the downward direction (i.e., normal to the chute surface or inclined plane). They developed the following expression for segregation flux of small particles:

$$N_b = n_v \frac{n_b}{n_a + n_b} n_p u_r \bar{D} [E_b + \bar{E} - E_m + 1] exp[-\frac{E_b - E_m}{\bar{E} - E_m}] \tag{4.1}$$

where N_b = flux of small particles (type b), n_v = number of voids per unit area, n_i = number of type i particles, n_p = number of particles per unit area in a layer, u_r = mean downstream velocity of a particle in a layer relative to those in underlying layers, $\bar{D}$ = mean particle diameter, E_b = ratio of small particle diameter to mean particle diameter, $\bar{E}$ = ratio of mean void diameter to mean particle diameter and E_m = minimum possible

voids diameter ratio. Similar segregation flux expression was derived for larger particles by replacing b with a everywhere in Equation 4.1. The above authors presented experimental data for polystyrene beads of varying sizes in a chute flow, in which all the smaller particles collect at the lower levels in the layer, confirming the percolation mechanism as described both here and in Section 2.1. In their work, comparisons of the distance along the chute at which the material segregates completely into two layers is found to be in agreement with experiments. Hirschfield and Rapaport [241], using molecular dynamics simulations, showed that in a chute flow larger particles rise to the top of the layer which is in agreement with the results of Savage and Lun [39].

Dolgunin et al. [238, 242] studied segregation in a chute flow for both size and density differences. For size segregation they used a close range (6.6 - 7.0 mm smooth steel balls) while the density segregation experiments were performed for nearly a 1:2 density ratio of two different materials. The interesting result from their work is that they obtained a non-monotonic (S-shaped) concentration profile for different components. They also validated their continuum mathematical model of segregation with very good agreement with experiments. Though a model involving the constitutive equation for segregation flux was developed earlier by Khakhar et al. [21] for density segregation in a tumbler using an effective medium approach, the work of Dolgunin et al. appears to be one of the first continuum models of segregation involving a chute flow, for both size and density. Later, Khakhar et al. [30] noted that the model of Dolgunin et al., however, is not rigorous and thus does not clearly specify the driving forces for the segregation or the dependence of the segregation flux on the particle properties.

The work of Khakhar et al. [30] and Ottino et al. [16] critically reviewed the different segregation models and observed that, although the theories for segregation provide some physical insight into the process and are reasonably successful in describing segregation in chute flows, few are grounded on fundamentals. They suggested that statistical mechanical studies (based on kinetic theory) of hard sphere mixtures can provide a starting point for understanding granular segregation. Therefore, they set out to study density and size segregation in a chute flow of cohesionless spherical particles by means of computations and theory based on the transport equations for a mixture of nearly elastic particles (i.e., using

statistical mechanics or kinetic theory). They noted that the kinetic-theory results permit a general understanding of the causes of segregation. They were successful in developing the segregation fluxes based on number fraction or concentration gradient (ordinary diffusion), granular temperature gradient (temperature diffusion) and granular pressure gradient (pressure diffusion). Granular temperature is proportional to the kinetic energy of the velocity fluctuations of the particles and is defined as:

$$T = (\langle u^2 \rangle - \langle u \rangle^2) \tag{4.2}$$

where u is the velocity and the angled bracket indicates a time average. Khakhar et al. [30] compared the results from kinetic theory of binary mixtures with computations using Monte Carlo (MC) simulations (for elastic particles) and particle dynamics (PD) or DEM simulations (for inelastic particles). Ordinary diffusion always results in mixing, whereas pressure and temperature diffusion produce segregation if density and size differences are present. In their work, the equations for the pressure and ordinary diffusion fluxes for equal-sized particles with different densities were identical to the corresponding equations for an ideal gas; the form of the binary diffusivity, however, was different. They observed that the temperature diffusion flux does not contribute to segregation in this case. Thus, denser particles always concentrate in regions of higher pressure, regardless of the granular temperature profile. The case of different-sized particles with equal density is more complex, and the direction of the segregation flux depends on both the temperature and pressure gradient (especially, for segregation in a flowing layer such as in a tumbler or a chute). In general, the gradient in temperature across the layer results in the smaller particles migrating to the higher-temperature regions. Khakhar et al. [30] also noted that extrapolating these results to temperature-induced segregation in a chute flow leads to a prediction that the smaller particles migrate to the top of the layer as the top layer has higher fluctuating velocity or granular temperature; this is the reverse of the predictions of Hirschfield and Rapaport [241] and Savage and Lun [39]. They argued that this aberration is due to the fact that gravitational effects were not considered in their study, and these effects might produce pressure gradients that could reverse the segregation flux, i.e., direction of the segregation flux depends on both the temperature and pressure gradient for size segregation.

More recently, Zhang et al. [247] studied how segregation can be enhanced in an industrial process, in this case, in a chute used for preparing materials for sintering in ironmaking. Size segregation is beneficial in preparing a well-bedded feedstock for high sintering quality. They tried to understand how a magnetic field can enhance the segregation in a chute by placing magnets beneath the chute in many different configurations. They used two dimensional (2D) DEM to simulate these different cases with magnets. Four different sizes of particles (disks) were considered. To test the accuracy of their simulation, they compared the velocity field of particles with a snapshot of the actual chute flow when the particles are leaving the chute tip, which is an indirect qualitative validation.

In the area of measurement of flow properties in a granular flow down an incline, the work of Barbolini et al. [248] deserves a mention here. They have outlined different techniques for the measurements of velocity and concentration profiles in a setup similar to chute flow. They also compared their velocity profile measurements with the velocity profiles found in the literature involving experiments with real snow avalanches and a significant agreement was observed.

In the present work, we examine the deposition behavior of both mono-sized and polydisperse dry granular materials in an inclined chute flow (quasi-2D). Unlike other studies in the past, for the first time, we perform a systematic study, both experimentally and numerically (using DEM), to observe the effects of different operating parameters such as chute angle, particle size, falling height and charge amount on the mass fraction distribution of granular materials after deposition. Tuning of the underlying contact force parameter of DEM allows to achieve realistic results and is used as a means of validating the model against available experimental data. The tuned model is then used to find the critical chute length for segregation based on a recently proposed theory by our group [31], which we elaborate further in the next section. As per the theory, segregation can be eliminated if a flow is perturbed above a critical forcing frequency via periodic flow inversion. This critical frequency, f_{crit}, is inversely proportional to the characteristic time of segregation, t_S. Mixing is observed instead of segregation when $L < U_{avg}t_S$, where L, U_{avg}, and t_S denote the length of the chute, the average stream-wise flow velocity of the particles, and the characteristic time of segregation, respectively.

4.2 HYPOTHESIS REVISITED: TIME MODULATION IN A CHUTE FLOW

In this section, an expression for the critical forcing frequency (or critical time or critical chute length) is developed, which is central to our hypothesis of flow modulation as described in Section 3.2.

Utilizing existing theoretical tools [21, 30], which are briefly reviewed in the preceding sections, one can estimate the value of the characteristic segregation time t_S. The critical forcing frequency f_{crit} can be obtained via a scaling argument as follows:

The variation of number fraction of small particles in the layer (c) is given by the convective-diffusion equation:

$$\frac{\partial c}{\partial t} + v_x \frac{\partial c}{\partial x} + v_y \frac{\partial c}{\partial y} = \frac{\partial}{\partial y}\left(D\frac{\partial c}{\partial y} - J_s\right) \tag{4.3}$$

neglecting the diffusion and segregation fluxes in the flow direction (x) (that is, assuming that the Péclet number in the x direction is large). The term on the right hand side is the diffusional flux with D and J_S being the diffusion coefficient and the segregating flux, respectively. Khakhar et al. [21] derived the convective-diffusion equation for density segregation, and they proposed the segregation flux expression for the more dense particles considering the "buoyant force" as the driving force (effective medium approach). An empirically similar expression for the segregation flux for a mixture of particles of different sizes flowing down an inclined plane was also proposed by Dolgunin and Ukolov [238, 242]. Savage and Lun [39] proposed a different segregation flux expression for mixtures of different sizes of particles. One can refer to the discussions in Section 4.1.

Surprisingly, though the mechanism of segregation for size and density segregation is different, the pattern of segregation is very similar in both cases (large or light particles rise on the top of the flowing layer, and the small or denser particles go down). Though a model for density segregation flux is available [21], a general expression for the segregation flux in the flowing layer due to size differences is not available. However, it can be derived following a procedure similar to density segregation as shown below. Recently, Hajra et al. [250] have

proposed the following form of the segregation velocity for a segregating species:

$$v_S = [K_T + (1 - c)K_S](1 - \bar{d}) \tag{4.4}$$

where $\bar{d} = d_1/d_2$ is the size ratio, d_1 and d_2 are the diameter of small (segregating species) and large particles, respectively; $c = \phi_1/\phi_t$ is the number fraction of the small particles, ϕ_1 is the concentration (volume fraction) of the small particles, $\phi_t = (\phi_1 + \phi_2)$ is the total solids volume fraction; K_T and K_S are the characteristic segregation velocities. K_T and K_S are lumped parameters, which depend on granular temperature, local void fraction, gravity, particle sizes, density, shape, roughness, coefficient of friction, coefficient of restitution, concentration of small and large particles, etc. Hence, the segregation flux of the segregating species could be written as

$$J_S = v_S \phi_1 \tag{4.5}$$

substituting for the expression of v_S from Equation 4.4 into Equation 4.5, we get

$$J_S = [K_T + (1 - c)K_S](1 - \bar{d})\phi_t c \tag{4.6}$$

If $\bar{d} = 1$ (for equal sized particles), then $v_S = 0$ and $J_S = 0$ (there is no size segregation).

Assuming the total volume fraction (ϕ_t) to be nearly constant, and substituting for the expression for the segregation flux J_S using Equation 4.6 we obtain, from Equation 4.3,

$$\frac{\partial c}{\partial t} + v_x \frac{\partial c}{\partial x} + v_y \frac{\partial c}{\partial y} = \frac{\partial}{\partial y}[D\frac{\partial c}{\partial y} - \{K_T + (1 - c)K_S\}(1 - \bar{d})\phi_t c] \tag{4.7}$$

If we put $K_S = 0$ then our flux expression is similar to the model of Khakhar et al. [21] derived for density segregation and to the model of Dolgunin and Ukolov [238] proposed for size segregation in chute flow. The characteristic segregation velocity, K_S accounts for the local motion due to the physical and mechanical properties of the particles such as size, shape, roughness, coefficient of restitution, coefficient of friction, etc.

Now, we can write down the expression for the characteristic segregation time as $t_S = R_1/[(K_T + (1 - c)K_S)(1 - \bar{d})]$, where R_1 is the radius of the small particles. Now using this value, we can define a segregation-based Péclet number as $Pe = \frac{(K_T + (1-c)K_S)(1-\bar{d})R_1}{D}$, where D is the collisional diffusivity. Rearranging the above expression, we get $Pe = [(K_T R_1/D) +$

70

$(1 - c)(K_S R_1/D)](1 - \bar{d})$. Because of the current theoretical uncertainty and the time-varying nature of the flow (as well as granular temperature, local void fraction, system non-uniformity, etc), we treat $\beta = K_T R_1/D$ and $\alpha = K_S R_1/D$ as the fitting parameters that should be a decreasing function of fluctuation energy of the flow and should be close to unity at small to moderate energies. This yields $Pe = \beta(1 - \bar{d}) + (1 - c)\alpha(1 - \bar{d})$. The particle diffusivity in sheared granular flows were obtained by Savage [251] from numerical simulations of shear flow of nearly elastic hard spheres. A scaling of the form $D = F(\nu)d^2\dot{\gamma}$ was obtained, where d is the particle diameter, $\dot{\gamma}$ is the shear rate, and $F(\nu)$ is a function of the solid volume fraction (ν). Hajra and Khakhar [155] confirmed the scaling experimentally. By using the diffusivity as given by Savage [251] ($D = 0.01R_1^2\dot{\gamma}$), we get t_S written as $t_S = \frac{t_D}{Pe} = \frac{R_1^2}{DPe} = \frac{100}{[\beta+(1-c)\alpha](1-\bar{d})\dot{\gamma}}$, where $\dot{\gamma}$ is the shear rate. This suggests that the critical perturbation frequency, f_{crit}, will vary linearly with the shear rate as

$$f_{crit} = 0.01\dot{\gamma}(1 - \bar{d})[\beta + (1 - c)\alpha] \tag{4.8}$$

Now we can derive the critical chute length to initiate segregation as follows: Khakhar et al. [21] verified that the flow down an inclined chute is essentially linear, so that $\dot{\gamma} = 2U_{avg}/H$, where U_{avg} is the average stream-wise flow velocity and H is the height of the particle stream flowing down the chute at a stable region. Therefore, by using the expression $U_{avg} = \dot{\gamma}H/2$, the critical chute length to initiate segregation is then given by (using Equation 4.8)

$$L_{crit} = U_{avg}t_S = U_{avg}/f_{crit} = \frac{100U_{avg}}{[\beta + (1 - c)\alpha](1 - \bar{d})\dot{\gamma}} = \frac{50H}{[\beta + (1 - c)\alpha](1 - \bar{d})} \tag{4.9}$$

4.3 EXPERIMENTAL SETUP

The experimental results are obtained on a test unit [252] as shown in Figure 26. The setup consists of an inclined chute of rectangular cross section made up of PMMA (polymethylmethacrylate) in a quasi-two-dimensional rectangular cell. The depth to width ratio is 1:8. The bottom of the chute is rough and it can be fixed at two different angles (45 degrees and 60 degrees) to the vertical. To control the depth of the moving bed along the chute, a pneumatic control gate is installed at the hopper opening to regulate the flow. The gate opening
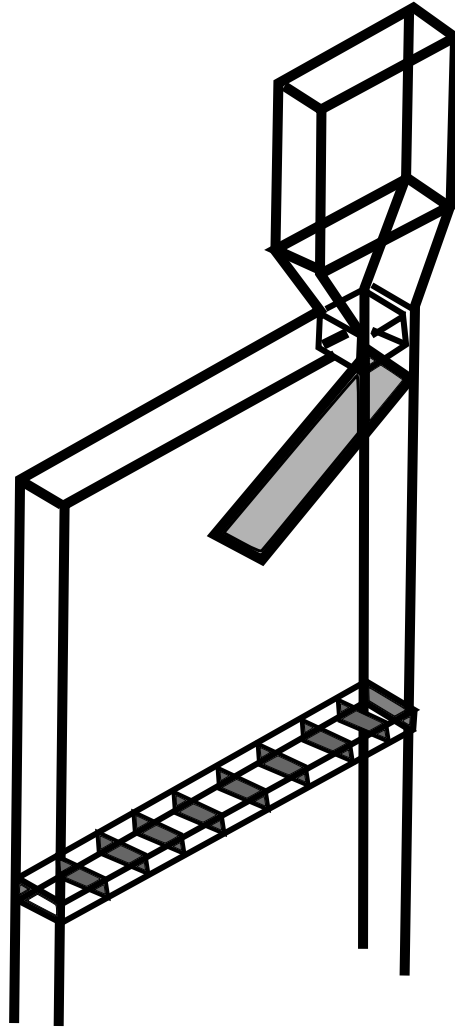
Figure 26: Schematic of the chute flow experimental setup showing a model hopper, chute and deposit bins (segregation box). The chute length is 600 mm, the vertical distance between the chute hinge and the hopper opening (flow control gate) is 100 mm, the hopper cross section is square (150 mm × 150 mm); the setup is quasi-2D with a depth of 150 mm and a width of 1200 mm (1:8 aspect ratio). There are 20 bins each having a volume of 60 mm × 60 mm × 150 mm (L × H × W). The bins can take up to three different vertical positions with respect to the chute hinge. Levels 1, 2 and 3 as described in the text are 800 mm, 1050 mm and 1300 mm below the chute hinge, respectively.

pressure is varied between 2 kg/cm^2 – 5 kg/cm^2, which causes the gate to open instantly. A horizontal tray (called a "segregation box") with 20 bins to collect the deposited materials can be slid in a rail inside the setup at three different levels (heights). Nearly spherical polystyrene particles of different sizes (6, 7 and 14 mm) are used as the test granular material. A vacuum cleaner is used to collect the particles from different bins of the segregation box. The collected particles are later weighed using a highly accurate electronic weighing balance (Sartorius make, Model GP 3202, capacity 3200 g with 0.01 g accuracy).

4.4   RESULTS & DISCUSSIONS

In this section, we discuss the results relating to the deposition behavior of both mono-sized and polydisperse dry granular materials in a chute flow. The results obtained from many experiments and DEM simulations are compared for the flow of a stream of granular material down an inclined chute. The effects of different parameters such as chute angle, particle size, falling height and charge amount on the mass fraction distribution of granular materials after deposition are also examined. Starting with the mono-dispersed case, we first tune the underlying contact force parameters of the DEM model so that we can obtain realistic results. Sensitivity of a model parameter, namely the yield stress of the material, on the final results has been carried out so that appropriate contact force parameters can be chosen to validate the model. The tuned model is then used to find the critical chute length for segregation based on the theory discussed in Sections 3.2 and 4.2.

4.4.1   Mono-dispersed Flow

4.4.1.1   DEM Simulation & Tuning of Force Model   The simulation parameters (chute angle, particle size, etc.) for various cases considered in the present study are inspired by experiments [252] performed on an identical setup (refer to Figure 26 in Section 4.3). Figure 27 shows the simulation setup, which closely resembles the actual experimental setup as described in Section 4.3. All the pertinent dimensions and other parameters like number

73
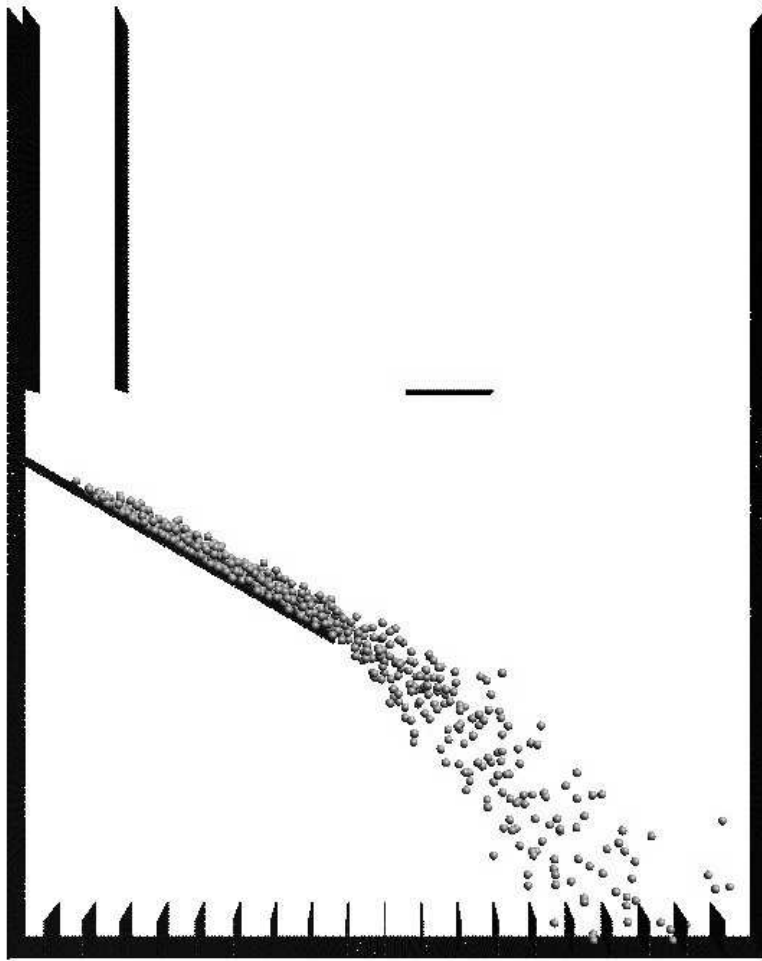
Figure 27: The chute flow setup as used in the numerical simulations. This typical snapshot shows 14 mm diameter particles flowing down a 600 mm chute inclined at 60 degrees with the vertical. Hopper with the gate (opened to the right, short black line) is also shown in this picture. The chute, bins and other fixed walls are made from 4 mm diameter particles. There are 20 bins spanning the full width of the setup (1200 mm). The simulation is periodic in the direction pointing into the plane of the paper. Bins are numbered from 1 to 20 (R to L): bins 1-10 are called wall-side bins and bins 11-20 are called chute-side bins.

Table 3: Material properties used in the simulations (and experiments)

Parameter	Value
Young's Modulus (E, GPa)	2.9
Density (ρ, kg/m^3)	951-1160
Coefficient of Friction (μ)	0.30
Poisson Ratio (ν)	0.33
Yield Stress (σ_y, MPa)	45.0

of particles (or mass of particles), density, size of particles, etc., are kept as close as possible to the experimental conditions so that results can be compared with reasonable accuracy.

A typical simulation evolves with particles starting from rest in the hopper after gravitational settling. The hopper gate is opened and as time elapses, the particles are acted upon by gravity resulting in their flow through the chute and finally the particles are deposited in various bins after leaving the chute (refer to Figure 27).

Before we present results for the different cases, let us discuss how the DEM model is tuned. We consider two force models in our PD simulations: elastic with viscous damping (referred to as *elastic* in Section 2.2.2) and elasto-plastic (referred to as *plastic* in Section 2.2.2). Table 3 shows the material properties that are used in the simulations. Figures 28 (a) and (b) compare the results from the *elastic* and *plastic* force models with the experimental data for two different experimental cases as mentioned in the caption. Though the simulation results agree well with the experiments for both types of force models, we choose the *plastic* force model because of its superior capability to capture the underlying physics. A *plastic* model was favored because all the model parameters can be directly derived from the material properties. In the *elastic* model, the damping parameter cannot be obtained from material properties.

(a)　　　　　　　　　　　　　　　　　　　　(b)
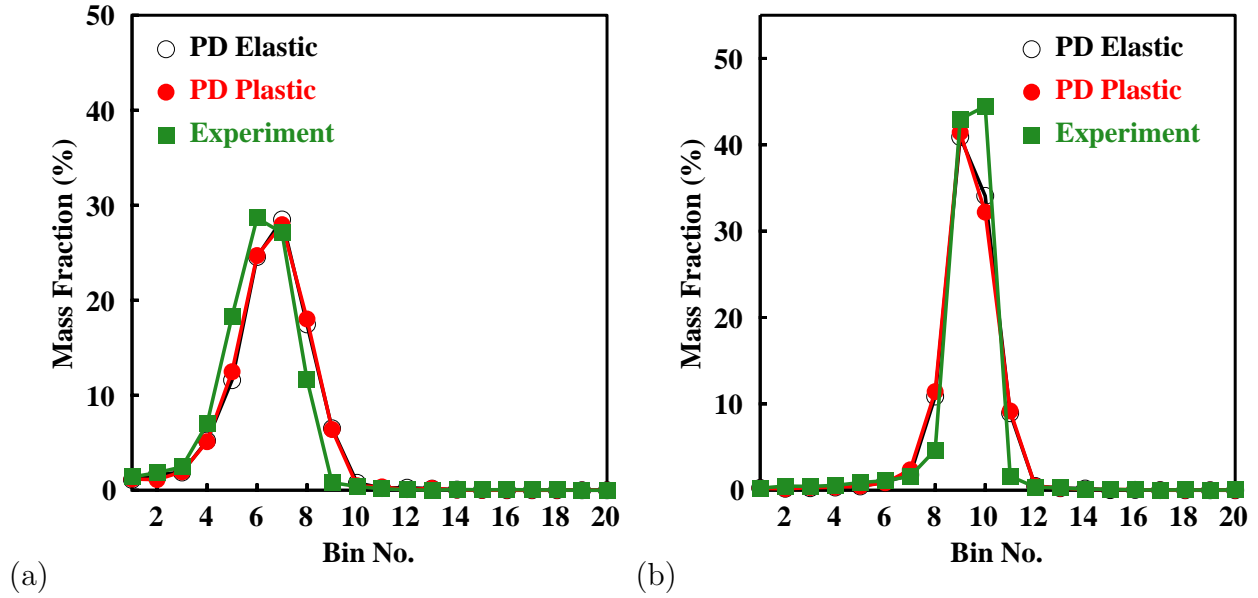
Figure 28: Comparison of simulation results from two force models with the data obtained from the experiments. The force models *PD Elastic* and *PD Plastic* denote elastic with viscous damping and elasto-plastic models, respectively. (a) corresponds to a case with 7 mm diameter polystyrene balls (1 kg) with a 60 degrees chute and the bins placed at level 1. (b) corresponds to 6 mm diameter polystyrene balls (0.537 kg) with a 45 degrees chute and the bins placed at level 1. Refer to Figure 26 for the positions of different levels.

First, we tune the yield stress used in the *plastic* force model to mimic realistic contact mechanics. The tuning is performed in the following way: we adjust the yield stress in order to match a single set of experimental data and then the adjusted yield stress is kept fixed in the model and is subsequently used to compare results from other experimental data or make predictions for different chute flow cases. Figure 29 shows that a yield stress of 45 MPa reproduces the experimental results very well. The peak position and peak height for the *plastic* model with a yield stress of 45 MPa are bin number 7 and 27.96%, respectively. This is close to the experimental observation of peak position at bin number 6 and peak height at 28.65%. The corresponding values for the next closest case (*plastic* model with 22.5 MPa yield stress) are bin number 7 and 31.69%, respectively. Note that here we prefer peak height over peak position to select the model as both the yield stresses give a close peak position when compared with the experiment. In addition to the above comparisons, we also perform two-sample Kolmogorov-Smirnov (K-S) test [253] to cross-check the agreement between the experimental result and *plastic* models with different yield stress parameters. The two-sample K-S test is generally performed for comparing two samples or distributions, as it is sensitive to differences in both location and shape of the empirical cumulative distribution functions (CDFs) of the two samples. The two-sample K-S test returns the probability (p) of observing the given statistic (i.e., whether the two distributions are from the same continuous distribution or not – a p value of 1.0 signifies that the two distributions are identical) and also quantifies a distance (k) between the empirical distribution functions of the two distributions. A lower k value signifies a better agreement between the two distributions. Table 4 summarizes the results of the two-sample K-S test performed [254] on the yield stress tuning data. The experimental data are used as one of the samples for all cases. One can clearly observe that the experimental data is best matched by the *plastic* force model with a yield stress of 1x (i.e., 45 MPa) as it produces the highest p value and the lowest k value. Therefore, we select the *plastic* model with 45 MPa yield stress to simulate various cases as described in the next sub-sections (coincidentally, the yield stress of polystyrene beads is $\sim$ 45 MPa, which indicates that our *plastic* model has a sound force model and captures the contact mechanics very well).
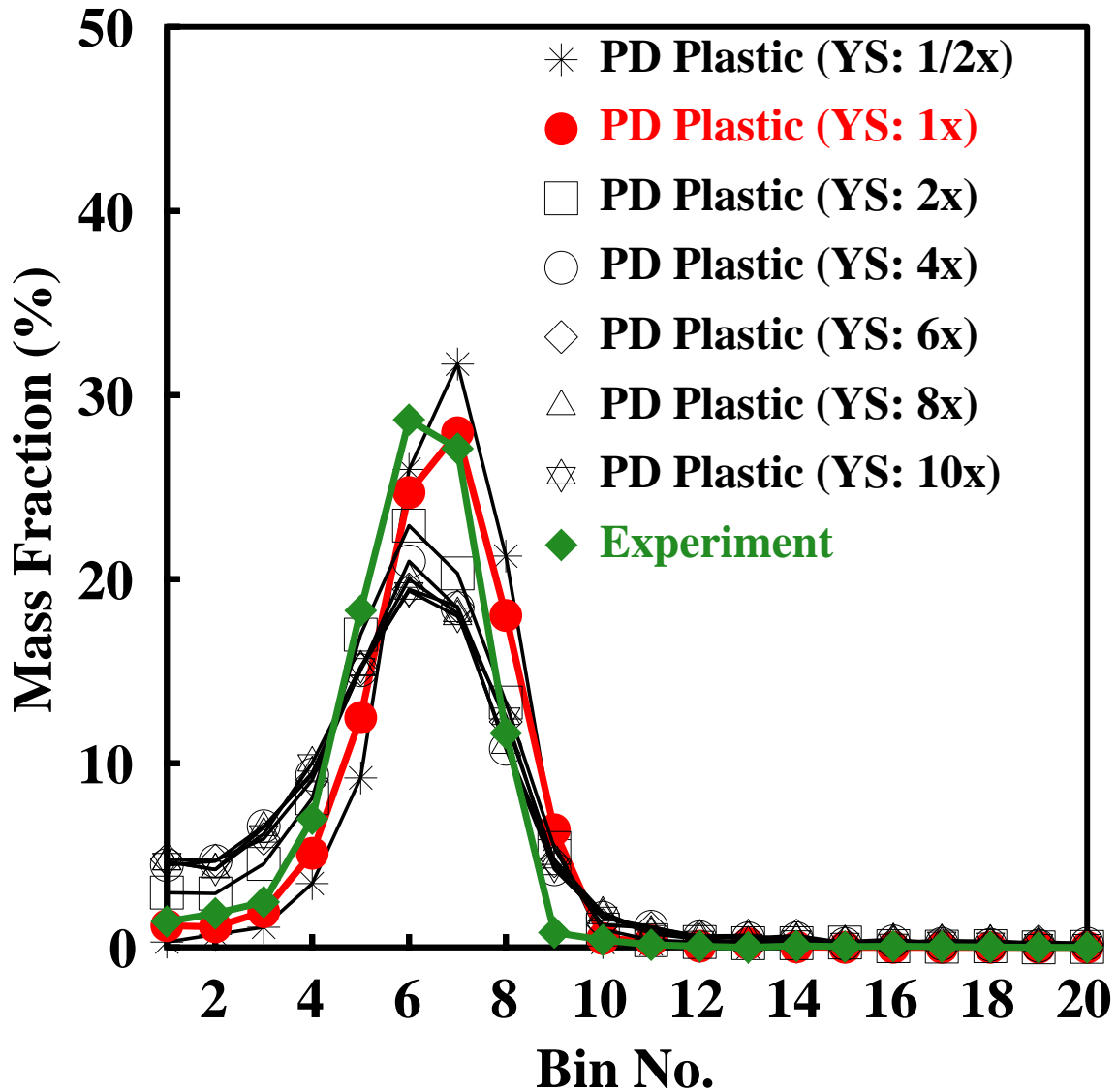
Figure 29: Tuning of the plastic force model parameter (YS : yield stress) for a case similar to the experimental condition as in Figure 28 (a). A base YS value of 1x corresponds to 45 MPa. Note that only two curves (corresponding to experiment and PD *plastic* model with YS = 45 MPa) have their line colors changed to emphasize their agreement as compared to other cases.

Table 4: Two-sample Kolmogorov-Smirnov (K-S) test results of elasto-plastic force model tuning data

Case	p value	k value
PD Plastic (YS: 1/2x) vs. Experiment	0.50	0.25
PD Plastic (YS: 1x) vs. Experiment	0.97	0.15
PD Plastic (YS: 2x) vs. Experiment	0.50	0.25
PD Plastic (YS: 10x) vs. Experiment	0.00 (test failed)	0.50

As Khakhar et al. [223] noted that thorough studies of the parametric sensitivity of the results of DEM simulations to the used parameters are lacking, we believe that Figure 28 is a small but important step in that direction. Though more rigorous studies in this direction are warranted, it is worthwhile to mention here that, recently, McCarthy et al. [100] have performed a similar validation study of DEM for a different system (annular cell).

The various simulations and the operating parameters are listed in Table 5. In the following sub-sections, simulation results for the various cases mentioned in Table 5 are presented and whenever applicable, comparison is made with the experimental data.

4.4.1.2 Case 1: Effect of Charge Amount The only parameter which is varied for this case is the total number (or mass) of particles in the hopper. This is also known as the charge amount in industrial practice. Refer to Table 5 for a complete description of all the operating parameters. The hopper is filled with three different amounts of particles separately and in each run, the particles are allowed to fall on the chute. Figure 30 shows the comparison between model and experiment of the effect of charge amount on mass fraction distribution. All peak positions are centered on bin number 7 and the agreement becomes better for higher charge amount. The peak heights are 26.72% (300 g, model), 35.02% (300 g, experiment), 31.10% (600 g, model), 38.31% (600 g, experiment), 32.28% (900 g, model)

Table 5: Different cases for mono-disperse simulation (and experiment) and the operating parameters used

Case	Operating parameters
Case 1: Effect of charge amount	**Mass of particles:** 0.3 kg ($N = 1455$ particles), 0.6 kg ($N = 2910$), 0.9 kg ($N = 4365$)
	Diameter of particles: 7 mm
	Chute angle: 45°
	Bin location: level 2 (1050 mm below chute hinge)
Case 2: Effect of particle size	**Diameter of particles:** 7 mm and 14 mm
	Mass of particles: 1 kg ($N_7 = 4850$, $N_{14} = 600$)
	Chute angle: 60°
	Bin location: level 1 (800 mm below chute hinge)
Case 3: Effect of falling height	**Bin location:** level 1, 2 and 3
	(level 3 is 1300 mm below chute hinge)
	Diameter of particles: 6 mm
	Mass of particles: 1 kg ($N = 5000$)
	Chute angle: 60°
Case 4: Effect of chute angle	**Chute angle:** 45° and 60°
	Diameter of particles: 6 mm
	Mass of particles: 0.537 kg ($N = 5000$)
	Bin location: level 1
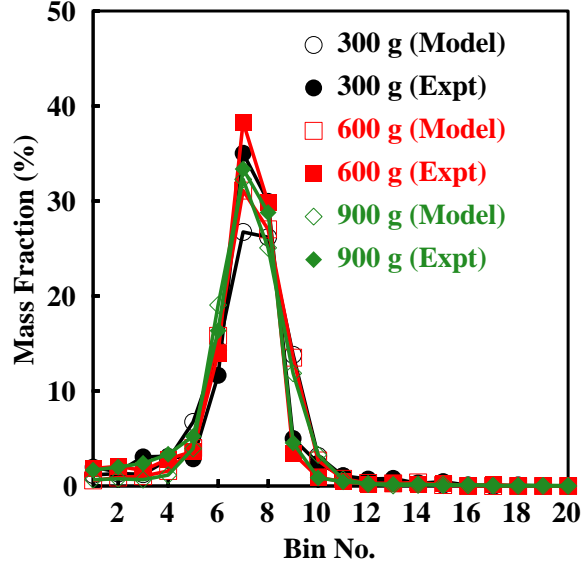
Figure 30: Effect of charge amount: comparison with experimental data.

and 33.37% (900 g, experiment). Clearly, there is a qualitative agreement between the trends for both model and experiment. In addition to comparing peak positions and peak heights of the distributions, we also perform a two-sample Kolmogorov-Smirnov (K-S) test on the corresponding experimental and DEM results to confirm that the two distributions (experiment vs. model) are from the same continuous distribution. A high probability (p = 96.5%) of observing the given statistic is obtained, which again confirms that there is a good agreement between experiment and model. The main observation from this graph is that there is no significant effect of the initial charge amount on where most of the particles get deposited after leaving the chute; however, there is some effect on the peak height or the maximum mass fraction of particles.

4.4.1.3 Case 2: Effect of Particle Size Two different sized particles, 7 mm and 14 mm, are considered separately. Figure 31 shows the comparison between modeling results and the experimental data. We can observe that the similarity between these two is significant (two-sample K-S test gives a very high p value of 96.5% for both particle sizes), yet there is
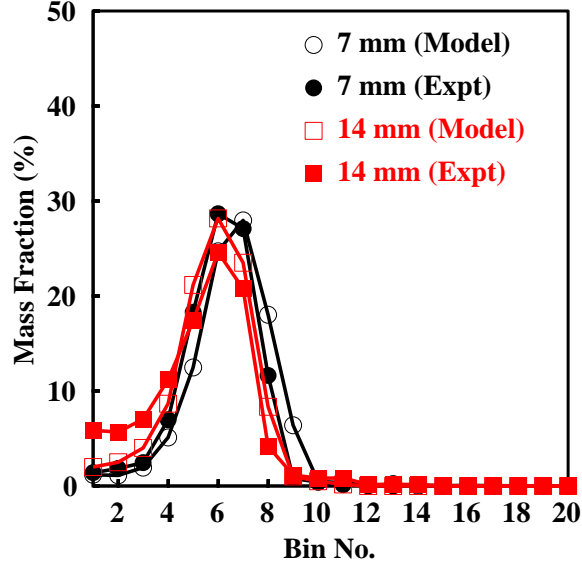
Figure 31: Effect of particle size: comparison with experimental data.

a slight mismatch at the wall side (bins 1–3) for 14 mm particles. However, the overall trend is comparable. If we closely observe the distributions, we can notice that despite doubling the particle size, the effect on the final distribution is not very significant. Also, the location of the densest region in the trajectory is nearly insensitive to the size of particles.

4.4.1.4 Case 3: Effect of Falling Height In this case, the falling height of particles is varied at three different levels (see Table 5). Figure 32 shows three snapshots of the particle trajectory corresponding to three different falling heights. Figure 33 offers the comparison between experiment and simulation of the mass fraction distribution for each of the falling heights. We can observe that, as expected, the densest region of the trajectory (highest mass fraction or peak of the distribution) shifts towards the wall side as the falling height is increased and the densest region also gets thinner (peak height decreases). The simulation accurately captures the right bin number for the maximum deposition for level 1 and level 2. There is some mismatch when the falling height is increased to level 3. The maximum % of mass fraction, for the case of level 1 in experiment is 30.84% (24.66% for level 2 and 17.67%
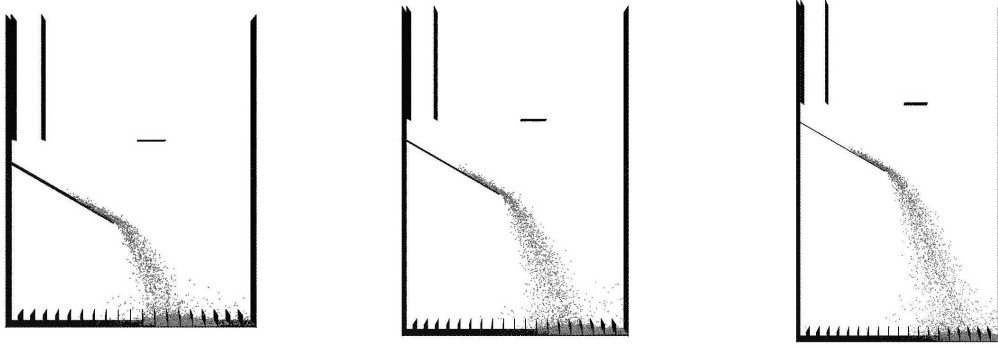
Figure 32: Snapshots showing trajectories for three different falling heights.

for level 3) and the corresponding simulation value is 30.1% (23.92% for level 2, and 19.78% for level 3). The two-sample K-S test gives a (p, k) value of (0.99, 0.10), (0.77, 0.20) and (0.77, 0.22) for level 1, 2 and 3, respectively, when compared with experiments. Therefore, we can conclude that the simulation captures the essential features (peak position, peak height and distribution shape) of the chute flow reasonably well.

4.4.1.5 Case 4: Effect of Chute Angle For this case, the chute angle is varied at two different levels: 45 degrees and 60 degrees, and all other parameters are kept constant. There is a high degree of agreement between model and experiment as is evident from the visual observation. We also perform the two-sample K-S test and obtain a (p, k) value of (0.97, 0.15) and (0.99, 0.10) for 45 degrees and 60 degrees chute angles, respectively. As expected from Figure 34, higher chute angle produces a wider trajectory with the peak (densest region) shifted towards the wall.

4.4.2 Polydisperse Flow

In this section, we discuss the experimental and simulation results for chute flow for a mixture of particles with different sizes. First, two cases are analyzed: the effect of falling height and of chute angle. Then, by varying the length of the chute, we show that employing the
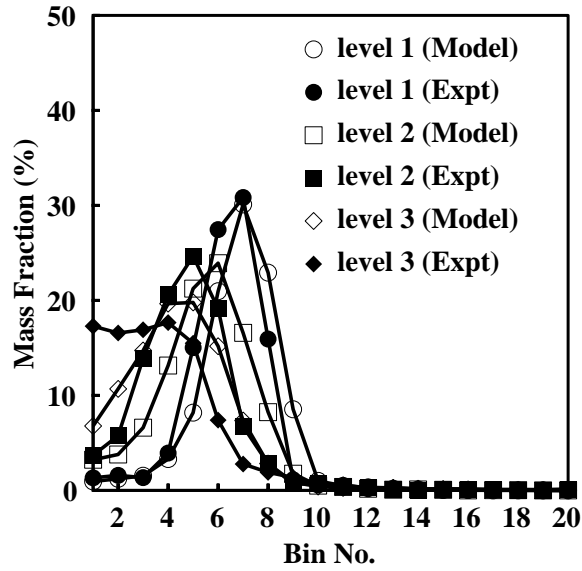
Figure 33: Comparison of simulation and experimental results for observing the effect of falling height: level 1 is 800 mm below chute hinge, level 2 is 1050 mm below chute hinge and level 3 is 1300 mm below chute hinge.
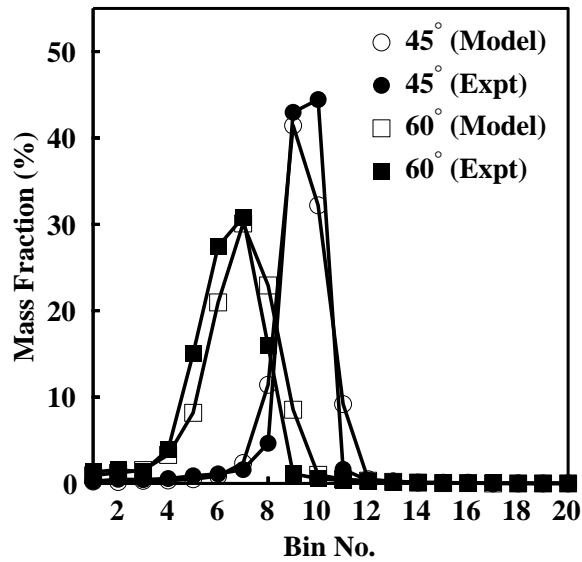
Figure 34: Effect of chute angle: the chute is fixed at two different angles, 45° and 60°, by keeping other parameters unchanged.

Table 6: Different cases for polydisperse simulation and operating parameters

Case	Operating parameters
Case 1: Effect of falling height	**Bin location:** level 2 and 3
	Diameter of particles: 6 mm, 7 mm and 14 mm
	Mass of particles: 6 mm : 0.5 kg (N=4641),
	7 mm: 0.3 kg (N=1455), 14 mm: 0.2 kg (N=119)
	Chute angle: 45°
Case 2: Effect of chute angle	**Chute angle:** 45° and 60°
	Diameter of particles: same as Case 1
	Mass of particles: same as Case 1
	Bin location: level 2

hypothesis of time modulation (as discussed in Section 4.2), we can obtain a critical chute length for segregation for the system considered in this study.

Following the discussion in Section 2.1, we can see that in our case, the size ratios of the particles are more than the spontaneous percolation threshold. Therefore, the spontaneous percolation is not expected to drive the segregation, and the shear-induced percolation should work as the main segregation mechanism.

The various cases of simulations and the operating parameters are listed in Table 6, which correspond to the same conditions as used in the experiments. The same tuned model from the mono-dispersed case is used for all the simulations. To match the experimental conditions, the particles are randomly placed in the hopper in the simulation because random mixtures are also used in the hopper during all the experiments. To ascertain that the initial randomness does not affect the final distribution, some sensitivity tests are done before actual simulations are performed. To do this, the initial arrangement of particles is generated using various random number generators (e.g., gsl_rng() from GNU Scientific
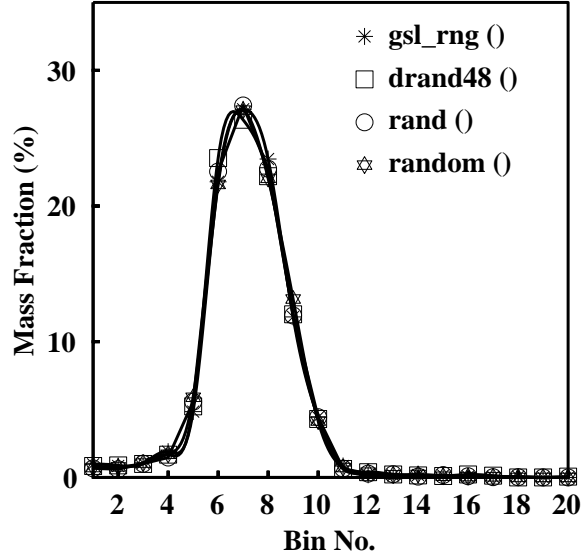
Figure 35: Effect of initial randomness of a mixture of 6 mm, 7 mm and 14 mm particles on final mass fraction distribution: Initial particle arrangements are randomly generated using different random number generators. Only the distribution for 6 mm particle size is shown here.

Library [255], drand48(), rand() and random() from standard C library). In each run, 6215 particles were generated using uniform random number generators. Figure 35 shows a mass fraction distribution plot where we can clearly establish that the final distribution is not sensitive to the random number generator used (i.e., on the initial randomness).

4.4.2.1 Case 1: Effect of Falling Height Figures 36 [(a): experiment, (b): simulation] show the mass fraction distribution of different-sized particles after they are mixed randomly in the hopper and allowed to flow over the chute. The chute angle is fixed at 45 degrees and the elevation of the bins is varied at level 2 and level 3, respectively. This controlled experiment singles out the effect of the falling height on mass fraction distribution and particle size distribution in a multi-sized mixture. Though the individual distributions corresponding to model and experiment do not agree quite well, they indicate similar trend

86

– the peaks shift to the wall side (towards lower bin numbers) as the falling height increases, for both experiment and simulation. It is evident that as the falling height increases, the larger particles tend to deposit towards the wall owing to their higher inertia.

4.4.2.2 Case 2: Effect of Chute Angle Figures 37 [(a): experiment, (b): simulation] show the mass fraction distribution of multi-sized particles for two chute angles. The chute angles are varied at 45 and 60 degrees, respectively, and the bins are kept at a fixed elevation of level 2 in both the cases. This controlled experiment singles out the effect of the chute angle on mass fraction distribution and particle size distribution in a multi-sized mixture. In spit of the fact that the individual distributions corresponding to model and experiment do not agree quite well, we can observe that like the mono-dispersed case, the peaks shift to the wall side (lower bin numbers) as the angle increases, and the corresponding height of the peaks also get lowered, for both experiment and simulation. It is evident that as the chute angle increases, the particles tend to deposit towards the wall owing to higher acceleration (as θ increases, $g \sin \theta$ also goes up).

4.4.2.3 Critical Chute Length for Segregation Following the discussion on the application of the hypothesis of time modulation in a chute flow in Section 4.2, now we attempt to quantify the critical chute length for the system under consideration. Figures 38 (a) and (b) show how the velocity profile of particles on a stable region of chute is calculated. This information is needed to obtain the shear rate ($\dot{\gamma}$) in the system. Starting with a base case as shown in Figure 38 (a), we systematically vary the chute length from 300 mm to 7000 mm by keeping other parameters (such as falling height, chute angle, etc.) unchanged. Then we monitor the mass fraction distribution for each of the simulation cases. A narrow distribution for all the particle sizes would mean that all the particles with different sizes have been deposited within a small region spanning only a few bins, and we consider this to be a case similar to mixing of particles (think of a mixture of particles in a container or bin).

A wider distribution for one particle size, on the other hand, would mean that there is considerable spread of that type of particles and the deposition would span across multiple bins. We consider this to be akin to segregation as all types of particles are no longer
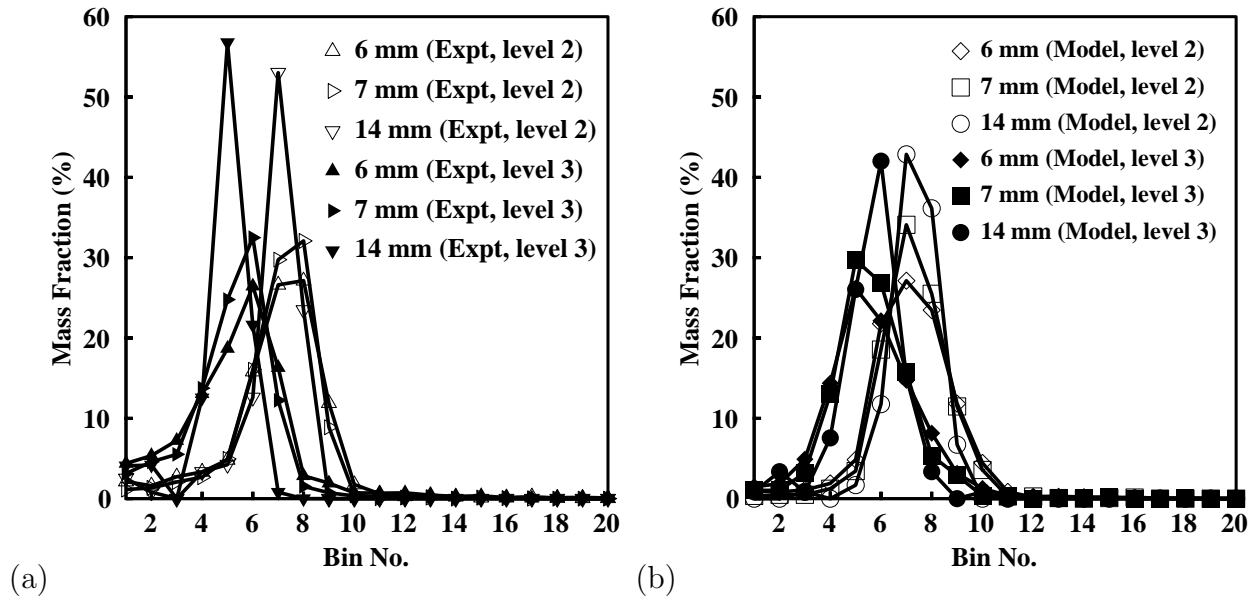
Figure 36: Effect of falling height on mass fraction distribution of a mixture of polydisperse particles: (a) shows experimental results and (b) corresponds to simulation.
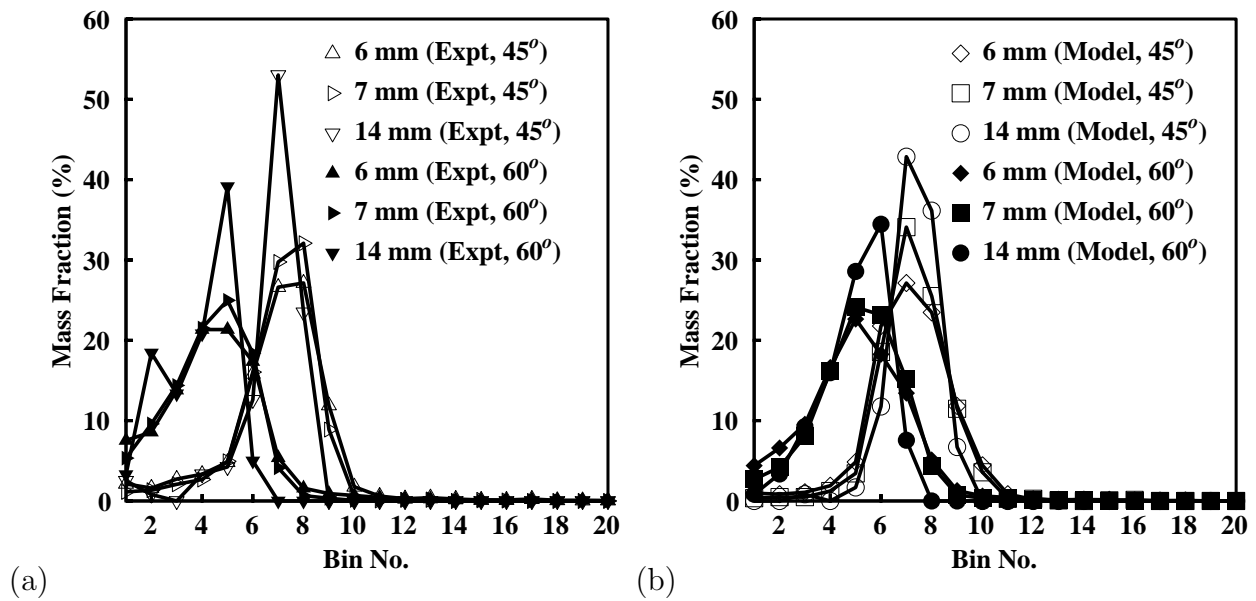
Figure 37: Effect of chute angle on mass fraction distribution of a mixture of polydisperse particles: (a) shows experimental results and (b) corresponds to simulation.

(a)   (b)
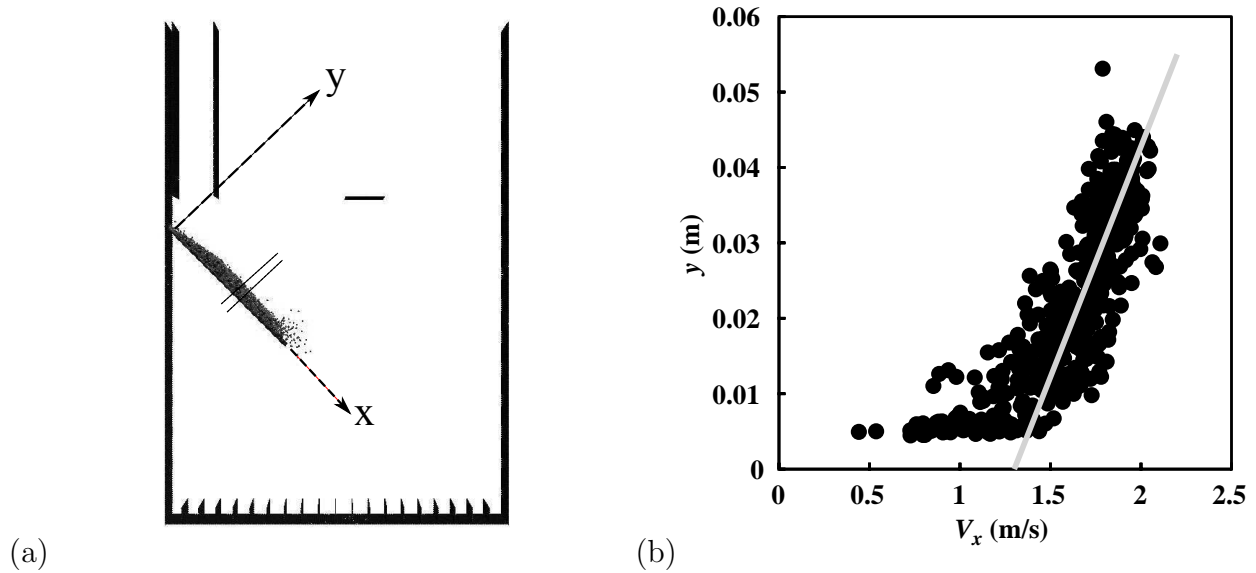
Figure 38: (a) A typical flowing layer on a 600 mm chute with 45 degrees inclination. The bins are placed at level 2 (1050 mm below chute hinge). The bed of particles consists of 6, 7 and 14 mm particles in a weight ratio of 5:3:2, respectively. (b) Velocity profile of particles is calculated on a small slice of width 28 mm centered at half chute length corresponding to the scenario shown in (a). Situation (a) is chosen because of a fully developed layer with uniform thickness around the middle of the chute.

deposited in one small region. Essentially, a narrow distribution for one particle size and a wider distribution for another particle size is a typical signature for segregation. Therefore, segregation will occur if various particle sizes have differing degrees of spread in the mass fraction distribution. This is evident from Figure 39 where we can observe that as the chute length increases, the distribution becomes wider (i.e., peak height reduces as the sum of the distributions is 100%) for smaller particles whereas larger particles continue to have a sharper peak. In this figure, to have a comparison on a uniform distance scale for all particle sizes and chute lengths, all the peak positions corresponding to 14 mm particle distribution have been rescaled so that it is denoted as bin number 0 (an arbitrary choice). The negative bin numbers correspond to the bins to the left of the 14 mm peak position (towards wall side) and the positive bin numbers correspond to the bins to the right (i.e., towards chute side). The important observation from these plots is that 6 mm and 7 mm particle sizes have a wider mass fraction distribution as compared to 14 mm particles for higher chute length. If we observe closely, we can notice that the 14 mm particle is always distributed only over a narrow distance (about 4 bins or 240 mm) for all chute lengths, whereas the 6 mm (or 7 mm) particles are distributed over a wider distance (from about 8 bins or 480 mm for chute length 300 mm to about 25 bins or 1.5 m for chute length 7 m). This signifies that as the chute length increases, there is more and more separation occurring between particles with different sizes. Therefore, from this distribution plot, we can get some idea about how segregation can be controlled by varying the chute length.

Now, turning our focus back to the theoretical prediction of the critical chute length to initiate segregation, we tabulate the pertinent parameters of Equation 4.9 for our case in Table 7. $\dot{\gamma}$ has been calculated from the slope of the linear portion of the velocity profile in Figure 38 (b). The equation gives a value of 4.0 m as the critical chute length for the present system under consideration. Now, if we plot the peak height (i.e., maximum mass fraction) for all the distributions (for all particle sizes) as a function of chute lengths, we obtain a plot as shown in Figure 40(a). It is evident from this plot that as the chute length increases initially, the peak height decreases rapidly and that after about $L = 5.4$ m of chute length, the peak height becomes nearly flat and does not change significantly. The peak height is a measure of the spread of the distribution: Lower peak height means wider spread, and a
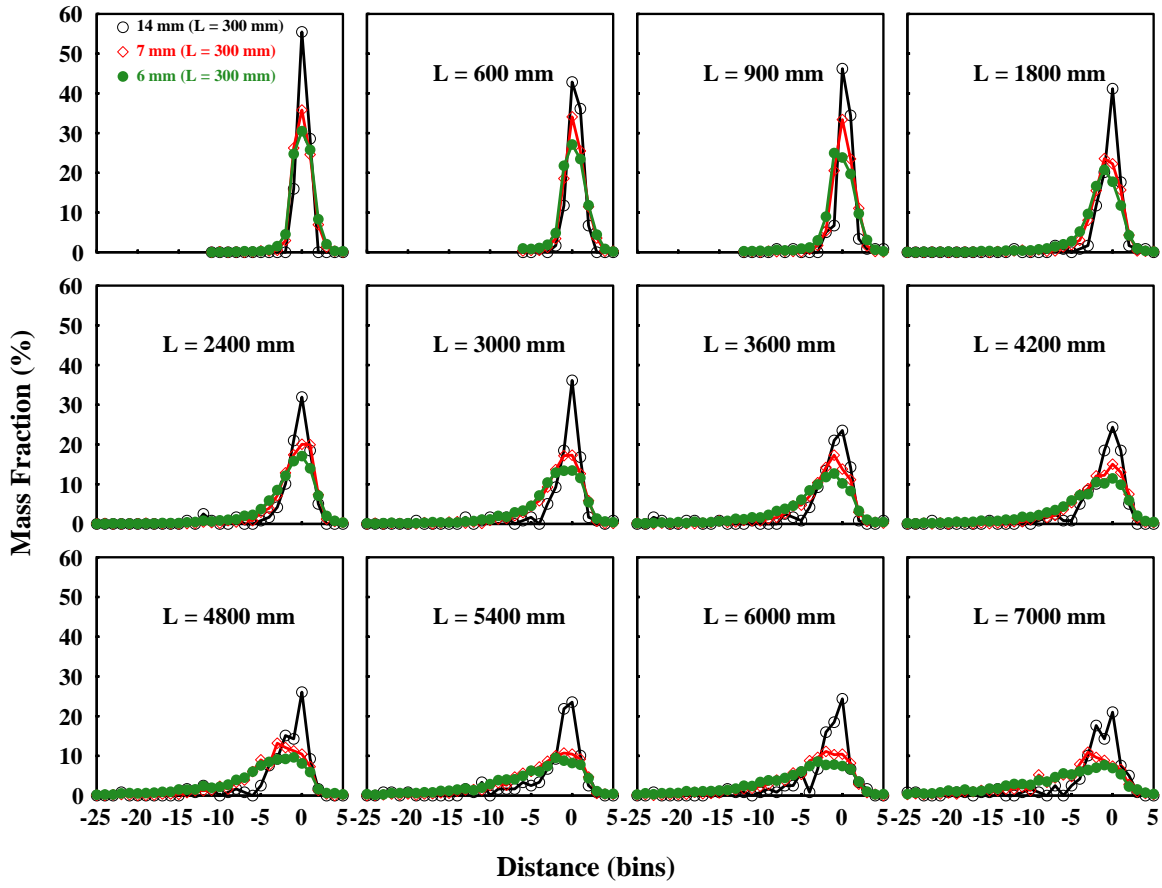
Figure 39: Mass fraction distribution of 14, 7 and 6 mm particles in a polydisperse chute flow for different chute lengths. To obtain a clear comparison, 14 mm particle peak positions for all chute lengths have been arbitrarily set to bin number 0. Other conditions are similar to Figure 38 (a).

Table 7: Parameters to calculate critical chute length from Equation 4.9

Parameter	Value
β	2.0
c	0.7467
α	2.1
$\bar{d}$	0.4286
U_{avg}	1.275 m/s
$\dot{\gamma}$	22.0 s^{-1}

wider spread signifies segregation. Also, in Figure 40(b), we plot the degree of mixing (a new mixing measure specific to chute flows), R (Equation 4.10), as a function of chute length. The degree of mixing R is defined as

$$R = W_{14}/(W_6 + W_{14}) \tag{4.10}$$

where W_i is the full width at half maximum (FWHM) of the mass fraction distribution for a particular particle size i (we consider 14 mm and 6 mm, the largest and smallest particle sizes, respectively). A value of $R = 0.5$ (i.e., $W_{14} = W_6$) indicates that the two sizes are completely mixed and $R \leq 0.25$ (when the spread of small particles is three times the spread of larger particles) signifies segregation. This plot also confirms the fact that segregation is initiated at about $L = 5.4$ m of chute length. Therefore, our theoretical prediction and the prediction from the computer model are of the same order of magnitude (4.0 m vs. 5.4 m) and this suggests that our theory of forcing frequency is capable of qualitatively explaining segregation phenomena, in this case, in a chute flow.
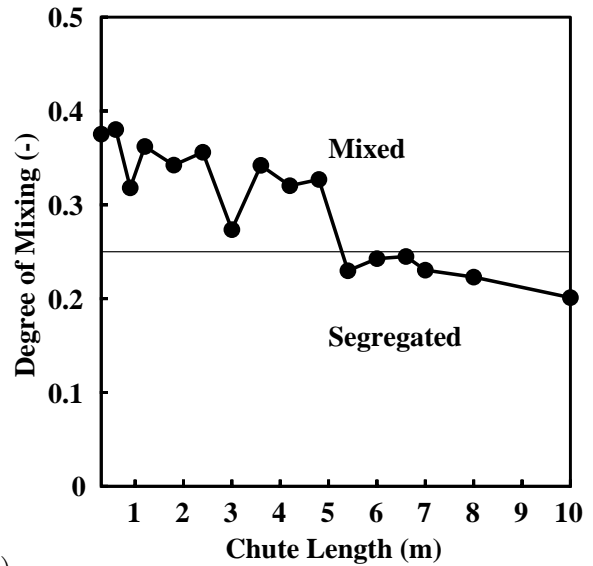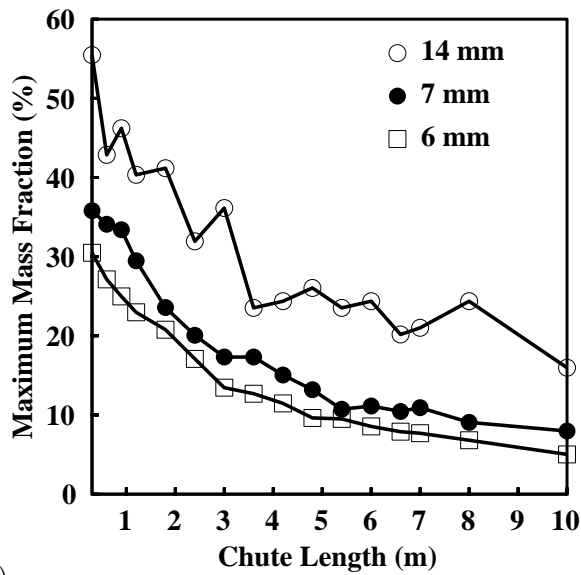
Figure 40: (a) Maximum mass fractions (peak heights) have been plotted as a function of chute length for a polydisperse chute flow simulation. Lower peak height corresponds to a wider distribution and hence signifies considerable segregation. (b) Degree of mixing R has been plotted as a function of chute length.

4.4.2.4 Critical Chute Length for Segregation: Finite vs. Periodic Chute The theory of time modulation applies to a fully developed shear flow. As we have seen in the earlier section, this assumption may not remain valid if longer chutes are used with a limited number of particles. A finite chute flow is essentially a batch flow where thinning of particle layers is possible if a longer chute is used and this may cause the particles to segregate in the flowing direction and not along the normal-to-flow direction. With this issue in mind, we test the limits of a finite chute flow in verifying our hypothesis, and in addition to that, we also employ a periodic chute flow setup to cross-examine if a batch flow is still the right situation to test the hypothesis.

Figure 41 shows how the average centroid positions (along the flow direction) of bigger (14 mm) and smaller (6 mm) particles change as a function of time for chutes with different lengths. The y axis corresponds to a quantity called $\bar{X}_c$, which is defined as $\bar{X}_c = \frac{(X_{c,big}-X_{c,small})}{0.5L_{plug}}$, where X_c is the centroid of the particle mass (for big or small) and L_{plug} is the length of the particle plug on the chute at the time in question. This quantity clearly measures the amount by which the two types of particles are separated on the chute along the flow direction. The x axis corresponds to the dimensionless time $\bar{t}$ as defined by $\bar{t} = \frac{t-t_{entry}}{t_{exit}-t_{entry}}$, where t_{entry} and t_{exit} correspond to the particle entry and exit time to/from the chute respectively. A value of $\bar{X}_c = 1.0$ signifies a complete separation of the bigger and smaller particles on the chute along the flow direction. As is evident from this figure, there is some degree of horizontal separation on chute for lengths above 4.8 m (the $\bar{X}_c$ for other intermediate chute lengths shorter than 4.8 m never exceeds 0.5). Therefore, the assumptions of shear flow (only vertical segregation) on these longer chutes is not completely valid. Therefore, we felt a need to further test our hypothesis using a periodic chute flow setup.

In the periodic chute flow setup, all the conditions are similar (particle numbers, etc.) to the finite chute length case except that the periodic chute is enclosed in a simulation box with length 600 mm and the chute angle is set at 20°. The choice for the above angle is due to the fact that a chute angle of 45° (as used in the experiments) does not produce a steady flow as the particles continue to accelerate indefinitely. Therefore, 20° is chosen as the chute angle for verifying our hypothesis for the periodic chute case.
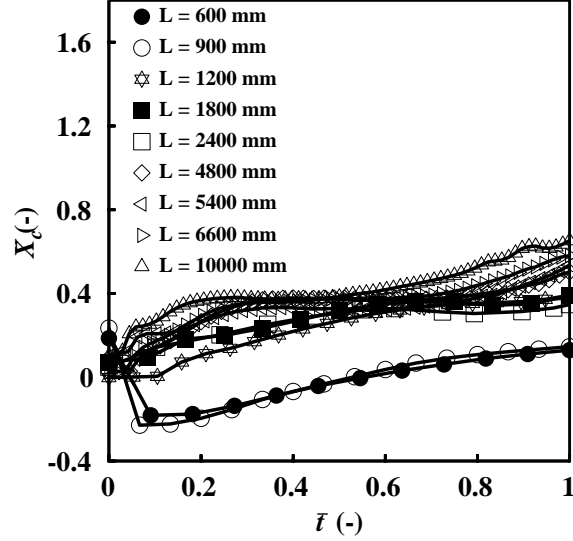
Figure 41: Normalized difference of the average centroid position of bigger and smaller particles on chute as a function of normalized time. Data for different chute lengths have been plotted together.

In order to calculate the characteristic segregation time t_S, the shear rate $\dot{\gamma}$ is calculated from the velocity profile at different times during the flow and an average value is obtained from different time samples. Figure 42 shows how the shear rate fluctuates over time and these data are used to find an average shear rate ($\bar{\dot{\gamma}}$). Table 8 tabulates all the pertinent data for calculation of t_S (refer Equation 4.9). Note that the fitting parameters α and β are kept the same as in the finite-length chute case and this yields a characteristic segregation time of about 7.2 s. Now, we investigate if we can arrive at this characteristic segregation time – as obtained from the theory – from direct observation of the concentration profile. To accomplish this, first we plot the concentration profiles of all types of particles at different time instances in the periodic chute flow. The bed of particles is sliced into many bins in the normal-to-flow direction, and the volumes of all types of particles in a particular bin is used to calculate the concentration of each kind of particle in that bin. It is obvious from Figure 43 that somewhere between 4–10 s, the bigger particles (14 mm) start to separate. The concentration of 14 mm particle becomes zero for about half of the bed height starting

95
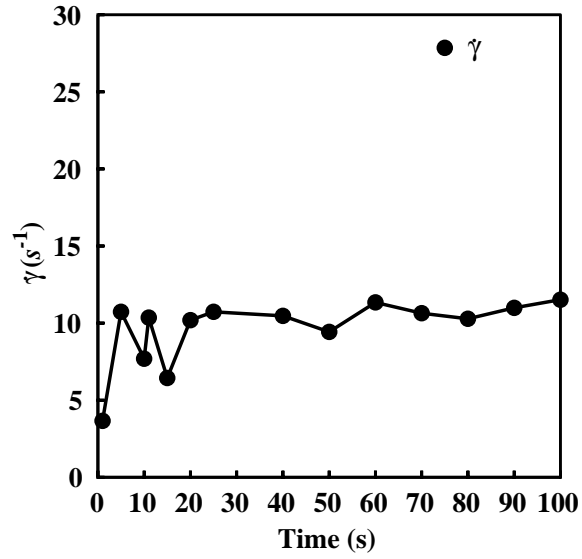
Figure 42: The shear rate fluctuation over time in a periodic chute flow.

Table 8: Parameters to calculate critical segregation time for a periodic chute flow from Equation 4.9

Parameter	Value
β	2.0
c	0.7467
α	2.1
$\bar{d}$	0.4286
$\dot{\gamma}$	9.61 s^{-1}

from time 4 s. To further narrow down the initiation time for segregation, we plot three different indices for segregation as function of time: the so-called Intensity of Segregation (IS) (Figure 44), the Relative Standard Deviation (RSD) (Figure 45) and also (1-M_L) (Figure 46), where M_L is the Lacey index. One can refer to Section 2.3 for the description of these indices. These indices are calculated considering 14 mm particles as the tracer particles. Clearly, all these indices suggest that after about 6.0 s (the vertical line in these graphs corresponds to 6.0 s), there is a clear segregation taking place in the periodic chute flow. Therefore, we can conclude that the direct observation in a periodic chute flow gives a characteristic segregation time which is of the same order of magnitude as the prediction from the theory (6.0 s vs. 7.2 s).
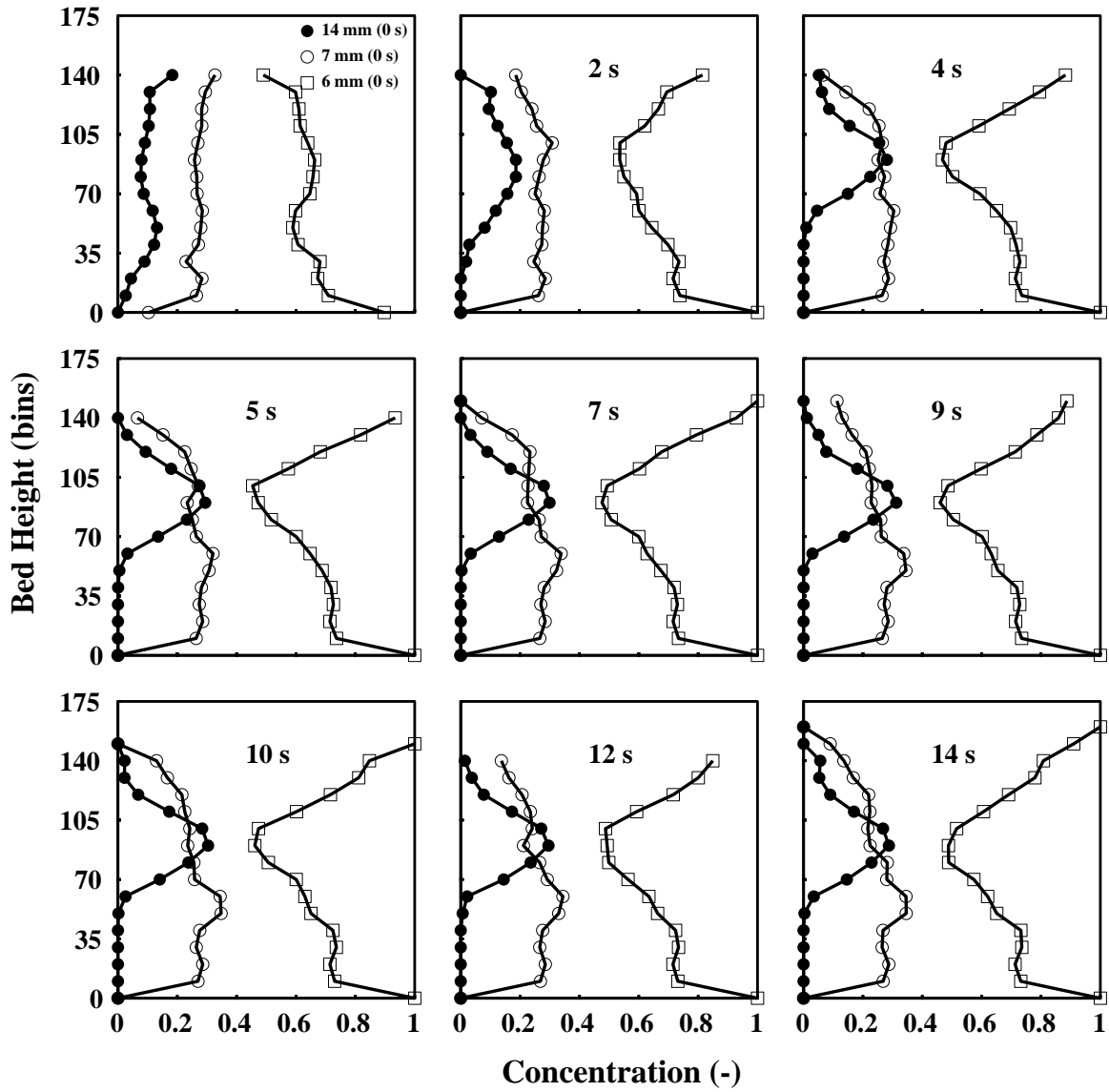
Figure 43: Evolution of concentration profiles in a periodic chute flow.
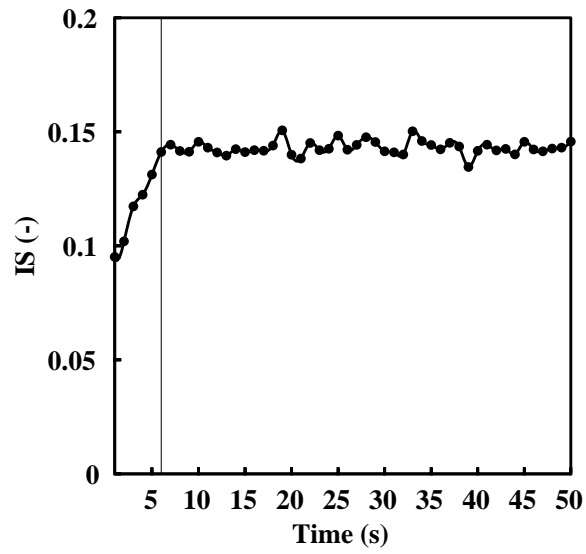
Figure 44: Evolution of Intensity of Segregation (IS) in a periodic chute flow. The vertical line demarcates the 6.0 s time after which the IS becomes flat.
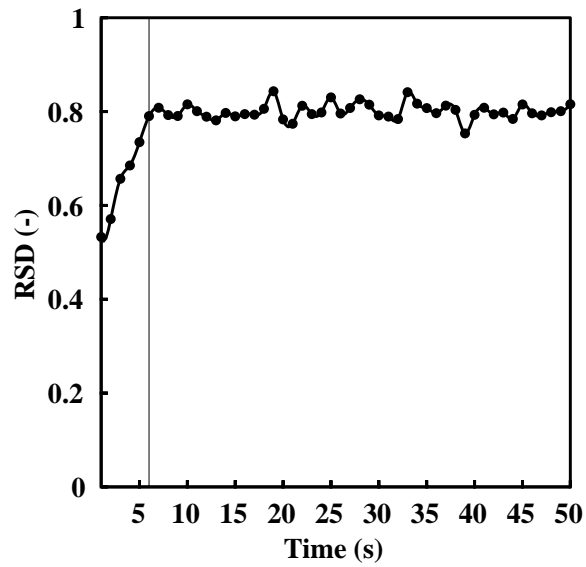
Figure 45: Evolution of the relative standard deviation (RSD) of concentration in a periodic chute flow.
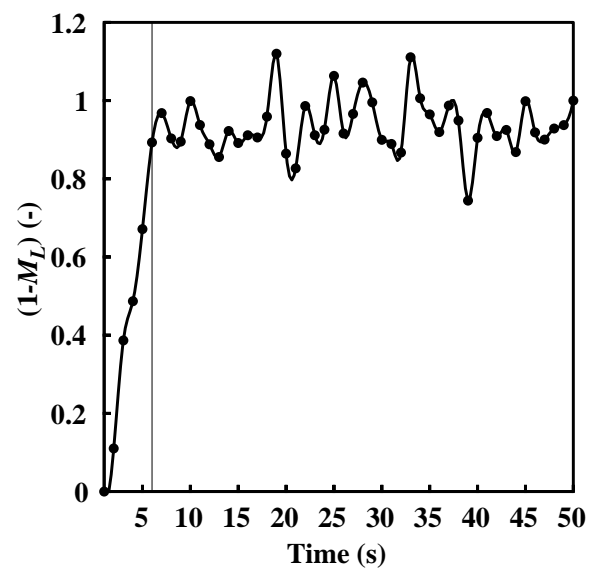
Figure 46: Evolution of the derived Lacey index (1-M_L) in a periodic chute flow.

5.0 RATE-BASED SEPARATION IN COLLISIONAL FLOWS

Separation of particles is extremely important in a number of solids processing industries. Rate-based separation processes hold promise as both more environmentally benign as well as less energy intensive when compared to conventional particle separations technologies such as vibrating screens or flotation methods. This approach is based on differences in the kinetic properties of the components of a mixture, such as the velocity of migration or diffusivity. In this Chapter, two examples of novel rate-based separation devices are demonstrated. The first rate-based separation example involves the study of the dynamics of gravity-driven particles through an array of obstacles. Both discrete element (DEM) simulations and experiments are used to augment the understanding of this device. Dissipative collisions (both between the particles themselves and with the obstacles) give rise to a diffusive motion of particles perpendicular to the flow direction and the differences in diffusion lengths are exploited to separate the particles. The extent of separation (i.e., how far one type of particle is removed from another) depends on the different distances traversed by the two types of particles and hence is directly proportional to the time of migration in the gravity field (i.e., time-dependent). The second example employs DEM to analyze a ratchet mechanism where a directed current of particles can be produced perpendicular to the direction of energy input. In this setup, a vibrating saw-toothed base is employed to induce different mobility for different types of particles. The effect of different operating conditions and design parameters on the separation efficiency are discussed.

5.1 SEPARATION OF GRANULAR MIXTURE BY AN ARRAY OF OBSTACLES
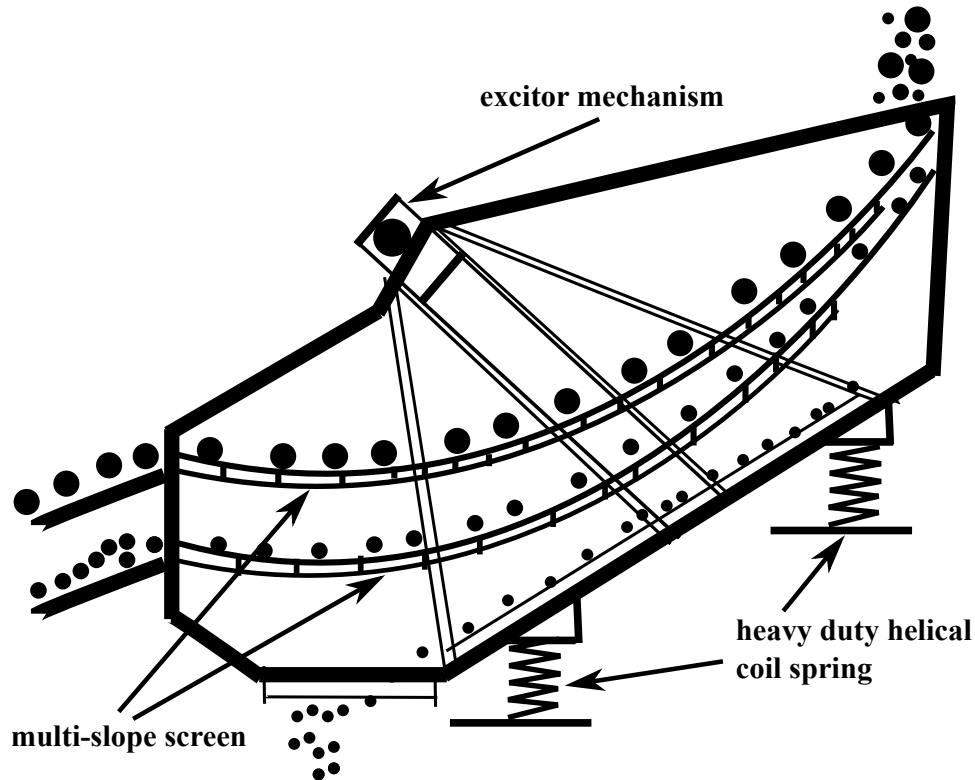
Figure 47: Schematic of a banana screen.

Particle separation is a routine task across many industries (chemical, pharmaceutical, food, metallurgical, etc.). Conventional separation devices (such as vibrating screens, see Figures 47 and 48) are energy intensive: energy is spent for separation as well as de-clogging of the screen. We should note that it has been mathematically proven that clogging is inevitable when the screen opening size is less than three particle diameters [256]. Moreover, industrial vibrating screens can weigh thousands of tons when loaded with materials and hence shaking the screen requires heavy energy input. Novel rate-based separation devices that require no or small energy input are environmentally benign (green) and clogging is not an issue in those devices. Obstacles arranged in a periodic lattice had been used in
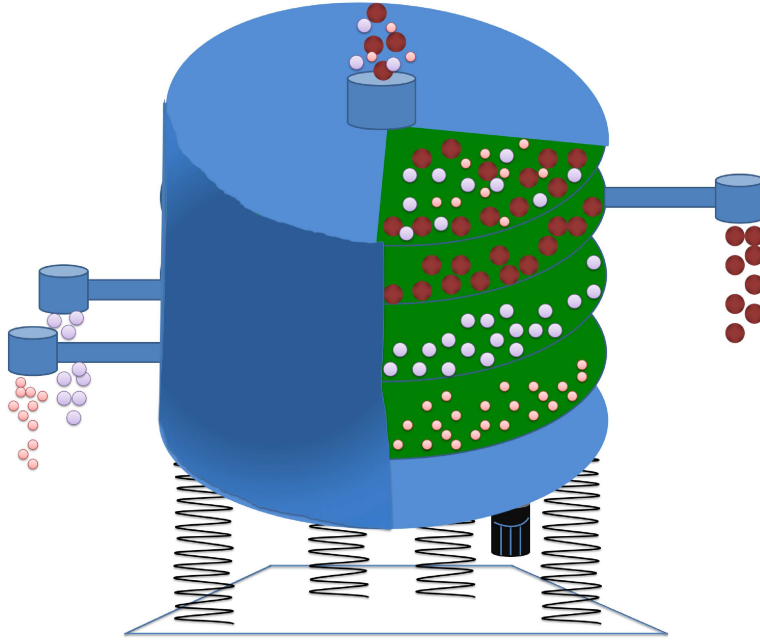
Figure 48: Schematic of a vibrating screen.

the past [257–260] to study transport and diffusion in many processes, especially to study microfluidic particle-separation devices (e.g., to separate macromolecules). The main idea behind these devices is to exploit the differences in diffusion lengths of different particles (macromolecules) to perform separation. In some previous studies [258, 261, 262], a special mechanism called a "geometric ratchet" was described as a way to separate constituents of a mixture (mainly macromolecules like DNA or other charged biomolecules in an electric field). A geometric ratchet mechanism does not require any external vibration or time-dependent forcing but consists, instead, of a 2D periodic array of asymmetric obstacles (see Figure 49). Because of the asymmetry of the obstacles, the particles average drift velocity acquires a component perpendicular to the direction of the external force (here, gravity), which constitutes the ratchet effect. A mixture of particles when poured in this kind of setup will separate out due to the drift-diffusive motion. Inspired by this principle, a device has been conceived where macroscopic particles are made to flow over an inclined chute fitted with an array of obstacles ('pegs') (refer to Figure 50).
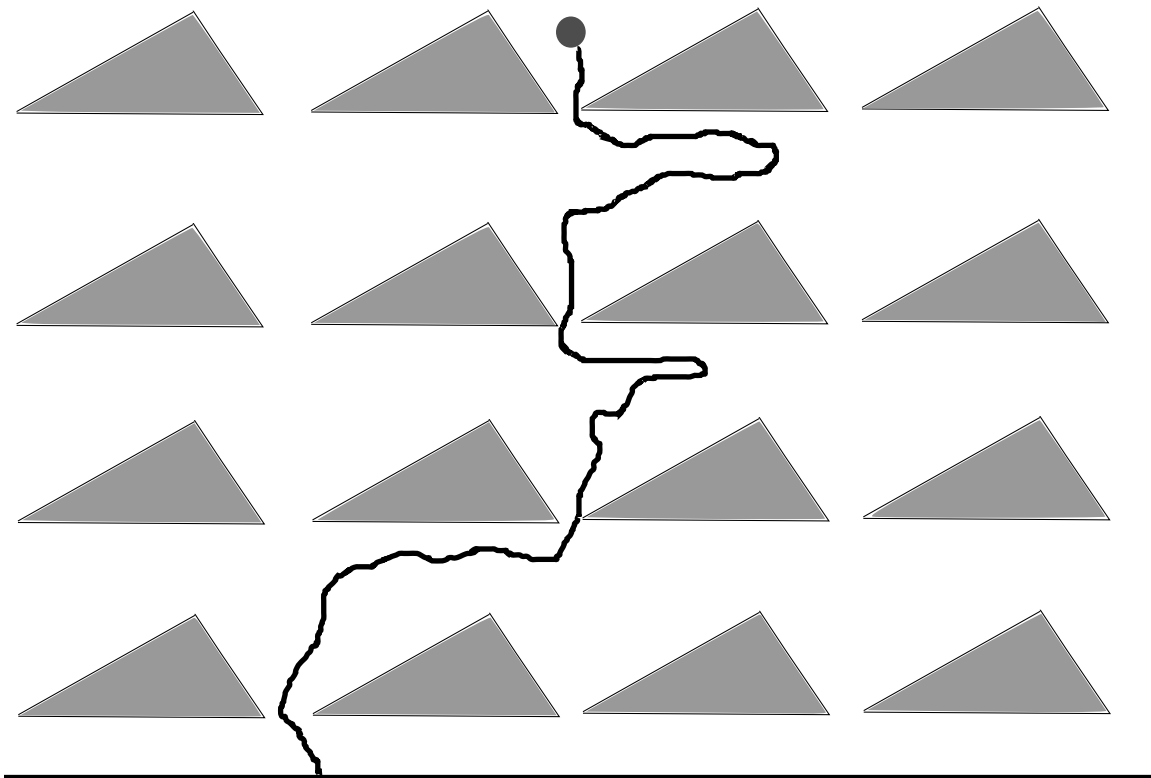
Figure 49: Schematic of a static separator or geometric ratchet showing the drift-diffusive motion of a particle.
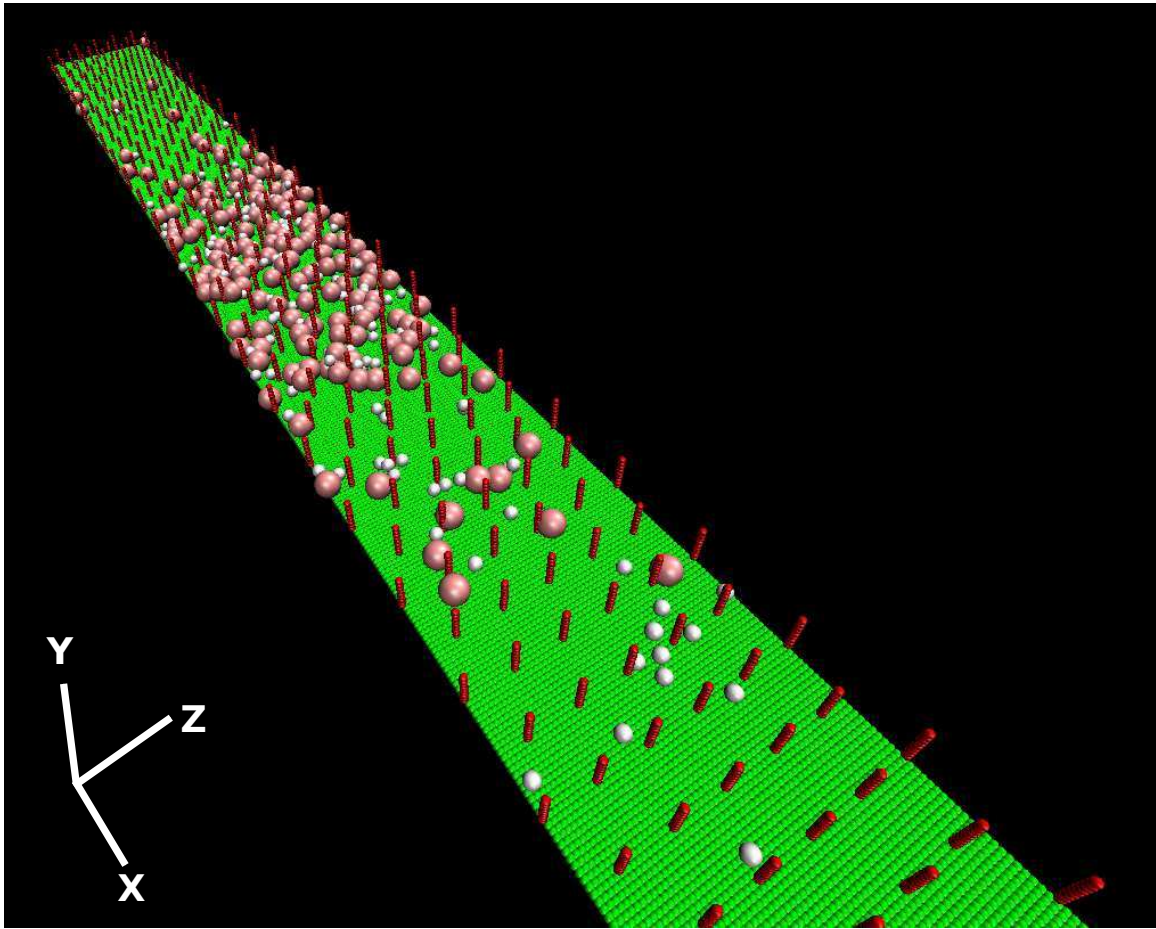
Figure 50: Schematic of the particle separation device via dissipative collisions.

The device as shown in Figure 50 is called a "static separator" as there is no external energy input to the system. The dynamics of gravity-driven particles through the array of obstacles are studied here to investigate its application as a separation device. Dissipative collisions (both between the particles themselves and with the obstacles) give rise to random trajectories of the particles and hence a drift-diffusive motion of particles is developed in this device. When a net force, for example gravity, acts on the system the particles will have a diffusive behavior superimposed on a convective regime – a scenario analogous to hydrodynamic chromatography [257].

Diffuse-dispersive motion of granular materials have been the subject of many studies. However, most of the studies dealt with the dynamics of a single particle and did not consider the collective behavior of an ensemble of particles which are very important in many applied situations. Single-particle dispersion has been studied in Galton-board devices [47, 263], in billiards [264], and also, in a rough inclined plane [134, 265]. The influence of interacting particles on diffusion processes is still an open problem [266, 267].

The purpose of this work is to study, for the first time, the dynamics of gravity driven particle flow through an array of obstacles and to characterize the system in order to determine its usability as a particle separator. This device is characterized by both a single-particle and a many-particle approach employing discrete element method (DEM) simulations and actual experiments. One interesting feature of this device is that the ensemble average behavior is deterministic and can be well characterized spatially and temporally. This is obviously beneficial from an industrial perspective as characterizing the diffusive behavior can lead to predictable separation states. The extent of separation (E_s) (i.e., how far one type of particle is removed from another in the longitudinal direction, based on the rate of a process) depends on the different distances traversed by the two types of particles and is proportional to time of migration (t).

This section is organized as follows: First the experimental and theoretical procedures are described. Subsequently, results for single particle and many-particle flows are presented, both for simulations and experiments.

106

5.1.1 Experimental Setup and Procedure

The device comprises an inclined chute fitted with obstacles in a triangular lattice. Figure 51 shows a top view of the setup with labels for different components. A perforated plastic (polypropylene) sheet (32 in. × 48 in.) with 1/8 in. thickness is used as the surface for the inclined chute. The holes (1/8 in. diameter) are staggered and the center-to-center spacing is 1/4 in. Cylindrical dowel pins made from stainless steel with 1/8 in. diameter are used as the pegs or obstacles. These pins are 3/4 in. long and can be inserted through the holes on the plastic sheet as per a desired peg-to-peg spacing (3/4 in. spacing was typical). There are 9 peg columns in the width direction and 45 peg rows along the length direction yielding an 1:5 aspect ratio. The pegs are also staggered – each peg is inserted exactly between two pegs of a previous row thus forming an equilateral triangle with 3/4 in. sides (see Figure 52 for a close-up view of the pegs). The plastic sheet is attached (bolted) to a rectangular structure made from five 1/16 in. thick L shaped channels ($2\frac{1}{4}$ in. legs). Four L channels with similar dimension as above are used as four legs of the setup, which can be varied in height in order to control the inclination angle of the device (a typical angle of 26 degrees was used in the experiments). These legs are fitted with friction shoes to hold them in place on the floor. The columns of pegs are enclosed by two side walls made from 1/32 in. thick aluminum L channels to contain the particle flow. These channels are slotted (1/8 in. wide) so that they can be pressed and held onto the plastic sheet using 4-40 screws, which would match the perforations on the sheet. In order to create a bumpy surface, the remaining holes on the plastic sheet are plugged using ≈ 3 mm (1/8 in.) transparent glass beads.

A mono-layer of nearly spherical particles with different material, color and size are used to observe the flow. A long rectangular plexi-glass plate can be placed (supported by the side walls) on the device as a cover to restrict some particles from jumping out of the device due to collisions at higher device inclination angles. The initial condition is obtained by placing a desired number of particles in a stencil placed centrally with respect to the width of the device, as shown in Figure 51. The stencil is fabricated from an aluminum plate and fifteen circular holes in a 5 × 3 rectangular array are cut to retain the particles. To collect the flowing materials as it exits the last row of pegs, a funnel or Y shaped receptacle (labeled
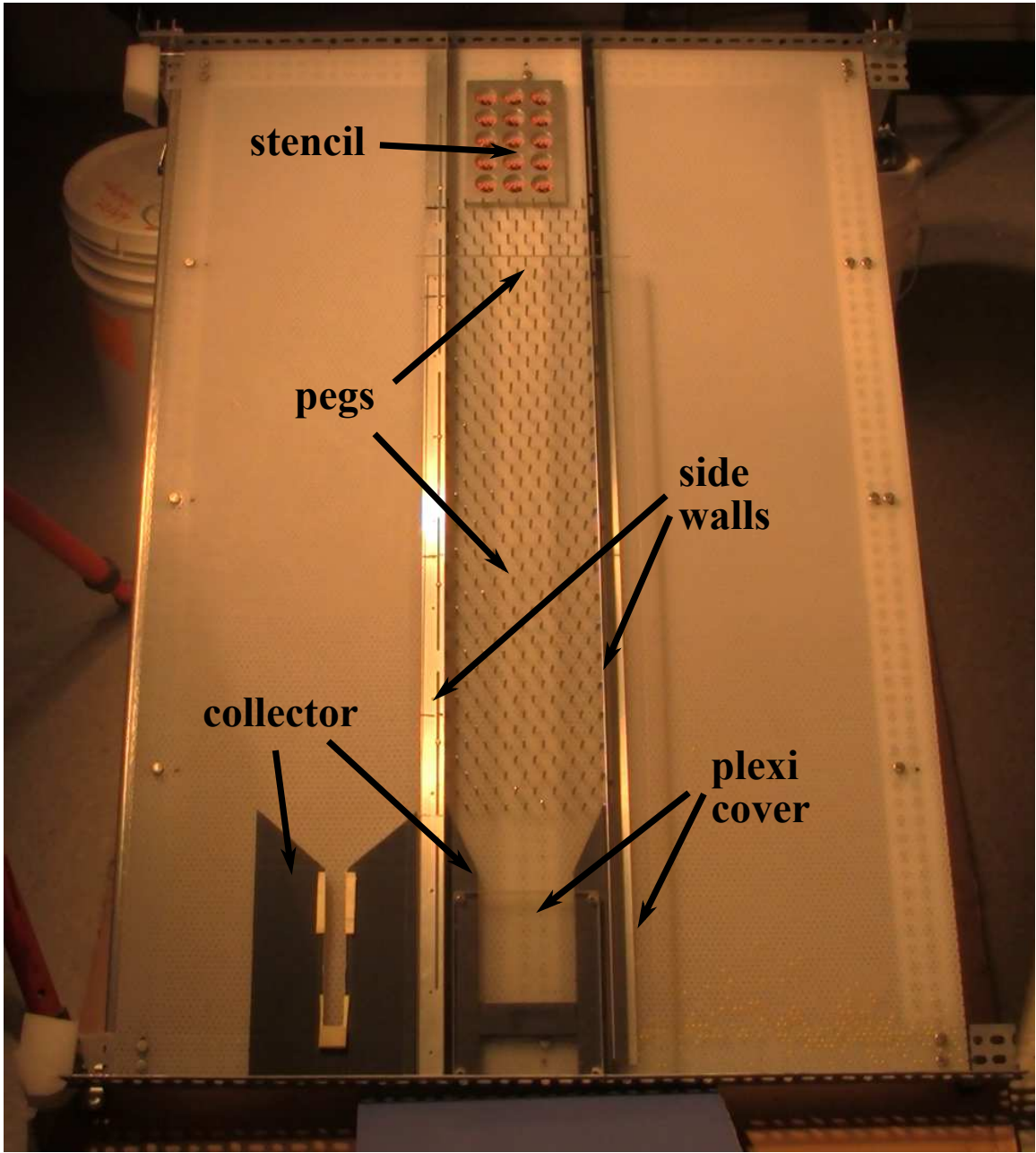
Figure 51: A device to separate particles via collisional flow.
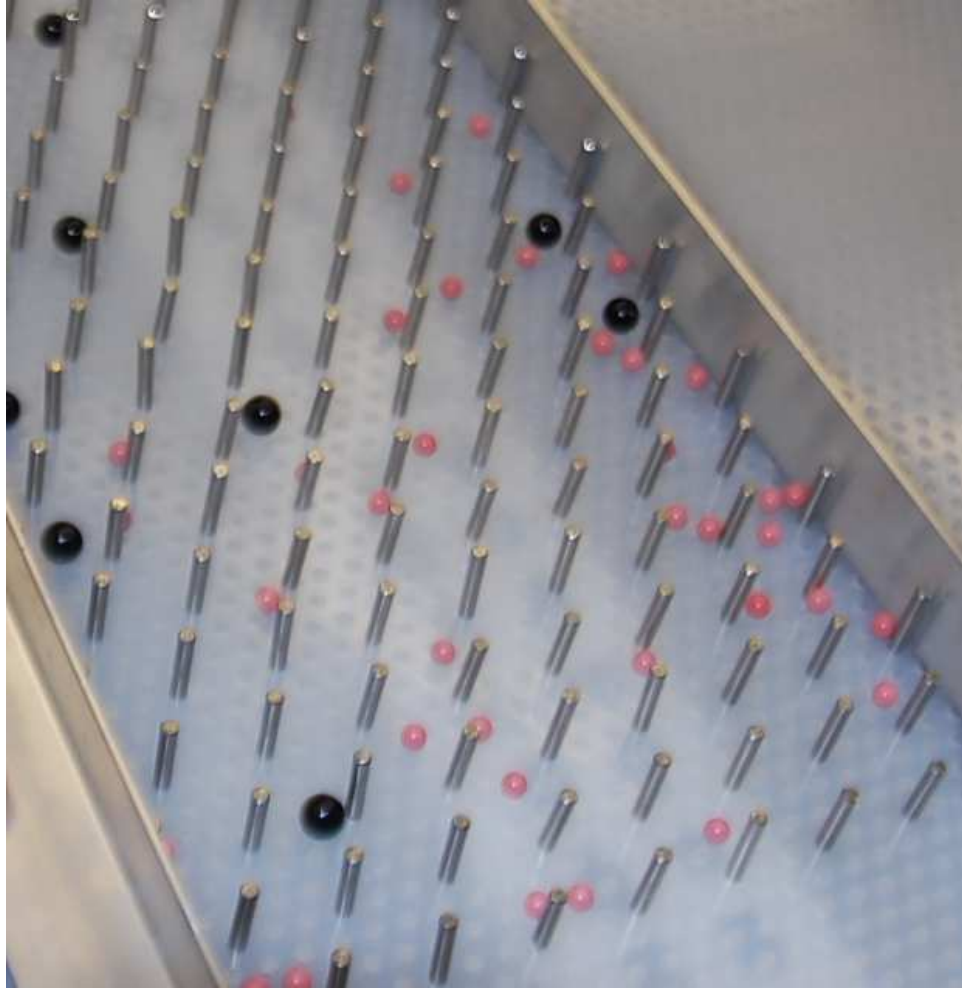
(a)
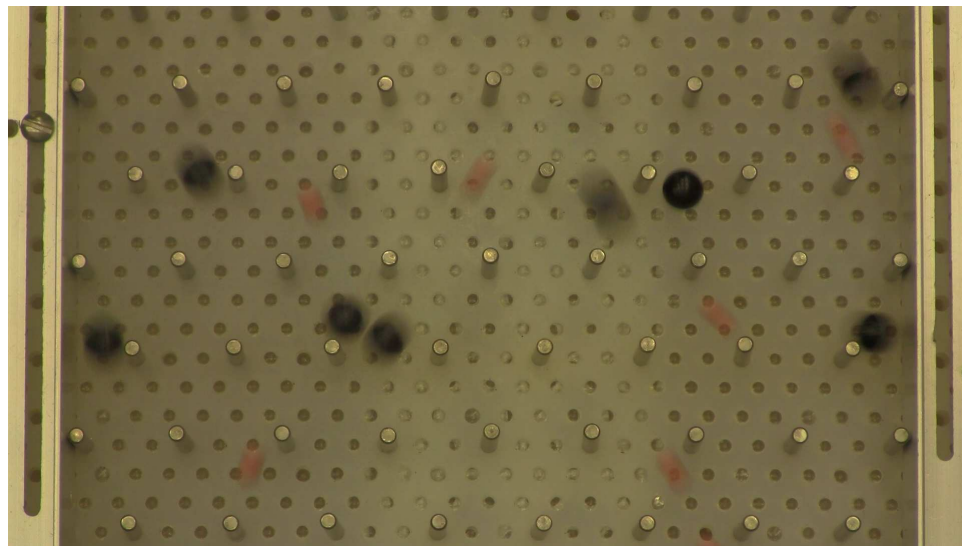
(b)

Figure 52: (a-b) A close-up view of the pegs or obstacles interacting with the particles during an experiment. The triangular lattice formed by the pegs can be seen clearly in (b).

"collector" in Figure 51) is placed at the end. The collector is placed to capture the particles as they arrive, which in turn, gives us a picture of the time dependent particle positions at exit, and hence, a measure of separation – the fastest particle (or the first to exit the device) deposits at the bottom of the collector and the slowest, or the last to arrive, deposits at the top. An ideal situation would be to have a very long, narrow and shallow compartment, which will allow only one particle of any size to enter at any time, thus forming a single line of particles where the particles will be arranged in the order they arrived. This will give us a quantitative measure of separation also. However, due to jamming issues at the entrance, the ideal situation could not be realized and instead two types of collectors (a narrow type and a wide type), which prevented considerable jamming are used. The narrow type collector has approximately 160 mm (L) × 20 mm (W) rectangular storage compartment whereas the wide type collector has about 130 mm × 90 mm storage compartment. The funnel angles (with horizontal) for narrow and wide collectors are approximately 45 degrees and 19 degrees, respectively. Sufficient care is taken to choose the depth of the compartment in such a way that it can only hold a single layer of particles (however, this is not always possible for some size ratios of particles). The distance between the last row of pegs to the bottom of the collector compartment is 200 mm (for wide-type collector) and 220 mm (for narrow-type collector). All of the above hardware for building the setup were purchased from McMaster-Carr and the particles were purchased from Engineering Laboratories (www.plasticballs.com). A typical diameter tolerance for the balls is ± 0.005 in. with a sphericity of 0.005 in.

Both a video (either Canon 3CCD Digital Video Camcorder/DV format or Canon Vixia HF 200 Camcorder/AVCHD format) and a still camera (Nikon D40) are used to record the collisional particle flow in this device. Care is taken to ensure that there is no perspective effect or parallax error (in other words, the field of view of the camera is perfectly parallel to the plastic sheet so that the tips of the pegs are only visible – as opposed to the sides of the pegs – and they appear as perfect circles in the video). The above is especially important for extracting collisional data from the video frames. The video camera produces interlaced video with approximately 30 (DV format) or 60 (AVCHD format) frames per second (fps). Open-source video processing program ffmpeg [268] is used to cut and de-interlace the videos,

and then extract individual frames for further processing. Each frame is first pre-processed by another open-source program ImageMagick [269], which digitizes the frames into a text file with pixel coordinates and their RGB information. This text file is then post-processed using an in-house C program to perform thresholding and other operations. The C program identifies particles and pegs using HSI (Hue Saturation Intensity) thresholding [270] and locates the center of mass of each particle. Collisional and kinematic data (such as time dependent displacement or exit time) can be collected from the centre of mass information of particles for a fixed amount of time for various operating conditions. Still images are also recorded of both the initial particle arrangement in the stencil and the final arrangement in the collector. Image processing is also performed on these still images to obtain quantitative information about particle separation. Again, HSI thresholding is applied on the images capturing the final arrangement of the particles in the collector. Concentration plots for both kinds of particles are obtained by dividing the length of the collector into many bins and then calculating the number of pixels of a particular color (particle) in that bin. This is again touched upon in the Results section.

Different methods of particle release from the top part of the device are tested. The aluminum stencil as a release device delivers the best results with lesser amount of jamming. In most of the trials, equal volume fraction binary mixtures are used. Jamming of particles near the walls caused by flow-blocking arches is an issue and this is intensified when another release method (such as using a funnel) is used. As is discussed later, under a given operating condition, there is an optimum loading of the device which causes particles to flow freely without jamming – and this is determined by performing various trials (by taking note of the relative ratio of the largest particle diameter to the peg spacing (edge-to-edge)) so that accurate statistical data can be extracted without significant jamming in the device, which might introduce spurious errors in the collected data.

5.1.2 Theory and Simulation

5.1.2.1 Random walk theory An attempt has been made to develop a simple theoretical model based on the work of Benito et al. [271]. Experiments and DEM based numerical

simulations are time consuming and the developed ad-hoc theoretical model would assist in exploring a larger range of parameters not readily accessible via experiments or simulations. The theoretical model, as described below, incorporates the idea of a random walk in determining the position of a particle in the device.

The exit time or the transit time of a particle through the device is calculated in the following way: A particle position is randomly generated just above the first row of pegs (above a height equal to the vertical peg spacing, $H_p = 2S\sin(\pi/3)$, where $2S$ is the center-to-center peg spacing) and then it is allowed to fall down by gravity until it encounters a peg in its path. If it does not encounter a peg in its path, it falls unhindered through the rest of the device longitudinally and the transit time is calculated from Equation 5.1 using kinematic principles involving a sphere rolling down an incline of length l and angle θ with the horizontal. In this equation, a is the acceleration of the sphere and is equal to $(5/7)g\sin\theta$.

$$t = \sqrt{(\frac{2l}{a})} \tag{5.1}$$

In the event of a collision with a peg, one has to decide about the direction of the trajectory of the particle. If the z-coordinate of the particle center (see Figure 53, x and z are the longitudinal and the transverse directions, respectively) is to the right of that of the peg then the particle rolls over the peg to the right and vice versa. At this point, one needs to find the new z position of the particle. This can be achieved by choosing a random number uniformly distributed between 0 and 1.0 (RAN(0,1)) and the new particle postion can be obtained from this random number via Equation 5.2:

$$z_p = z_{peg} + A(R_{peg} + R_p) + A(2S - 2R_{peg} - 2R_p)RAN(0,1) \tag{5.2}$$

Here, z_{peg} is the z-coordinate of the center of the colliding peg; R_{peg} and R_p are the radii of the peg and the particle, respectively. S is the half peg spacing (centre-to-centre) and A is a factor equal to +1 (or -1) if the particle moves to the right (or left) after collision. Figure 53 explains the relative dimensions used in Equation 5.2.

Once a new position is identified, a new calculation begins for the trajectory of the particle following the same procedure as explained above. The time between two collisions
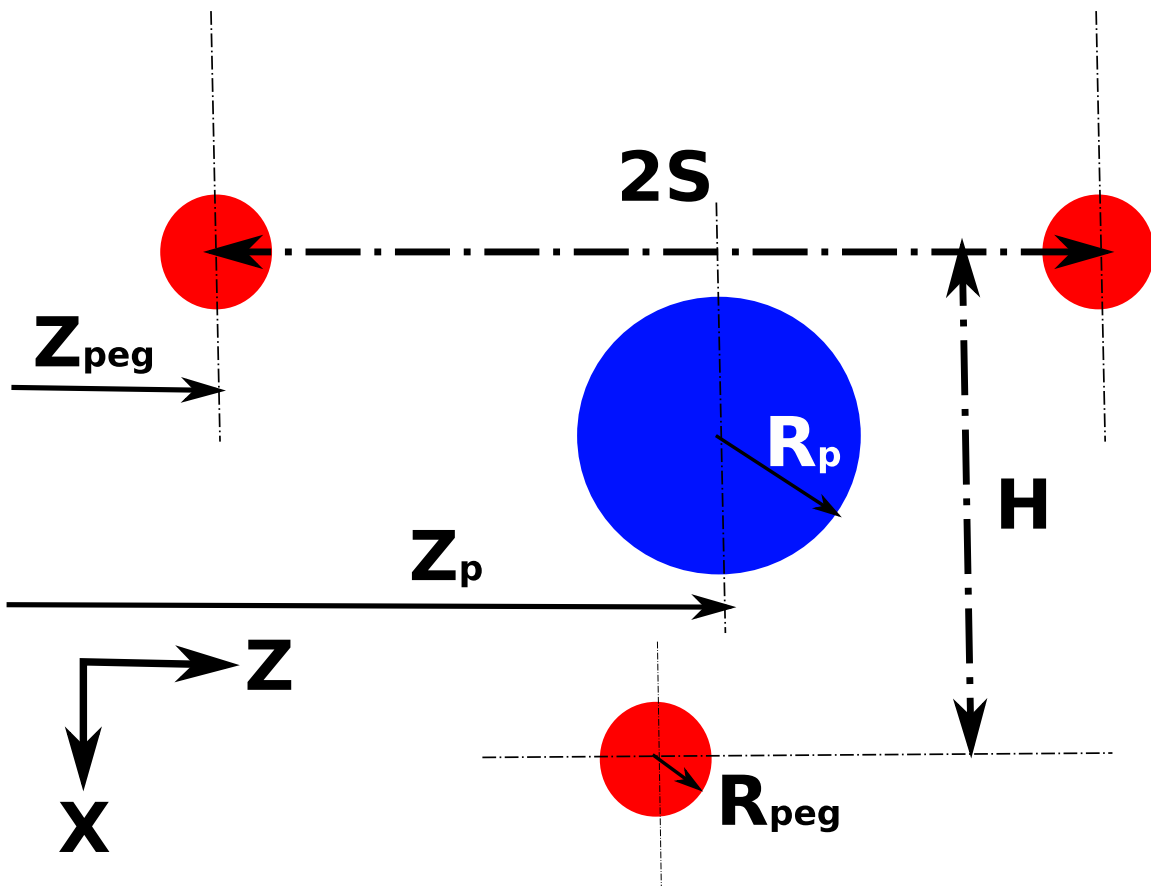
Figure 53: Schematic showing relative positions of the peg and particle centers.

is calculated from Equation 5.1 by replacing the variable l with the vertical peg spacing (i.e., $H_p = 2S\sin(\pi/3)$) and a counter is used to add all the times between collisions until the particle exits the last row of pegs. Following this method, one can find the exit time of a particle as well as the number of collisions it sustains. Finally, these data can be plotted on a histogram to obtain the probability distribution of exit time and collision frequency.

5.1.2.2 DEM simulation Apart from the ad-hoc theory as described in the previous sub-section, DEM simulations are also performed to obtain similar probability distributions of exit time of a single particle and also other kinematic information (such as velocity) for a monolayer of particles. In order to speed up the computations, a smaller chute length (208 mm as opposed to 726 mm in experiment) is used in some of the simulations. The chute and the pegs are made from particles with a typical diameter of 1 mm. For a binary mixture, typical flowing particle diameters are 2 and 4 mm. Periodic boundaries are used in the transverse direction with a typical simulation box width of 52 mm (1:4 aspect ratio). A typical peg center-to-center distance of 10.4 mm is used. The inclination angle of the device is set to 15 degrees with the horizontal (refer to Figure 50 for a typical DEM simulation setup). For a multi-particle case, a binary mixture is used with equal numbers of small and large particles in a 1:2 size ratio. Table 9 lists the various design and operating parameters for both DEM simulations and experiments. It is to be noted here that we are not interested in reproducing any experimental results exactly in DEM simulations, instead, efforts are made to prove the concept of separation independently using both of these methods.

5.1.3 Results

5.1.3.1 Single particle results Here, we present results from single particle investigations, both from the random walk theory and DEM simulations.

Random walk theory: A computer program is written to implement the random walk theory. More than 10,000 trials are performed to obtain the exit time and collisional statistics. Figure 54 shows the probability distribution of a single particle's exit time and the number of collisions it suffers. The exit times have been scaled by the theoretical exit time

Table 9: Various design and operating parameters used in DEM simulations and in experiments for the collisional separation device

Parameter	Simulation	Experiment
L (pegged length)	208 mm, 679 mm, 6.79 m	726 mm
W (pegged width)	varies, 52 mm typical	152 mm
$2S$	varies, 10.4 mm typical, same as column and row spacing	19.05 mm, same as column spacing, $\neq$ row spacing
$2R_{peg}$	varies, 1.0 mm typical	3.18 mm
$2R_p$	2 mm, 4 mm	4.65 mm, 6.9 mm, 7.8 mm
θ	15 degrees	26 degrees
Initial Condition (multi-particle)	equal numbers on a rectangular lattice	equal volume on a stencil

of an unhindered particle (refer to Equation 5.1). As per the theory, the most-probable exit time of a single particle with 4.65 mm diameter is about 1.5 times that of an unhindered particle of same size. Also, there is a 70% (most-probable) chance that the particle will suffer about 2 collisions with the pegs in its journey through the device. In order to obtain an idea about how the exit time and the number of collisions with the obstacles depend upon the effective diameter (defined as $d_{eff} = R_p/(S - R_{peg})$, to be discussed later) of a particle, the average exit times and the number of collisions of over more than 10,000 trials have been plotted as a function of d_{eff} in Figure 55. Both the graphs resemble an S-shaped curve where there is a sudden jump of the exit time (or number of collisions) after a certain particle size. Efforts are also made to corroborate the exit times obtained from the ad-hoc theory with the exit times observed in actual experiments (averages of 30 trials are computed for two different sizes of acrylic balls). Table 10 shows a comparison and it is imperative to say that the theory does not predict the exit times accurately (but it is congruent with the observation that smaller particles are faster).

DEM simulations: There are three different pertinent characteristic lengths that are important for separation in this device: peg diameter ($2R_{peg}$), peg spacing ($2S$) and particle diameter ($2R_p$). We are interested in observing the effects of all these length scales on the exit time distribution of a single particle. Figure 56 shows the effect of peg diameter on the exit time distribution of a particle. The particle diameter is 4 mm and the peg diameter varies at 1, 2, 4, 6 and 8 mm. The edge-to-edge distance between two pegs is kept constant at 6.4 mm and the device has a length of 208 mm and a width of 52 mm. More than 1000 trajectories are simulated with random starting position of the particle in order to obtain the statistics. The distributions did not change significantly if more trials beyond 1000 are included. The exit times are scaled by the transit time of an unhindered (i.e., when there were no obstacles) particle of the same size. One can observe from Figure 56 that the most-probable exit time for a particle is not sensitive to the obstacle diameter: an eightfold increase in peg diameter reduces the most-probable exit time by only about 25%. Also, the cases corresponding to $d_{peg} < d_p$ are slightly different from the ones with $d_{peg} > d_p$, with the most-probable scaled exit time changing from about 8.0 to 6.0, respectively.
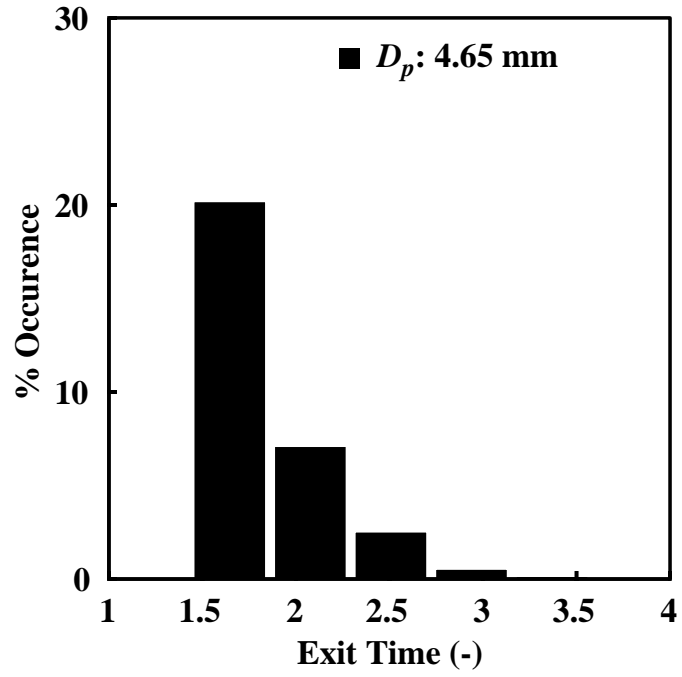
(a)
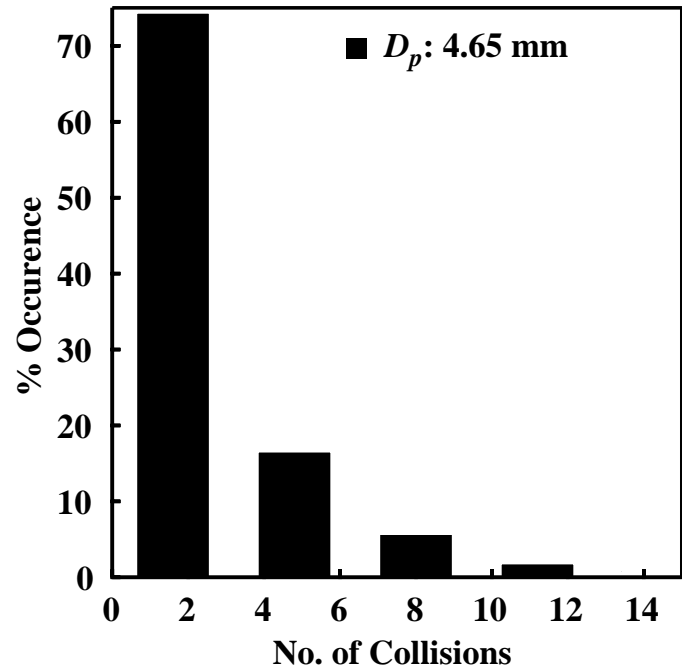
(b)

Figure 54: Probability distribution plot for (a) exit time and (b) number of collisions with obstacles for a single particle with 4.65 mm diameter. Other parameters are same as the experimental conditions listed in Table 9.
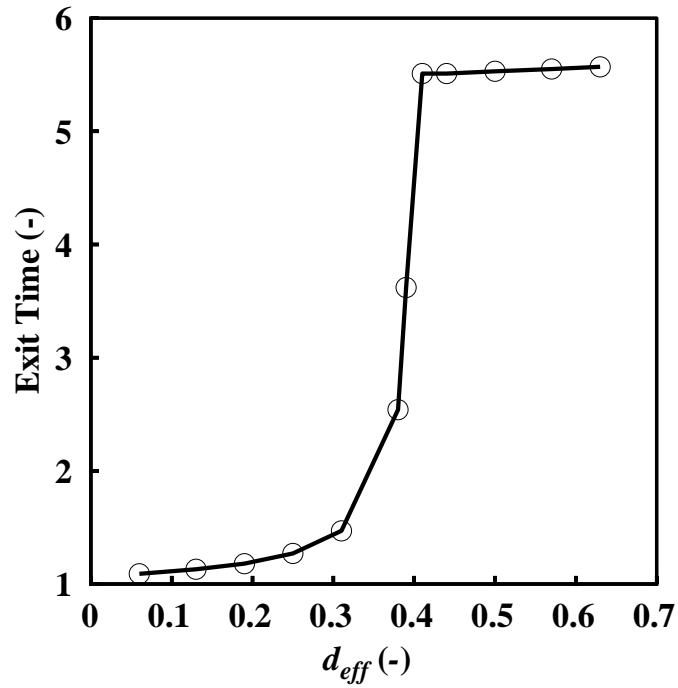
(a)
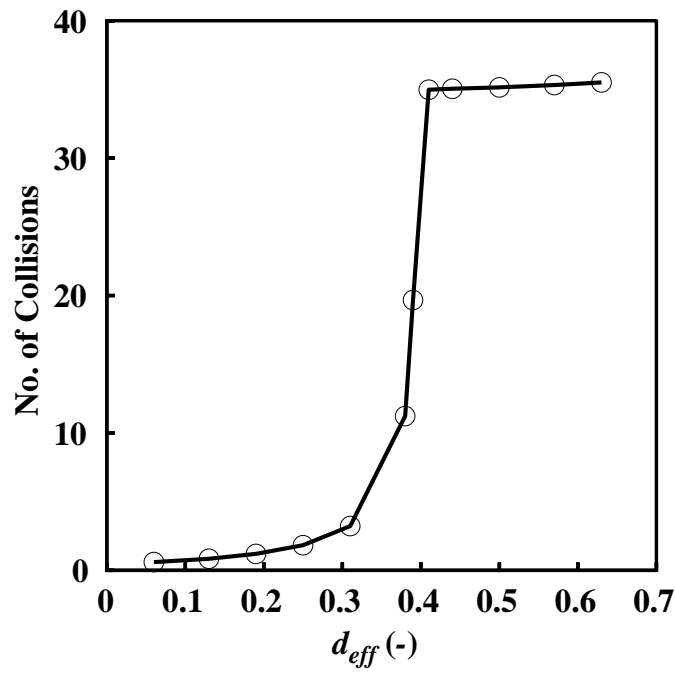
(b)

Figure 55: Average exit time and number of collisions as a function of the effective diameter of particles. Other parameters are same as the experimental conditions listed in Table 9.

Table 10: Comparison of exit time of a single particle between ad-hoc theory and experiments

Diameter	Exit Time Theory	Exit Time Experiment
4.88 mm	0.96 s	4.97 s
6.9 mm	3.84 s	5.76 s

Figures 57[a–c] show the effect of peg spacing on the probability distribution of exit time of a single particle on the device. Starting with a base case of 10.4 mm peg spacing, exit time distributions have been obtained by varying the peg spacing by 1.5 and 2.0 times (the edge-to-edge spacing is 9.4, 14.6 and 19.8 mm, respectively). The particle diameter is 4 mm and peg diameter is 1 mm. The device has a length of 208 mm. As before, the exit times are scaled by the transit time of an unhindered particle. One can observe that the most-probable exit time of a particle is very sensitive to the peg spacing – doubling the peg spacing reduces the exit time nearly by half. From the above observation, it is very clear that there are only two important characteristic lengths in this device, namely peg spacing $(2S)$ and particle diameter $(2R_p)$, which will control separation. One can combine these length scales into a ratio – $R_p/(S - R_{peg})$, which can be used as an operating parameter. In essence, the ratio $R_p/(S - R_{peg})$ is nothing but the ratio of a particle diameter to the edge-to-edge peg spacing, which is also a measure of a particle's collision probability with a peg and can be denoted as the effective diameter of a particle, d_{eff}. The results shown in Figures 57[a–c] can be represented as a function of d_{eff}. We observe that the most-probable exit time reduces as d_{eff} is reduced (e.g., when $d_{eff} = 0.43$, 0.27 and 0.20, the corresponding most-probable dimensionless exit times are ≈ 5, 3 and 2.5, respectively). This again confirms the hypothesis that a particle with a smaller d_{eff} will favor fewer collisions (with larger mean free path between successive collisions) and hence would not establish a diffusive motion and exit the device faster.

119
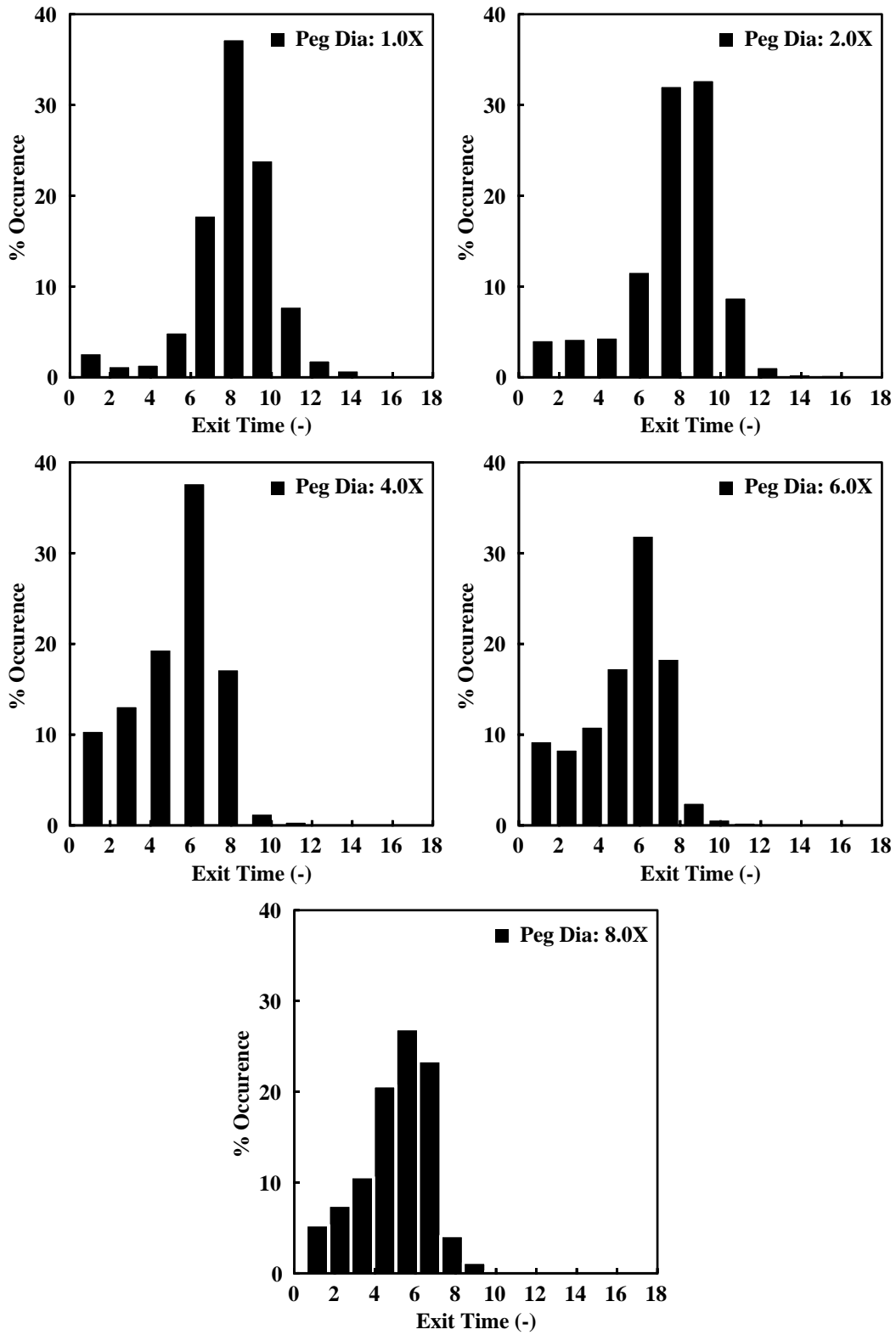
Figure 56: Effect of obstacle diameter on the exit time distribution of a single particle. 1.0x, 2.0x, 4.0x, 6.0x and 8.0x correspond to 1, 2, 4, 6 and 8 mm peg diameter, respectively. Particle diameter is 4 mm.
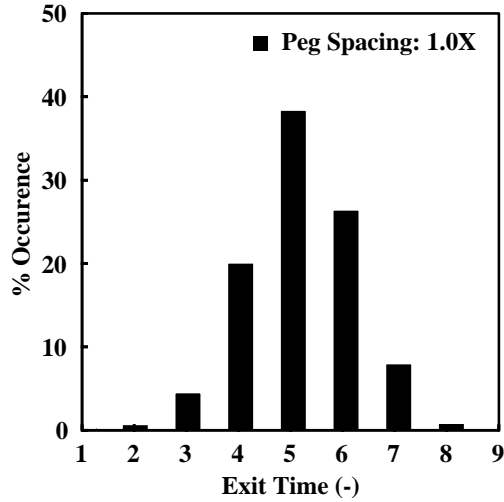
(a)
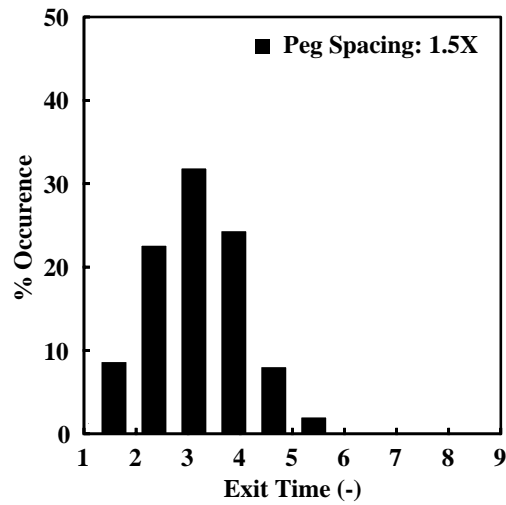
(b)
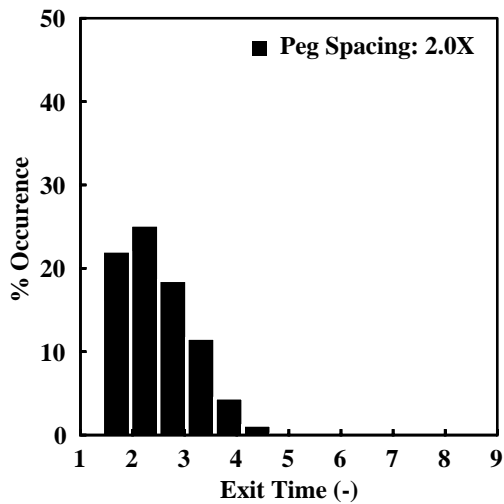
(c)

Figure 57: Effect of peg spacing on the exit time distribution of a single particle. (a), (b) and (c) correspond to 10.4, 15.6 and 20.8 mm center-to-center peg spacing, respectively. Particle and peg diameters are 4 mm and 1 mm, respectively.

5.1.3.2 Multi-particle results   The goal of this part of the work is to study the influence of the collective effects on the multi-particle dynamics in the separation device and to determine if the single particle observations still hold for a multi-particle case.

DEM Results: Figure 58 shows simulation results of the average velocities of a mixture of small and large particles (1:2 size ratio) in the longitudinal (x) direction. A steady velocity regime is clearly achieved due to the fact that there is a balance between the energy dissipated during collisions (between particles and also with pegs) and the energy gained during the flow over the chute surface when there is no collision. One can clearly observe that the single particle predictions still hold here: smaller particles are faster – in this case by 40% – as a smaller d_{eff} means fewer collisions and faster transit. In the current case, a 679 mm long and 52 mm wide device is considered with 10.4 mm peg center-to-center spacing. Chute and pegs are made from 1 mm particles. Therefore, we expect that particle separation is possible in this device which can be confirmed from simulations (refer to Figure 59). A monolayer of particles start from a uniformly mixed state (small and big particles are placed alternately on a rectangular lattice) and are allowed to flow over the obstacles in a very long device (6.79 m or 10x longer). The distribution of particles is obtained by the following method: The length of the device is divided into many bins and the number of particles (of both types) having their x-coordinates within the range of a particular bin are counted, and then the fraction of particles are plotted in the y axis as a function of longitudinal position on the device. At initial times, the particles are mixed at one end of the device and as time progresses, we can observe three distinct particle regions – an extended leading region (region I in the bottom-right sub-figure of Figure 59) consisting only of smaller particles (as they are faster), an intermediate mixed region (region II) , and a relatively shorter trailing region (region III) comprising only larger particles. Note that after about 25 s, the particles reach an effective separated state.

Since we observe jamming in many experiments, numerical investigations are also performed to study the effect of particle loading on the extent of separation (E_s). The extent of separation E_s is defined in Equation 5.3:

$$E_s = \frac{(<V_{small}> - <V_{big}>)t}{L} \tag{5.3}$$
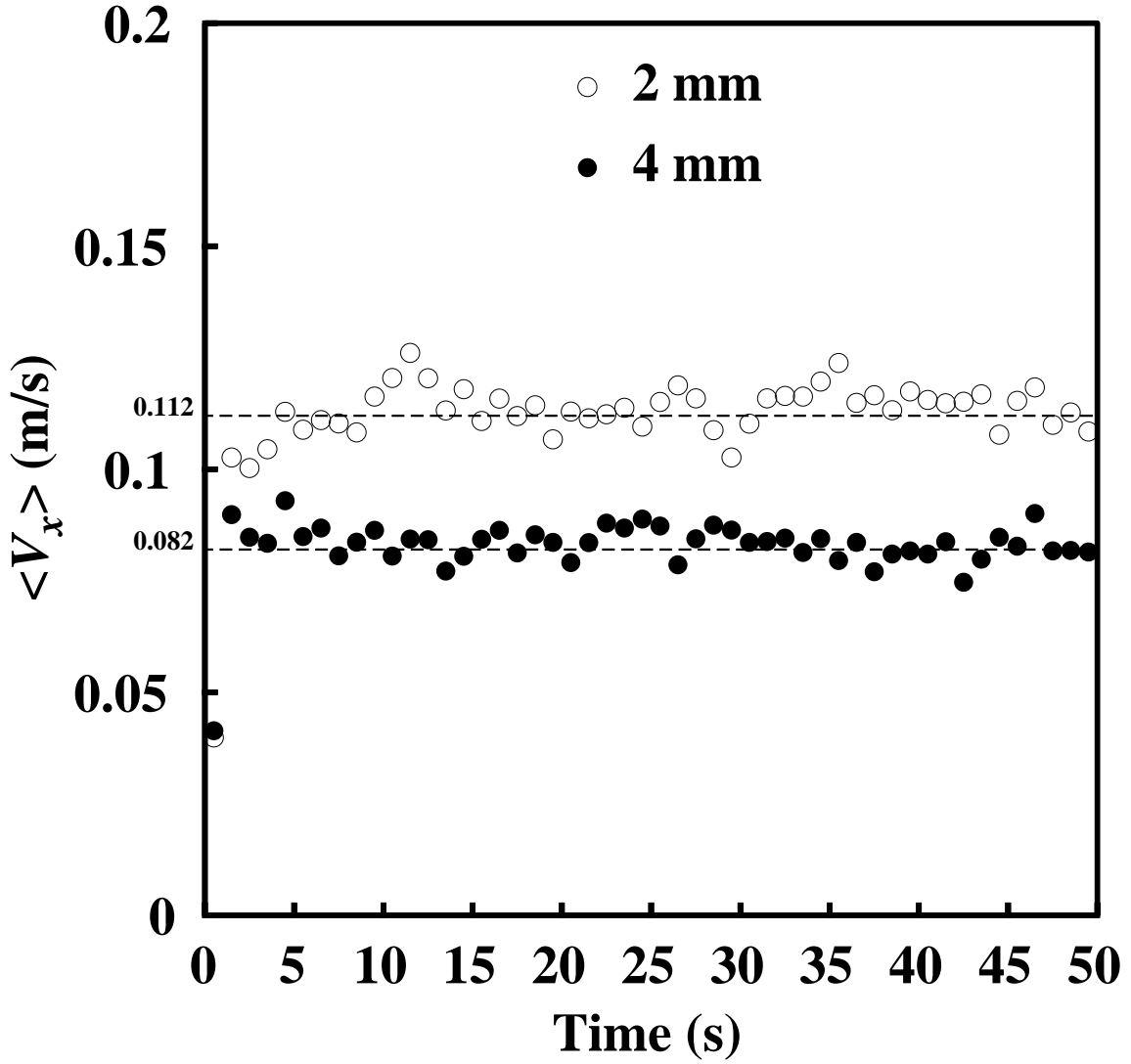
Figure 58: Average x-velocity of small and large particles in a multi-particle collisional flow over the device.
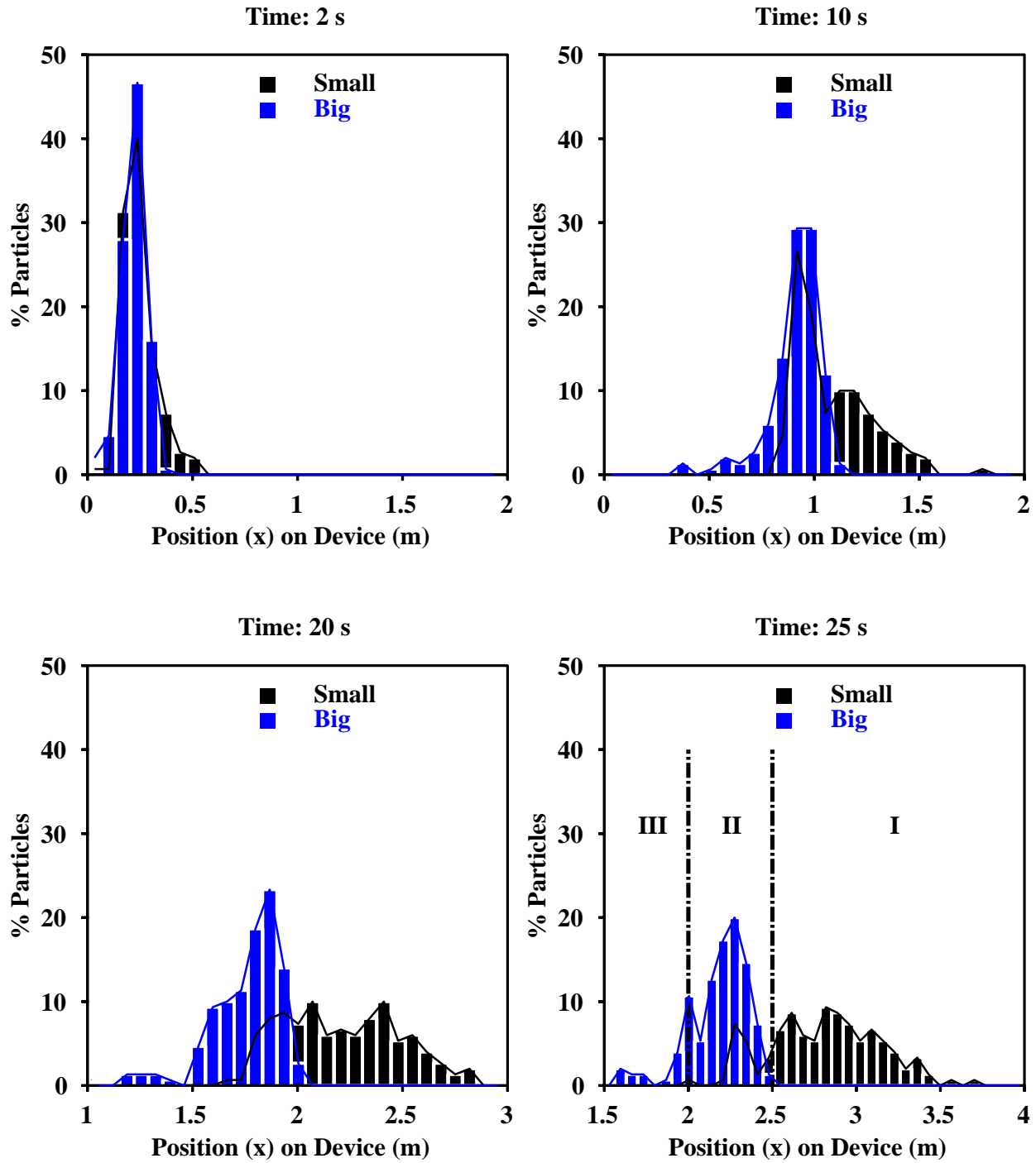
Figure 59: Spatial distribution of particles at different time instances showing progress of separation. Small and big particles correspond to 2 and 4 mm diameter, respectively. Three distinct particle regions as described in the text have been shown in the bottom-right sub-figure. The line over the bars passes through the data corresponding to the bin centers of a histogram.

where $<V_{small}>$, $<V_{big}>$ are the average longitudinal (x) velocities of small and big particles respectively. t is the time allowed for migration and L is the length of the device. The extent of separation is plotted as a function of % area coverage of particles (equal number of small and big particles are used) in Figure 60. The area coverage of particles denotes the loading of the device, and is calculated as the ratio of the cross-sectional area of all flowing particles to the non-pegged surface area of the device. We can clearly observe that as the loading (area coverage) increases, the extent of separation decreases dramatically. This graph can be used to select an optimum number of particles for effective separation, without significant jamming. We found that for the given design and operating parameters of the device [$2S$ = 10.4 mm, d_{peg} = 1 mm, L = 679 mm (periodic), W = 52 mm, d_p = 2 and 4 mm, θ = 15°, t = 30 s], 150 small and 150 big particles are sufficient to obtain an effective separation without significant jamming.

Experimental Results:

Numerical investigations encouraged us to perform experiments with many particles in an actual setup (refer to Section 5.1.1). Two different types of collectors are used to observe direct separation of particles in this device when particles exit the last row of obstacles. Equal volume mixtures of 4.65 mm (small, pink color) and 7.8 mm (big, black color) acrylic balls are used. Each experiment is repeated at least four times and the results presented here are the average of those observations. In the first set of experiments, 18 small and 90 big particles are used (50:50 v/v). To generate the initial condition, each circular hole of the aluminum stencil is filled with 3 big and 15 small particles (total six holes are filled). Figure 61 shows the initial and final conditions of one of the trials for this experiment. Thresholding and binning of pixels of the image corresponding to the final positions of particles yield Figure 62, which shows the spatial distribution of particles along the collector length. Data for each bin corresponds to the number fraction of a particular type (color) of particle calculated with respect to the total number of pixels of that type in the given length of the collector considered. As mentioned earlier, a minimum of four trials are performed to verify the reproducibility of the results and the calculated distribution corresponds to the average of those trials. It is evident from these plots that the device is capable of separating a mixture.
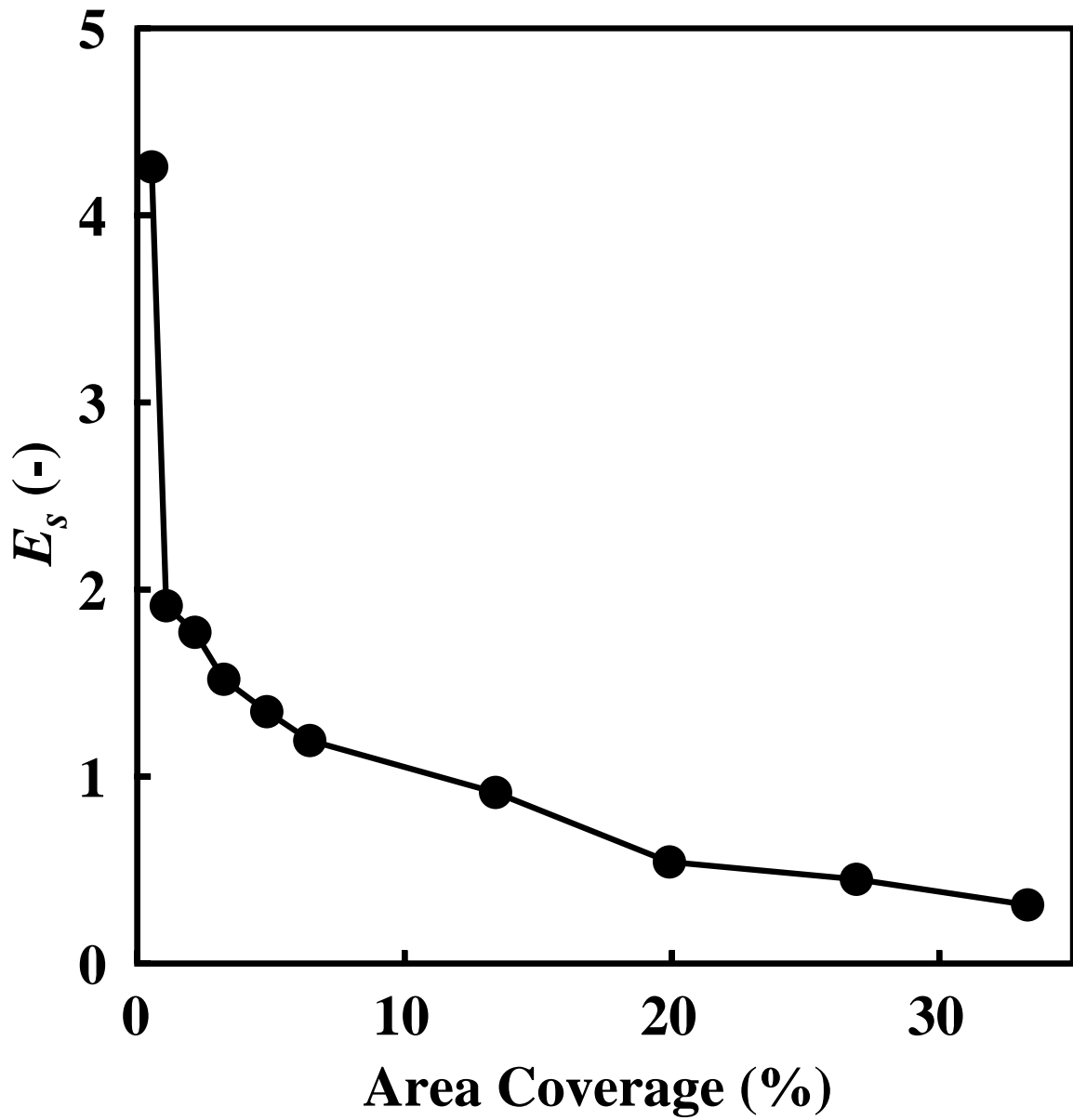
Figure 60: The extent of separation (E_s) as a function of area coverage of particles in the device.
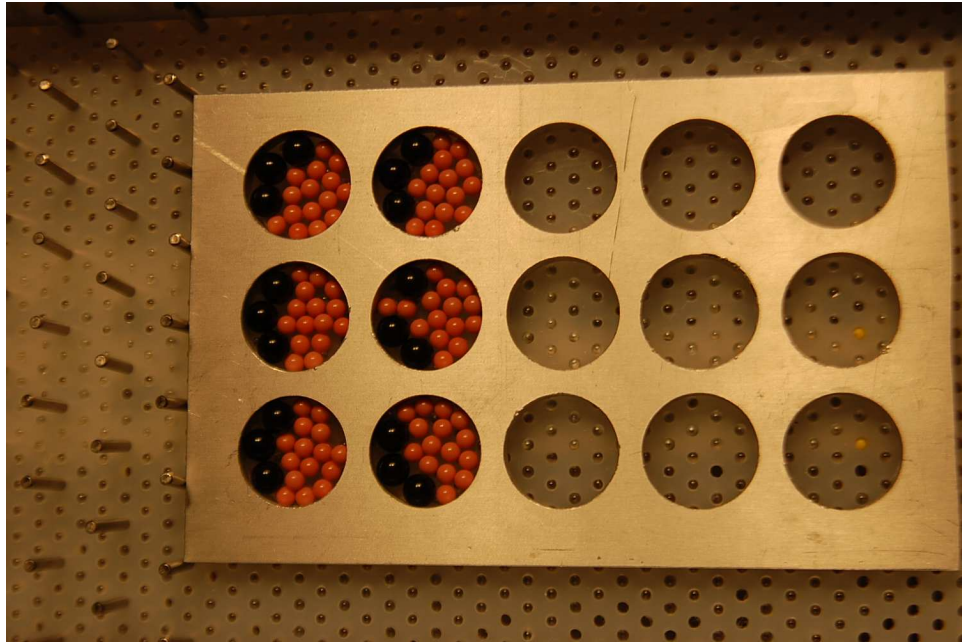
(a)
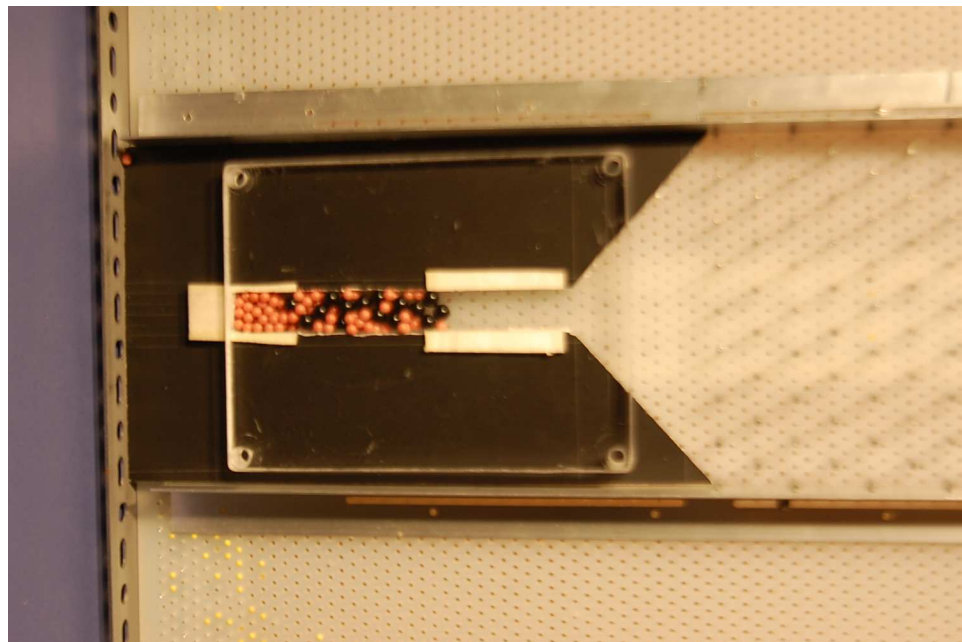
(b)

Figure 61: (a) Initial and (b) final conditions of one experiment consisting of 18 big and 90 small balls (50:50 v/v) with a narrow-type collector.
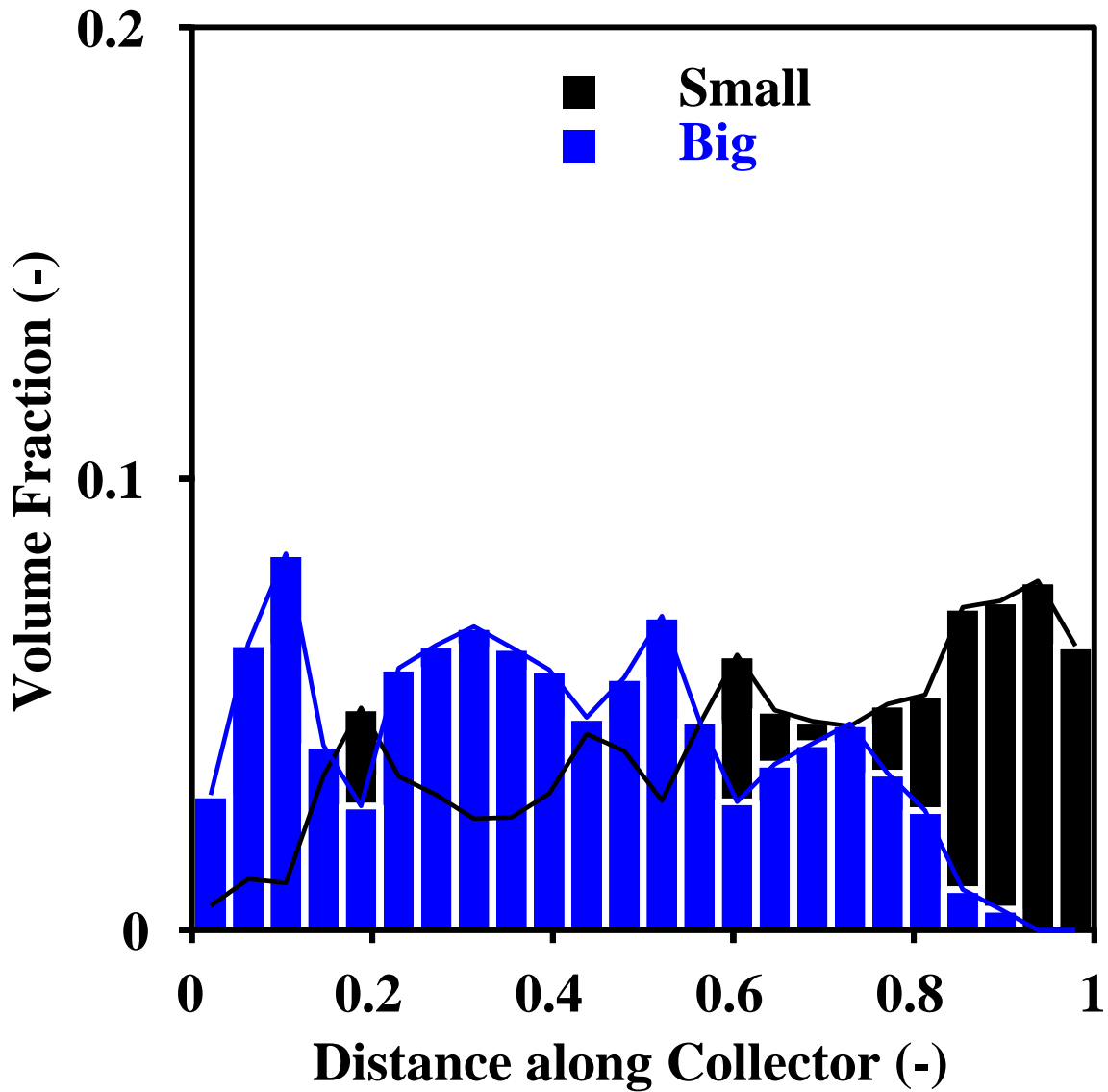
Figure 62: Spatial distribution of small and big particles along the length of a narrow-type collector for a set of experiments with 18 big and 90 small particles (50:50 v/v). Average of four repeat experiments has been plotted here. HSI thresholding has been used to extract the data for both types of particles in 24 bins. The bottom of the collector, which is 220 mm below the last row of pegs, corresponds to distance 1.0 of the scaled x axis.

In order to confirm this observation, a wider collector at the end is also placed for another set of experiments involving 30 big and 150 small particles (50:50 v/v). Figure 63 shows the initial and final conditions of one of the trials for this set of experiments. Similar image processing technique yields the final spatial distribution of each type of particles in the collector, which is depicted in Figure 64. In order to compare the automated image processing results with manual counting of particles in each bin, we have plotted a similar spatial distribution of particles in the collector for one of the trials belonging to the same set of experiments in Figure 65. There is a very close agreement between the HSI thresholding and hand calculation, which gives us confidence about the fidelity of the image processing technique. From Figure 64 (or Figure 65), we can clearly observe that most of the smaller particles occupy the bottom of the collector as they are faster, and the bigger ones arrive late owing to their higher probability for sustaining many more collisions, which slows them down. The peaks of the distributions are clearly widely separated, suggesting that this device is an efficient particle separator (although a longer chute is necessary to get complete separation).

5.2 SEPARATION OF GRANULAR MIXTURE BY RATCHET MECHANISM

As outlined in Section 1, while segregation is often an undesired effect, sometimes separating the particles from the mixture is the ultimate goal. Mixtures of different sized particles can separate when set in motion in a number of methods, including rotating drums, shear flow, vertical shaking, horizontal shaking, etc [272, 273]. In this part of the work, we seek to investigate and further the body of knowledge on granular separation by ratchet mechanism using particle dynamics (PD). In other areas of science and technology (like in biology – "brownian motors" in cells, diffusion sorting of macromolecules) [261, 262], ratchets have been the subject of intense research efforts because they can produce a directed current of particles without any net average force in the direction of particle motion. This is somewhat counterintuitive. Using this concept, a new method of separation of particles was first
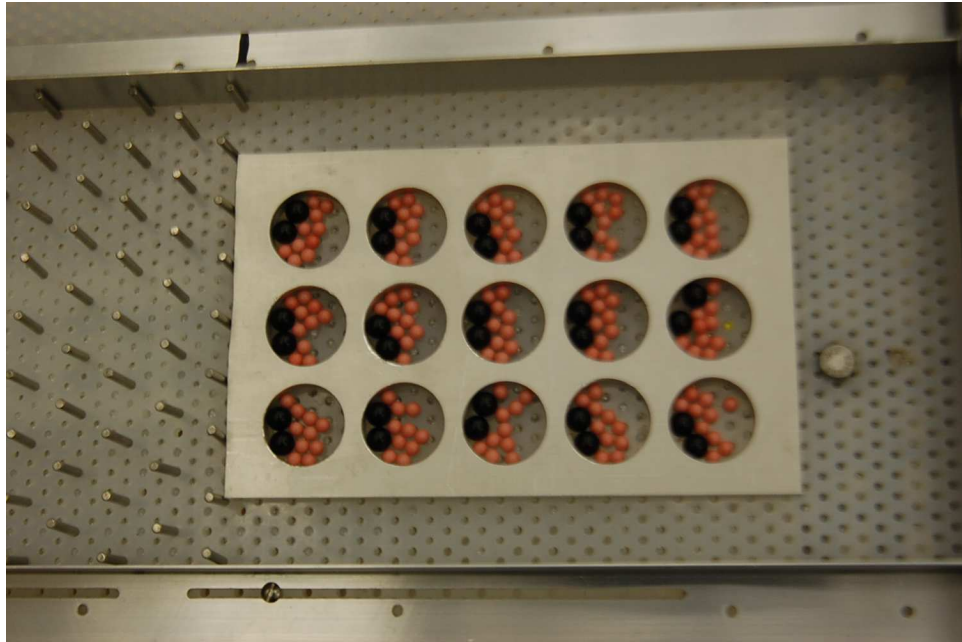
(a)
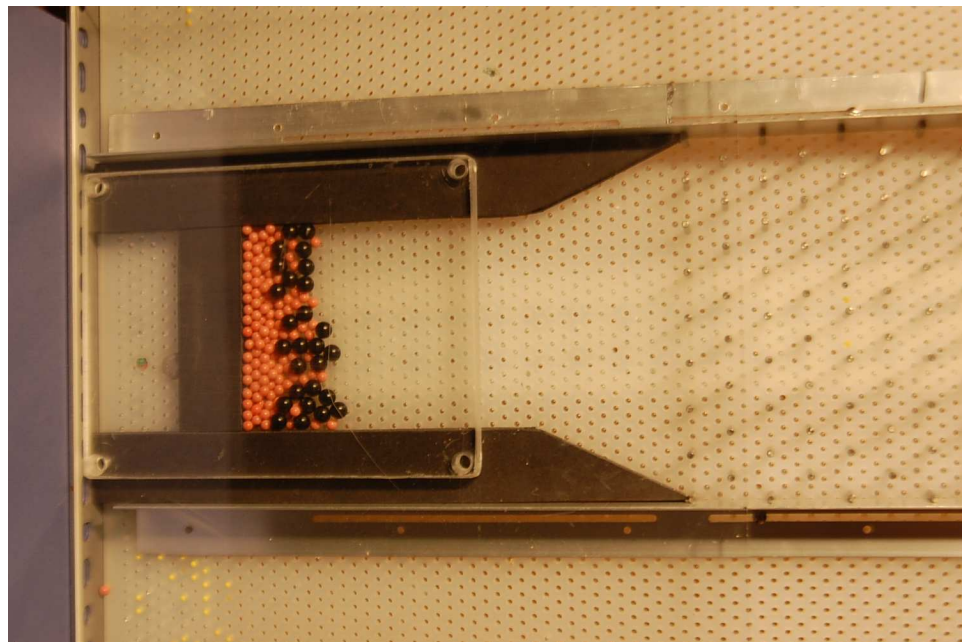
(b)

Figure 63: (a) Initial and (b) final conditions of one experiment consisting of 30 big and 150 small balls (50:50 v/v) with a wide-type collector.
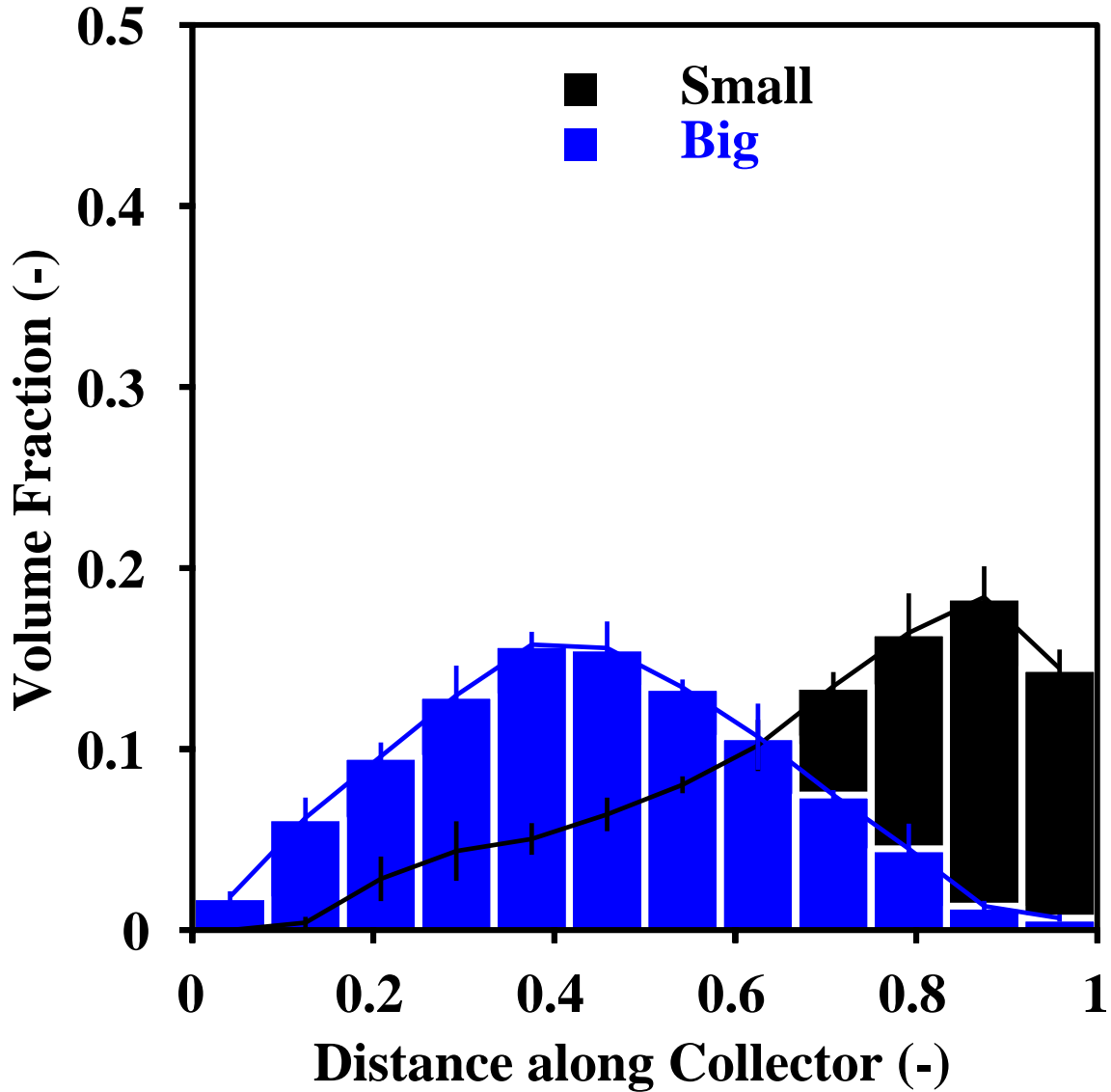
Figure 64: Spatial distribution of small and big particles along the length of a wide-type collector for a set of experiments with 30 big and 150 small particles (50:50 v/v). Error bars obtained from four repeat experiments have also been shown. HSI thresholding has been used to extract the data for both types of particles in 12 bins. The bottom of the collector, which is 200 mm below the last row of pegs, corresponds to distance 1.0 of the scaled x axis.
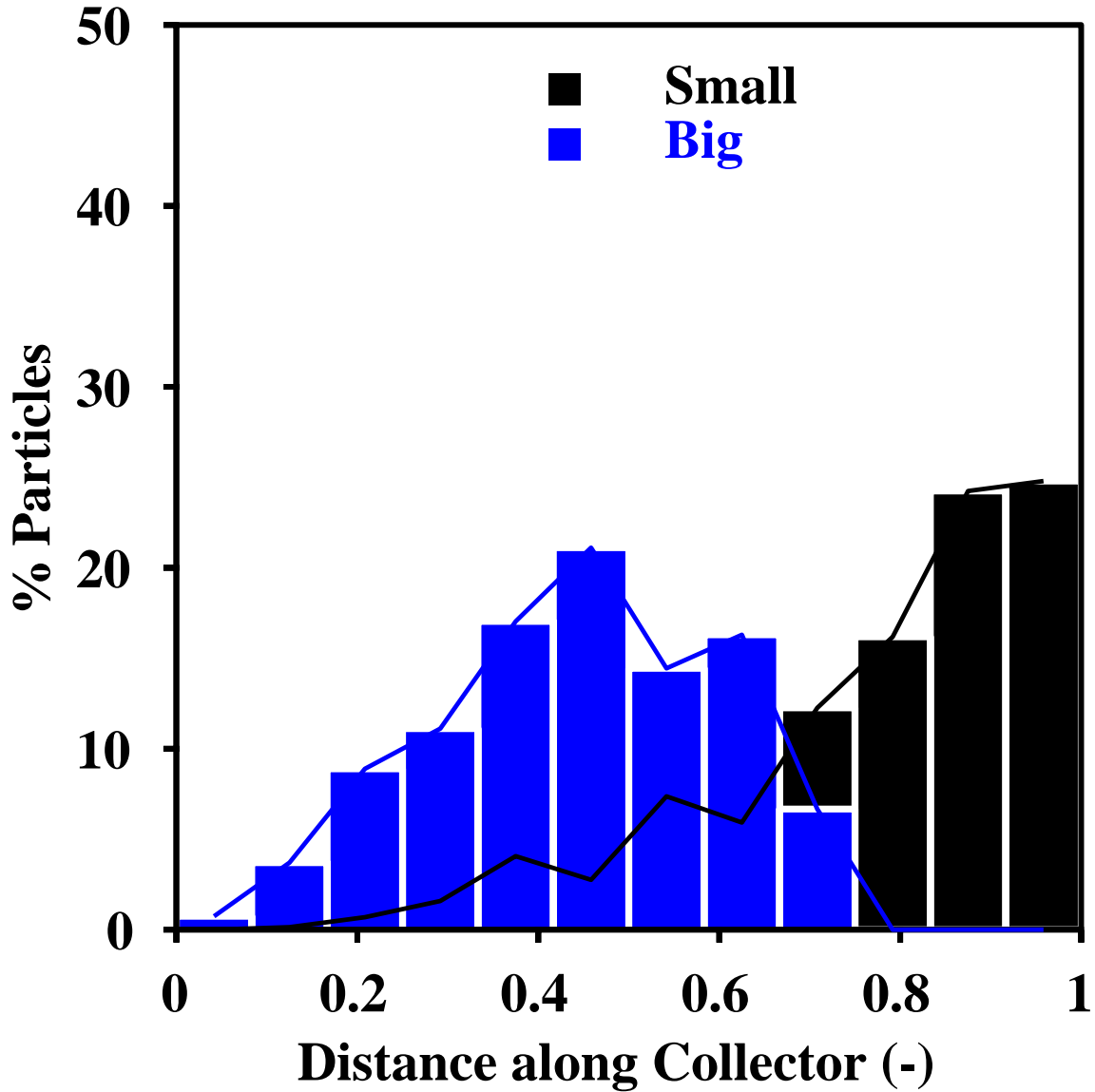
Figure 65: Spatial distribution of small and big particles along the length of a wide-type collector for an experiment with 30 big and 150 small particles (50:50 v/v). Manual counting has been used to extract the number fraction data for each bin for both types of particles. The bottom of the collector, which is 200 mm below the last row of pegs, corresponds to distance 1.0 of the scaled x axis.

proposed by Farkas et al. [274,275]. The central idea of separation using ratchet mechanism is to produce horizontal size segregation in a vertically vibrated layer of granular material using a sawtoothed base [276] (see Figure 66). For example, in a mixture with two-sized particles, vibration will cause the large particles to rise to the top of the layer, and the vibrating base with a sawtooth surface profile will produce stratified flows either in the same or in the opposite directions at different heights within the layer. The result of combining vibration and a sawtooth profile is that, under proper conditions, the large and small particles may be horizontally driven in opposite directions. Basically, the ratchet creates a symmetry-breaking flow pattern, which emerges perpendicular to the direction of the energy input. This method has a tremendous potential as an industrially viable separation device owing to the fact that the components of the mixtures can be easily collected without any further processing, many ratchets can work in parallel yielding high throughput and the quality of the separation can be tuned by changing the ratchet width or the loading rate.

There have been some studies (both numerical and experimental) undertaken recently [273, 276–280] on this method of separation. These studies have shown that the response of a particular type of particle to a ratchet system depends significantly upon the size and shape of the ratchet, the driving force, and the properties of the particles themselves. The direction in which spherical particles move on the ratchet depends on the size and elasticity of the particles, among other things. Thus two species of particles (equal size and density, but different hardness) may move in opposite directions on the same ratchet base. Whether a particular combination of particle and ratchet will display net motion to the left, to the right, or any coordinated motion at all is not clear *a priori*. Also, which combination will produce separation is also not clear at present and this highlights the need for further study of these systems. Moreover, no consensus about a theoretical model has emerged yet which can relate the ratchet design and operating parameters to the quality of separation.

Since many earlier studies employed 2-D systems, we seek to examine a full 3-D ratchet system in this part of the work. In the past [274, 277], the effects of different design and operating parameters (like ratchet height, asymmetry, particle properties, loading, etc.) were studied in 2-D setups using either event driven algorithms or MD-like simulations with Lennard-Jones type force potentials, here the main aim of the current work is to get more
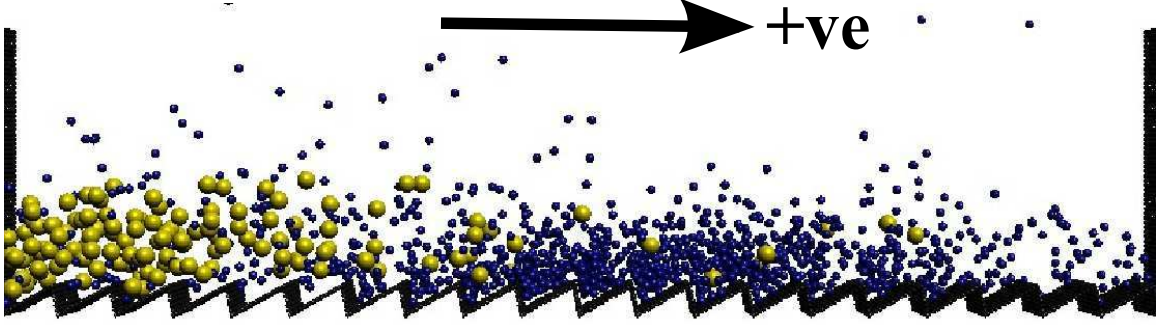
Figure 66: Simulation snapshot of a typical ratchet device in action. The asymmetry parameter $a = 0.9$. A positive displacement is obtained in this setup when particles move to the right of the figure (in the direction of the arrow, i.e., they encounter less steeper side of the tooth as it vibrates).

insights into the effect of only a few parameters using full 3-D particle dynamics simulations with realistic force models to find conditions for separation.

5.2.1 Simulation Setup

The discrete element method (DEM) is used to investigate the separation capability of a ratchet. Figure 66 shows a typical snapshot of the progress of a DEM simulation. The system is fully three dimensional with a typical length $L \approx 60d$, height $H \approx 100d$ and width $W \approx 5d$ (simulation box size was $L \times W \times H$), where d is the diameter of the largest particle size present in the system. In some cases (for long devices), two side walls are used to contain the particles, however, in many cases the simulations are periodic in all the three directions. The height H is chosen such that no particle crosses the top boundary. Figure 67 shows a schematic of ratchet teeth. Each tooth can be characterized by three parameters as shown: the height h, the width w, and the asymmetry parameter a defined as $a = l/w$, where l is the length of the projection of the longer side of the tooth on the horizontal direction. In exploring the parameter space, h is varied at different levels as discussed later. In a typical simulation, each tooth has $w \approx 3d$, $a = 0.9$ and $p \approx 5d$. Here, p is the depth of a tooth (see
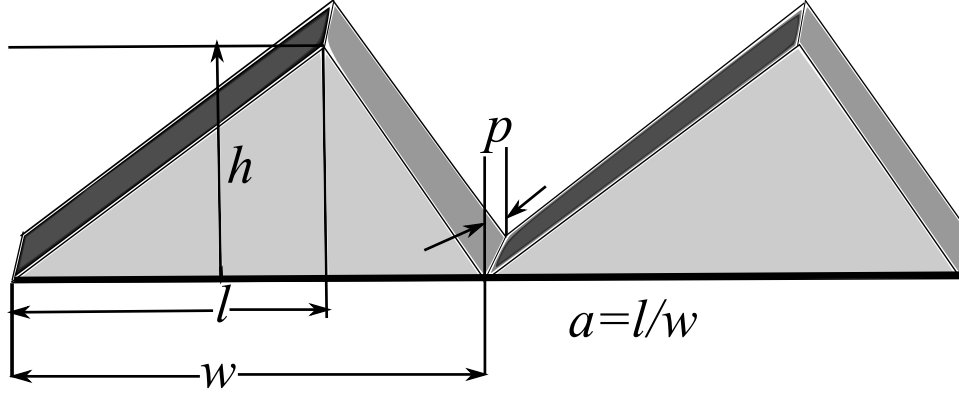
Figure 67: Schematic of ratchet teeth showing relative dimensions.

Figure 67). For periodic simulations, 20 identical ratchet teeth have been used. The device is subjected to a sinusoidal oscillation with frequency f and amplitude A_v. The dimensionless acceleration $\Gamma = 4\pi^2 f^2 A_v/g$ (g = acceleration due to gravity) is fixed at 2.61 (with $f \approx 12$ Hz, $A_v \approx 2d$). The loading or the number of particle layers $[N_h = (n_1 d_1 + n_2 d_2)/L]$ used are around 10 for the periodic simulations.

An elastic with viscous damping force model (see Section 2.2.2.1) is used to simulate the various cases. In order to speed up the computations (which does not affect the flow kinematics), fictitious soft particles are used while maintaining the required size or density ratios. For all cases, an equal volume fraction (50:50 v/v) was used for both types of particles. A typical simulation starts with both kinds of particles uniformly mixed in a binary mixture in a rectangular area just above the ratchets, and the particles are allowed to settle under the action of gravity. For periodic simulations, the initial rectangular region extended to the full length of the device.

5.2.2 Results

The system under study is a very complex one with many parameters. It is nearly impossible to explore the parameters space exhaustively, though in the past, some studies have tried

to investigate a few important ones (such as sawtooth shape, layer width, frequency of vibration, material hardness, etc.). However, these studies were limited in the sense that the simulation methods used were far from being realistic (inappropriate force model was used for macroscopic particles) and the results were not exhaustive – they depended on the system at hand and cannot be used in a general way. Moreover, they were interested in observing the direction of transport, and due to that, in many cases, non-segregating (mono-disperse) particles were used. In this study, we try to focus on only a single geometrical parameter but perform an exhaustive study within that small parameter-space using binary mixtures with both size and density differences. The dependence of one of the very important parameters – namely, the ratchet height – on separation in this device has been exhaustively examined here, and unlike other studies, we present results for the direct numerical simulation of a long ratchet device in order to directly observe the possibility of separation, if any, for a given particle parameter set.

Figure 68 shows the dependence of ratchet height on the distance travelled by the two types of particles of a binary mixture. Both size and density separations are considered individually. Periodic boundary conditions in the length direction ($L \approx 60d$) are used to record the distance travelled by particles for a given duration of time (200 s in this case). The results have been presented here as dimensionless quantities with the distance being scaled by the device length L. The following parameter set is used: h/d is varied from 0.0 (a flat base) to 6.25 (beyond which there will be essentially no transport as the teeth would be too high to produce any horizontal motion of the particles), where d is taken as the size of the bigger particle for size separation or just the particle size for a density separation case; w, Γ, a, N_h, etc. are the same as described in the previous sub-section. It is obvious from Figure 68 that the direction of the horizontal transport (of all types of particles together) can be switched for certain parameter combinations (to be specific, by using taller ratchets – which is in agreement with the observations made in other studies, such as by Farkas et al. [274]). All particles can either move in a negative direction or in a positive direction and this transition happens at a particular h/d ratio. For example, for a size ratio of 2:1, this switching of transport direction happens somewhat earlier at around $h/d = 3.65$. Also, there is an indication that for some size and density ratios and certain h/d, the smaller (heavier)
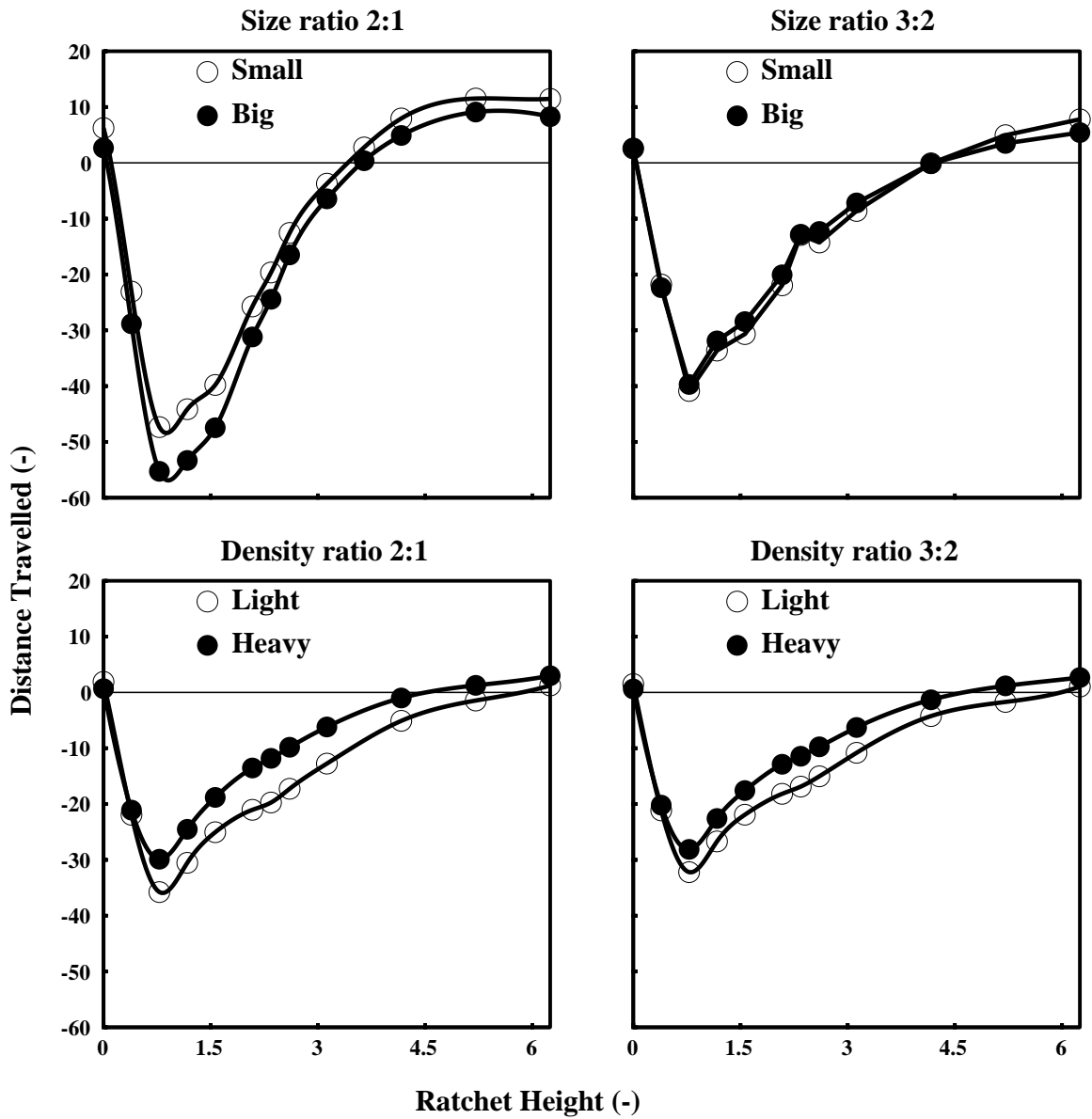
Figure 68: Effect of ratchet height on the distance travelled (separation) by particles for various size and density ratios. A horizontal line with ordinate 0 has also been drawn to show the switching of particle direction.

particles may have a net positive movement whereas the bigger (lighter) ones can move in the negative direction (i.e., two kinds of particles can also move in opposite directions, in addition to all particles moving either in positive or negative direction). Figure 68 shows that this may be possible for size ratio 2:1 at $h/d \approx 3.53$. Another interesting observation from Figure 68 is that, for all cases, the distance travelled by the particles goes through a clear minimum at around $h/d \approx 0.78$. Therefore, this particular h/d ratio creates the maximum driving force for all kinds of particles to travel in a particular direction.

It is also interesting to note a unique behavior of particles for a size ratio of 3:2 as compared to other size or density ratios from Figure 69. In this figure, the differences in the migration distances have been plotted for all size and density ratios on a single graph. The curve for size ratio 3:2 crosses the zero line at about $h/d \approx 4.0$. This suggests that for h/d <4.0, all particles move to the negative direction with smaller particles moving faster than the larger ones and for h/d >4.0, all particles move to the positive side (switching of direction) but with larger particles moving faster than the smaller ones (switching of speed). In all other cases, this is not observed – the particle transport direction switches from negative to positive direction in a similar way, but the two types of particles never switch their speeds. The separation is expected to be pronounced (calculated from the differences in distances travelled by two kinds of particles, see Figure 69) for a size ratio of 2:1 (and also for a density ratio of 2:1, but to a lesser extent). However, the other size and density ratio – 3:2 – does not point to considerable separation as compared to the 2:1 case. Therefore, we observe that a particular size or density ratio should exist in order for the particles to separate, and this would only occur at a certain ratchet height ($h/d \approx 0.78$), given other design and operating parameters. It is interesting to note that a size ratio of 2:1 indicates more separation vis-à-vis a 2:1 density ratio (the maximum differences in distances travelled by the two types of particles being 9.18 for 2:1 size ratio, and 7.91 for 2:1 density ratio), whereas this observation is reversed for a size ratio of 3:2 vis-à-vis a 3:2 density ratio (the maximum differences in distances travelled by two types of particles being 2.25 and 5.45, respectively).

From Figures 68 and 69, we note that, in general, larger or lighter particles travel faster in this device (with the exception of size ratio 3:2 where both kinds of particles can travel faster depending upon the h/d ratio as discussed earlier). Therefore, we expect that for
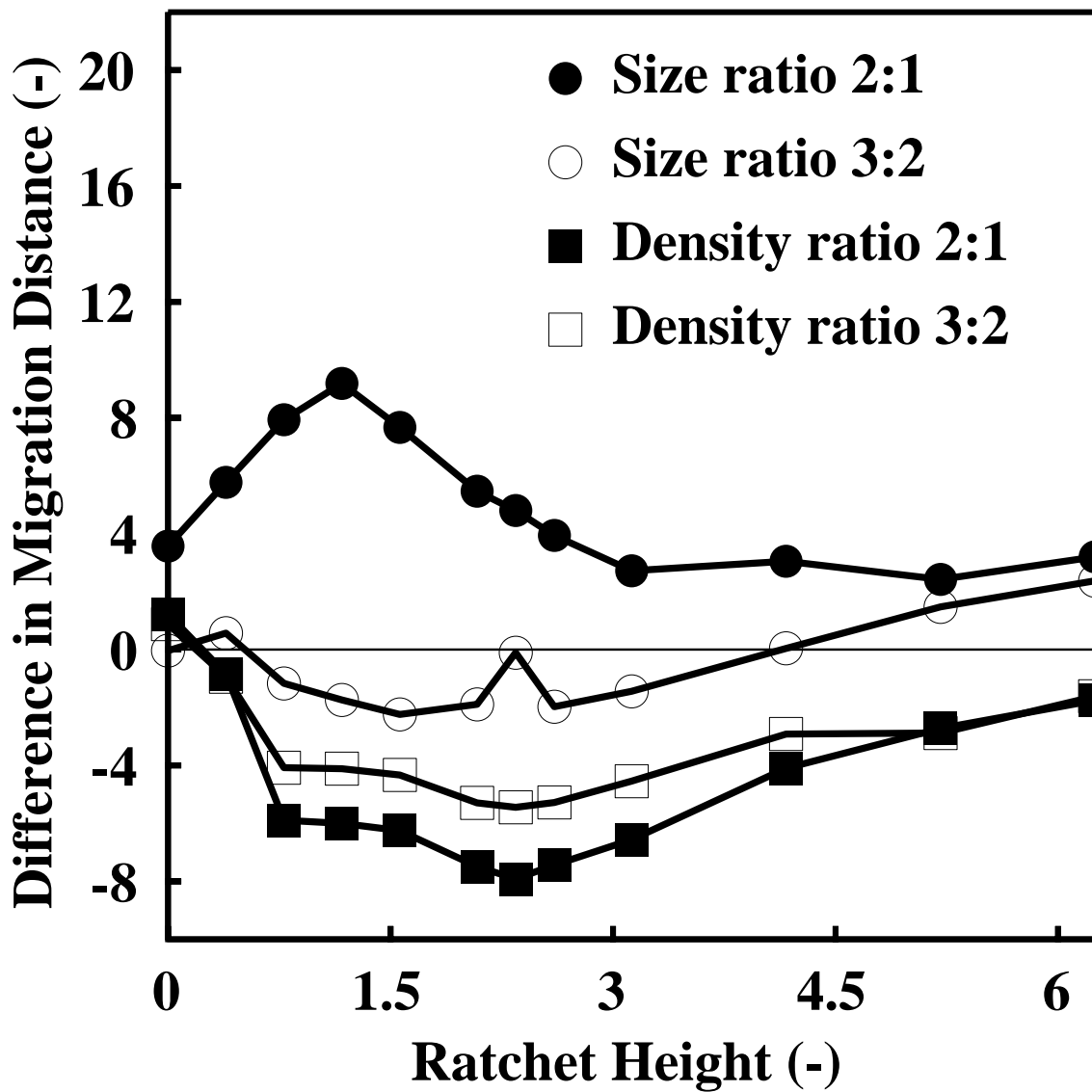
Figure 69: Data from Figure 68 have been plotted to show the effect of ratchet height on the differences in migration distances (separation) by particles for various size and density ratios. The differences in migration distances correspond to (small - big) or (light - heavy).

a combined size and density separation case where the bigger particles are lighter and the smaller particles are heavier, the degree of separation may be enhanced or amplified. In order to do that, we plot similar data (as given in Figures 68 and 69) in Figures 70 and 71, respectively, for a combined size (2:1) and density (1:2) ratio. Surprisingly, we do not get a better separation as compared to the pure 2:1 size ratio case – the highest difference in the distances (scaled) travelled by the two types of particles is 8.91 for the combined case as compared to a higher value of 9.18 for a pure 2:1 size ratio case. Therefore, it is interesting to note that, for the cases we studied, a combined effect of size and density differences may slightly lower the ability of the device to separate particles effectively as is evident from the current investigation. However, the shapes of the graphs and other features of the process remain similar to that of the pure size or density ratio cases.

In order to directly observe the separation of particles, we consider simulating a long ratchet device with a 2:1 size ratio while keeping the density constant (h/d was kept fixed at 1.17). We also consider other cases such as a 2:1 density ratio case (with $h/d = 1.17$) and a case with 2:1 size ratio but with an h/d ratio of ≈ 3.53 that predicted an opposing flux of materials through the device as per Figure 68. The other parameters of these simulations are similar to the ones described in Section 5.2.1 except the h/d ratio, and the length L of the device. For 2:1 size and density ratio cases, L is $\approx 1500d$ (made 25x longer than the periodic simulations). The initial condition is obtained by locating the particles near the right side of the device (inside a $53d$ wide window) for $h/d = 1.17$, as the predicted movement (as per Figure 68) of all kinds of particles is to the left of the device, yielding a negative travelling distance. For the case where the particles are expected to move in opposite directions (i.e, for size ratio 2:1 with $h/d \approx 3.53$), the binary mixture is placed symmetrically in the middle of the device (inside a window of width $53d$), and the device length L is $\approx 2040d$ (34x longer than a periodic device).

Figure 72 shows the progress of separation for a size ratio of 2:1 and $h/d \approx 1.17$ as a function of time. To obtain these plots, the device length is divided into many bins and the number of particles inside a particular bin is counted from their positions. Initially, the binary mixture starts from a completely mixed state from the right side of the device as can be seen from the spatial distribution corresponding to time 1 s in Figure 72. As time
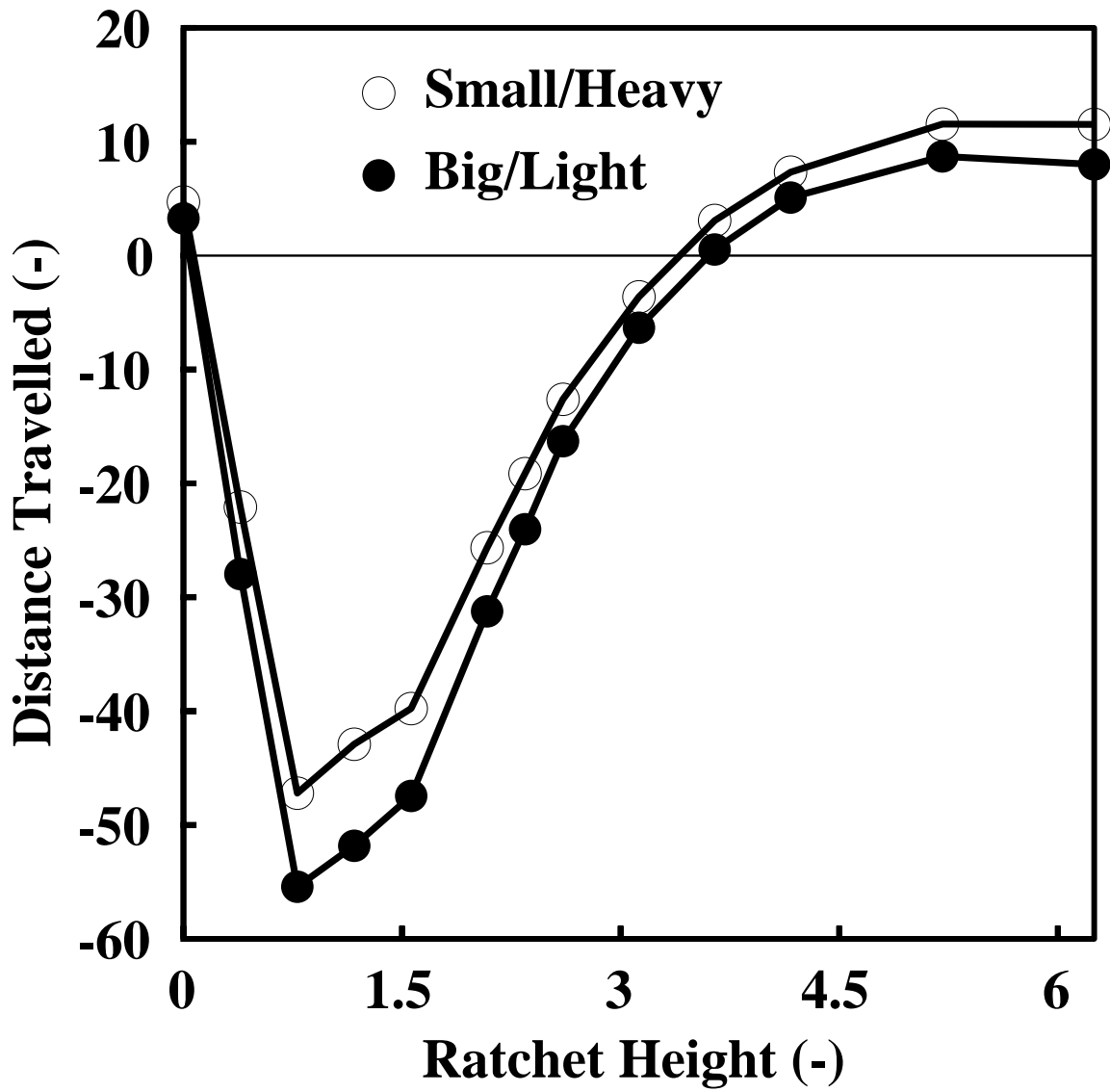
Figure 70: Effect of ratchet height on the distance travelled (separation) by particles for a combined size and density case. Size ratio of big and small particles is 2:1 and density ratio is 1:2 (bigger particles are lighter and vice versa).
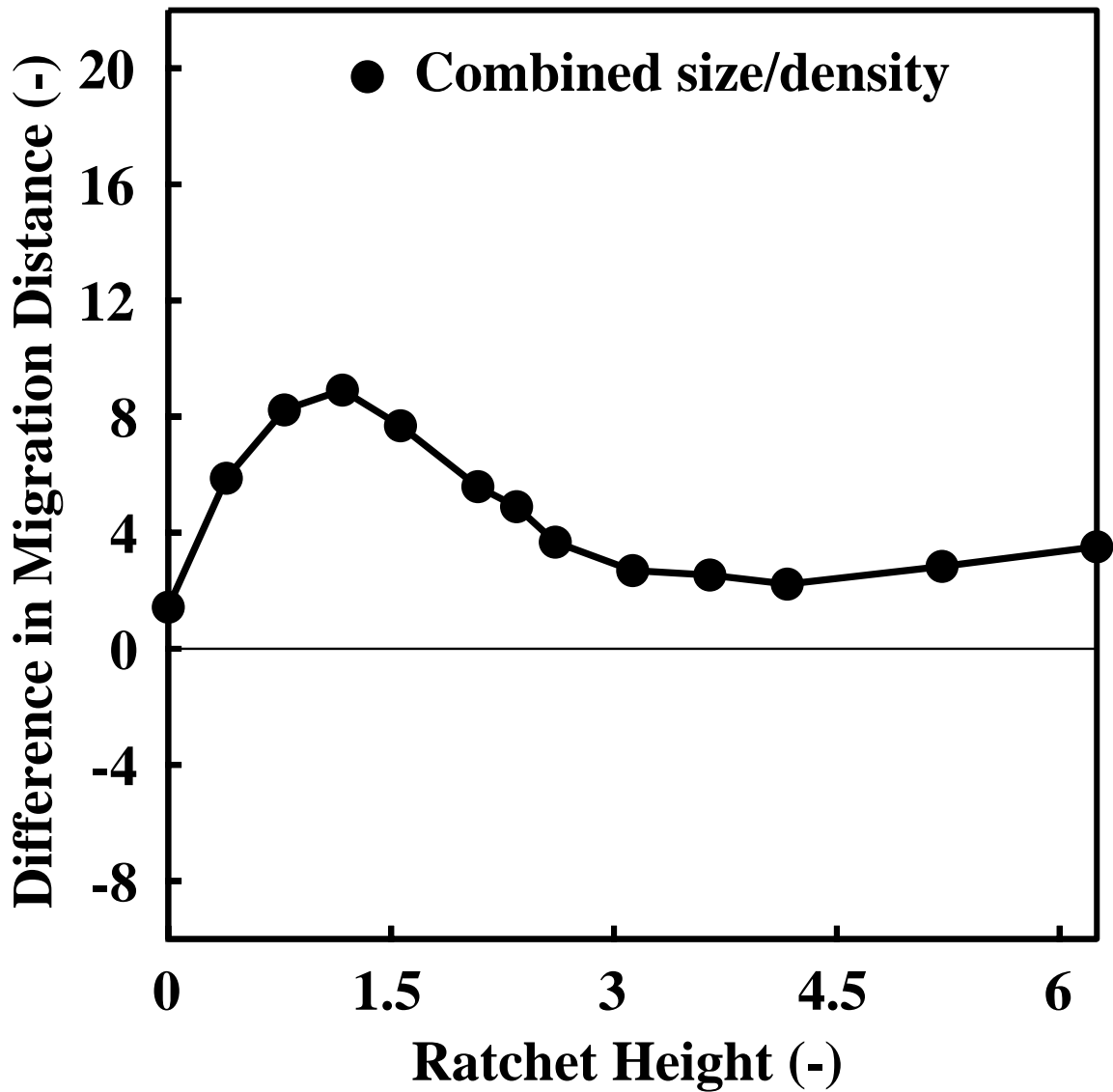
Figure 71: Data from Figure 70 have been plotted to show the effect of ratchet height on the differences in migration distances (separation) for a combined size and density case. The differences in migration distances correspond to (small/heavy - big/light).
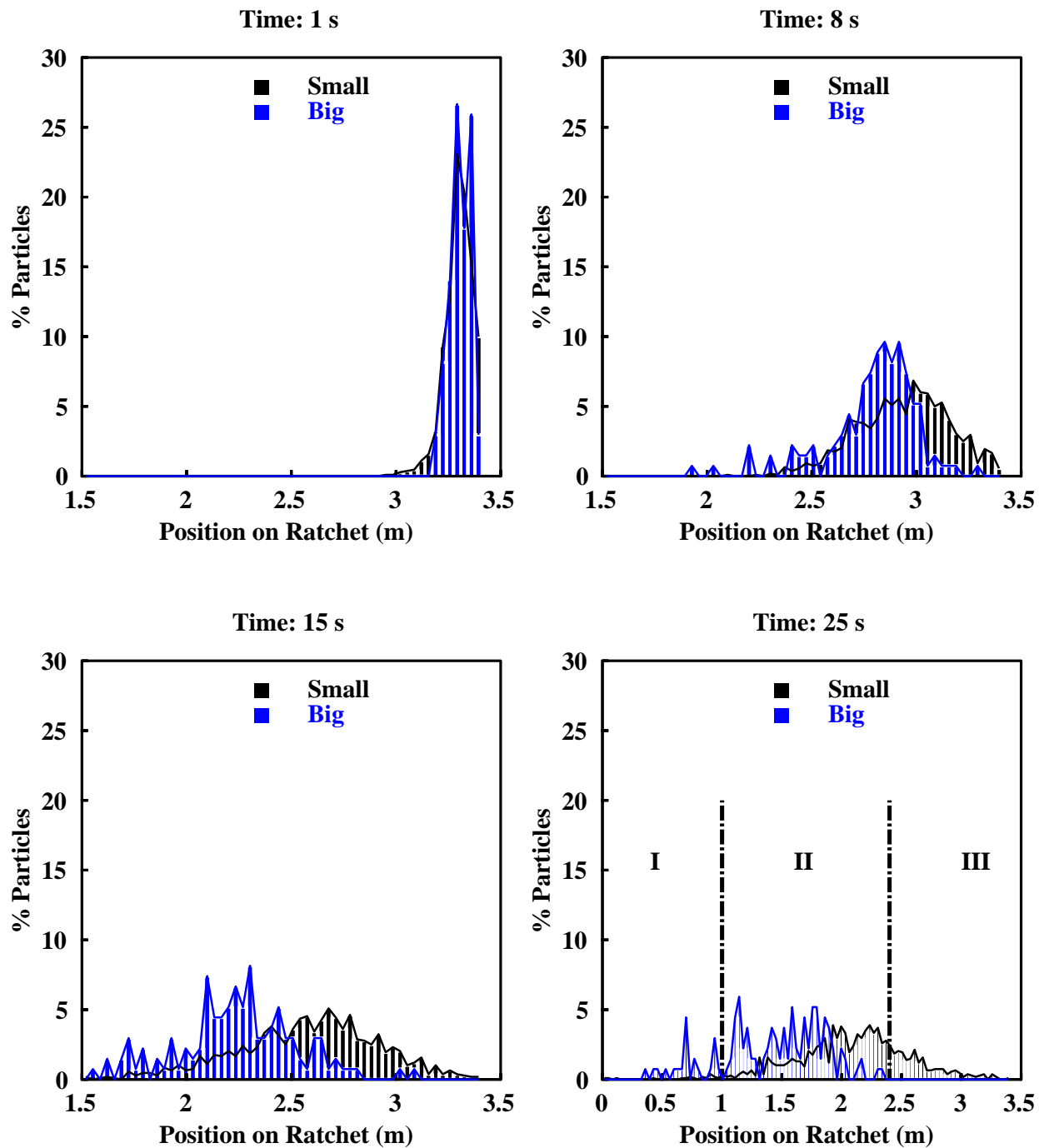
Figure 72: Spatial distribution of particles at different time instances showing progress of separation in the ratchet device for a size ratio of 1:2. Three distinct particle regions as described in the text have been shown in the bottom-right sub-figure.

progresses, we can observe that all types of particles travel to the left of the device (negative distance) and their distributions tend to broaden and move apart from each other. The larger particles travel faster than the smaller ones, and at larger times, we can notice three distinct particle regions – a leading small region consisting only of larger particles (region I in the bottom-right sub-figure of Figure 72), an extended overlapping region of mixtures (region II), and a trailing small region comprising only smaller particles (region III). Therefore, it is possible to get some degree of separation in this device for a given design and operating parameters. This distribution plot complements Figure 68 and confirms the hypothesis that a ratchet can produce a directed current of particles in the direction perpendicular to the energy input. Figure 73 shows similar progress of separation for a 2:1 density ratio case with $h/d \approx 1.17$. However, as noted earlier, the separation quality is not as good as a 2:1 size ratio case (comparing equivalent time instances).

Figure 74 shows the spatial distribution of both kinds of particles for a size ratio of 2:1 but with $h/d \approx 3.53$. As described earlier, the binary mixture is placed symmetrically at the middle of the device. As suggested by Figure 68, it is expected that there will be an opposing flux of materials through the device for this parameter combination – however, as is evident from the graph, it is inconclusive to suggest such outcome in the given time frame (1–12 s).

From all of the above figures, we can clearly observe that a ratchet device has a considerable intermediate mixture region compared to regions with pure materials, and hence, the separation quality is expected to be of inferior quality when compared to the collisional separation device described in Section 5.1, where the pure particle regions covered a relatively larger area. However, many ratchet devices can be made to work in series (resulting in more migration time t), and the separation quality can be progressively enhanced due to the fact that the extent of separation (E_s) is proportional to the migration time (t) (refer to Equation 5.3).
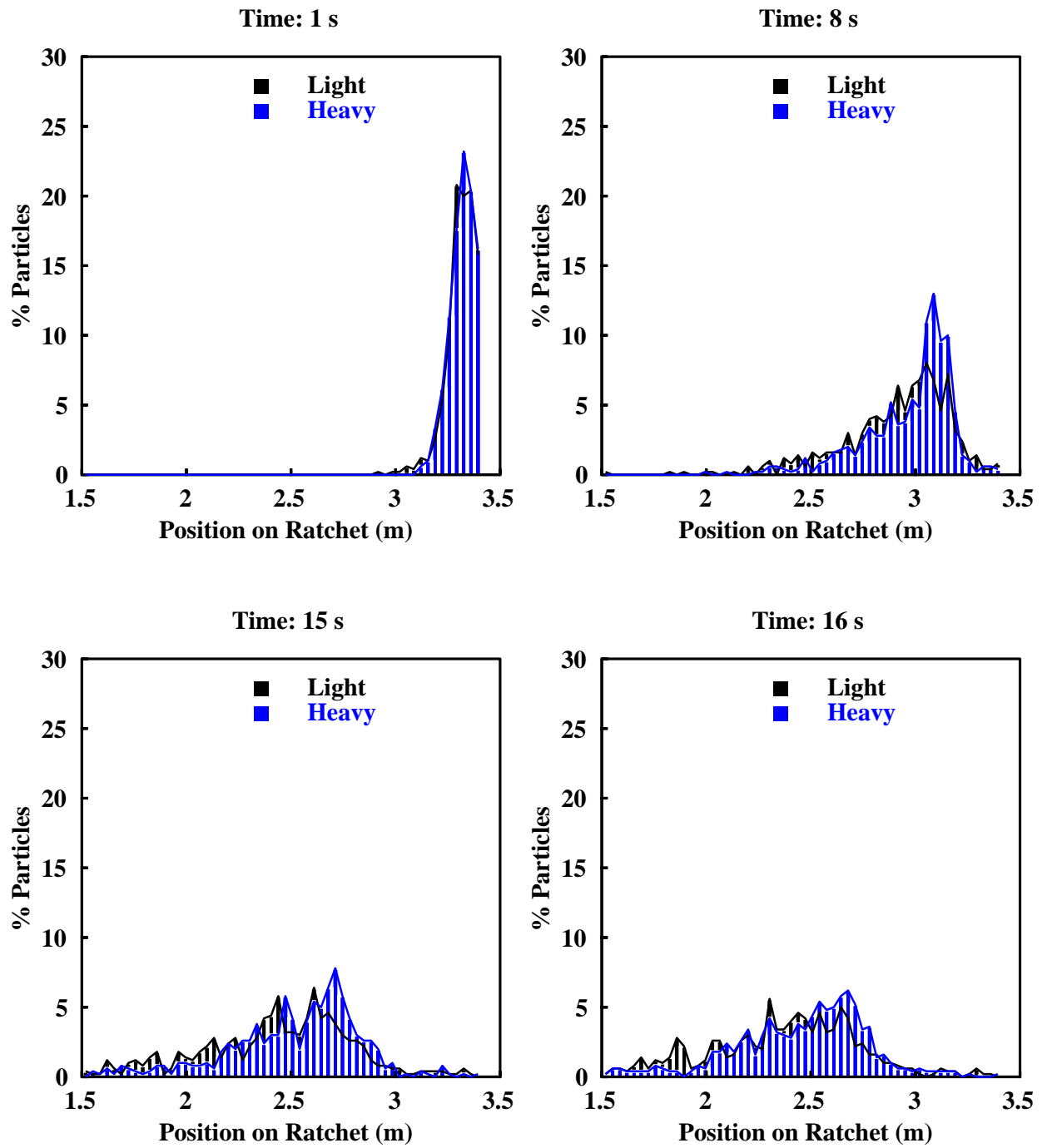
Figure 73: Spatial distribution of particles at different time instances showing progress of separation in the ratchet device with a density ratio of 2:1.
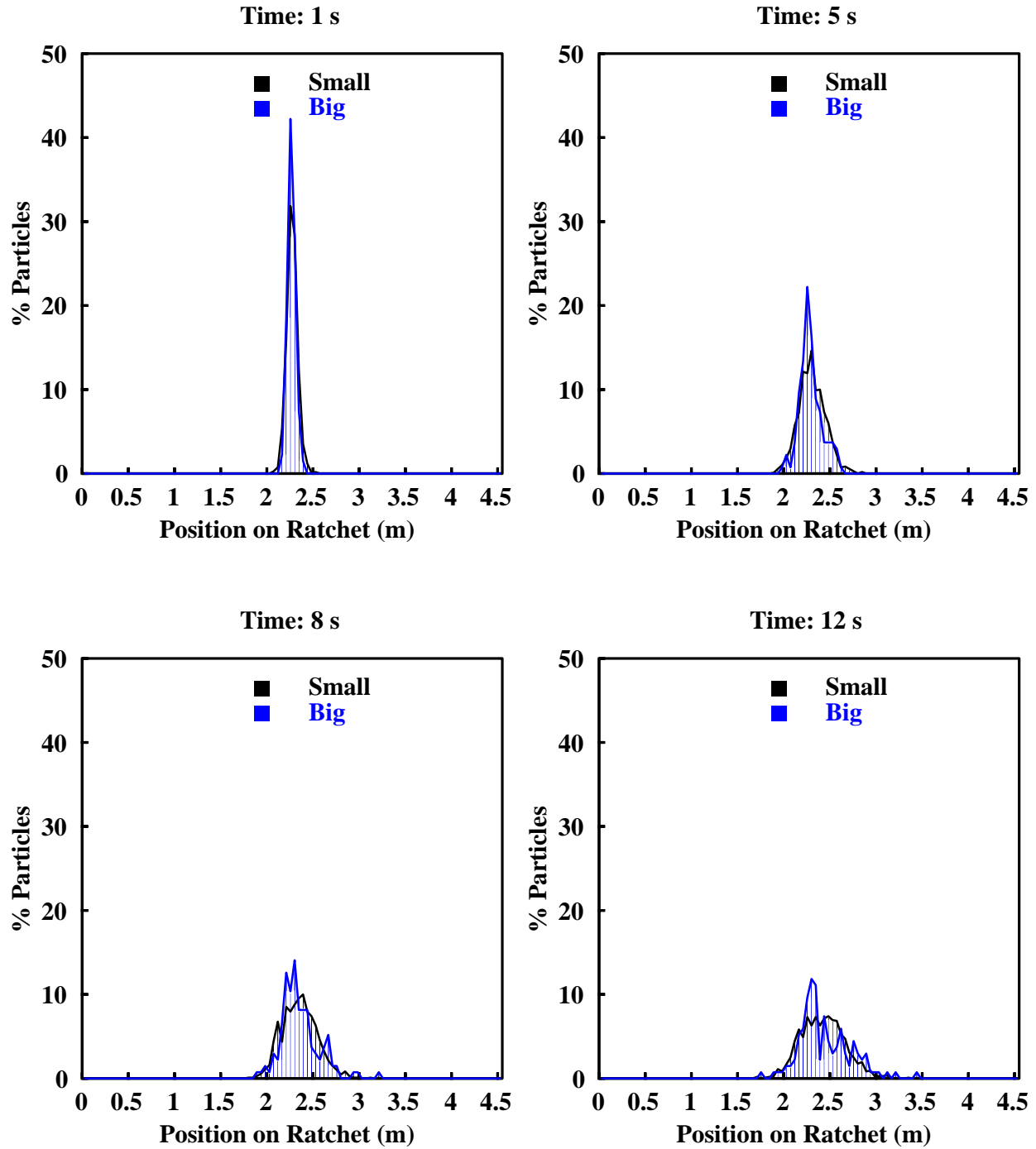
Figure 74: Spatial distribution of particles (size ratio 2:1) at different time instances showing progress of separation in a ratchet device with $h/d \approx 3.53$, which is expected to give rise to opposing flux of materials.

146

6.0   SUMMARY AND OUTLOOK

In this chapter, a brief summary of the major contributions of the current work is presented along with an outlook on future extensions. A short discussion on the many challenges to link the fundamental physics of particle flow and the current industrial needs is also included here.

6.1   CONTROLLING SEGREGATION IN TUMBLERS

Segregation in granular materials has been studied for a long time but its theoretical understanding even in the most simple cases is yet not complete. When particles differ in almost any mechanical property, a small agitation leads to flow induced segregation. Controlling or minimizing segregation continues to be a complicated problem. Industries use empirical designs based on the past experiences, which often have no theoretical basis. A literature search yields no previous studies dealing with issues involving novel baffle shapes and their placements in a solids mixer and how their designs will affect mixing and segregation. In this work, for the first time, we use experiments and simulations to study the effects of various design parameters, such as baffle shapes and placement, on the mixing of binary mixtures with different sizes or densities. It has been demonstrated that segregation in a rotating drum can be dramatically reduced by introducing periodic flow inversions within the drum by employing novel baffle designs. Both experimental observations and simulation results agree qualitatively and the simulation tool is further used to test our hypothesis, which states that the time modulation in the shearing layer is the key to thwarting segregation.

Segregation can be minimized if the particle flow is inverted at a rate above a critical forcing frequency. For a rotating drum, this translates to the probability distribution of the number of times a particle passes through the flowing layer per rotation of the drum. A broader probability distribution signifies that the orientation of a particle will become essentially uncorrelated to its previous orientation. Therefore, the baffle designs that produce a broader distribution are expected to yield better mixing results. It has been shown that the peak height of the layer pass distribution correlates strongly with the experimentally obtained intensity of segregation. This observation actually demonstrates that the hypothesis of flow inversion can be used for designing new baffles and examining the effectiveness of a new design. Moreover, the characterization tool (layer-pass simulations) that is developed to test the hypothesis can easily be used to examine different baffle configurations and predict their performances.

As noted by Khakhar et al. [223], the time is ripe to exploit the knowledge gained about surface flows and to apply it to design and scale-up solids processing devices. In this spirit, the current work has attempted to test the hypothesis regarding a critical forcing frequency (flow inversion) to mitigate segregation. The hypothesis has been embodied in a mathematical form by utilizing the existing knowledge (continuum-derived) developed by other researchers, and is used as an elimination tool to select optimum designs of tumbler mixers from a host of promising baffle designs.

6.2   SEGREGATION IN A CHUTE FLOW

Granular materials are omnipresent. Many man-made or natural processes involve flow of granular materials. Industrial applications typically involve handling and processing of a large amount of multi-sized granular materials, which may have different shapes and densities. These processes require many solids handling devices like hopper, chute, etc. In this work, a simple chute flow consisting of both mono-sized and polydisperse spherical granular particles is analyzed. Effects of various parameters like charge amount, particle size, falling height and chute angle are studied systematically to examine how the mass fraction distri-

bution in the trajectories are affected by these parameters. A contact force parameter of the DEM model has been adjusted in order to obtain reliable results and account for the deviation from experimental observations. The tuned model is then used to find the critical chute length for segregation as per our hypothesis regarding a critical forcing frequency. Both a finite length chute and a periodic chute are used to test the hypothesis beyond doubt.

In the present investigation, we are only concerned about the mass fraction distribution of particles in the bins placed below the chute. However, there are many applications where the distribution of porosity or voidage of the bed is of utmost importance (like in a blast furnace or in many fluidized beds where a gas has to pass through the particle bed). Therefore, the present work can be extended to calculate the porosity or voidage of the particle bed after deposition and the effects of many parameters on that. With regards to the significance and practical applications of the results described in this part of the work, it is sufficient to say that a reliable model can be used to design and probe any granular flow system employing a chute for transfer of materials. And, there are plenty of industrial applications where these investigations would help in improving productivity and product quality.

6.3 RATE-BASED SEPARATION IN COLLISIONAL FLOWS

While segregation is often an undesired effect, sometimes separating the components of a particle mixture is the ultimate goal in many industrial processes. Rate-based separation processes hold promise as both green and less energy intensive, when compared to conventional particle separations technologies such as vibrating screens or flotation methods.

It has been demonstrated, for the first time, that a device inducing diffusive motion to the constituents of a mixture by way of gravity-driven collisional flow through an array of obstacles can be used to separate particles effectively, without any external energy input. The effects of various design and operating parameters on the extent or quality of separation are investigated by means of a simple single particle model (based on a random walk theory) along with experiments and DEM simulations. It has been found that the ratio of the particle size to the available gap between two obstacles (called effective diameter or d_{eff}) is a key

parameter controlling the separation. This parameter is also a measure of the probability of a particle colliding with a peg. Smaller particles are found to be faster (lower d_{eff}, and hence, relatively fewer number of collisions) than the larger ones, in both simulations and experiments. Also, the extent of separation deteriorates as the loading of the device is increased due to relatively high number of dissipative collisions for all types of particles, which effectively reduce their relative mobility (in the extreme case, jamming occurs). Realization of a complete theoretical model to predict the length (L) or time (t) required for obtaining a desired extent of separation in a particular device with a given design and operating parameter is still elusive and could be the topic of future research.

In another example of a novel separation technique, it has been demonstrated that a ratchet mechanism employing a vibrating saw-toothed base can be used to induce different mobility for different types of particles. A directed current of particle is produced perpendicular to the energy input. In contrast to the collisional separation device considered in Section 5.1 where smaller particles travel faster, the larger or lighter particles in general move faster in a ratchet device. Therefore, it is shown that the final goal of separation can be achieved by means of different opposing mechanisms or exploiting phenomena which might seem to be at odds when compared in a general sense. It has been demonstrated and confirmed in this study that a ratchet can be used to separate particles, but the quality of separation is not as good as a gravity-driven collisional separation device. Also, a complete theoretical or a mathematical description of the process relating different design and operating parameters in the device still remains an open question owing to the complexity of the process, which is characteristic of any system involving granular materials ("complex systems").

A common feature of these two rate-based separation devices is that the extent of separation (E_s) is proportional to the time (t) allowed for migration. Therefore, more migration time can be achieved if the devices can be made to work in series (instead of a single long device), i.e., the output of one device could be directed as the input of another, and by doing so, the separation quality can be progressively enhanced.

6.4 OUTLOOK

Various solids processing industries rely on routine handling of powders and particles for many bulk solids processes such as mixing and separation, press feeding, die filling, tableting, packaging, bin storage, conveying, coating, etc. Solids handling is often the major bottle-neck in the series of steps for making a final product. Practitioners are regularly asked to develop and scale-up processes for making granular products with critical quality parameters that are rooted in a micro-scale of scrutiny. Examples include microscale compositional variance in a multicomponent mixture (like pet food or tablets), the microstructure of products made by an agglomeration process, the mesoscale structural features of a particulate-filled composite, or the effect of die filling on the structure of a pressed piece or tablet. The present work, to some extent, aimed to elucidate the linkages between the fundamental physics of particle flow and the industrial needs as outlined above. Though some progress has been made to understand the segregation process [27], many formidable challenges await solutions in both the fundamental understanding and industrially relevant applications.

Perhaps, the biggest difficulty in solids processing is the issues of scaling. The following question would be of interest for future investigations dealing with granular flows: How do the stress and flow fields scale when the same power ratio or specific energy input has been utilized in a solids processing device? As a future step that is both industrially and scientifically relevant, a combined approach including experimental investigation, simulation and development of theory will always be helpful in searching answers to many elusive questions. The challenges in simulating large scale industrial systems are many. DEM is the gold standard when it comes to direct numerical simulation of particle systems. At present, a million spherical particles can be simulated using DEM on an ordinary workstation. For non-spherical particles, however fewer can be simulated. Industrially relevant realistic systems can easily contain 10^9 particles. Therefore, the direct numerical simulations at the particle level for industrial systems is in the range of current super computers for spherical particles, but this is not cost effective for larger systems or those containing non-spherical particles. Therefore, a logical future research direction would be the application of high performance computing techniques such as general purpose graphics processing units (GPGPUs) (a very

151

recent work in this direction has been performed by Radeke et al., 2010 [83]) along with the development of faster algorithms (especially, the contact detection algorithms, which consume bulk of the computing time) to speed-up calculations and make industrial scale direct numerical simulations possible on readily available hardware (such as desktop computers or workstations). As suggested by Williams et al. [115], the future is towards developing "smart software" that will dynamically load the optimal algorithm for contact detection suitable for the problem at hand.

APPENDIX A

OTHER STUDIES

A.1 SIMULATION OF MESOSCOPIC PHENOMENA

Throughout this dissertation, we have mostly discussed the application of particle dynamics to simulate macroscopic phenomena. Here in this Appendix, we show how another tool – called dissipative particle dynamics or DPD – can be used to tackle problems in the mesoscopic length scale. We briefly review this emerging tool, its merits and demerits and finally discuss one example where an attempt has been made to use this tool in solving a practical problem involving droplets.

A.1.1 Non-spherical Droplet Generation

Let us turn our focus in the discussion of another exciting engineering problem involving particles but at a different length scale: Generation of non-spherical droplets for microfluidic applications. Non-spherical particles, which can be processed from droplets (droplets are used as precursors to the final particles), have a broad range of applications including cosmetics, bio-technology, structural materials and pharmaceuticals [281]. Droplets and particles have the potential to become important tools for drug delivery and biosensing. Microfluidic technology holds tremendous promise [282] as it can perform typical laboratory operations using a fraction of the volume of reagents in significantly less time. Reagents can be tremendously reduced from milliliters and microliters to nanoliters and femtoliters

whereas hours of reaction time could be decreased to mere seconds or less (which is central to the concept of "lab on a chip"). One subcategory of microfluidics is droplet-based microfluidics. Unlike continuous flow systems, droplet-based systems focus on creating discrete volumes (nanoliters or less) with the use of immiscible phases. Droplet-based microfluidics involves the generation and manipulation of discrete droplets. This method produces highly monodisperse droplets in the nanometer to micrometer diameter range, at a very high rate. Due to high surface area to volume ratios at the microscale, heat and mass transfer times and diffusion distances are shorter, facilitating faster reaction times.

Interfacial tension between two immiscible phases naturally favors minimization of surface area and this produces spherical shapes as a sphere has minimum surface area for a given volume. Therefore, non-spherical shape is not a thermodynamically favorable state and hence, the challenges for producing irregular shaped droplet can be easily understood. Non-spherical shape opens up the possibility of having unique properties otherwise impossible to obtain in spherical shape. For example, when converted to non-spherical particles, they can pack more densely than spherical ones [283]. Also, irregularly shaped particles can behave differently from spherical ones under the same hydrodynamic [284], electric, and magnetic conditions (see references in [281]). Since the properties of non-spherical particles are strongly dependent on their shape, methods must be developed to control not only their size, but also shape to obtain reproducible and uniform behavior. Though experimentally it is possible to produce non-spherical droplets and particles using droplet-based microfluidic [282] systems, it remains difficult to produce large quantities of monodisperse non-spherical particles of tunable geometry and adjustable properties. A literature search revealed no previous computational work on the tuning of the shape of a droplet though experimental work on stable non-spherical shape using interfacial particle jamming has been reported [285–287]. Therefore, in this work, we seek to address the challenges of non-spherical droplet generation from a computational perspective. The broad objective of this part of the work is to explore different ideas that would enable us to tune the shape of a spherical droplet by using a computational tool called dissipative particle dynamics (DPD). The background and details of DPD follows in the next sub-section.

154

A.1.2 Methodology: Dissipative Particle Dynamics

Dissipative particle dynamics (DPD) is an emerging technique to explore the mesoscopic length scale (few μm). First developed by Hoogerbrugge and Koelman [288], this technique seeks to bridge the gap between two length scales – microscopic (few nm) and mesoscopic. DPD is a coarse graining method based on molecular dynamics (MD) [289] which can take care of hydrodynamic behavior of complex fluids like colloids, gels, polymer melts, etc. This method is based on the simulation of soft spheres, whose motion is governed by certain collision rules [290], which is discussed below. In structure, a DPD algorithm looks much like DEM or MD where particles move according to Newton's laws. However, each DPD particle or soft sphere represents mesoscopic description of the fluid, and does not represent individual atoms or molecules, but loosely corresponds to "lumps" of fluids or clusters of molecules called a "bead". Therefore, unlike conventional molecular dynamics (MD) where we need to know the detailed interaction between each atoms or molecules, a coarse graining is applied in DPD and no detailed molecular level information is needed. Coarse graining results in larger time and length scales (higher than atomistic scales) and permits the use of larger time steps than MD simulations. Therefore, complex physical systems with hydrodynamic behavior (complex fluids) can easily be simulated with a reasonable computational cost. Imagine simulating a very tiny volume of a complex fluid by considering each and every atom in the domain (as in MD, for example, one mole of something would require more than 6×10^{23} molecules) vis-à-vis using coarse graining where each bead is a collection of many molecules (a rough calculation using the data from Gao et al. [291] shows only 98,304 beads will be required in DPD to simulate the same volume of fluid versus about half a million molecules if it were simulated by classical MD).

The transport equations for a simple DPD particle i are shown in Equation A.1.

$$\frac{d\mathbf{r}_i}{dt} = \mathbf{v}_i \;, \quad \frac{d\mathbf{v}_i}{dt} = \sum_{j \neq i} (\mathbf{F^C}_{ij} + \mathbf{F^D}_{ij} + \mathbf{F^R}_{ij}) \tag{A.1}$$

where

$$
\mathbf{F^C} =
\begin{cases}
a_{ij}(1 - r_{ij})\hat{\mathbf{r}}_{ij} & for\ r_{ij} < r_c \\
0 & for\ r_{ij} \geq r_c
\end{cases}
\tag{A.2}
$$

$$
\mathbf{F^D} = -\gamma w^D(r_{ij})(\hat{\mathbf{r}}_{ij} \cdot \mathbf{v}_{ij})\hat{\mathbf{r}}_{ij}
\tag{A.3}
$$

$$
\mathbf{F^R} = \sigma w^R(r_{ij})\zeta_{ij}\Delta t^{-1/2}\hat{\mathbf{r}}_{ij}
\tag{A.4}
$$

In the equations above, $\mathbf{r}$ and $\mathbf{v}$ are position and velocity vectors; a_{ij} is the maximum repulsion between particles within a pre-defined cutoff radius, r_c; ζ_{ij} is a random number with zero mean and unit variance chosen independently for each pair of interacting particles i and j, and at each time-step Δt. The terms $\mathbf{F^C}$, $\mathbf{F^D}$ and $\mathbf{F^R}$ respectively represent:

- **Conservative Force**: which is a soft repulsion between particles that enforces elastic collisions.
- **Dissipative Force**: which reduces the relative velocity between two particles, simulating viscous effects.
- **Random Force**: which is the result of all thermal molecular motion within particles i and j, adding heat to the system.

These forces also act along the line of centers and conserve linear and angular momentum. The coefficients γ and σ characterize the magnitude of the dissipative and random forces, which vanish for $r > r_c$. Both w^D and w^R are weighting functions which satisfy the following condition [292]:

$$
w^D(r) = [w^R(r)]^2, \quad \gamma = \frac{\sigma^2}{2k_B T}
\tag{A.5}
$$

Equation A.5 ensures a balance of kinetic energy within the DPD model based on the Fluctuation-Dissipation Theorem, where k_B is the Boltzmann constant and T is the temperature of the system. This theorem states that a perturbation within a system at the molecular level dissipates as the system returns to equilibrium [293–295]. In essence, $\mathbf{F^D}$ and $\mathbf{F^R}$ serve as a thermostat in order to maintain the temperature, ensuring the system is not artificially heated.

A.1.3 Boundary Conditions

The manner in which the walls are prescribed in DPD is an unresolved matter in the literature. Wall particles are "frozen" (i.e., of the lowest thermal energy within the system), but the soft repulsion between particles does not prevent actual fluid elements from "penetrating" the wall. In addition, there is the problem of the wall particles decreasing the overall fluid temperature. Various researchers have sought to combat this by analytically solving for effective wall forces [296], increasing the density of particles at the wall [297], or by introducing a random velocity distribution (with fixed mean) for the wall particle [295].

DPD time and length scale calculation has been described by Moeendarbary et al. [298]. These units allow us to model systems with length scales from nanometers to micrometers and overall time scales of up to a few seconds.

A.1.4 Results: Non-spherical Droplet Generation

Since a spherical shape is the most stable configuration for a droplet, we employ a few charged particles ("stabilizers") to perturb the stable spherical state. Equation A.6 shows the repulsive force between a charged particle pair, which in essence, is a Coulombic interaction:

$$\mathbf{F^Q} = \frac{1}{4\pi\varepsilon_0}\frac{q_i q_j}{r^2}\hat{\mathbf{r}}_{ij} \tag{A.6}$$

where ε_0 is the dielectric constant of the medium, q_i and q_j are charges on the particles and r is the separation distance between particles. If both charges have the same sign (like charges) then the product $q_i q_j$ is positive and the direction of the force on q_i is given by $\hat{\mathbf{r}}_{ji}$; the charges repel each other. If the charges have opposite signs then the product $q_i q_j$ is negative and the direction of the force on q_i is given by $-\hat{\mathbf{r}}_{ji}$; the charges attract each other. In a typical simulation, we use three kinds of DPD particles/beads: droplet, solvent and stabilizer particles. The initial configuration is a cluster of droplet particles in a near spherical shape in the matrix of solvent particles. The droplet particles are surrounded by charged stabilizer particles. A typical initial configuration is shown in Figure 75 along with an intermediate stage, which shows that DPD can be used to tune the shape of a spherical droplet.
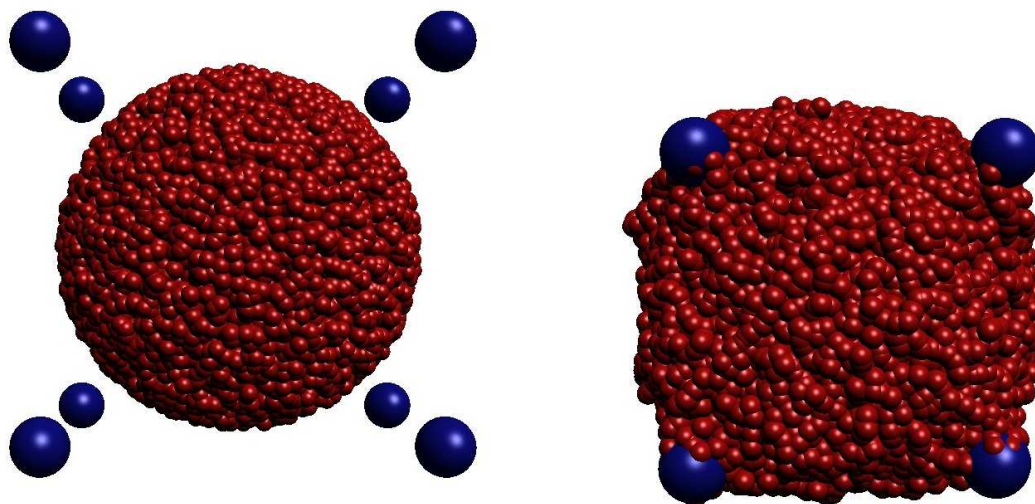
Figure 75: (Left) Initial spherical shape of a DPD droplet consisting of 22,528 particles (red). Eight (8) charged particles (blue) are positioned at the corners of a cube enclosing the spherical droplet. There are 90,112 solvent particles which are not shown here for clarity. (Right) Intermediate stage showing the evolution of the non-spherical shape.

A.1.5   Outlook

In future, the following further studies are proposed to systematically investigate the realization of a non-spherical droplet:

1. **Assessing different initial configurations:** In order to get a droplet in cubic, tetrahedral or bipyramidal shape, one needs to change the orientation and numbers of the stabilizer particles. Therefore, examination of the effects of different initial configurations on the final shape of the droplet is a good starting point.

2. **Exploring the parameters space:** The parameter a_{ij} determines the magnitude of the maximum repulsive force between a pair of DPD particles, i and j. Exploration of the parameters space by changing a_{ij} and the charges q_i on the stabilizer particles would

aid in identifying proper parameters for a desired shape.

3. **Evaluating size effects:** Since the system sizes accessible to simulations are rather small, one can draw conclusions about the behavior of larger real systems by investigating the size effects, i.e., how the system properties will vary with the system size. This can be evaluated by using different volumes of the simulation box.

4. **Evaluating density effects:** The system density ρ (equal to the number of DPD particles per unit volume) determines how many total particles will be in the simulation box. Typically, the density chosen is a free parameter, but since the number of interactions for each particle increases linearly with the density, the required computation time (CPU time) t per time-step and per unit volume increases as ρ^2 [290]. Therefore, for efficiency reason, many workers used a value of $\rho = 3.0$, which is the lowest possible density where the scaling relation for excess pressure in the equation of state still holds good. However, the effect of density on final droplet shape is not clear and this can be a topic of future investigations.

5. **Exploring other ideas:** Using armored particle layers around a droplet to stabilize a non-spherical shape by jamming the interface is a fairly common practice [281, 285–287, 299, 300]. Such techniques can be implemented in the droplet simulation to stabilize the non-spherical shape.

APPENDIX B

NOMENCLATURE

English Symbols

$2S$	center-to-center peg spacing (Ch. 5)
A	a factor equal to ± 1 (Ch. 5)
A_v	amplitude of vibration of ratchet device (Ch. 5)
a	radius of contact spot (Ch. 2)
(a)	asymmetry parameter of ratchet tooth (Ch. 5)
a_{ij}	maximum repulsion between particles i and j (Appendix A)
C	concentration of tracer particle (Ch. 2)
$\langle C \rangle$	mean concentration of tracer particle (Ch. 2)
c	dimensionless collisional viscosity (Ch. 3)
(c)	concentration (Ch. 4)
D	drum diameter (Ch. 3)
(D)	(particle) diffusivity (Ch. 4)
d	particle diameter (Ch. 3)
(d)	diameter of largest particle in a ratchet device (Ch. 5)
$\overline{d}$	particle size ratio (Ch. 3, 4)
d_{eff}	effective diameter of a particle (Ch. 5)
d_p	diameter of a particle (Ch. 5)
dt	time-step (Ch. 2)
E	elastic modulus (Ch. 2)
E^*	effective elastic modulus (Ch. 2)
E_i	elastic modulus of particle i (Ch. 2)
E_s	extent of separation (Ch. 5)

English Symbols

$\hat{e_{ij}}^n$	normal unit vector (Ch. 2)
$\hat{e_{ij}}^t$	tangential unit vector (Ch. 2)
$\mathbf{F^C}_{ij}$	conservative force on particle i due to particle j in DPD (Appendix A)
$\mathbf{F^D}_{ij}$	dissipative force on particle i due to particle j in DPD (Appendix A)
f	number fraction of segregating species (Ch. 3)
(f)	frequency of vibration of ratchet device (Ch. 5)
f_{crit}	critical forcing frequency (Ch. 3, 4)
f_e	effective forcing frequency (Ch. 3)
$\overrightarrow{F_{ij}}$	force on particle i due to particle j (vector) (Ch. 2)
$\overrightarrow{F_{ij}}^n$	normal force on particle i due to particle j (vector) (Ch. 2)
$\overrightarrow{F_{ij}^t}$	tangential force on particle i due to particle j (vector) (Ch. 2)
$\overrightarrow{F_n}$	normal force (vector) (Ch. 2)
$\overrightarrow{F_t}$	tangential force (Ch. 2)
F_{ij}^n	normal force on particle i due to particle j (Ch. 2)
F_{ij}^t	tangential force on particle i due to particle j (Ch. 2)
F_{max}	maximum force (Ch. 2)
F_n	normal force (Ch. 2)
F^Q	Coulombic force (Appendix A)
$\mathbf{F^R}_{ij}$	random force on particle i due to particle j in DPD (Appendix A)
Fr	Froude number (Ch. 3)
F_t	tangential force at particle-particle contact (Ch. 2)
F_{t_o}	old tangential force (Ch. 2)
F_y	yield force (Ch. 2)
G	shear modulus (Ch. 2)
G^*	effective shear modulus (Ch. 2)
G_i	shear modulus of particle i (Ch. 2)
$\overrightarrow{g}$	acceleration due to gravity (vector) (Ch. 2)
g	acceleration due to gravity (Ch. 3)
H	particle bed height in a chute (Ch. 4)
(H)	height of simulation box (Ch. 5)
H_p	vertical center-to-center peg spacing (Ch. 5)
h	ratchet tooth height (Ch. 5)
$h(x,t)$	height of a dynamic sand pile (Ch. 2)
I_p	moment of inertia of a particle (Ch. 2)
J_S	segregation flux (Ch. 4)

English Symbols

K_S	segregation constant, size (Ch. 3, 4)
K_T	segregation constant, density (Ch. 3, 4)
k_B	Boltzmann constant (Appendix A)
k_n	normal force constant (Ch. 2)
k_t	tangential stiffness (Ch. 2)
k_y	plastic stiffness (Ch. 2)
L	effective baffle length (Ch. 3)
(L)	chute length (Ch. 4)
(L)	separation device length or length of simulation box (Ch. 5)
L_{plug}	length of particle plug on chute (Ch. 4)
l	length of the projection of the longer side of ratchet tooth on horizontal (Ch. 5)
M_L	Lacey mixing index (Ch. 2)
M_P	Poole mixing index (Ch. 2)
m_p	mass of a particle (Ch. 2)
N	total number of particles (Ch. 2, 3, 4)
N_c	number of concentration measurement locations (Ch. 2, 3)
N_h	number of particle layers (Ch. 5)
Pe	segregation-based Péclet number (Ch. 4)
p	depth of a ratchet tooth (Ch. 5)
q_i	charge on particle i (Appendix A)
$\bar{R}$	ratio of contact curvature due to plastic deformation and effective radius (Ch. 2)
$\overrightarrow{R}$	radius of particle (vector) (Ch. 2)
R	radius of a particle (Ch. 2)
(R)	drum radius (Ch. 3)
(R)	degree of mixing (Ch. 4)
R^*	effective radius (Ch. 2)
R_1	radius of small particle (Ch. 4)
R_p	contact curvature due to plastic deformation (Ch. 2)
(R_p)	radius of a particle (Ch. 5)
R_{peg}	radius of a peg (Ch. 5)
$R(x,t)$	thickness of rolling layer (Ch. 2)
$\overrightarrow{r_i}$	radius of particle i (vector) (Ch. 2)
r	radius of a particle (Ch. 2)
(r)	separation distance between particles (Appendix A)
$\mathbf{r}_i$	position vector of a DPD particle (Appendix A)
$\mathbf{r}_{ij}$	vector connecting centers of two DPD particles i and j (Appendix A)

English Symbols

$\overrightarrow{r_j}$	radius of particle j (vector) (Ch. 2)
S_{ij}	separation between centers of particle i and particle j (Ch. 2)
T	total contact detection time (Ch. 2)
(T)	granular temperature (Ch. 4)
(T)	temperature of a DPD system (Appendix A)
$\bar{t}$	dimensionless time (Ch. 4)
t	time allowed for migration of particles (Ch. 5)
t_c	duration of collision (Ch. 2)
t_D	diffusion time (Ch. 4)
t_{entry}	particle entry time on chute (Ch. 4)
t_{exit}	particle exit time from chute (Ch. 4)
t_S	characteristic segregation time (Ch. 3, 4)
U_{avg}	average stream-wise flow velocity of particles in a chute (Ch. 4)
u	velocity of particle (Ch. 4)
$\langle V_{big} \rangle$	average longitudinal velocity of big particles (Ch. 5)
$\langle V_{small} \rangle$	average longitudinal velocity of small particles (Ch. 5)
$\overrightarrow{v_i'}$	velocity of particle i (vector) (Ch. 2)
$\overrightarrow{v_j'}$	velocity of particle j (vector) (Ch. 2)
$\overrightarrow{v_p}$	particle velocity (vector) (Ch. 2)
$\mathbf{v}_i$	velocity vector of a DPD particle (Appendix A)
v_S	segregation velocity (Ch. 3)
v_t	tangential velocity (Ch. 2)
W	width or depth of simulation box (Ch. 5)
W_i	full width at half max (FWHM) for distribution of particle type i (Ch. 4)
w	ratchet tooth width (Ch. 5)
w^D	weighting function for dissipative force in DPD (Appendix A)
w^R	weighting function for random force in DPD (Appendix A)
$\bar{X}_c$	scaled difference of particle mass centers on chute (Ch. 4)
X_c	centroid of particle mass on chute (Ch. 4)
$\dot{x}_t$	velocity at time t (Ch. 2)
x_t	position at time t (Ch. 2)
z_p	z coordinate of a particle (Ch. 5)
z_{peg}	z coordinate of the center of a peg (Ch. 5)

Greek Symbols

α	computational overlap between contacting particles (Ch. 2)
(α)	a fitting parameter (Ch. 4)
$\dot{\alpha}$	relative normal velocity of particles in contact (Ch. 2)
α_{max}	maximum deformation (Ch. 2)
α_o	a constant in time-step equation (Ch. 2)
α_y	deformation at yield point (Ch. 2)
β	a fitting parameter (Ch. 4)
β_m	dynamic angle of repose of granular materials (Ch. 3)
β_s	angle of repose of granular materials (Ch. 3)
Γ	dimensionless acceleration of ratchet device (Ch. 5)
γ	magnitude of dissipative force in DPD (Appendix A)
$\dot{\gamma}$	shear rate (Ch. 4)
γ_n	damping parameter (Ch. 2)
$\dot{\gamma}_o$	shear rate at midpoint of layer in a tumbler (Ch. 3)
Δs	tangential displacement (Ch. 2)
Δt	time-step (Ch. 2)
δ_o	maximum shear layer thickness (Ch. 3)
ε_0	dielectric constant (Appendix A)
ζ_{ij}	a random number with zero mean and unit variance (Appendix A)
λ	wave speed (Ch. 2)
ν	Poisson ratio (Ch. 2)
(ν)	solid volume fraction (Ch. 4)
ν_i	Poisson ratio for particle i (Ch. 2)
ξ	a fitting parameter (Ch. 3)
ρ	density (Ch. 2)
σ	standard deviation of the composition of a mixture (Ch. 2)
σ_{MIX}	standard deviation of the composition of a completely mixed mixture (Ch. 2)
σ_{SEG}	standard deviation of the composition of a completely segregated mixture (Ch. 2)
σ_y	yield stress (Ch. 2)
τ_{mean}	mean residence time of particle in layer (Ch. 3)
ϕ_i	concentration of species i (Ch. 4)
ϕ_t	total solids volume fraction (Ch. 4)
ω	drum rotation rate (Ch. 3)
$\vec{\omega_p}$	angular velocity of a particle (vector) (Ch. 2)

Abbreviations

AVCHD	advanced video codec high definition (Ch. 5)
BCRE	Bouchaud, Cates, Ravi & Edwards (model) (Ch. 2)
BdG	Boutreux & de Gennes (model) (Ch. 2)
CAD	computer aided design (Ch. 2)
CCD	charge-coupled device (Ch. 5)
CDF	cumulative distribution function (Ch. 4)
CPU	central processing unit (Ch. 2)
DEM	discrete element method (Ch. 1-6)
DNA	deoxyribonucleic acid (Ch. 5)
DPD	dissipative particle dynamics (Appendix A)
DV	digital video (Ch. 5)
FWHM	full width at half max (Ch. 4)
GNU	GNU's not Unix (Ch. 4)
GPGPU (GPU)	general purpose graphics processing units (Ch. 2, 6)
HPC	high performance computing (Ch. 2, 6)
HSI	hue-saturation-intensity (Ch. 5)
IS	intensity of segregation (Ch. 2, 3, 4)
MC	Monte Carlo (simulation) (Ch. 4)
MD	molecular dynamics (Ch. 2, Appendix A)
NBS	no binary search (Ch. 2)
OOP	object-oriented programming (Ch. 2)
PD	particle dynamics (Ch. 1)
PMMA	polymethylmethacrylate (Ch. 4)
RGB	red-green-blue (Ch. 5)
RPM	revolutions per minute (Ch. 3)
RSD	relative standard deviation (Ch. 2, 4)

Subscripts

1	small or segregating species
avg	average
B	Boltzmann
big	big
c	collision or centroid or cell
$crit$	critical
D	diffusion
e	effective
eff	effective
$entry$	entry
$exit$	exit
i	particle i
ij	on particle i due to particle j
j	particle j
L	Lacey
max	maximum
n	normal
o	old
P	Poole
p	particle
peg	peg
$plug$	plug
S	segregation or size
s	separation
$small$	small
T	density
t	tangential or at time t
y	yield

Superscripts

$\mathbf{C}$	conservative
$D, \mathbf{D}$	dissipative
n	normal
Q	Coulombic
$R, \mathbf{R}$	random
t	tangential

BIBLIOGRAPHY

[1] Isabel Margarita Figueroa Amenabar. *Exploring analogies between granular materials and fluids.* PhD thesis, University of Pittsburgh, 2009.

[2] P. A. Cundall and O. D. L. Strack. A discrete numerical model for granular assemblies. *Géotechnique*, 29:47–65, 1979.

[3] A. Munjiza and K. R. F. Andrews. NBS contact detection algorithm for bodies of similar size. *International Journal for Numerical Methods in Engineering*, 43(1):131–149, 1998.

[4] Watson L. Vargas-Escobar. *Discrete Modeling of Heat Conduction in Granular Media.* PhD thesis, University of Pittsburgh, Pittsburgh, 2002.

[5] http://www.mgm.ms.unimelb.edu.au/about.php, last accessed 4th September, 2011.

[6] B. J. Ennis, J. Green, and R. Davies. The legacy of neglect in the US. *Chemical Engineering Progress*, 90(4):32–43, 1997.

[7] R. M. Nedderman. *Statics and Kinematics of Granular Materials.* Cambridge University Press, 1992.

[8] F. J. Muzzio, C. L. Goodridge, A. Alexander, P. Arratia, H. Yang, O. Sudah, and G. Mergen. Sampling and characterization of pharmaceutical powders and granular blends. *International Journal of Pharmaceutics*, 250:51–64, 2003.

[9] P. P. Thomas and Y. B. G. Varma. Fluidised bed frying of granular food materials. *Powder Technology*, 69:213–222, 1992.

[10] Amit Chatterjee, A. Sathe, M. Srivastava, and P. Mukhopadhyay. Flow of materials in rotary kilns used for sponge iron manufacture: Part I. Effect of some operational variables. *Metallurgical and Materials Transactions B*, 14(3):375–381, 1983.

[11] Dennis R. Van Puyvelde. Simulating the mixing and segregation of solids in the transverse section of a rotating kiln. *Powder Technology*, 164:1–12, 2005.

[12] S Pirard, G Lumay, N Vandewalle, and J Pirard. Motion of carbon nanotubes in a rotating drum: The dynamic angle of repose and a bed behavior diagram. *Chemical Engineering Journal*, 146(1):143–147, 2009.

[13] R. L. Brown. The fundamental principles of segregation. *Inst. Fuel*, 13:15–19, October 1939.

[14] J. C. Williams. The segregation of particulate materials. *Powder Technol.*, 15:245–251, 1976.

[15] T. Mullin. Mixing and de-mixing. *Science*, 295:1851, 2002.

[16] J.M. Ottino and D.V. Khakhar. Mixing and segregation of granular materials. *Ann. Rev. Fluid Mech.*, 32:55–91, 2000.

[17] S.L. Conway, T. Shinbrot, and B.J. Glasser. A taylor vortex analogy in granular flows. *Nature*, 431:433–437, 2004.

[18] K. M. Hill, D. V. Khakhar, J. F. Gilchrist, J. J. McCarthy, and J. M. Ottino. Segregation-driven organization in chaotic granular flows. *PNAS*, 96:11701–11706, 1999.

[19] Hernan A. Makse, S. Havlin, P. R. King, and H. E. Stanley. Spontaneous stratification in granular mixtures. *Nature*, 386:379–381, 1997.

[20] O. Pouliquen, J. Delour, and S. B. Savage. Fingering in granular flows. *Nature*, 386:816–817, 1997.

[21] D. V. Khakhar, J. J. McCarthy, and J. M. Ottino. Radial segregation of granular mixtures in rotating cylinders. *Phys. Fluids*, 9:3600–3614, 1997.

[22] J. B. Knight, H. M. Jaeger, and S. R. Nagel. Vibration-induced size separation in granular media: The convection connection. *Phys. Rev. Lett.*, 70:3728–3730, 1993.

[23] N. Burtally, P. J. King, and M. R. Swift. Spontaneous air-driven separation in vertically vibrated fine granular mixtures. *Science*, 295:1877–1879, 2002.

[24] J. M. Ottino. *The kinematics of mixing: stretching, chaos, and transport.* Cambridge Univeristy Press, New York, 1989.

[25] P. Tang and V. M. Puri. Methods for minimizing segregation: A review. *Particulate Science and Technology*, 22:321–337, 2004.

[26] H. M. Jaeger, S. R. Nagel, and R. P. Behringer. Granular solids, liquids and gases. *Rev. Mod. Phys.*, 68:1259–1273, 1996.

[27] J. M. Ottino and D. V. Khakhar. Fundamental research in heaping, mixing, and segregation of granular materials: challenges and perspectives. *Powder Technology*, 121:117–122, 2001.

[28] J. Bridgwater. Fundamental powder mixing mechanisms. *Powder Technology*, 15:215–231, 1976.

[29] M. B. Donald and B. Roseman. Mixing and de-mixing of solid particles: Part I. mechanisms in a horizontal drum mixer. *Brit. Chem. Eng.*, 7:749 – 752, 1962.

[30] D. V. Khakhar, J. J. McCarthy, and J. M. Ottino. Mixing and segregation of granular materials in chute flows. *Chaos*, 9:594–610, 1999.

[31] Deliang Shi, Adetola A. Abatan, Watson L. Vargas, and J. J. McCarthy. Eliminating segregation in free-surface flows of particles. *Physical Review Letters*, 99:148001, 2007.

[32] M. Kwapinska, G. Saage, and E. Tsotsas. Continous versus discrete modelling of heat transfer to agitated beds. *Powder Technology*, 181:331–342, 2008.

[33] B. Chaudhuri, F. J. Muzzio, and M. S. Tomassone. Modeling of heat transfer in granular flow in rotating vessels. *Chemical Engineering Science*, 61:6348–6360, 2006.

[34] W. L. Vargas and J. J. McCarthy. Heat conduction in granular materials. *AIChE Journal*, 47:1052–1059, 2001.

[35] D. K. Kafui and C. Thornton. Fully-3D DEM simulation of fluidised bed spray granulation using an exploratory surface energy-based spray zone concept. *Powder Technol.*, 184(2):177 – 188, May 2008.

[36] Julio M. Ottino. The art of mixing with an admixture of art: Fluids, solids, and visual imagination. *Physics of Fluids*, 22(2):021301+, 2010.

[37] Heinrich Jaeger, Sidney Nagel, and Robert Behringer. The physics of granular materials. *Physics Today*, 49(4):32–38, 1996.

[38] P. G. de Gennes. Granular matter: a tentative view. *Rev. Mod. Phys.*, 71:S374–S382, 1999.

[39] S. B. Savage and C. K. K. Lun. Particle size segregation in inclined chute flow of cohesionless granular solids. *J. Fluid Mech.*, 189:311–335, 1988.

[40] N. Standish. *Principles in burdening and bell-less charging.* Nimaroo Publishers,, Wollongong, Australia, 1st edition, 1979.

[41] J. Li, A. B. Yu, J. Bridgwater, and S. L. Rough. Spontaneous inter-particle percolation: A kinematic simulation study. *Powder Technology*, 203(2):397 – 403, January 2010.

[42] S. R. De Silva, A. Dyroy, and G. G. Enstad. Segregation mechanism and their quantification using segregation testers. In A. D. Rosato and D. L. Blackmore, editors, *Segregation in Granular Flows*, IUTAM Symposium Series, pages 11–29. Kluwer Academic Press, 2000.

[43] J. C. Williams. The segregation of powders and granular materials. *Fuel Soc. J.*, 14:29–35, 1963.

[44] J. C. Williams and M. I. Khan. The mixing and segregation of particulate solids of different particle size. *Chem. Eng.*, 269:19–25, 1973.

[45] H. Matthée. Segregation phenomena relating to bunkering of bulk materials: Theoretical considerations and experimental investigations. *Powder Technology*, 1(5):265–271, February 1968.

[46] Tatsuo Tanaka. Segregation models of solid mixtures composed of different densities and particle sizes. *Industrial & Engineering Chemistry Process Design and Development*, 10(3):332–340, 1971.

[47] J. Masliyah and J. Bridgwater. Particle percolation: A numerical study. *Trans. Inst. Chem. Engrs.*, 52:31–52, 1974.

[48] J. Bridgwater, M. H. Cooke, and A. M. Scott. Interparticle percolation: equipment development and mean percolation velocities. *Trans. Inst. Chem. Eng.*, 56:157, 1978.

[49] J. A. Drahun and J. Bridgwater. The mechanisms of free surface segregation. *Powder Technology*, 36(1):39 – 53, 1983.

[50] Hernan Makse, Shlomo Havlin, Peter King, and Eugene Stanley. Spontaneous stratification in granular mixtures. *Nature*, 386(6623):379–382, 1997.

[51] Y. Kajiwara, T. Inada, and T. Tanaka. Two dimensional analysis on the formation process of burden distribution at blast furnace top. *Trans. ISIJ*, 28:916, 1988.

[52] T. Tanaka, Y. Kajiwara, T. Inada, and C. Yamagata. Flow dynamics of granular materials in a blast furnace. In *Ironmaking Conference Proceedings*, page 237, 1988.

[53] T. Inada, Y. Kajiwara, and T. Tanaka. A mathematical model for particle size distribution in bell-type charging at blast furnace top. *ISIJ International*, 29(9):761, 1989.

[54] J. P. Bouchaud, M. E. Cates, J. R. Prakash, and S. F. Edwards. A model for the dynamics of sandpile surfaces. *J. Phys. I, France*, 4:1383, 1994.

[55] A. Mehta, editor. *Granular matter: an interdisciplinary approach.* Springer-Verlag, New York, 1994.

[56] P.-G. de Gennes. Surface dynamics of a granular material. *C. R. Acad. Sci. (Paris)*, 321(II):501, 1995.

[57] T. Boutreux and P. G. de Gennes. Surface flows of granular mixtures. I. General principles and minimal model. *J. Phys. I, France*, 6:1295–304, 1996.

[58] T. Boutreux. *PhD Thesis*. PhD thesis, Paris VI University, Paris, 1998.

[59] T. Boutreux. Surface flows of granular mixtures: II. Segregation with grains of different size. *The European Physical Journal B - Condensed Matter and Complex Systems*, 6(3):419–424, 1998.

[60] Hernán Makse. Stratification instability in granular flows. *Physical Review E*, 56(6):7008–7016, 1997.

[61] T. Boutreux, H. A. Makse, and P. G. de Gennes. Surface flows of granular mixtures. *The European Physical Journal B - Condensed Matter and Complex Systems*, 9(1):105–115, 1999.

[62] Pierre Jop, Yoãl Forterre, and Olivier Pouliquen. A constitutive law for dense granular flows. *Nature*, 441(7094):727–730, 2006.

[63] C. Campbell. Granular material flows – an overview. *Powder Technology*, 162(3):208–229, 2006.

[64] H. Zhu, Z. Zhou, R. Yang, and A. B. Yu. Discrete particle simulation of particulate systems: A review of major applications and findings. *Chemical Engineering Science*, 63(23):5728–5770, 2008.

[65] C. Thornton (Guest Editor). Special issue on numerical simulations of discrete particle systems. *Powder Technology*, 109:3–292, 2000.

[66] J. P. Bardet. Introduction to computational granular mechanics. In B. Cambou, editor, *Behavior of granular materials*, pages 99–169. Springer-Verlag, 1998.

[67] K. Z. Y. Yen and T. K. Chaki. A dynamic simulation of particle rearrangement in powder packings with realistic interactions. *Journal of Applied Physics*, 71:3164–3173, 1992.

[68] C. Thornton and C. W. Randall. Applications of theoretical contact mechanics to solid particle system simulation. In M. Satake and J. T. Jenkins, editors, *Micromechanics of Granular Material*, pages 133–142. Elsevier Science Publishers, Amsterdam, 1988.

[69] M. Satake. Constitution of mechanics of granular materials through the graph theory. In S. C. Cowin and M. Satake, editors, *U.S.-Japan Seminar in Continuum Mechanics and Statistical Approaches in the Mechanics of Granular Materials*, pages 47–62, 1978.

[70] Q. M. Tai and M. H. Sadd. A discrete element study of the relationship of fabric to wave propagational behaviours in granular material. *Int. J. Numer. Anal. Meth. Geomech.*, 21:295–311, 1997.

[71] Y. Kaneko, T. Shiojima, and M. Horio. DEM simulation of fluidized beds for gas-phase olefin polymerization. *Chemical Engineering Science*, 54:5809–5821, 1999.

[72] Y. Tsuji, T. Kawaguchi, and T. Tanaka. Discrete particle simulation of two-dimensional fluidized bed. *Powder Technology*, 77:79–87, 1993.

[73] O. R. Walton and R. L. Braun. Viscosity, granular-temperature, and stress calculations for shearing assemblies of inelastic, frictional disks. *J. Rheol.*, 30:949–980, 1986.

[74] H. J. Herrmann and S. Luding. Modeling granular media on the computer. *Continuum Mech. Thermodyn.*, 10:189–231, 1998.

[75] C. S. Campbell. Rapid granular flows. *Ann. Rev. Fluid Mech.*, 22:57–90, 1990.

[76] Ng T-T. Small-strain response of random arrays of spheres using DEM. *J. Eng. Mech.*, 122:239–244, 1996.

[77] C. Thornton. Force transmission in granular media. *KONA*, 15:81–90, 1997.

[78] R. Yang, R. Zou, K. Dong, X. An, and A. Yu. Simulation of the packing of cohesive particles. *Computer Physics Communications*, 177(1-2):206–209, July 2007.

[79] C. Thornton, K. K. Yin, and M. J. Adams. Numerical simulation of the impact fracture and fragmentation of agglomerates. *Journal of Physics D: Applied Physics*, 29:424–435, 1996.

[80] J. J. McCarthy. Micro-modeling of cohesive mixing processes. *Powder Technol.*, 138 (1):63–67, 2003.

[81] M. P. Allen and D. J. Tildesley. *Computer Simulation of Liquids*. Clarendon Press, Oxford, 1987.

[82] H. Zhu, Z. Zhou, R. Yang, and A. B. Yu. Discrete particle simulation of particulate systems: Theoretical developments. *Chemical Engineering Science*, 62(13):3378–3396, 2007.

[83] Charles Radeke, Benjamin Glasser, and Johannes Khinast. Large-scale powder mixer simulations using massively parallel GPU architectures. *Chemical Engineering Science*, 65(24):6435–6442, 2010.

[84] J. Roth, F. Gahler, and H.-R. Trebin. A molecular dynamics run with 5 180 116 000 particles. *International Journal of Modern Physics C*, 11(2):317–322, 2000.

[85] Kai Kadau, Timothy Germann, and Peter Lomdahl. Molecular dynamics comes of age: 320 billion atom simulation on BlueGene/L. *International Journal of Modern Physics C*, 17(12):1755–1761, 2006.

[86] Thorsten Pöschel and Thomas Schwager. *Computational Granular Dynamics (Models and Algorithms)*. Springer, Berlin, Heidelberg, New York, 2005.

[87] C. S. Campbell and C. E. Brennen. Chute flows of granular material: some computer simulations. *Journal of Applied Mechanics*, 52:172–178, 1985.

[88] K. L. Johnson. *Contact Mechanics*. Cambridge University Press, Cambridge, 1987.

[89] H. Hertz. üeber die berührung fester elastischer körper. *J. f. reine u. angewandte Math.*, 92:1–15, 1882.

[90] J. Lee and H. J. Herrmann. Angle of repose and angle of marginal stability: molecular dynamics of granular particles. *Journal of Physics A*, 26:373–383, 1993.

[91] J. T. Oden and J. A. C. Martins. Models and computational methods for dynamic friction phenomena. *Computer Methods in Applied Mechanics and Engineering*, 52(1-3):527–634, 1985.

[92] V. Buchholtz and T. Poschel. Numerical investigations of the evolution of sandpiles. *Physica A*, 202:390–401, 1994.

[93] R. D. Mindlin and H. Deresiewicz. Compliance of elastic bodies in contact. *J. Appl. Mech.*, 20:327, 1953.

[94] J. Schäfer, S. Dippel, and E. Wolf. Force schemes in simulations of granular materials. *J. Phys. I*, 67:1751–1776, 1991.

[95] J. J. McCarthy and J. M. Ottino. Particle dynamics simulation: A hybrid technique applied to granular mixing. *Powder Technology*, 97:91–99, 1998.

[96] A. Di Renzo. Comparison of contact-force models for the simulation of collisions in DEM-based granular flow codes. *Chemical Engineering Science*, 59(3):525–541, February 2004.

[97] H. Kruggel-Emden, E. Simsek, S. Rickelt, S. Wirtz, and V. Scherer. Review and extension of normal force models for the discrete element method. *Powder Technology*, 171(3):157–173, February 2007.

[98] S. T. Nase, W. L. Vargas, A. A. Abatan, and J. J. McCarthy. Discrete characterization tools for wet granular media. *Powder Technol.*, 116:214–223, 2001.

[99] C. Thornton and Z. Ning. A theoretical model for the stick/bounce behavior of adhesive, elastic-plastic spheres. *Powder Technology*, 99:154–162, 1998.

[100] J. J. McCarthy, V. Jasti, M. Marinack, and C. F. Higgs. Quantitative validation of the discrete element method using an annular shear cell. *Powder Technology*, 203(1):70 – 77, October 2010.

[101] Y. C. Zhou, B. H. Xu, A. B. Yu, and P. Zulli. Numerical investigation of the angle of repose of monosized spheres. *Physical Review E*, 64(2), 07 2001.

[102] J. A. Greenwood, H. Minshall, and D. Tabor. Hysteresis losses in rolling and sliding friction. *Proceedings of the Royal Society of London. Series A, Mathematical and Physical Sciences*, 259(1299):480–507, 1961.

[103] N. V. Brilliantov and T. Pöschel. Rolling as a "continuing collision". *The European Physical Journal B - Condensed Matter and Complex Systems*, 12(2):299–301, 1999.

[104] N. V. Brilliantov and T. Pöschel. Rolling friction of a viscous sphere on a hard plane. *EPL (Europhysics Letters)*, 42(5):511+, June 1998.

[105] L. Verlet. Computer experiments on classical fluids. I. Thermodynamical properties of Lennard-Jones molecules. *Physical Review*, 159(1):98 – 103, 1967.

[106] G. Grest. Vectorized link cell Fortran code for molecular dynamics simulations for a large number of particles. *Computer Physics Communications*, 55(3):269–285, 1989.

[107] B. Mirtich. *Impulse-based dynamic simulation of rigid body systems.* PhD thesis, University of California, Berkeley, California, 1988.

[108] Javier Bonet and Jaime Peraire. An alternating digital tree (ADT) algorithm for 3D geometric searching and intersection problems. *International Journal for Numerical Methods in Engineering*, 31(1):1–17, 1991.

[109] R. ÓConnor, J. Gill, and J. R. Williams. A linear complexity contact detection algorithm for multi-body simulation. In *Proc. 2nd U.S. Conf. on Discrete Element Methods*, pages 53 – 64, MIT, MA, 1993.

[110] Mats Oldenburg and Larsgunnar Nilsson. The position code algorithm for contact searching. *International Journal for Numerical Methods in Engineering*, 37(3):359–386, 1994.

[111] Eric Perkins and John R. Williams. A fast contact detection algorithm insensitive to object sizes. *Engineering Computations: Int J for Computer-Aided Engineering*, 18(1/2):48–62, 2001.

[112] Jean-Albert Ferrez. *Dynamic triangulations for efficient 3D simulation of granular materials.* PhD thesis, EPFL, Lausanne, EPFL, 2001.

[113] Z. Yao. Improved neighbor list algorithm in molecular simulations using cell decomposition and data sorting method. *Computer Physics Communications*, 161(1-2):27–35, 2004.

[114] E. Nezami, Y. Hashash, D. Zhao, and J. Ghaboussi. A fast contact detection algorithm for 3-D discrete element method. *Computers and Geotechnics*, 31(7):575–587, 2004.

[115] John Williams, Eric Perkins, and Ben Cook. A contact algorithm for partitioning N arbitrary sized objects. *Engineering Computations: International Journal for Computer-Aided Engineering and Software*, 21(2 − 4):235–248, 2004.

[116] D. Mason. Faster neighbour list generation using a novel lattice vector representation. *Computer Physics Communications*, 170(1):31–41, 2005.

[117] A. Munjiza, E. Rougier, and N. W. M. John. MR linear contact detection algorithm. *International Journal for Numerical Methods in Engineering*, 66(1):46–71, 2006.

[118] K. Han, Y. T. Feng, and D. R. J. Owen. Performance comparisons of tree-based and cell-based contact detection algorithms. *Engineering Computations: International Journal for Computer-Aided Engineering and Software*, 24(2):165–181, 2007.

[119] Rainald Löhner. The empty bin: A data structure for spatial search of time-varying data. *Communications in Numerical Methods in Engineering*, 23(12):1111–1119, 2007.

[120] Kejing He, Shoubin Dong, and Zhaoyao Zhou. Multigrid contact detection method. *Physical Review E*, 75(3):036710, 2007.

[121] Hiroshi Mio, Atsuko Shimosaka, Yoshiyuki Shirakawa, and Jusuke Hidaka. Cell optimization for fast contact detection in the discrete element method algorithm. *Advanced Powder Technology*, 18(4):441–453, 2007.

[122] John Peters, Raju Kala, and Robert Maier. A hierarchical search algorithm for discrete element method of greatly differing particle sizes. *Engineering Computations: International Journal for Computer-Aided Engineering and Software*, 26(6):621–634, 2009.

[123] Luyi Lu, Zhaolin Gu, Kangbin Lei, Sheng Wang, and Kiwamu Kase. An efficient algorithm for detecting particle contact in non-uniform size particulate system. *Particuology*, 8(2):127–132, 2010.

[124] Wan-Qing Li, Tang Ying, Wan Jian, and Dong-Jin Yu. Comparison research on the neighbor list algorithms: Verlet table and linked-cell. *Computer Physics Communications*, 2010.

[125] M. Moore and J. Wilhelms. Collision detection and response for computer animation. *Computer Graphics*, 22(4):289–298, 1988.

[126] M. C. Lin. *Efficient collision detection for animation and robotics.* PhD thesis, University of California, Berkeley, California, 1993.

[127] J. C. Latombe. *Robot motion planning.* Kluwer Academic Press, 1991.

[128] F. P. Preparata and M. I. Shamos. *Computational geometry.* Springer-Verlag, New York, 1985.

[129] H. Samet. *Spatial data structures: quadtree, octrees and other hierarchical methods.* Addison Wesley, 1989.

[130] Tathagata Bhattacharya and J. J. McCarthy. Improved particle-particle contact detection using efficient data structures. Poster presentation, AIChE Annual Meeting. Salt Lake City, Utah, November 2010.

[131] L. T. Fan, Yi ming Chen, and F. S. Lai. Recent developments in solids mixing. *Powder Technology*, 61(3):255–287, 1990.

[132] Derrick K. Rollins, Donna L. Faust, and Duane L. Jabas. A superior approach to indices in determining mixture segregation. *Powder Technology*, 84(3):277 – 282, September 1995.

[133] P. V. Danckwerts. The definition and measurement of some characteristics of mixtures. *Appl. Sci. Res.*, A3:279–296, 1952.

[134] P. M. C. Lacey. Developments in the theory of particle mixing. *J. Appl. Chem.*, 4:257, 1954.

[135] K. R. Poole, R. F. Taylor, and G. P. Wall. Mixing powders to fine scale homogeneity: studies of batch mixing. *Trans. Inst. Chem. Eng.*, 42:T305–T315, 1964.

[136] H. Henein, J. Brimacombe, and A. Watkinson. Experimental study of transverse bed motion in rotary kilns. *Metallurgical and Materials Transactions B*, 14(2):191–205, June 1983.

[137] J. Mellmann. The transverse motion of solids in rotating cylinders - forms of motion and transition behavior. *Powder Technology*, 118(3):251–270, August 2001.

[138] A. A. Boateng and P. V. Barr. Granular flow behaviour in the transverse plane of a partially filled rotating cylinder. *Journal of Fluid Mechanics*, 330:233–249, 1997.

[139] Suman K. Hajra, Tathagata Bhattacharya, and J. J. McCarthy. Improvement of granular mixing of dissimilar materials in rotating cylinders. *Powder Technology*, 198(2):175–182, March 2010.

[140] Isabel Figueroa, Watson L. Vargas, and Joseph J. McCarthy. Mixing and heat conduction in rotating tumblers. *Chemical Engineering Science*, 65(2):1045–1054, January 2010.

[141] Nan Gui, JianRen Fan, and Kefa Cen. A macroscopic and microscopic study of particle mixing in a rotating tumbler. *Chemical Engineering Science*, 65(10):3034–3041, May 2010.

[142] Y. Xu, C. Xu, Z. Zhou, J. Du, and D. Hu. 2D DEM simulation of particle mixing in rotating drum: A parametric study. *Particuology*, 8(2):141–149, 2010.

[143] M. M. H. D. Arntz, W. K. den Otter, W. J. Briels, P. J. T. Bussmann, H. H. Beeftink, and R. M. Boom. Granular mixing and segregation in a horizontal rotating drum: A simulation study on the impact of rotational speed and fill level. *AIChE Journal*, 54(12):3133–3146, 2008.

[144] Watson L. Vargas, Suman K. Hajra, Deliang Shi, and J. J. McCarthy. Suppressing the segregation of granular mixtures in rotating tumblers. *AIChE Journal*, 54(12):3124–3132, 2008.

[145] Nan Gui and JianRen Fan. Numerical simulation of motion of rigid spherical particles in a rotating tumbler with an inner wavelike surface. *Powder Technology*, 192(2):234–241, 2009.

[146] D. C. Rapaport. Simulated three-component granular segregation in a rotating drum. *Physical Review E (Statistical, Nonlinear, and Soft Matter Physics)*, 76(4):041302, 2007.

[147] Lori Sanfratello, Arvind Caprihan, and Eiichi Fukushima. Velocity depth profile of granular matter in a horizontal rotating drum. *Granular Matter*, 9:1–6, 2007.

[148] J Bielenberg, G Gladysz, and A Graham. A parametric study of axial segregation in granular systems. *Chemical Engineering Science*, 62(16):4177–4181, 2007.

[149] Toshihiro Kawaguchi, Kenji Tsutsumi, and Yutaka Tsuji. MRI measurement of granular motion in a rotating drum. *Particle & Particle Systems Characterization*, 23(3-4):266–271, 2006.

[150] H. P. Kuo, P. Y. Shih, and R. C. Hsu. Coupled axial-radial segregation in rotating drums with high fill levels. *AIChE Journal*, 52(7):2422–2427, 2006.

[151] H. P. Kuo, Y. C. Hsiao, and P. Y. Shih. A study of the axial segregation in a rotating drum using deformable particles. *Powder Technology*, 166(3):161–166, August 2006.

[152] S. E. Cisar, P. B. Umbanhowar, and J. M. Ottino. Radial granular segregation under chaotic flow in two-dimensional tumblers. *Phys. Rev. E*, 73:031304, 2006.

[153] N. Jain, J. M. Ottino, and R. M. Lueptow. Combined size and density segregation and mixing in noncircular tumblers. *Physical Review E*, 71(5):051301, 2005.

[154] J. E. Maneval, K. M. Hill, B. E. Smith, A. Caprihan, and E. Fukushima. Effects of end wall friction in rotating cylinder granular flow experiments. *Granular Matter*, 7(4):199–202, November 2005.

[155] S. K. Hajra and D. V. Khakhar. Radial mixing of granular materials in a rotating cylinder : Experimental determination of particle self-diffusivity. *Physics of Fluids*, 17:013101, 2005.

[156] Luis M. Gonzalez and Joaquim J. B. Romero. Solids movement in rotary kilns in the slumping regime: Model using a control plane parallel to the steepest descent. *Particle & Particle Systems Characterization*, 22(2):119–132, 2005.

[157] H. P. Kuo, R. C. Hsu, and Y. C. Hsiao. Investigation of axial segregation in a rotating drum. *Powder Technology*, 153(3):196–203, June 2005.

[158] P. Porion, N. Sommier, A. M. Faugere, and P. Evesque. Dynamics of size segregation and mixing of granular materials in a 3D-blender by NMR imaging investigation. *Powder Technology*, 141(1-2):55–68, 2004.

[159] S. K. Hajra and D. V. Khakhar. Sensitivity of granular segregation of mixtures in quasi-two-dimensional fluidized layers. *Physical Review E*, 69:031304, 2004.

[160] H. Li and J. J. McCarthy. Controlling cohesive particle mixing and segregation. *Phys. Rev. Lett.*, 90:184301, 2003.

[161] Suman K. Hajra and D. V. Khakhar. Improved tumbling mixers and rotary kilns. Indian Patent 213856, 2003.

[162] D. V. Khakhar, A. V. Orpe, and S. K. Hajra. Segregation of granular materials in rotating cylinders. *Physica A-Statistical Mechanics and Its Applications*, 318:129 – 136, 2003.

[163] R. Y. Yang, R. P. Zou, and A. B. Yu. Microdynamic analysis of particle flow in a horizontal rotating drum. *Powder Technology*, 130(1-3):138–146, February 2003.

[164] Zhixiao Zhang, Yong Chi, Shuiqing Li, Xiaojiang Shen, and Kefa Cen. A new DPIV proceeding algorithm and its application in particle motion study in a rotary drum. *Journal of Thermal Science*, 11(2):186–192, May 2002.

[165] D. C. Rapaport. Simulational studies of axial granular segregation in a rotating cylinder. *Physical Review E*, 65(6):061306+, Jun 2002.

[166] B. Laurent. Convection and segregation in a horizontal mixer. *Powder Technology*, 123(1):9–18, February 2002.

[167] B. K. Mishra, T. N. Patra, and C. V. R. Murty. Mixing and segregation of particles in rotating drums using the discrete element method. *Geotechnical Special Publication*, 117:386 – 391, 2002.

[168] Y. L. Ding, R. Forster, J. P. K. Seville, and D. J. Parker. Segregation of granular flow in the transverse plane of a rolling mode rotating drum. *International Journal of Multiphase Flow*, 28(4):635–663, April 2002.

[169] Y. L. Ding, R. N. Forster, J. P. K. Seville, and D. J. Parker. Scaling relationships for rotating drums. *Chemical Engineering Science*, 56(12):3737–3750, June 2001.

[170] Y. L. Ding, J. P. K. Seville, R. Forster, and D. J. Parker. Solids motion in rolling mode rotating drums operated at low to medium rotational speeds. *Chemical Engineering Science*, 56(5):1769–1780, March 2001.

[171] R. J. Spurling, J. F. Davidson, and D. M. Scott. The transient response of granular flows in an inclined rotating cylinder. *Chemical Engineering Research and Design*, 79(A1):51–61, January 2001.

[172] S. N. Dorogovtsev and J. F. F. Mendes. Time of avalanche mixing of granular materials in a half filled drum. *The European Physical Journal E: Soft Matter and Biological Physics*, 5(4):441–444, July 2001.

[173] D. V. Khakhar, A. V. Orpe, and J. M. Ottino. Continuum model of mixing and size segregation in a rotating cylinder: concentration-flow coupling and streak formation. *Powder Technology*, 116(2-3):232 – 245, May 2001.

[174] T. Shinbrot, M. Zeggio, and F. J. Muzzio. Computational approaches to granular segregation in tumbling blenders. *Powder Technology*, pages 224–231, May 2001.

[175] J. J. McCarthy, D. V. Khakhar, and J. M. Ottino. Computational studies of granular mixing. *Pow. Technol.*, 109:72–82, 2000.

[176] A. Samadani and A. Kudrolli. Segregation transitions in wet granular matter. *Phys. Rev. Lett.*, 85:5102–5105, 2000.

[177] N. Thomas. Reverse and intermediate segregation of large beads in dry granular media. *Phys. Rev. E*, 62(1):961–974, Jul 2000.

[178] Saikat Chakraborty, Prabhu R. Nott, and J. Ravi Prakash. Analysis of radial segregation of granular mixtures in a rotating drum. *The European Physical Journal E: Soft Matter and Biological Physics*, 1(4):265–273, April 2000.

[179] Sanjay Puri and Hisao Hayakawa. Radial and axial segregation of granular mixtures in the rotating-drum geometry. *Advances in Complex Systems (ACS)*, 04(04):469–479, 2001.

[180] Roberto Monetti, Alan Hurd, and V. M. Kenkre. Simulations for dynamics of granular mixtures in a rotating drum. *Granular Matter*, 3(1):113–116, 2001.

[181] R. Khosropour, E. Valachovic, and B. Lincoln. Flow and pattern formation in a binary mixture of rotating granular materials. *Physical Review E*, 62(1):807–812, 2000.

[182] D. Eskin and H. Kalman. A numerical parametric study of size segregation in a rotating drum. *Chemical Engineering and Processing*, 39(6):539–545, November 2000.

[183] Hernán A. Makse. Continuous avalanche segregation of granular mixtures in thin rotating drums. *Physical Review Letters*, 83(16):3186–3189, Oct 1999.

[184] C. M. Dury and G. H. Ristow. Radial segregation through axial migration. *Europhysics Letters*, 48(1):60–65, October 1999.

[185] D. V. Khakhar, J. J. McCarthy, J. F. Gilchrist, and J. M. Ottino. Chaotic mixing of granular materials in two-dimensional tumbling mixers. *Chaos*, 9:195–205, 1999.

[186] I. S. Aranson and L. S. Tsimring. Dynamics of axial separation in long rotating drums. *Physical Review Letters*, 82(23):4643–4646, 1999.

[187] S. N. Dorogovtsev. Avalanche mixing of granular solids. *EPL (Europhysics Letters)*, 41:25+, January 1998.

[188] Leonid Prigozhin and Haim Kalman. Radial mixing and segregation of a binary mixture in a rotating drum: Model and experiment. *Physical Review E*, 57(2):2073–2080, 1998.

[189] Christian Dury, Renate Knechte, and Gerald Ristow. Size segregation of granular materials in a 3D rotating drum. In *High-Performance Computing and Networking*, pages 863–865. Springer Berlin / Heidelberg, 1998.

[190] Dmitri V. Ktitarev and Dietrich E. Wolf. Stratification of granular matter in a rotating drum: cellular automaton modelling. *Granular Matter*, 1(3):141–144, December 1998.

[191] T. Elperin and A. Vikhansky. Granular flow in a rotating cylindrical drum. *Europhysics Letters*, 42(6):619–623, June 1998.

[192] K. M. Hill, A. Caprihan, and J. Kakalios. Bulk segregation in rotated granular material measured by magnetic resonance imaging. *Physical Review Letters*, 78(1):50–53, January 1997.

[193] Pik-Yin Lai, L. C. Jia, and C. K. Chan. Friction induced segregation of a granular binary mixture in a rotating drum. *Physical Review Letters*, 79(25):4994+, December 1997.

[194] Christian M. Dury and Gerald H. Ristow. Radial segregation in a two-dimensional rotating drum. *Journal de Physique I*, 7(5):737–745, May 1997.

[195] B. A. Peratt and J. A. Yorke. Continuous avalanche mixing of granular solids in a rotating drum. *EPL (Europhysics Letters)*, 35:31+, July 1996.

[196] G. H. Ristow. Dynamics of granular materials in a rotating drum. *EPL (Europhysics Letters)*, 34(4):263–268, May 1996.

[197] J. J. McCarthy, T. Shinbrot, G. Metcalfe, J. E. Wolf, and J. M. Ottino. Mixing of granular materials in slowly rotated containers. *AIChE Journal*, 42:3351–3363, 1996.

[198] F. Cantelaube and D. Bideau. Radial segregation in a 2D drum: An experimental analysis. *Europhysics Letters*, 30(3):133–138, April 1995.

[199] E. Clément, J. Rajchenbach, and J. Duran. Mixing of a granular material in a bidimensional rotating drum. *Europhysics Letters*, 30(1):7–12, April 1995.

[200] Guy Metcalfe, Troy Shinbrot, J. J. McCarthy, and Julio M. Ottino. Avalanche mixing of granular solids. *Nature*, 374:39–41, 1995.

[201] G. Baumann, I. M. Janosi, and D. E. Wolf. Surface-properties and flow of granular material in a 2-dimensional rotating-drum model. *Physical Review E*, 51(3):1879–1888, March 1995.

[202] Thorsten Pöschel and Volkhard Buchholtz. Complex flow of granular material in a rotating cylinder. *Chaos, Solitons & Fractals*, 5(10):1901–1912, 1995.

[203] G. Baumann, I. M. Janosi, and D. E. Wolf. Particle trajectories and segregation in a two-dimensional rotating drum. *Europhysics Letters*, 27(3):203–208, July 1994.

[204] G. H. Ristow. Particle mass segregation in a two-dimensional rotating drum. *Europhysics Letters*, 28(2):97–101, October 1994.

[205] M. Alonso, M. Satoh, and K. Miyanami. Optimum combination of size ratio, density ratio and concentration to minimize free surface segregation. *Powder Technology*, 68(2):145–152, November 1991.

[206] S. J. Rao, S. K. Bhatia, and D. V. Khakhar. Axial transport of granular solids in rotating cylinders. Part 2: Experiments in a non-flow system. *Powder Technology*, 67(2):153–162, 1991.

[207] P. Sai, G. Surender, A. Damodaran, V. Suresh, Z. Philip, and K. Sankaran. Residence time distribution and material flow studies in a rotary kiln. *Metallurgical and Materials Transactions B*, 21(6):1005–1011, December 1990.

[208] N. Nityanand, B. Manley, and H. Henein. An analysis of radial segregation for different sized spherical solids in rotary cylinders. *Metallurgical and Materials Transactions B*, 17(2):247–257, June 1986.

[209] H. Henein, J. Brimacombe, and A. Watkinson. An experimental study of segregation in rotary kilns. *Metallurgical and Materials Transactions B*, 16(4):763–774, 1985.

[210] Amit Chatterjee and P. Mukhopadhyay. Flow of materials in rotary kilns used for sponge iron manufacture: Part III. Effect of ring formation within the kiln. *Metallurgical and Materials Transactions B*, 14(3):393–399, 1983.

[211] Amit Chatterjee, A. Sathe, and P. Mukhopadhyay. Flow of materials in rotary kilns used for sponge iron manufacture: Part II. Effect of kiln geometry. *Metallurgical and Materials Transactions B*, 14(3):383–392, 1983.

[212] C. Wightman and F. J. Muzzio. Mixing of granular material in a drum mixer undergoing rotational and rocking motions II. Segregating particles. *Powder Technology*, pages 125–134, August 1998.

[213] M. Hehl, H. Kröger, H. Helmrich, and K. Schügerl. Longitudinal mixing in horizontal rotary drum reactors. *Powder Technology*, 20(1):29–37, 1978.

[214] J. Lehmberg, M. Hehl, and K. Schügerl. Transverse mixing and heat transfer in horizontal rotary drum reactors. *Powder Technology*, 18:149–163, 1977.

[215] G. W. J. Wes, A. A. H. Drinkenburg, and S. Stemerding. Solids mixing and residence time distribution in a horizontal rotary drum reactor. *Powder Technology*, 13(2):177–184, 1976.

[216] Abouzeid, T. S. Mika, K. V. Sastry, and D. W. Fuerstenau. The influence of operating variables on the residence time distribution for material transport in a continuous rotary drum. *Powder Technology*, 10(6):273–288, December 1974.

[217] R. Hogg and D. W. Fuerstenau. Transverse mixing in rotating cylinders. *Powder Technology*, 6:139–147, 1972.

[218] Sato K. Inoue, I. Yamaguchi K. Motion of a particle and mixing process in a horizontal drum mixer. *Kogaku Kogaku*, 34:1323–30, 1970.

[219] R. Hogg, G. Mempel, and D. W. Fuerstenau. The mixing of trace quantities into particulate solids. *Powder Technology*, 2:223–228, 1968-69.

[220] R Hogg. Diffusional mixing in an ideal system. *Chemical Engineering Science*, 21(11):1025–1038, 1966.

[221] Christian M. Dury and Gerald H. Ristow. Competition of mixing and segregation in rotating cylinders. *Phys. Fluids*, 11(6):1387, 1999.

[222] S. K. Hajra and D. V. Khakhar. Combined density and size segregation in rotating cylinders. In preparation, 2007.

[223] D. V. Khakhar and J. M. Ottino. Scaling of granular flow processes: from surface flows to design rules. *AIChE Journal*, 48(10):2157–2166, 2002.

[224] J. Duran. *Sands, Powders, and Grains*. Springer, 2000.

[225] G. H. Ristow. *Pattern Formation in Granular Materials*. Springer, 2000.

[226] J. M. Ottino and R. M. Lueptow. Materials science - On mixing and demixing. *Science*, 319:912–913, 2008.

[227] J. T. Jenkins and S. B. Savage. A theory for the rapid flow of identical, smooth, nearly elastic spherical particles. *J. Fluid Mech.*, 130:187–202, 1983.

[228] C. Wightman, P. R. Mort, F. J. Muzzio, R. E. Riman, and R. K. Gleason. The structure of mixtures of particles generated by time-dependent flows. *Powder Technology*, 84:231–240, 1995.

[229] S. J. Fiedor and J. M. Ottino. Mixing and segregation of granular matter: multilobe formation in time-periodic flows. *J. Fluid Mech.*, 533:223–236, 2005.

[230] Nitin Jain, J. M. Ottino, and R. M. Lueptow. Effect of interstitial fluid on a granular flowing layer. *Journal of Fluid Mechanics*, 508(-1):23–44, 2004.

[231] A. V. Orpe and D. V. Khakhar. Scaling relations for granular flow in quasi-two-dimensional rotating cylinders. *Physical Review E*, 64(3), September 2001.

[232] O. Walton. Application of molecular dynamics to macroscopic particles. *International Journal of Engineering Science*, 22:1097–1107, 1984.

[233] interp2() function of Matlab® R2010a (The Mathworks Inc., Natick, MA, USA) is used with 'linear' option as the interpolation method.

[234] C. Campbell. Flow regimes in inclined open-channel flows of granular materials. *Powder Technology*, 41(1):77–82, January 1985.

[235] M. Farrell, C. Lun, and S. Savage. A simple kinetic theory for granular flow of binary mixtures of smooth, inelastic, spherical particles. *Acta Mechanica*, 63(1):45–60, November 1986.

[236] Thorsten Poschel. Granular material flowing down an inclined chute: a molecular dynamics simulation. *Journal de Physique II*, 3(1):27–40, January 1993.

[237] O. R. Walton. Numerical simulation of inclined chute flows of monodisperse, inelastic, frictional spheres. *Mech. Mat.*, 16:239–247, 1993.

[238] V. Dolgunin. Segregation modeling of particle rapid gravity flow. *Powder Technology*, 83(2):95–103, May 1995.

[239] X. Zheng. Molecular dynamics modelling of granular chute flow: density and velocity profiles. *Powder Technology*, 86(2):219–227, 1996.

[240] Olivier Pouliquen and Nathalie Renaut. Onset of granular flows on an inclined rough surface: Dilatancy effects. *Journal de Physique II*, 6(6):923–935, June 1996.

[241] D. Hirshfeld and D. C. Rapaport. Molecular dynamics studies of grain segregation in sheared flow. *Physical Review E*, 56(2):2012–2018, 1997.

[242] V. Dolgunin, A. Kudy, and A. Ukolov. Development of the model of segregation of particles undergoing granular flow down an inclined chute. *Powder Technology*, 96(3):211–218, May 1998.

[243] S. Dippel and D. Wolf. Molecular dynamics simulations of granular chute flow. *Computer Physics Communications*, 121-122:284–289, 1999.

[244] L. E. Silbert, D. Ertaş, G. S. Grest, T. C. Halsey, D. Levine, and S. J. Plimpton. Granular flow down an inclined plane: Bagnold scaling and rheology. *Phys Rev E Stat Nonlin Soft Matter Phys*, 64(5 Pt 1), November 2001.

[245] C. Ancey. Dry granular flows down an inclined channel: experimental investigations on the frictional-collisional regime. *Phys Rev E Stat Nonlin Soft Matter Phys*, 65(1 Pt 1), January 2002.

[246] M. Y. Louge. Model for dense granular flows down bumpy inclines. *Phys Rev E Stat Nonlin Soft Matter Phys*, 67(6 Pt 1), June 2003.

[247] Jiayuan Zhang, Ziguo Hu, Wei Ge, Yongjie Zhang, Tinghua Li, and Jinghai Li. Application of the discrete approach to the simulation of size segregation in granular chute flow. *Industrial & Engineering Chemistry Research*, 43(18):5521–5528, September 2004.

[248] M. Barbolini, A. Biancardi, L. Natale, and M. Pagliardi. A low cost system for the estimation of concentration and velocity profiles in rapid dry granular flows. *Cold Regions Science and Technology*, 43(1-2):49–61, November 2005.

[249] O. Baran, D. Ertaş, T. C. Halsey, G. S. Grest, and J. B. Lechman. Velocity correlations in dense gravity-driven granular chute flow. *Phys Rev E Stat Nonlin Soft Matter Phys*, 74(5 Pt 1), November 2006.

[250] Suman K. Hajra and J. J. McCarthy. Unpublished work. Combined density and size segregation model was applied in a zig-zag chute flow, 2008.

[251] S. B. Savage. Disorder, diffusion and structure formation in granular flow. In D. Bideau and A. Hansen, editors, *Disorder and Granuar Media*, pages 255–285. Elsevier Science, Amsterdam, 1993.

[252] Tathagata Bhattacharya. Controlling size segregation of burden materials and prediction of void distribution in the upper part of blast furnace. LTP Project No:.SI/LTP/02/05, Tata Steel, Research & Development Division, Tata Steel, Jamshedpur 831007, India, July 2007.

[253] F. J. Massey. The Kolmogorov-Smirnov test for goodness of fit. *Journal of the American Statistical Association*, 46(253):68–78, 1951.

[254] kstest2() function of Matlab® R2011a (The Mathworks Inc., Natick, MA, USA) is used to perform two-sample Kolmogorov-Smirnov test.

[255] GSL – GNU Scientific Library at http://www.gnu.org/software/gsl/, last accessed 22nd June, 2010.

[256] N. Roussel, Thi Lien Huong Nguyen, and P. Coussot. General probabilistic approach to the filtration process. *Physical Review Letters*, 98(11):114502, 2007.

[257] L. R. Huang, E. C. Cox, R. H. Austin., and J. C. Sturm. Continuous particle separation through deterministic lateral displacement. *Science*, 304:987 – 990, May 2004.

[258] Alexander van Oudenaarden and Steven G. Boxer. Brownian ratchets: Molecular separations in lipid bilayers supported on patterned arrays. *Science*, 285(5430):1046–1048, August 1999.

[259] Chia-Fu Chou, Olgica Bakajin, Stephen W. P. Turner, Thomas A. J. Duke, Shirley S. Chan, and Edward C. Cox. Sorting by diffusion: An asymmetric obstacle course for continuous molecular separation. *PNAS*, 96(24):13762 – 13765, 1999.

[260] L. R. Huang, E. C. Cox, R. H. Austin, and J. C. Sturm. Tilted brownian ratchet for dna analysis. *Anal. Chem.*, 75(24):6963 – 6967, 2003.

[261] Deniz Ertaş. Lateral separation of macromolecules and polyelectrolytes in microlithographic arrays. *Physical Review Letters*, 80(7):1548–1551, 1998.

[262] C Keller, Florian Marquardt, and C Bruder. Separation quality of a geometric ratchet. *Physical Review E*, 65(4):041927, 2002.

[263] L. T. Fan, F. S. Lai, Y. Akao, K. Shinoda, and E. Yoshizawa. Numerical and experimental simulation studies on the mixing of particulate solids and the synthesis of a mixing system. *Comput. Chem. Eng.*, 2:19, 1978.

[264] J. P. Bouchaud and P. Le Doussal. Numerical study of a D-dimensional periodic lorentz gas with universal properties. *J. Stat. Phys.*, 41:225 – 248, 1985.

[265] L. Samson, I. Ippolito, G. G. Batrouni, and J. Lemaitre. Diffusive properties of motion on a bumpy plane. *Eur. Phys. J. B.*, 3:377, 1998.

[266] T. E. Harris. Diffusion with "collisions" between particles. *J. Appl. Prob.*, 2(2):323–338, December 1965.

[267] C. Aslangul. Classical diffusion of N interacting particles in one dimension: General results and asymptotic laws. *Europhys. Lett.*, 44:284, 1998.

[268] www.ffmpeg.org, last accessed 24th August, 2011.

[269] www.imagemagick.org, last accessed 24th August, 2011.

[270] Rafael C. Gonzalez and Richard E. Woods. *Digital image processing*. Prentice Hall, 3rd edition, 2007.

[271] J. G. Benito, G. Meglio, I. Ippolito, M. Re, and A. M. Vidales. Exit distribution function crossover in a galton board. *Granular Matter*, 9:159 – 168, 2007.

[272] A. Rosato. A perspective on vibration-induced size segregation of granular materials. *Chemical Engineering Science*, 57(2):265–275, 2002.

[273] J. F. Wambaugh, C. Reichhardt, and C. J. Olson. Ratchet-induced segregation and transport of nonspherical grains. *Phys. Rev. E*, 65(3):031308, Mar 2002.

[274] Z. Farkas, P. Tegzes, A. Vukics, and T. Vicsek. Transitions in the horizontal transport of vertically vibrated granular layers. *Phys. Rev. E*, 60(6):7022–7031, Dec 1999.

[275] Zénó Farkas, Ferenc Szalai, Dietrich E. Wolf, and Tamás Vicsek. Segregation of granular binary mixtures by a ratchet mechanism. *Phys. Rev. E*, 65(2):022301, Jan 2002.

[276] D. C. Rapaport. Mechanism for granular segregation. *Phys. Rev. E*, 64(6):061304, Nov 2001.

[277] Xiaodong Shi, Guoqing Miao, and Hua Zhang. Horizontal segregation in a vertically vibrated binary granular system. *Physical Review E*, 80(6):061306, 2009.

[278] G. Costantini, A. Puglisi, and U. M. B. Marconi. Models of granular ratchets. *Journal of Statistical Mechanics: Theory and Experiment*, 2009(07):P07004, 2009.

[279] A Igarashi and C Horiuchi. Granular segregation by an oscillating ratchet mechanism. *Acta Physica Polonica B*, 35(4):1471–1480, April 2004.

[280] A. Bae, W. Morgado, J. Veerman, and G. Vasconcelos. Single-particle model for a granular ratchet. *Physica A: Statistical Mechanics and its Applications*, 342(1-2):22–28, 2004.

[281] Ho Shum, Adam Abate, Daeyeon Lee, André Studart, Baoguo Wang, Chia-Hung Chen, Julian Thiele, Rhutesh Shah, Amber Krummel, and David Weitz. Droplet microfluidics for fabrication of non-spherical particles. *Macromolecular Rapid Communications*, 31(2):108–118, 2010.

[282] Shia-Yen Teh, Robert Lin, Lung-Hsin Hung, and Abraham Lee. Droplet microfluidics. *Lab Chip*, 8(2):198–220, 2008.

[283] Aleksandar Donev, Ibrahim Cisse, David Sachs, Evan Variano, Frank Stillinger, Robert Connelly, Salvatore Torquato, and PM Chaikin. Improving the density of jammed disordered packings using ellipsoids. *Science*, 303(5660):990–993, 2004.

[284] Satoru Yamamoto and Takaaki Matsuoka. Viscosity of dilute suspensions of rodlike particles: A numerical simulation method. *The Journal of Chemical Physics*, 100(4):3317–3324, 1994.

[285] Anand Bala Subramaniam, Manouk Abkarian, L. Mahadevan, and Howard Stone. Non-spherical bubbles. *Nature*, 438(7070):930–930, 2005.

[286] S. Bon, S. Mookhoek, P. Colver, H. Fischer, and S. Vanderzwaag. Route to stable non-spherical emulsion droplets. *European Polymer Journal*, 43(11):4839–4842, November 2007.

[287] H. L. Cheng and S. S. Velankar. Controlled jamming of particle-laden interfaces using a spinning drop tensiometer. *Langmuir*, 25(8):4412–4420, 2009.

[288] P. J. Hoogerbrugge and J. M. V. A. Koelman. Simulating microscopic hydrodynamic phenomena with dissipative particle dynamics. *Europhysics Letters*, 19(3):155–160, 1992.

[289] Eirik Flekkøy, Peter Coveney, and Gianni De Fabritiis. Foundations of dissipative particle dynamics. *Physical Review E*, 62(2):2140–2157, 2000.

[290] R. D. Groot and P. B. Warren. Dissipative particle dynamics: Bridging the gap between atomistic and mesoscopic simulation. *Journal of Chemical Physics*, 107(11):4423–4435, September 1997.

[291] Lianghui Gao, Julian Shillcock, and Reinhard Lipowsky. Improved dissipative particle dynamics simulations of lipid bilayers. *Journal of Chemical Physics*, 126(1):015101, January 2007.

[292] P. Español and P. Warren. Statistical mechanics of dissipative particle dynamics. *EPL (Europhysics Letters)*, 30(4):191–196, 1995.

[293] Alec Clark, Moti Lal, Noel Ruddock, and Patrick Warren. Mesoscopic simulation of drops in gravitational and shear fields. *Langmuir*, 16(15):6342–6350, 2000.

[294] M. Ripoll, M. H. Ernst, and P. Español. Large scale and mesoscopic hydrodynamics for dissipative particle dynamics. *The Journal of Chemical Physics*, 115(15):7271–7284, 2001.

[295] Xijun Fan, Nhan Thien, Ng Yong, Xuhong Wu, and Diao Xu. Microchannel flow of a macromolecular suspension. *Physics of Fluids*, 15(1):11–21, 2003.

[296] Revenga Z. Espaol, M. Revenga, I. Zúñiga, and P. Español. Boundary conditions in dissipative particle dynamics. *Computer Physics Communications*, 121-122:309–311, 1999.

[297] S. M. Willemsen, H. C. J. Hoefsloot, D. C. Visser, P. J. Hamersma, and P. D. Iedema. Modelling phase change with dissipative particle dynamics using a consistent boundary condition. *J. Comput. Phys.*, 162(2):385–394, 2000.

[298] E Moeendarbary, T Ng, H Pan, and K Lam. Migration of DNA molecules through entropic trap arrays: a dissipative particle dynamics study. *Microfluidics and Nanofluidics*, 8(2):243–254, 2010.

[299] Andre R. Studart, Ho Cheung Shum, and David A. Weitz. Arrested coalescence of particle-coated droplets into nonspherical supracolloidal structures. *J. Phys. Chem. B*, 113(12):3914, 2009.

[300] K. Stratford, R. Adhikari, I. Pagonabarraga, J. C. Desplat, and M. E. Cates. Colloidal jamming at interfaces: A route to fluid-bicontinuous gels. *Science*, 309(5744):2198–2201, 2005.